An investigation in the use of satellite data to develop a geomagnetic secular variation model over southern Africa

By

Emmanuel Nahayo

A thesis submitted in fulfilment of academic
requirements for the Degree of
Master of Science
in the School of Physics,
University of KwaZulu-Natal.

Durban, March 2011.

Abstract

Time variations of the geomagnetic field can be classified into two main categories of internal and external origin with respect to the surface of the Earth. It has been found that the variations that take place on longer time scales ($\sim$ 1 year and longer) are commonly known as secular variation (SV) and are of internal origin. There is a need to develop SV models using satellite data as the use of ground data is not always possible with many limitations including the limited data points and lack of data over ocean areas that are not easily accessible. Two regional geomagnetic field modelling techniques namely polynomial surface modelling (PolyM) and Spherical Cap Harmonic Analysis (SCHA) were applied to CHAMP satellite data recorded between 2001 and 2005 to investigate the use of satellite data to develop a geomagnetic SV model over southern Africa. The restricted area of investigation is between 10° and 40° South in latitude and between 10° and 40° East in longitude. The resulting regional models of this investigation were validated against the two widely used global field models IGRF 10 and CHAOS using the available ground survey data obtained during the same period over southern Africa. The results suggest that the regional field models can be derived based entirely on satellite data. However, the regional SV models can be improved by combining both high quality satellite and ground survey data, since they lack the high quality of a global field model like CHAOS.

Dedication

This thesis is dedicated to my wife Denyse Uwamwezi and my daughter Joyce I. Nahayo.

Acknowledgements

I would like to thank my supervisor and co-supervisor (Prof. Michael J. Alport and Dr. Pieter B. Kotzé, respectively) who have been always there to listen and give advice. I am deeply grateful to them for many discussions that helped me sort out the technical details of my work. I am also thankful to them for encouraging the use of correct grammar and consistent notation in my writings and for carefully reading and commenting on many revisions of this thesis.

Special thanks should be given to my examiners, Prof ADM Walker and Dr SJ Webb, for their valuable comments and suggestions to improve the manuscript.

I am grateful to Dr. John B. Habarulema for reading this thesis and commenting on the use of correct grammar in my writings.

I am also indebted to Dr. Monika Korte who gave me a source code for SCHA modelling technique. Without her support it would not have been possible to finish my study.

Most importantly, none of this would have been possible without the love and patience of my family. My immediate family members to whom this thesis is dedicated to, have been a constant source of love, concern, support and strength all the time. I would like to express my heart-felt gratitude to them.

Finally, I appreciate the financial support from the National Research Foundation and the Hermanus Magnetic Observatory for funding this study, paying university tuition fees and making computer resources available.

Declaration - Plagiarism

I, ..., declares that

1. The research reported in this thesis, except where otherwise indicated, is my original research.

2. This thesis has not been submitted for any degree or examination at any other university.

3. This thesis does not contain other persons data, pictures, graphs or other information, unless specifically acknowledged as being sourced from other persons.

4. This thesis does not contain other persons' writing, unless specifically acknowledged as being sourced from other researchers. Where other written sources have been quoted, then:

(a) Their words have been re-written but the general information attributed to them has been referenced

(b). Where their exact words have been used, then their writing has been placed in italics and inside quotation marks, and referenced.

5. This thesis does not contain text, graphics or tables copied and pasted from the Internet, unless specifically acknowledged, and the source being detailed in the thesis and in the References sections.

Signed

.....

Contents

List of Tables

List of Figures

Chapter 1

Introduction

The majority of the magnetic field measured at the Earth's surface has its origin in electrical currents flowing in the liquid outer core. These electrical currents result from a dynamo process where convective motions of the fluid outer core stretch and distort field lines in a self-sustaining manner. This field is known as the *main* or *core field* (Mandea *et al.*, 2007). In addition to this dominant contribution of the Earth's magnetic field, the lithospheric field arising from rocks that formed from the molten state and thus contain information about the magnetic field at the time of their solidification must also be considered. Another significant contribution is that of external sources which originate in the ionosphere and magnetosphere. These variable sources include the daily solar quiet variations, the ring current variations, the contributions from the magnetic storms and many other current systems like the field-aligned currents, and the auroral and equatorial electrojets. Measurable secondary magnetic fields can be induced by electrical currents generated in electrically conducting materials in the mantle by time-varying external magnetic fields. Finally, the motion of charged particles (ions) in the ocean, moving through the core-generated magnetic field can also produce electrical currents and measurable magnetic fields.

The temporal variation of the geomagnetic field covers a large range of time-scales, from seconds to millennia. Variations on short time scales are mostly dominated by external sources, while variations on longer timescales ($\backsim$ 1 year and longer) are collectively known as *secular variation* (SV) and are predominantly of internal origin (Kotzé, 2003). It has been known that secular change is a comparatively local phenomenon and that it does not proceed in a regular way all over the Earth, giving rise to regions where the field changes more rapidly than elsewhere, for instance southern Africa and the surrounding ocean areas.

Accurate models of the geomagnetic main field and its SV are very important for the evaluation of the temporal changes, but also for many other studies such as the physics of the Earth's deep interior, global and regional mapping (Langlais and Mandea, 2000).

Regional modelling is a powerful method for detailed description of potential fields over areas where an appropriate dense set of data is available. The data may include shipborne measurements at sea level, ground observations, aeromagnetic measurements at altitudes up to 4 or 5 km, and satellite measurements such as CHAMP at altitudes of 300 km and higher. In general, regional models are usually based on denser data than global models, and are therefore more accurate over their regions of application than the global models, and their release is also more timely.

One region where the most rapid decrease of field intensity is observed at the Earth's surface stretches across southern Africa and south Atlantic ocean (Korte *et al.*, 2007). An urgent need therefore exists to monitor the time-variation of the geomagnetic field over southern Africa. Two regional modelling techniques (polynomial surface modelling (PolyM) and Spherical Cap Harmonic Analysis (SCHA)) were applied to CHAMP satellite data recorded between 2001 and 2005 to investigate the possibility of developing geomagnetic SV field models over southern Africa.

1.1 Scientific objectives

The aim of this study is to investigate the use of satellite data to develop geomagnetic SV models over southern Africa. In particular, night and quiet-time CHAMP satellite data recorded over southern Africa during the period 2001-2005 between 10°S and 40°S in latitude and 10°E and 40°E in longitude are to be selected with a help of Dst indices. The two regional modelling techniques (PolyM and SCHA) are applied to this dataset and the resulting models are validated against global field models IGRF 10 and CHAOS.

1.2 Motivation

Southern Africa is one of several areas on Earth where the rapid decrease of field intensity is observed. The accurate regional SV models can help to understand the time-variation of geomagnetic field over this region and play an important role in studying core-mantle interactions to understand better the geomagnetic polarity reversals (Gubbins, 1994). The derivation of regional SV models based entirely on satellite data therefore needs to be investigated.

1.3 Thesis layout

This thesis consists of 6 chapters. Chapter 1 gives the general introduction to the topic. In chapter 2, the literature review emphasizing the work done in geomagnetic field modelling and the different modelling techniques, particulary the ones applicable for restricted areas, is presented. Chapter 3 gives a comprehensive description of the data sources and selection criteria along with the details of instrumentation used for data collection. Different methods of data collection and analysis are also discussed in this chapter. In chapter 4 CHAMP satellite data are modelled using the surface polynomial modelling technique and an investigation of the occurrence of SV impulses (geomagnetic jerks) in 2003 and 2004 over southern Africa is conducted. Chapter 5 deals with spherical cap modelling and the detailed comparison between regional and global models. Chapter 6 gives the conclusions about major findings of this investigation and gives suggestions how regional SV modelling can be improved over southern Africa.

Chapter 2

Literature review: Geomagnetic field modelling

2.1 The geomagnetic field

2.1.1 Introduction

The terrestrial magnetic field is a complex system with contributions from different sources. As observed on the Earth's surface, the field contains components of internal (core and lithospheric fields) (fig. 2.1) and external origins (ionospheric and magnetospheric fields). The geomagnetic field changes on different space and time scales. The core field that represents the dominant part of the Earth's magnetic field and its variation over time scales of decades to centuries is referred to as secular variation (Verbanac, 2007). The lithospheric field includes sources located both in the upper mantle and in the crust, varying from the fractions of nT to several thousands nT.

The ionospheric and magnetospheric fields are respectively related to ionospheric current systems (equatorial and polar electrojets) and magnetospheric currents (in the magnetopause in the direction of the Sun, tail and ring currents surrounding equatorial region at a distance of several Earth radii)(fig. 2.2). The values of those fields at the Earth's surface are of few tens of nT, but can reach few hundreds, even thousands nT during magnetic storms. The variations with periods from seconds to few days are generally external in origin.

2.1.2 The internal field

The main part of the Earth's magnetic field is due to a geodynamo mechanism operating in the liquid, metallic, outer core, and is known as the main field or core field (Mandea *et al.*, 2000). The geomagnetic field can, to a first order approximation, be regarded

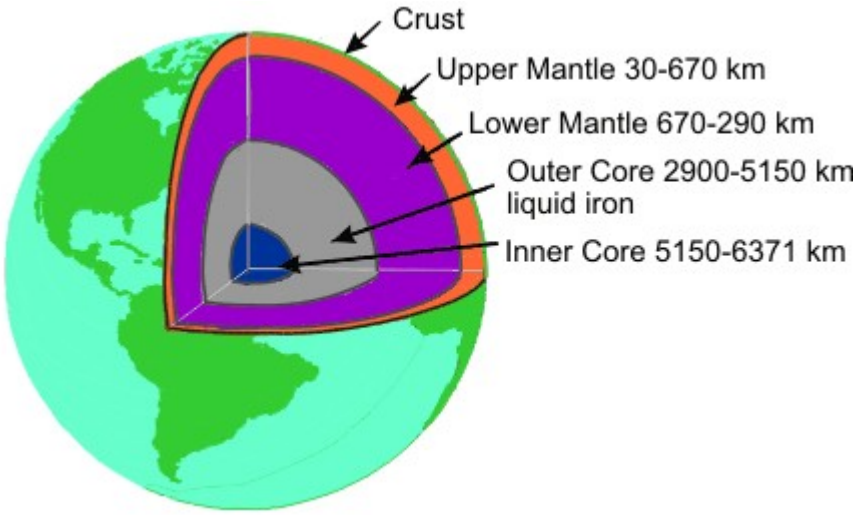

Figure 2.1: Earth's interior . Figure adopted from the website of Natural Resources Canada (NRCan, 2008).

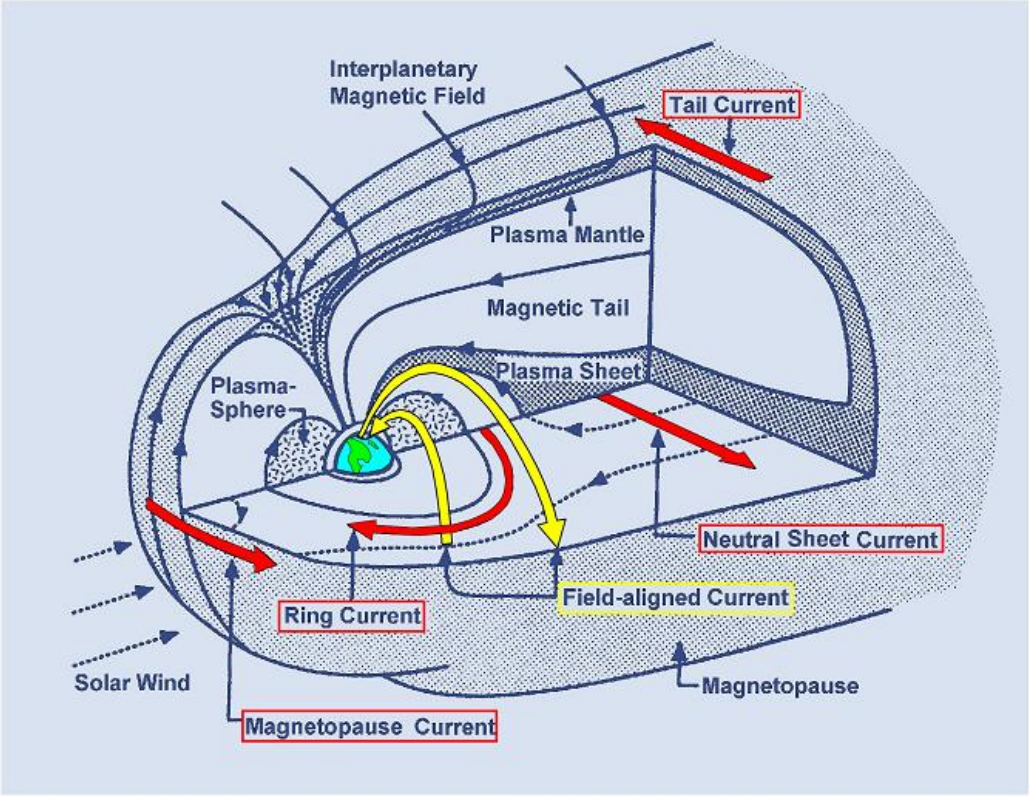

Figure 2.2: Sketch of current systems that contribute to the external magnetic field. Figure adopted from Kivelson and Russell (1995).

as a dipolar electromagnet at the center of the Earth, which is inclined at 11.5° to the rotational axis (fig. 2.3). Its strength at the Earth's surface varies from approximately 30000 nT near the equator to 60000 nT near the poles. The magnetic field is often visualised in terms of magnetic field lines or lines of force which move from the north pole of the magnet to the south pole (fig. 2.3).

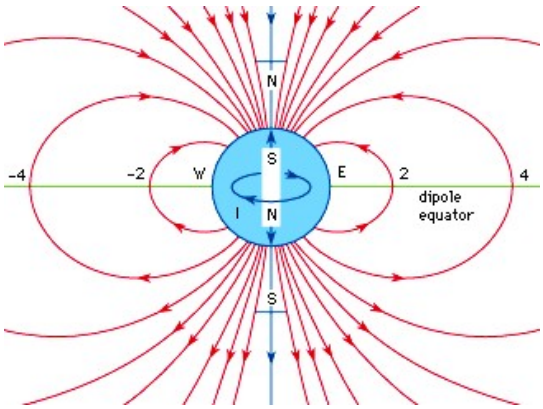

Figure 2.3: Sketch of dipole magnetic field lines. Figure adopted from the website of the Encyclopedia Britannica (Encyclopeadia Britannica, 1994).

The Earth is composed of layers: a thin outer crust, a silicate mantle, an outer core and an inner core. Both temperature and pressure increase with depth within the Earth. The temperature increases at a rate of 25°/km. The temperature at the core mantle boundary is roughly 4800°C, hot enough for the outer core to exist in a liquid state. Because of the increased pressure, the inner core is a solid composed primarily of nickel and iron, with a small percentage of lighter elements. The outer core is in constant motion due to both the Earth's rotation and convection. The convection is driven by the upward motion of the light elements as the heavier elements freeze onto the inner core (fig. 2.4).

The best known hypothesis for generating a geomagnetic field is that the liquid outer core of the Earth maintains an electric current as a self-excited dynamo (Campbell, 1997). From Maxwell's equations, the electric and changing magnetic fields are closely linked and can affect each other.

Faraday's law of induction states that the electromotive force induced in a circuit is directly proportional to the time rate of change of magnetic flux through the circuit,

$$\nabla \times \boldsymbol{E} = -\frac{\partial \boldsymbol{B}}{\partial t} \tag{2.1}$$

where $\boldsymbol{E}$ and $\boldsymbol{B}$ are electric field and magnetic field vectors respectively.

According to the principle of electrical motors, the motion of an electrical conductor through a magnetic field will cause electrons to flow thus generating an electrical current. To understand the self-excited dynamo concept, consider the following me-

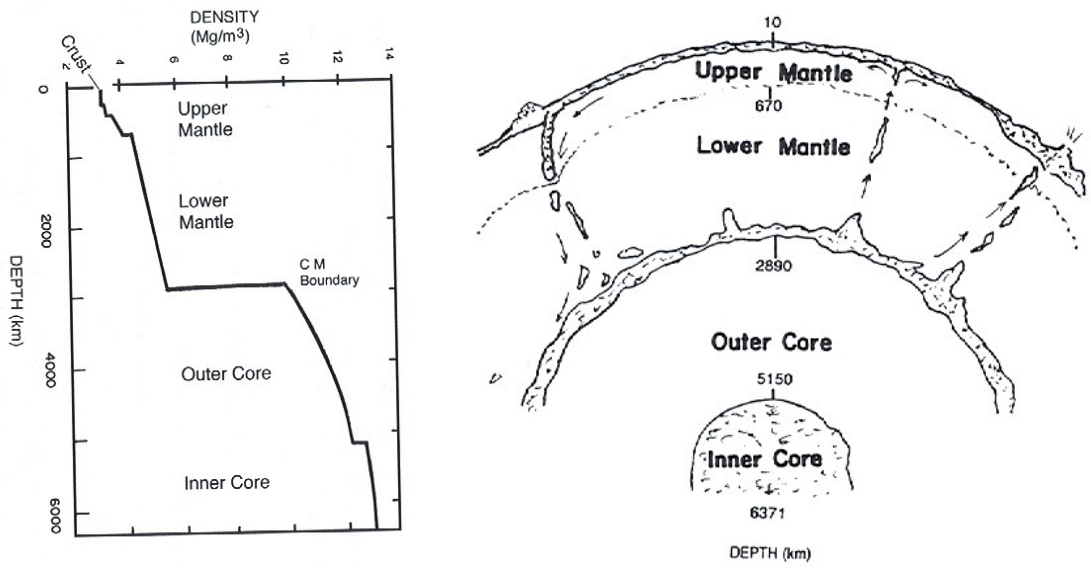

(a) (b)

Figure 2.4: (a) Density variation with depth within the Earth. (b) schematic representation of regions within the Earth. Figures are adopted from Campbell (1997).

chanical model. Recall that the right hand rule means that when the current direction is indicated by the thumb pointing along a clockwise in the horizontal plane, the resulting field, $\boldsymbol{B}$, inside the circle will be directed axially downward, as the fingers would point (fig. 2.5). Also, the motion of a conductor (at velocity v) in a magnetic field will generate a current in the direction that a right-hand screw (fig. 2.5) would turn while moving the vector $\boldsymbol{v}$ into the vector $\boldsymbol{B}$ (Campbell, 1997).

Figure 2.6 illustrates the mechanical form of the simplistic self-excited dynamo. Starting with a small upward-directed field, $\boldsymbol{B}$, and the rotating disk, at the brush connection (on the right) the right-hand rule describes the direction of a current, radially outward on the disk that proceeds through the brush connection and then down the spiral wire encircling the dynamo axis. The current in the spiral wire then increases the strength of the field, causing the self-generation of more current. The spin of rotating disk drives the system to larger and larger $\boldsymbol{B}$ field generation (Campbell, 1997).

The Earth's magnetic field is generated in the fluid outer core by the self–exciting dynamo process. Electrical currents flowing in the slowly moving molten iron core generate the magnetic field. This is known as the main field and exhibits long-term changes which occur at irregular and unpredictable rates. Superimposed on the main field is a contribution from permanent magnetism near the surface of the Earth, known as lithospheric anomalies, which is associated with variations in the geological or geophysical properties of the material making up the crust. This field is some 400 times smaller than the core contributions and generally ranges from 0 to $\pm$1000 nT. It is carried by the crust and the upper part of the Earth's mantle, within a thin layer 10

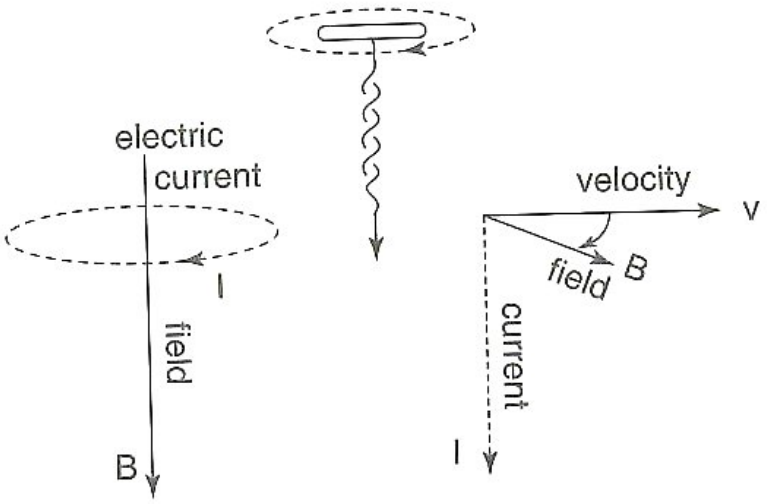

Figure 2.5: Right-hand screw (shown at the top) correspondence for (at left) direction of $\boldsymbol{B}$ *field from loop of current I, and (at right) direction of current I, from motion of conductor moving at velocity* $\boldsymbol{v}$ *in a magnetic field* $\boldsymbol{B}$*. Figure adopted from Campbell (1997).*

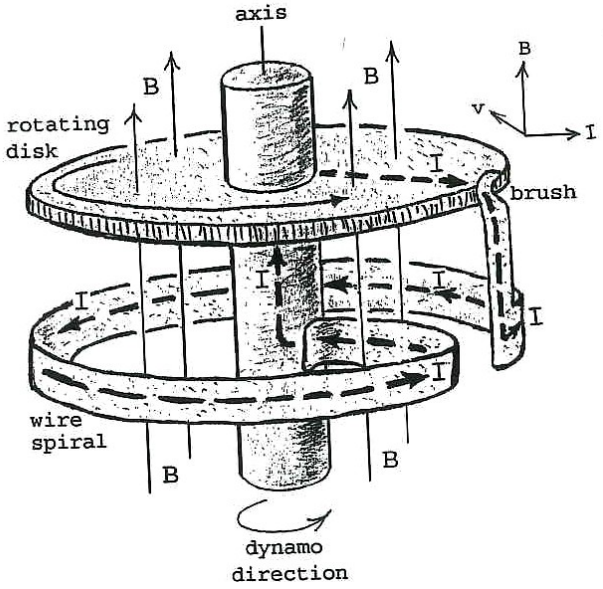

Figure 2.6: Self-excited dynamo current machine. Figure adopted from Campbell (1997)

km - 70 km thick, depending on the location.

2.1.3 The external field

The external magnetic field is generated from magnetic sources outside the Earth, and is mainly produced by tidal motions in the ionosphere and interactions of the Earth's magnetosphere with the solar wind.

The geomagnetic field has a regular variation with a fundamental period of 24 hours (fig. 2.7). This regular variation is dependent on local time, latitude, season and solar cycle. It is caused by electrical currents in the upper atmosphere at altitudes between 100 and 130 km above the Earth's surface. At these altitudes the atmosphere is significantly ionised by the Sun's ultraviolet and X-rays radiation. These ions are moved by winds and tides arising from the heating effects of the Sun and the gravitational pull of the Sun and the Moon. This creates the required conditions for a dynamo to operate that are the motion of a conductor in a magnetic field and the formation of two cells one in the Sun-lit Northern hemisphere in an anti-clockwise direction and the other in the Sun-lit Southern hemisphere in a clockwise direction. The magnetic effect of these current systems is observed on the ground at observatories as solar quiet-day variation (Chapman, 1964).

In addition to the regular daily variation, the Earth's magnetic field also exhibits irregular disturbances leading to the occurrence of magnetic storms. These magnetic storms are caused by interaction of the solar wind, and disturbances therein, with the Earth's magnetic field (fig. 2.8). Events such as coronal mass ejections and solar flares are the main drivers of magnetic storms (fig. 2.9) obscuring the daily variation.

The solar flare is an explosive phenomenon that usually occurs in a single active region around a group of sunspots and lasts for a relatively short period of time (minutes to hours). It is the most intense and energetic among various types of solar activity (Zirin, 1988). It occurs when magnetic energy that has built up in the solar atmosphere is suddenly released. As the magnetic energy is being released, particles including electrons, protons and heavy nuclei are heated and accelerated in the solar atmosphere. When the material from the solar flare reaches the Earth, the upper atmosphere of the Earth becomes more ionized and expands. This contributes to the current systems that have an effect on the observed geomagnetic field on Earth (fig. 2.10a).

The coronal mass ejection (CME) is an ejection of material from the solar corona, usually observed with a white-light coronagraph (fig. 2.10b). The ejected material is a plasma consisting primarily of electrons and protons (in addition to small quantities of heavier elements such as helium, oxygen, and iron), plus the entraining coronal magnetic field.

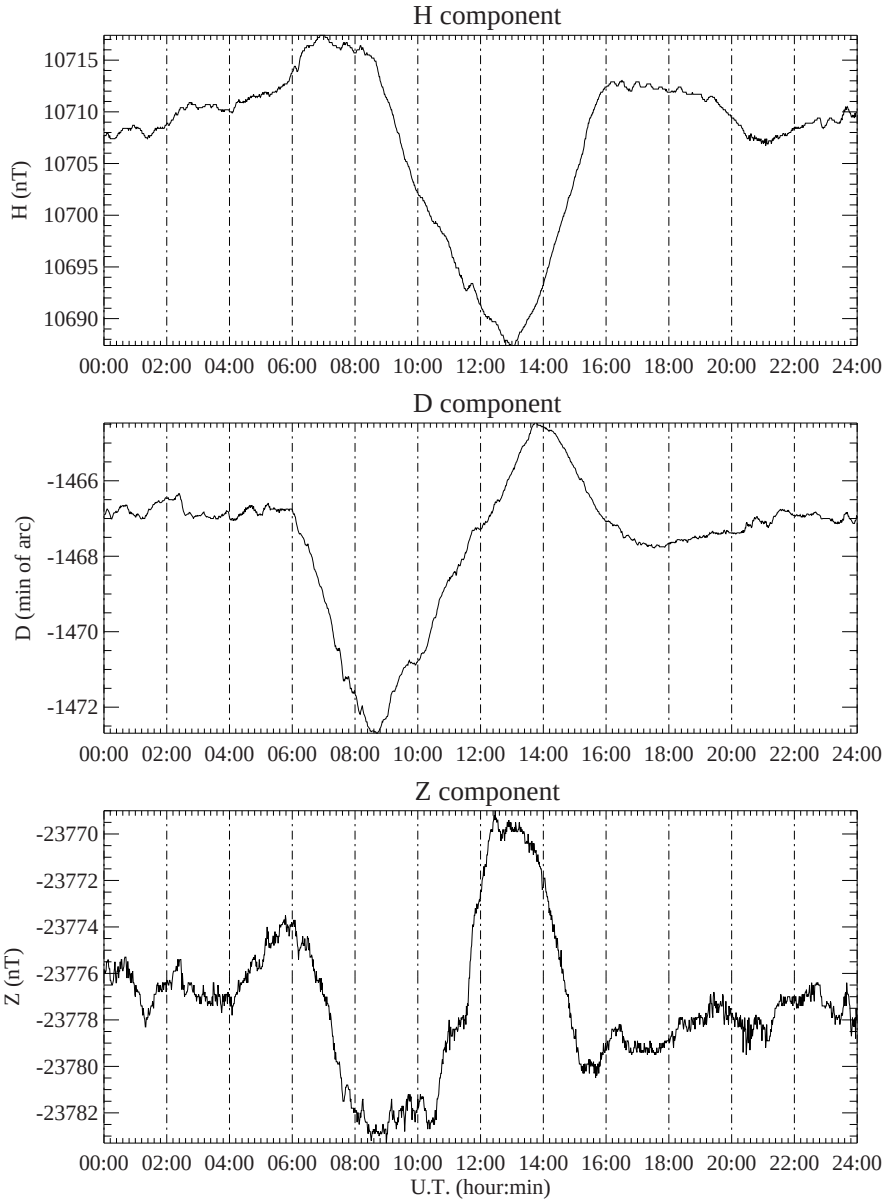

Figure 2.7: The plot of a solar-quiet magnetic variation day of 1-min average data recorded on 22^{nd} June 2004 at Hermanus Magnetic Observatory.

However, how the Sun's magnetic field connects with the geomagnetic field makes a big difference in how solar activity affects Earth (Fox and Murdin, 2001). When a mass of plasma is ejected from the Sun, the plasma travels outward in the solar wind. These plasma bursts have their own magnetic fields which are carried along with the plasma. When the direction of the solar wind field is opposite the direction of Earth's field, magnetic reconnection occurs, and the magnetosphere essentially becomes joined to the solar magnetic field. In this condition, the Earth is much more prone to the effects of the solar wind. Solar wind particles can enter the magnetosphere more easily, and those already within the magnetosphere are energised. This results in creation of current systems as illustrated in fig. 2.2. If the magnetic field of the solar wind is in the

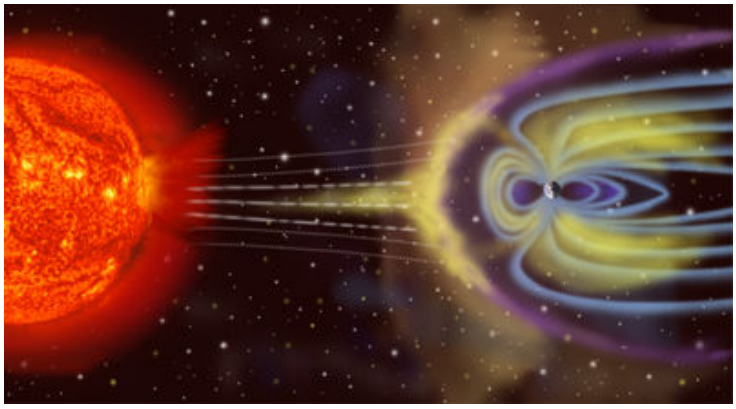

Figure 2.8: Solar particles interact with Earth's magnetosphere. Figure adopted from the website of Encyclopeadia of Earth (Stone, 2008).

same direction as the Earth's field, then magnetic reconnection does not occur and the magnetosphere is much more protected from the solar wind. Under these conditions, the effects of CMEs are much less significant (Fox and Murdin, 2001).

2.1.4 Geomagnetic field observations

The geomagnetic field vector, B, is described as illustrated in fig. 2.11 by the orthogonal components X (north component), Y (east component, positive eastwards) and Z (vertical component, positive downwards), the total intensity F, the horizontal intensity H, the inclination (or dip) angle I (the angle between the horizontal plane and the field vector, measured positive downwards) and declination (or magnetic variation) D (the horizontal angle between true north and the field vector, measured positive eastwards).

Declination, inclination and total intensity can be computed from the orthogonal components using the following equations:

$$D = tan^{-1}\left(\frac{Y}{X}\right) \tag{2.2}$$

$$I = tan^{-1}\left(\frac{Z}{H}\right) \tag{2.3}$$

$$F = \sqrt{H^2 + Z^2} \tag{2.4}$$

where H is given by

$$H = \sqrt{X^2 + Y^2} \tag{2.5}$$

The study of Earth's geomagnetic field requires the continuous recording of the magnetic field at selected locations that must be magnetically clean and remain so for the

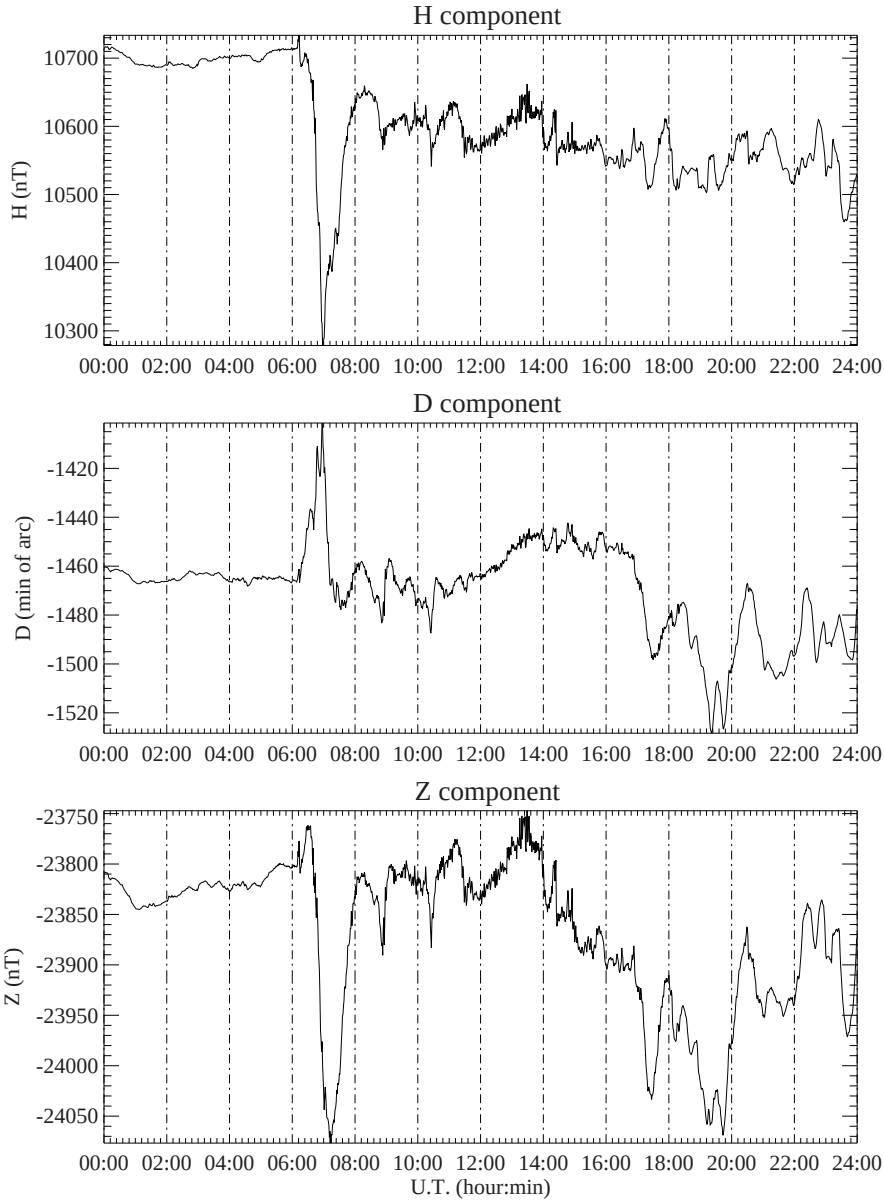

Figure 2.9: The plot of a very disturbed magnetic variation day of 1-min average data recorded on 29^{th} October 2003 at Hermanus observatory. It is shown that between 6:00 and 8:00 UT the change of magnetic variation reached around 400 nT in the H component.

foreseeable future. These locations are known as magnetic observatories where the absolute vector observations of the Earth's magnetic field are recorded accurately and continuously, with a time resolution of one minute or less, over a long period of time ($\sim$1 year and longer). Most of observatories have joined the International Real-time Magnetic Observatory Network (INTERMAGNET). The locations of 2007 operating INTERMAGNET observatories around the world are shown in Figure 2.12.

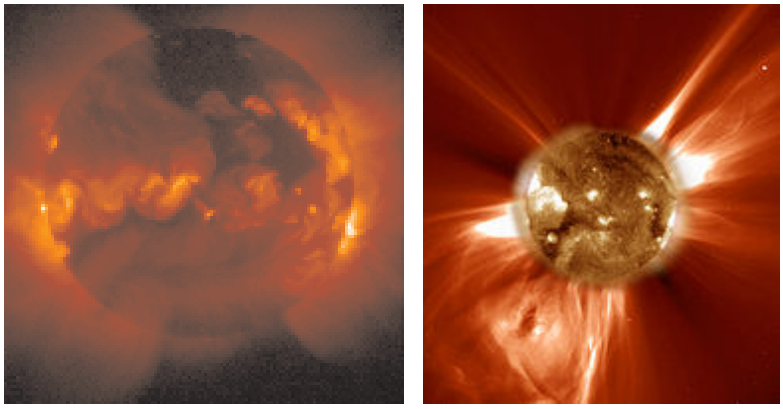

(a) Solar flare (b) Coronal mass ejection

Figure 2.10: (a) Soft x-ray image of a solar flare on the Sun (adopted from the website of National Aeronautics and Space Administration (NASA, n.d.)). (b) A coronal mass ejection (adopted from the website of National Aeronautics and Space Administration (Nemiroff, 2007)).

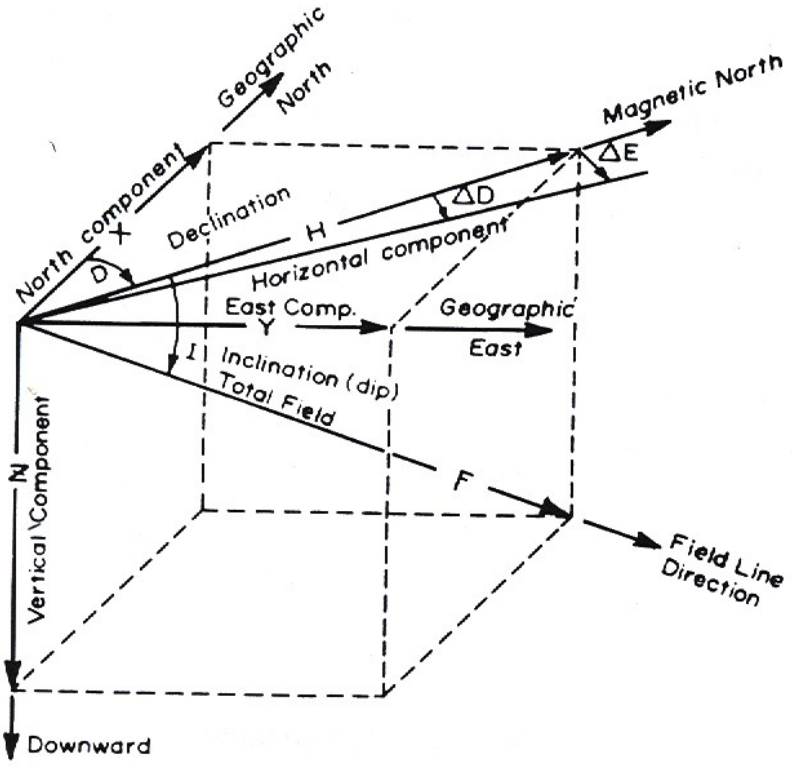

Figure 2.11: The geomagnetic field components. Figure adopted from Campbell (1997).

2.2 Geomagnetic secular variation

Haines (1985) defines the SV as the temporal change in the Earth's main magnetic field over many years. That is, it is the time derivative of the main magnetic field with periods greater than several years. Being analytic, it may be expanded in a power

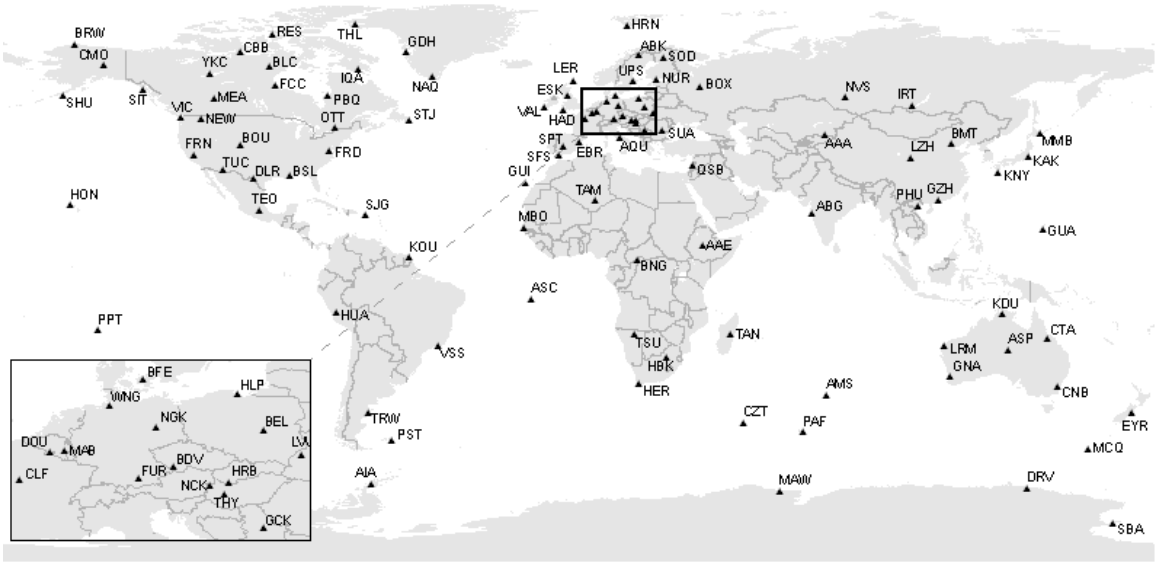

Figure 2.12: The 2007 INTERMAGNET observatories map. Figure adopted from the INTERMAGNET website (INTERMAGNET, 2007).

series:

$$\dot{B}(s,t) = b_0(s) + b_1(s)t + b_2(s)t^2 + \dots \tag{2.6}$$

where s denotes the spatial dependence (latitude, longitude, altitude) and t denotes the time dependence. The main field may be determined by integration:

$$B(s,t) = B(s,0) + b_0(s)t + \frac{1}{2}b_1(s)t^2 + \frac{1}{3}b_2(s)t^3 + \dots \tag{2.7}$$

where the integration constant $B(s,0)$ is the main field at the epoch $t = 0$.

Haines (1985) further states that the SV, in practice, within the context of equation 2.6, is used in the study of fluid motions in the core, the conductivity of the core and mantle, electric currents in the ionosphere and magnetosphere, and ultimately the origin and maintenance of the Earth's magnetic field itself. And within the context of equation 2.7, since the Earth's field is continually changing, SV is used to update magnetic data that would otherwise be unusable for epochs other than those close to which the data were acquired.

Time variations of the geomagnetic field can be classified into two main categories of internal or external origin with respect to the surface of the Earth. Even if it is not possible to establish a precise boundary between the two contributions, by applying spherical harmonics analysis to the geomagnetic field time variations, it has been found that the variations on time scales shorter than 1 year are of external origin while those that take place on longer time scales (commonly referred to as SV) are of internal origin

(Kotzé, 2003). The rapid variations of the geomagnetic field are mainly due to factors external to the earth and essentially related to solar activity. The rapid geomagnetic variations are driven by external currents in the ionosphere and magnetosphere, and internal telluric currents induced in the Earth (Pulkkinen *et al.*, 2003).

The Earth's magnetic field occasionally shows rapid changes in its temporal variations. These events are known as SV impulses or geomagnetic jerks and can be observed as a change in the slope of SV observations. The extent, duration and the underlying processes causing geomagnetic jerks are still debated. Indeed, the question of whether geomagnetic jerks are external or internal in origin has been a matter of debate since the 1980s, mainly because of the difficulty in separating internal from external contributions to the magnetic data (Chambodut *et al.*, 2007), but an internal origin has been supported by many authors including Alexandrescu *et al.* (1996), Bellanger *et al.* (2001) and Bloxham *et al.* (2002). At the Earth's surface, geomagnetic jerks in the field components are represented as two second-degree polynomials of time with a change in curvature at the times of the event; the corresponding SV (the first time derivative of the geomagnetic field) has a V-shaped feature (Courtillot *et al.*, 1984).

2.2.1 Secular variation in southern Africa

Korte *et al.* (2007) state that one region where the most rapid decrease of field intensity is observed at the Earth's surface stretches across southern Africa and the south Atlantic ocean. This coincides with a region known as the South Atlantic Anomaly where the field is already 30% weaker compared to other locations at the same latitude. Global geomagnetic field models show that the changes are associated with the growth of a patch of reverse magnetic flux, compared to the dominating dipole flux direction, at the core-mantle boundary beneath southern Africa and the south Atlantic ocean (Wardinski and Holme, 2006).

To monitor the variation of the geomagnetic field in southern Africa, three geomagnetic observatories have continuously recorded the geomagnetic field across the sub-continent over many years (60, 40 and 30 years at HER, TSU and HBK respectively). These are the observatories at Hermanus (HER) and Hartebeesthoek (HBK) in South Africa and at Tsumeb (TSU) in Namibia. The observations over the past decades reveal that significant changes occurred in the gradients of the temporal behaviour of the geomagnetic field (fig. 2.13).

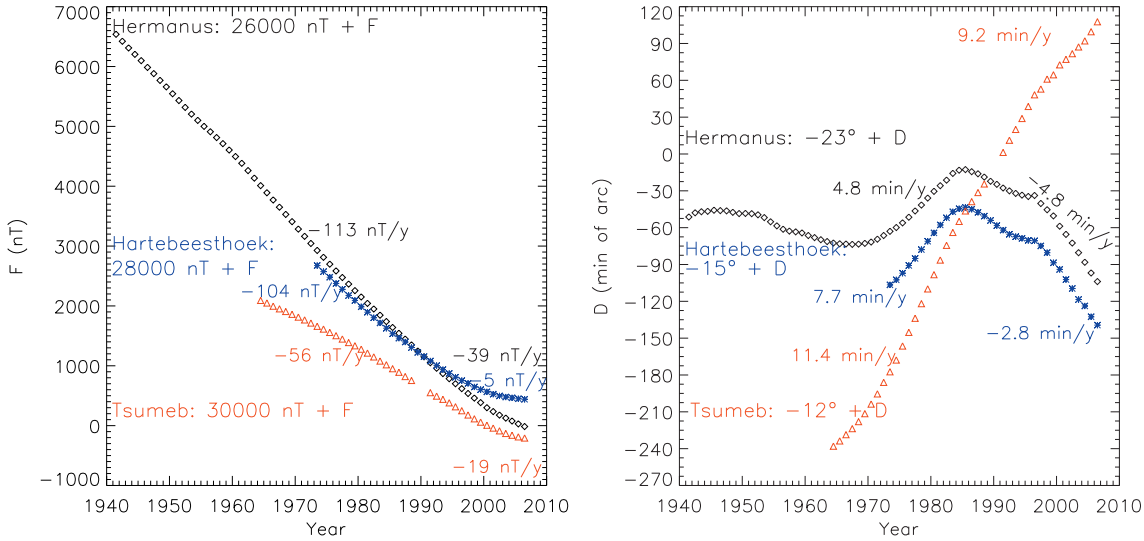

(a) (b)

Figure 2.13: (a) Annual mean total field (F). (b) Annual mean declination (D)

2.3 Geomagnetic field modelling techniques

2.3.1 Global modelling

Maxwell's great contribution to the understanding of electromagnetic phenomena was to show that all the measurements and laws of field behavior could be derived from a few compact mathematical expressions. In the study of Earth's magnetic field, one of these equations is adjusted for the assumptions that only negligible electric field changes occur and the amount of current flowing across the boundary between the Earth and its atmosphere is relatively insignificant, thus for the magnetic field $\boldsymbol{B}$ at the Earth's surface,

$$\boldsymbol{\nabla} \times \boldsymbol{B} = \mathbf{0}. \tag{2.8}$$

This equation requires that the field be obtained from the negative gradient of a scalar potential V,

$$\boldsymbol{B} = -\boldsymbol{\nabla} V. \tag{2.9}$$

The other condition to be met is that the divergence of the field is zero,

$$\boldsymbol{\nabla} \cdot \boldsymbol{B} = 0. \tag{2.10}$$

Now, putting Equations (1.8) and (1.9) together, we obtain Laplace's equation

$$\boldsymbol{\nabla} \cdot \boldsymbol{\nabla} V = \nabla^2 V = 0. \tag{2.11}$$

The familiar technique of global modelling is Spherical Harmonic Analysis. It comes from the mathematical solution of Laplace's equation subject to the appropriate bound-

ary conditions. The solution comprises of two parts from an internal and external origin,

$$V = V_i + V_e. \tag{2.12}$$

When V is determined from measurements of the field about Earth, analyses show that essentially all the contribution comes from the V_i part of the potential function expansion (Campbell, 1997). In spherical coordinates,

$$V_i(r, \theta, \lambda) = a \sum_{n=1}^{\infty} (\frac{a}{r})^{n+1} \sum_{m=0}^{n} [g_n^m cos(m\lambda) + h_n^m sin(m\lambda)] P_n^m(\theta), \tag{2.13}$$

where a is the Earth's radius, and r, θ, and λ are radial distance, colatitude and longitude respectively. The g_n^m and h_n^m are the Gauss coefficients and the $P_n^m(\theta)$ are the associated Legendre functions with order m and degree n . The IGRF model was developed based on the above equation.

2.3.2 Some regional modelling techniques

Theoretically, regional modelling is a powerful method for detailed description of potential fields over areas where an appropriate dense set of data is available. The advent of satellite magnetic measurements brought a major breakthrough for the reconstruction of a regional magnetic field at short wavelengths. For a limited portion of the Earth, spherical harmonics which are well known for global modelling, are no longer suitable, since the orthogonality over the restricted area no longer exists (Thébault *et al.*, 2004). Another intrinsic limitation of global modelling is the fact that data covering the entire globe is needed for a global model to be well defined. This implies that its realisation takes a significant time, always longer than the preparation of a regional model (De Santis *et al.*, 1997). Common techniques, like polynomial modelling in latitude and longitude or rectangular harmonic analysis have been used successfully before the availability of satellite data but the resulting models could not be properly upward or downward continued (Haines, 1990). The spherical cap harmonic analysis proposed by Haines (1985) is an attractive regional modelling technique. Its formalism resembles a natural extension of the spherical harmonic analysis. The method is claimed to be valid over any spherical cap at any altitude above the surface of the Earth (Thébault *et al.*, 2004). Some difficulties were however encountered by practitioners of this technique leading to a new proposal for spherical cap harmonic modelling known as the Revised Spherical Cap Harmonic Analysis (Thébault *et al.*, 2006a).

2.3.2.1 Surface polynomials

The first analytical method used to produce regional models was that of surface polynomials, by which is meant polynomials that are functions of only colatitude θ and longitude λ, not of radial distance r. For example the declination D would be expressed as:

$$D = a_0 + a_1\theta + a_2\lambda + a_3\theta^2 + a_4\theta\lambda + a_5\lambda^2 + \cdots \tag{2.14}$$

where a_0, a_1, a_2, a_3, a_4, a_5,$\cdots$ are polynomial coefficients.

The detailed theory and application of this technique is given in chapter 4.

2.3.2.2 Rectangular Harmonic Analysis (RHA)

This technique is applied over a small portion (less than 2,000,000 km^2) of the Earth's surface that can be considered as a two-dimensional surface. In the region of interest, data can be collected at different close altitudes and converted in x, y and z coordinates. The solution of Laplace's equation in x, y and z coordinates gives the potential expression in the form of a double Fourier series of sines and cosines multiplied by an exponential of z (Haines, 1990):

$$\begin{aligned} V = Ax + By + Cz &+ \sum_{m=1}^{M_0}\{a_0^m cos(mx) + b_0^m sin(mx)\}exp\{-k_x mz\} \\ &+ \sum_{n=1}^{N_0}\{a_n^0 cos(ny) + c_n^0 sin(ny)\}exp\{-k_y nz\} \\ &+ \sum_{m=1}^{M}\sum_{n=1}^{N}\{a_n^m cos(mx)cos(ny) + b_n^m sin(mx)cos(ny) \\ &+ c_n^m cos(mx)sin(ny) + d_n^m sin(mx)sin(ny)\}exp\{-\sqrt{(k_x m)^2 + (k_y n)^2}z\}, \end{aligned} \tag{2.15}$$

where A, B, C, a_0^m, b_0^m,a_n^0, c_n^0, a_n^m, b_n^m,c_n^m and d_n^m are coefficients.

the negative gradient of which gives the magnetic field $\boldsymbol{B}$:

$$\boldsymbol{B} = -\boldsymbol{\nabla} V. \tag{2.16}$$

The x, y, and z are ordinary cartesian, or rectangular coordinates with z vertically upward. The origin of the coordinate system is usually taken at the center of the region of data to be modelled. To use this technique, the spherical coordinates r, θ, and λ are converted into the rectangular coordinates x, y, and z. In the way that RHA is normally used, the coordinates are scaled so that the x, and y data dimensions are 2π. The k_x and k_y are functions of this scaling: $k_x = 2\pi/L_x$ and $k_y = 2\pi/L_y$, where

L_x and L_y are the dimensions of the rectangular region in the x, and y coordinates respectively.

Haines (1990) stated that one of the limitations of this technique is that the terms Ax, By and Cz do not tend to zero as z tends to infinity, as a potential should if it is due to internal sources. Furthermore, it is not possible to incorporate the measurements from different altitudes for example ground data at $z = 0$ km and CHAMP satellite data at $z = 400$ km because the exponential does not provide the natural decrease of a newtonian potential field (Thébault, 2003).

2.3.2.3 Spherical Cap Harmonic Analysis (SCHA)

The method of Spherical Cap Harmonic Analysis (SCHA) is the analogue of the method of ordinary spherical harmonic analysis, being applied to a spherical cap rather than to the whole sphere (Haines, 1985). The potential for internal sources is expressed as:

$$V(r,\theta,\phi) = a\sum_{k=0}^{K}\sum_{m=0}^{k}(\frac{a}{r})^{n_k(m)+1}P^m_{n_k(m)}(cos\theta)[g^m_k cos(m\phi) + h^m_k sin(m\phi)], \qquad (2.17)$$

where r, θ and ϕ represent the geocentric spherical coordinates; radius, colatitude, and longitude respectively; a is the reference radius; $P^m_{n_k(m)}$ $(cos\theta)$ is the associated Legendre function, with integral order m and real degree $n_k(m)$; K is the ordering index; g^m_k and h^m_k are the spherical cap coefficients. This technique has the ability to incorporate the measurements collected between the ground altitude and the satellite altitude while still complying with Maxwell's equations (Thébault, 2003).

The details about this technique are given in chapter 5.

2.3.2.4 Revised Spherical Cap Harmonic Analysis (R-SCHA)

The Revised Spherical Cap harmonic Analysis (R-SCHA) is a revision of the Spherical Cap Harmonics Analysis developed by Haines (1985). This technique was proposed to overcome the shortcomings of SCHA that are the slow convergence for relatively small caps and the failure of correctly modelling the radial dependence. Also, none of the basis functions proposed by Haines (1985) is appropriate for adjusting fields decreasing as r^{-n} where r is a real integer (Thébault *et al.*, 2004).

Thébault (2006b) states that in a source free region, the Laplace equation is solved inside a cone, and boundary conditions are applied to each surface:

$$\Delta V = 0 \tag{2.18}$$

$$V|_{\partial_{\theta_0}\Omega} = F(r,\phi) \tag{2.19}$$

$$\frac{\partial V}{\partial r}|_{\partial_a\Omega} = -G_a(\theta,\phi) \tag{2.20}$$

$$\frac{\partial V}{\partial r}|_{\partial_b\Omega} = -G_b(\theta,\phi) \tag{2.21}$$

where Δ is the Laplacian in spherical coordinates and V is the geomagnetic field potential, $\partial_{\theta_0}\Omega$ is the lateral surface defined by the semi-aperture θ_0. And the lower and the upper surfaces of radius a and b respectively, are defined by $\partial_a\Omega$ and $\partial_b\Omega$ (fig. 2.14). This boundary value is split up into two parts and each sub-problem is solved separately. It provides a complete set of basis functions that is the most appropriate for the study of the magnetic field (Thébault, 2003).

The potential can be written in terms of three infinite series expansions (Thébault *et al.*, 2006a):

$$\begin{aligned} V(r,\theta,\phi) = a\sum_{k\geqslant 1}\sum_{m\geqslant 0}(\frac{a}{r})^{n_k+1}[G^{i,m}_{n_k}cos(m\phi) + H^{i,m}_{n_k}sin(m\phi)]P^m_{n_k}(\theta) \\ + a\sum_{l\geqslant 1}\sum_{m\geqslant 0}(\frac{a}{r})^{n_l}[G^{e,m}_{n_l}cos(m\phi) + H^{e,m}_{n_l}sin(m\phi)]P^m_{n_l}(\theta) \\ + a\sum_{p\geqslant 0}\sum_{m\geqslant 0}R_p(r)[G^m_p cos(m\phi) + H^m_p sin(m\phi)]K^m_p(\theta) \end{aligned} \tag{2.22}$$

with integer order m but non-integer degrees n_k and n_l. The functions $P^m_{n_k}$ and $P^m_{n_l}$ are the associated Schmidt-normalised Legendre functions, while $K^m_p(\theta)$ are the conical, or Mehler functions (Thébault *et al.*, 2006a). The constant a represents the mean Earth's radius.

2.4 Some global geomagnetic field models

2.4.1 International Geomagnetic Reference Field model (IGRF)

The geomagnetic field at the Earth's surface is strongly dominated by the long wavelength (up to 4000 km) main field from the Earth's core. For numerous applications in navigation and ionospheric modelling, the geomagnetic field is well approximated by this main field component (Maus *et al.*, 2005). Furthermore, marine, aeromagnetic

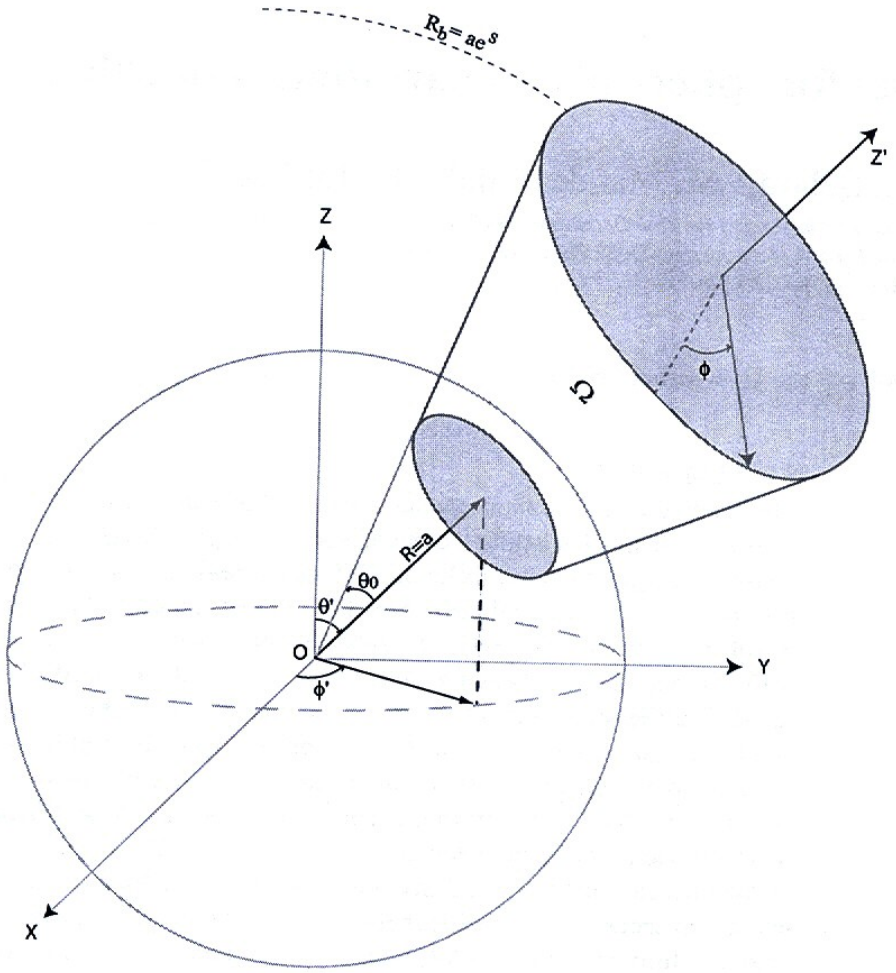

Figure 2.14: Definition of the domain of study Ω bounded by the terrestrial surface $r = a$ and the upper surface $r = ae^S$ with $S \neq 0$. The real scalar S is chosen such that the data recorded by satellites lie inside the volume (defined by the cone between the caps). $\partial\Omega_{\theta_0}$ is the boundary $\theta = \theta_0$, and $\partial\Omega_a$ and $\partial\Omega_b$ respectively are the lower and the upper caps. Figure adopted from Thébault et al. *(2004).*

and ground magnetic surveys in geophysical exploration and geological mapping require the subtraction of a standard main field model. For these purposes, the International Association of Geomagnetism and Aeronomy (IAGA) publishes the International Geomagnetic Reference Field (IGRF), which includes a spherical harmonic representation of the main field in 5 year intervals as well as the predicted SV for the next 5 year period (Maus *et al.*, 2005). The IGRF is compiled by a task force of IAGA working group V-MOD from submitted candidate models. The 10^{th} generation IGRF model is the latest version. It consists of definitive coefficients sets for 1945 through 2000 and preliminary sets for 2005 and coefficients for extrapolating from 2005 to 2010. This model predicts a constant SV over a 5 year interval.

2.4.2 CHAOS model

CHAOS is a model of Earth's magnetic field derived from CHAMP, Ørsted, and SAC-C magnetic satellite data. Ørsted is the Danish satellite that was launched in 1998 to measure the Earth's magnetic field. SAC-C is an international Earth observing satellite mission developed as a partnership between countries that include USA, Brazil, Italy, France, Argentina and Denmark. The SAC-C satellite was successfully launched on November 21, 2000. The CHAOS model was developed using more than 6.5 years of high-precision geomagnetic measurements from three satellites: Ørsted, CHAMP and SAC-C taken between March 1999 and December 2005 . The time change of the low-degree ($n < 14$) coefficients was described by cubic B-splines, a technique that has not been used previously for models that are based solely on satellite data (Olsen *et al.*, 2006).

Chapter 3

Data source and selection

3.1 Introduction

The investigation of the use of satellite magnetic field data to develop a geomagnetic SV model was conducted using the CHAMP satellite data for the period 2001-2005 over the southern Africa region covering the area between 10°S and 40°S in latitude and 10°E and 40°E in longitude. The developed SV model was validated against global field models (IGRF 10 and CHAOS) using the available ground data from geomagnetic field surveys (conducted by the Hermanus Magnetic Observatory) during the same period over the same region.

3.1.1 Some geomagnetic indices

The selection of geomagnetic field data was conducted using the geomagnetic activity indices.

3.1.1.1 K-index

The K-index quantifies disturbances in the horizontal component of Earth's magnetic field with an integer in the range 0-9 with 1 being calm and 5 or more indicating a geomagnetic storm. It is derived from the maximum fluctuations of horizontal components observed by a magnetometer during a 3-hour interval. The conversion table from the maximum fluctuation (nT) to K-index varies from one observatory to the other in such a way that the historical occurrence rate of certain levels of K are about the same at all observatories. In practice this means that observatories at higher geomagnetic latitude require higher levels of fluctuation for a given K-index.

The K-index is determined in eight three hourly intervals (0000-0300, 0300-0600, ..., 2100-2400). The maximum positive and negative deviations during the 3-hour period

are used to determine the total maximum fluctuation. These maximum deviations may occur any time during the 3-hour period. The logarithm of the largest excursion in H or D component over a 3-hour period is placed on a scale from 0 to 9.

3.1.1.2 Kp index

The Kp index (Bartels *et al.*, 1939) is obtained from 13 magnetometer stations at mid-latitudes. When the stations are not greatly influenced by the auroral electrojet currents, conditions are termed as magnetically quiet. However, if the auroral zone expands equatorward, these stations can record the effects of the auroral electrojet current system, the magnetospheric ring current and field-aligned currents that connect it to the ionosphere. This occurs during the so-called magnetically disturbed periods. The mid-latitude stations are rarely directly under an intense horizontal current system and thus magnetic perturbations can be dominant in either the H or D component.

3.1.1.3 Auroral Electrojet index (AE)

The AE index is obtained from a number (usually greater than 10) of stations distributed in local time in the latitude region that is typical of the northern hemisphere auroral zone (Davis and Sugiura, 1966). For each of the stations, the north-south magnetic perturbation H is recorded as a function of universal time. A superposition of these data from all the stations enables a lower bound or maximum negative excursion of the H component to be determined; this is called the AL index. Similarly, an upper bound or maximum positive excursion in H is determined; this is called the AU index. The range of these two indices (AU-AL) is called the AE index.

3.1.1.4 Disturbance Start Time index(Dst)

The Dst index is an index of magnetic activity derived from a network of four mid-latitude geomagnetic observatories (fig. 3.1): Honolulu (21.3°N, 157.8°W), Hermanus (34.4°S, 19.2°E), San Juan (15.6°N, 87.2°W) and Kakioka (36.2°N, 140.2°W).

The Dst index represents the axially symmetric disturbance of the magnetic field at the dipole equator on the Earth's surface. Major disturbances in Dst are negative, meaning decreases in the geomagnetic field. These field decreases are produced mainly by the equatorial current system in the magnetosphere, usually referred to as the ring current. The neutral sheet current flowing across the magnetospheric tail makes a small contribution to the field decreases near the Earth. Positive variations in Dst are mostly caused by the compression of the magnetosphere from solar wind pressure increases (Sugiura, 1964).

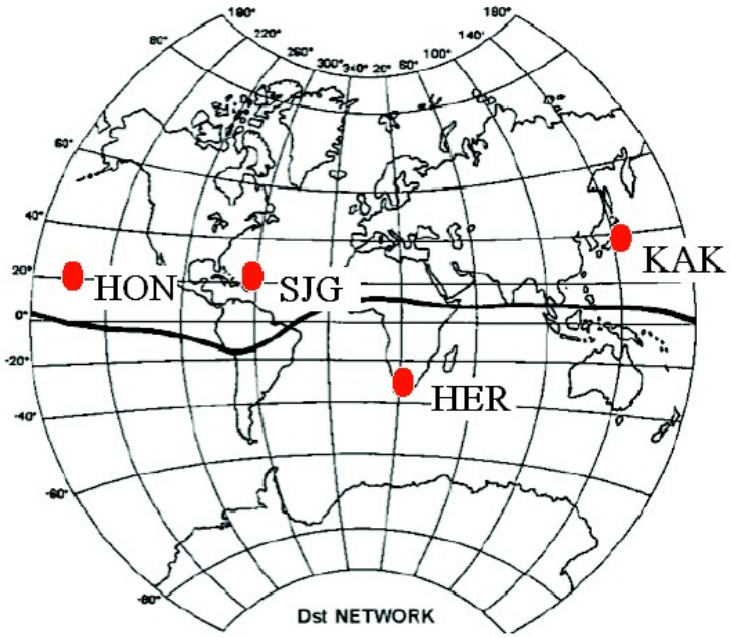

Figure 3.1: The Dst network observatories. Figure adopted from the website of World Data Center for geomagnetism, Kyoto (Kyoto University, 1991).

3.2 CHAMP satellite data

3.2.1 CHAMP satellite mission

The CHAMP(CHAllenging Mini-satellite Payload) mission was proposed by the German researcher Dr. Christoph Reigber in 1994 at GeoForschungsZentrum Postdam (GFZ), Germany. The German small satellite CHAMP was launched on July 15, 2000 into a circular, near polar 454 km altitude orbit. Its mission was to map the Earth's gravitational geopotential by the analysis of observed orbit perturbations, the magnetic geopotential via on-board magnetometry, and perform atmosphere profiling by GPS radio occultation measurements (Reigber *et al.*, 2002).

It was designed to have an initial altitude of 454 km decaying to about 300 km over the mission's lifetime of 5 years (fig. 3.2). The low altitude orbit supports the spatial resolution of the geopotential field whereas the long mission duration helps to recover temporal field variations (Reigber *et al.*, 2002).

The satellite consisted of a trapezoidal body of 0.6 m height, 4 m length and 1.6 m/0.4 m bottom/top width and 4 m long boom extending in the flight direction (fig. 3.3). The mass was 522 kg including 32 kg of payload mass.

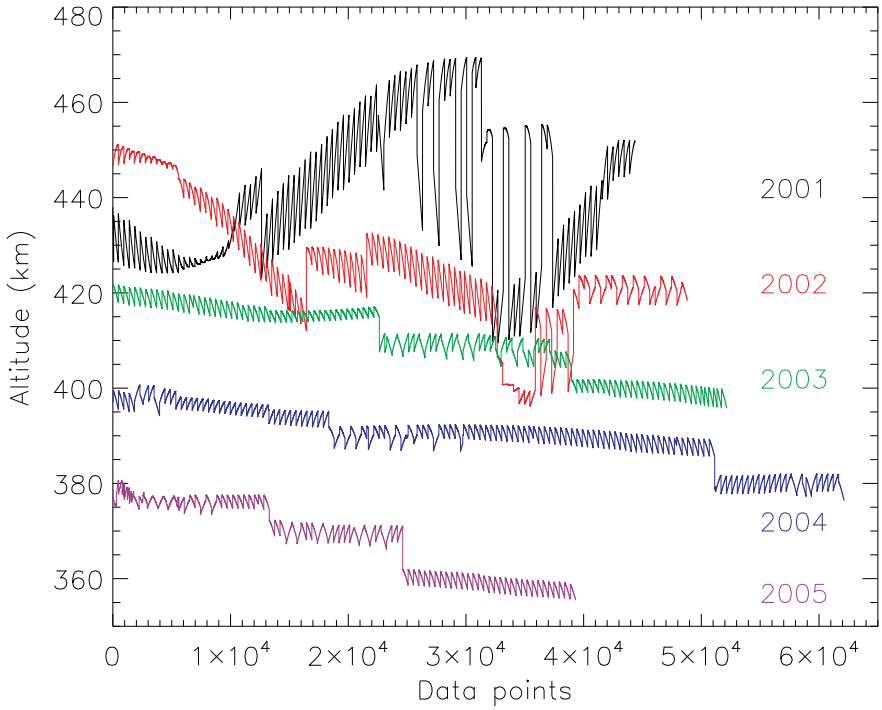

Figure 3.2: The CHAMP satellite fly altitude for the selected night and quiet magnetic data for the considered months (only the used data) in the period between 2001 and 2005.

3.2.2 Fluxgate Magnetometer

The Fluxgate magnetometer (FGM) was developed and manufactured by the Technical University of Denmark in Lyngby, Denmark. Its design is based on a compact spherical coil sensor (fig. 3.4). It was probing the components of the Earth's magnetic field. It was therefore regarded as the prime instrument for magnetic field investigations in the CHAMP mission. For redundancy reasons and to resolve disturbances by the electronic units inside the spacecraft, two FGM sensors separated by 60 cm were used.

The special features of the magnetometer are based on the design of the sensor. Three orthogonal sets of coils are wound on the surface of a 82 mm diameter sphere in a configuration which generates a homogeneous field within the spherical volume. The current through these coils is controlled by a feedback loop thus cancelling the ambient magnetic field in the interior. Three ring core sensors in the centre act as null-indicators.

The FGM characteristics include the coverage of the full ±65000 nT range of the Earth's field in X, Y and Z components. The overall noise level is of the order of 50 pT (rms). And in nominal operation mode the field vector is sampled at a rate of 50 Hz providing a spatial resolution along the orbit of approximately 150 m (Lühr, 2001).

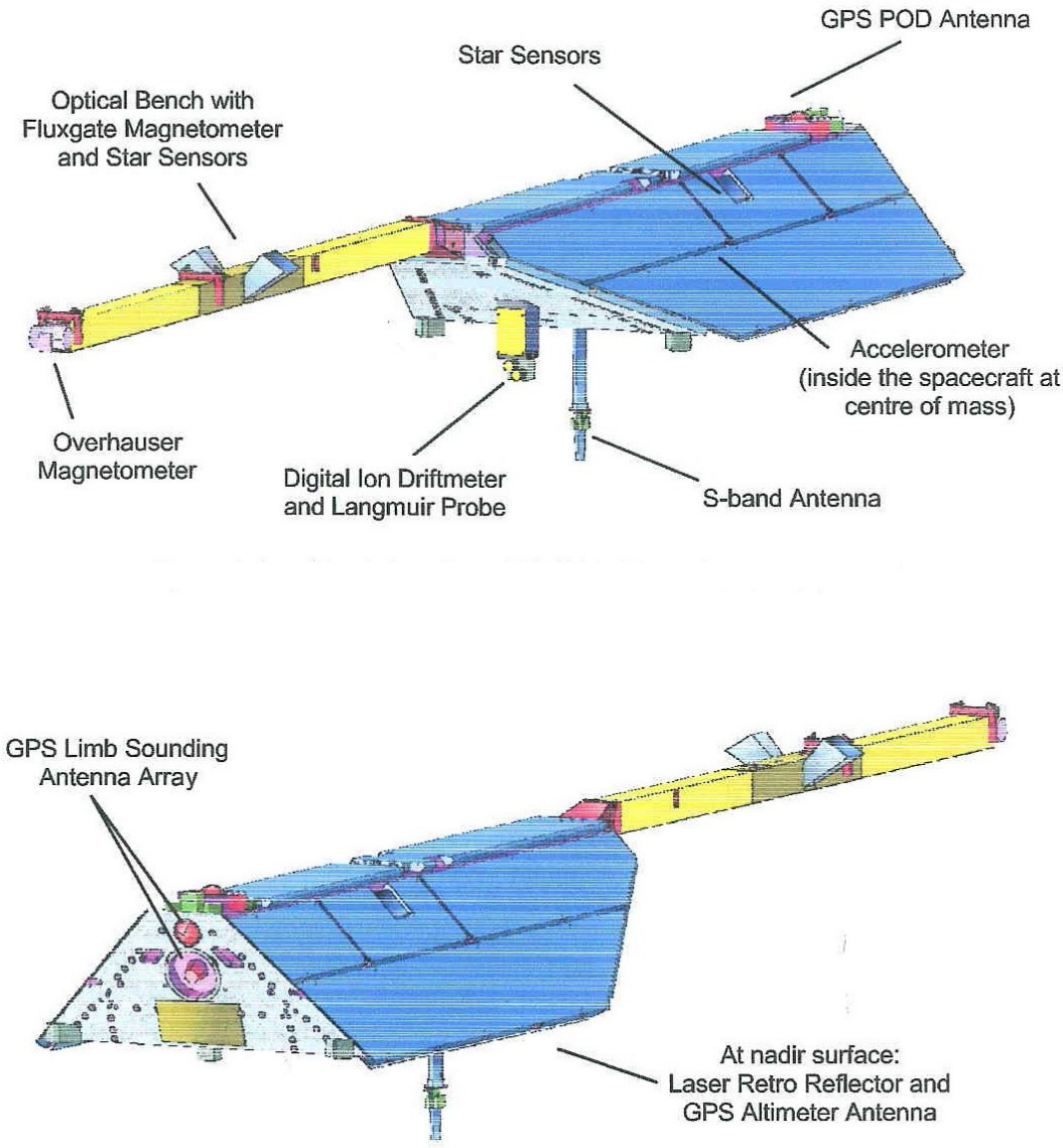

Figure 3.3: Front side and rear side of the CHAMP satellite with the location of instruments. Figure adopted from Lühr (2001).

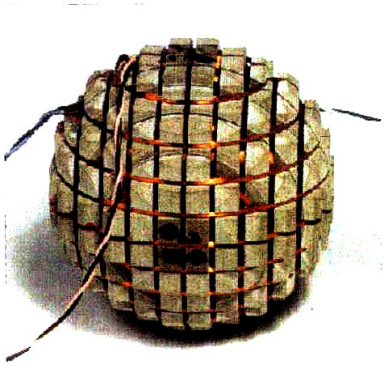

Figure 3.4: CHAMP FGM sensor. Figure adopted from Lühr (2001).

3.2.3 Satellite data selection

The CHAMP satellite data was selected with the help of a selected geomagnetic index. Significant current systems exist within and on the boundary of the magnetosphere, resulting in large magnetic fields described by various magnetic activity indices. For this investigation however, it was assumed that ring currents dominate at mid-latitudes considered and these can be represented by the Dst index (Kotzé, 2001).

The data selection was done for five years (2001, 2002, 2003, 2004 and 2005). Data selection was based on developing two models of equal time interval in a year (January - June and June - December) and one model for the whole year (January - December). Therefore the focus was mainly on the months of January, June and December. In some cases the data coverage or distribution was poor for a particular month and this was handled by taking the last few days of the previous month or the first few days of the next month. In particular, only quiet time data corresponding to a Dst index between -20 nT and +20 nT measured during the universal time intervals 16:00 - 24:00 and 00:00 - 05:00 were considered. The summary of data selection is given in figs. 3.5 and 3.6 and Table 3.1.

Table 3.1: Satellite data selection: 2001 - 2005

Year	Month	Total number of data points	Data points from neighboring months
	January	12634	-
2001	June	18682	-
	December	13397	3131 (The last 10 days of November)
	January	16444	-
2002	June	16214	-
	December	12916	-
	January	13358	-
2003	July	16317	-
	December	13195	-
	January	18038	6011 (The first 10 days of February)
2004	June	32794	14829 (10 days of May and 10 days of July)
	December	9927	534 (2 days in November, the $19^{th}$and 23^{rd})
	January	8091	5903 (The first 14 days of February)
	February	10363	-
2005	June	11343	-
	July	10553	-
	December	17450	2754 (The last 5 days of November)

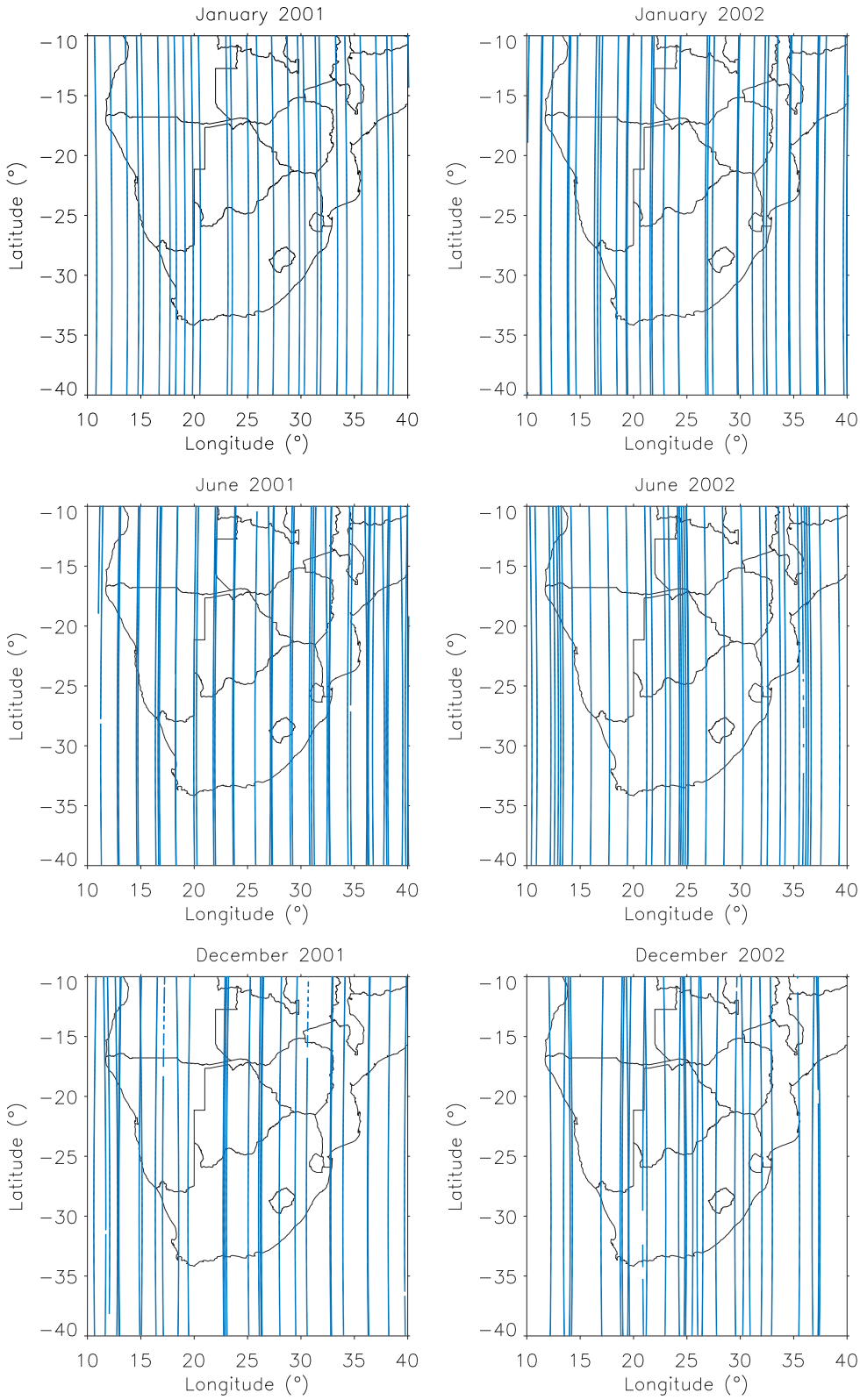

Figure 3.5: The plots showing the CHAMP satellite passes of the selected night and quiet time data points for the 5 year period between 2001 and 2005 for the selected months January, June and December. Due to a very bad data coverage for June in 2003, July was selected instead. In 2005, February and July were selected to avoid poor data quality and coverage in January. Most of the plotted data were recorded during the universal time intervals 16:00 - 24:00 and 00:00 - 05:00 when the Dst index was between -20 nT and +20 nT.

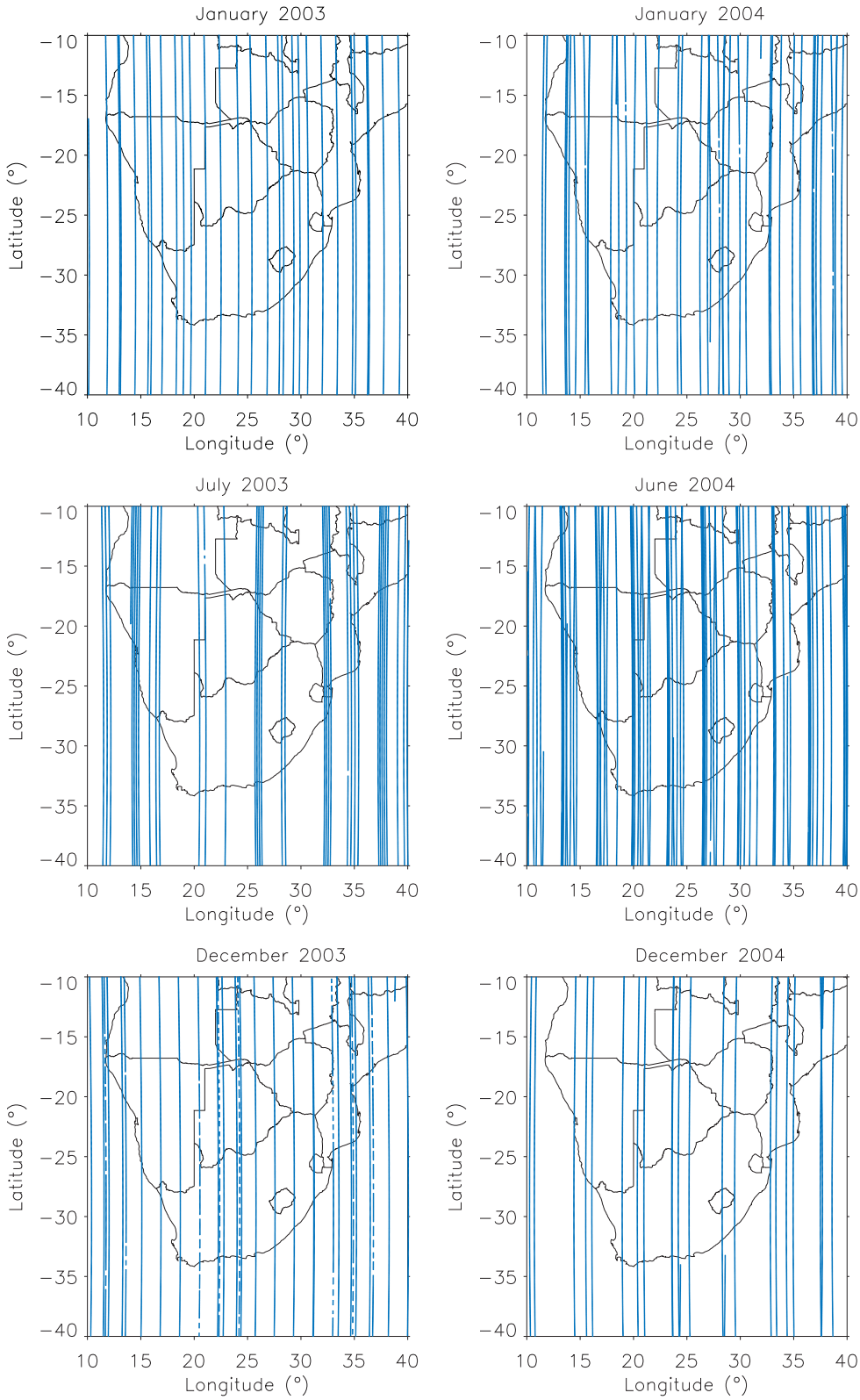

Figure 3.6: Continuation of Fig. 3.5 for years 2003 and 2004

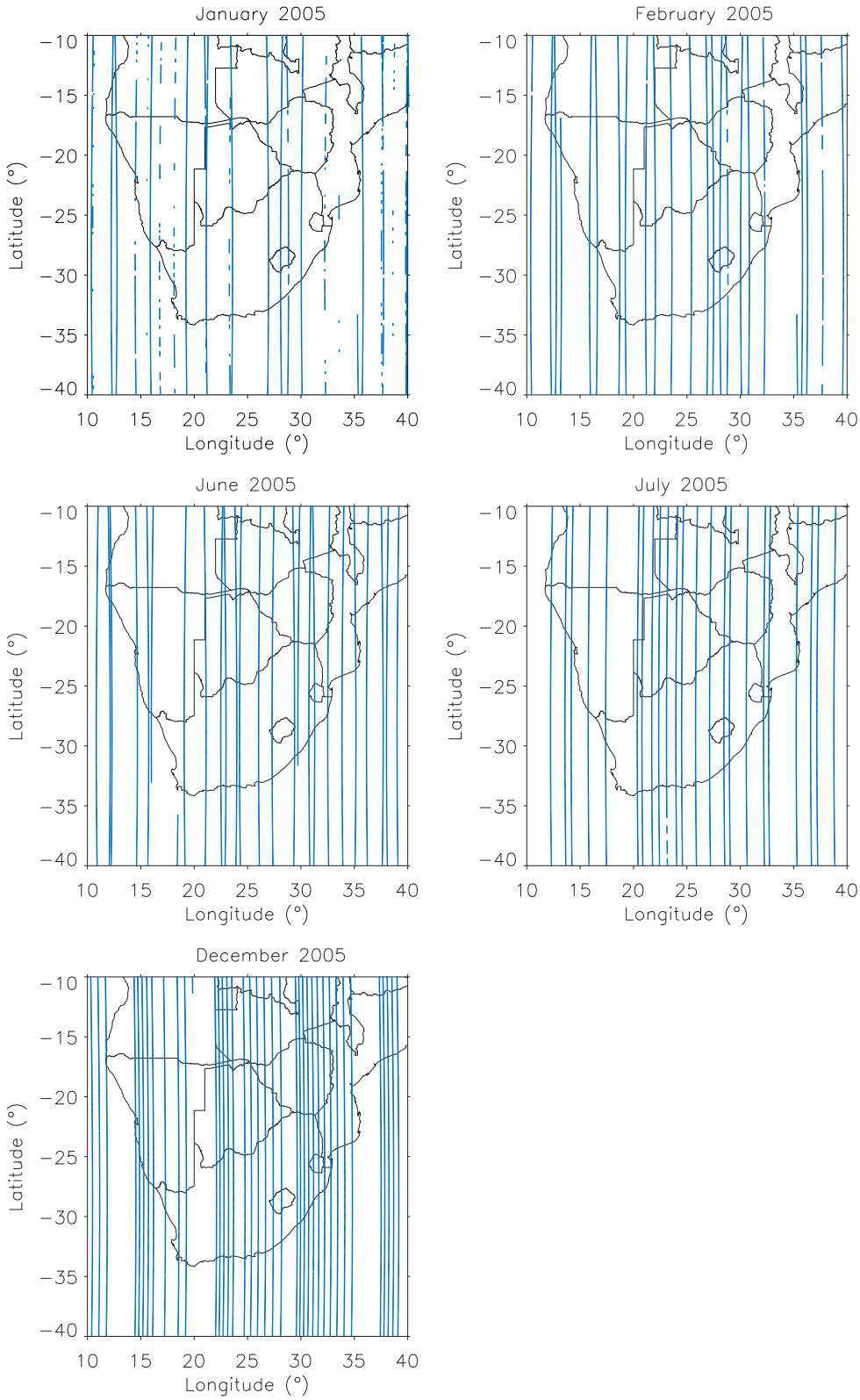

Figure 3.7: Continuation of Fig. 3.5 for year 2005

3.3 Ground data

3.3.1 Introduction

The prime function of Hermanus Magnetic Observatory (HMO) as part of the world-wide network of magnetic observatories is to monitor and model variations of the Earth's magnetic field. For this purpose, the HMO operates continuous magnetic field recording observatories at Hermanus (HER) and Hartebeesthoek (HBK) in South Africa and Tsumeb (TSU) and Keetmanshop (KMH) in Namibia. In addition, in southern Africa, the HMO has been executing geomagnetic repeat surveys on a routine basis for close to 60 years. These surveys normally include countries such as South Africa, Namibia, Zimbabwe and Botswana and have been conducted at regular intervals of 5 years until 2000 at almost 70 repeat station beacons. Results obtained during these field surveys were used to derive mathematical models of the main geomagnetic field components measured, using polynomials that can be expressed as a function of latitude and longitude. Concrete pillars marking these stations ensure that the observation points are exactly re-occupied during successive surveys.

However due to the rapid change of the geomagnetic field in this region, it was decided to conduct field surveys on an annual basis, but at 10 selected repeat stations at annual intervals for 2002, 2003 and 2004. Magnetic data were successfully collected at 8 of these repeat stations (4 in South Africa, 3 in Namibia and 1 in Botswana). Unfortunately it was not possible to visit the 2 stations in Zimbabwe. The experience gained from these surveys has shown that the limited number of stations over the southern African region is insufficient to accurately model the SV due to the increasing temporal and spatial gradients. A better spatial resolution however demanded an increase in the density of the repeat stations (Nahayo, 2006).

In 2005 as part of a collaborative project, called COMPASS (COmprehensive Magnetic Processes under the African Southern Sub-continent) between the HMO in South Africa and the GFZ German Research Centre for Geosciences in Potsdam, 40 stations (separated by distances ranging from 300 to 400 km) were selected. In this collaborative project there are 22, 12 and 6 stations in South Africa, Namibia and Botswana respectively as depicted in fig. 3.8.

From 2005, these 40 stations have been visited every year by 2 teams of both HMO and GFZ observers using similar geomagnetic instruments, DI Flux theodolites and fluxgate variometers.

However, the ground data used in the validation of the models in this study were taken from 13 points where geomagnetic data was collected for the period between 2001 and 2005. Their geodetic coordinates are given in Table 3.2.

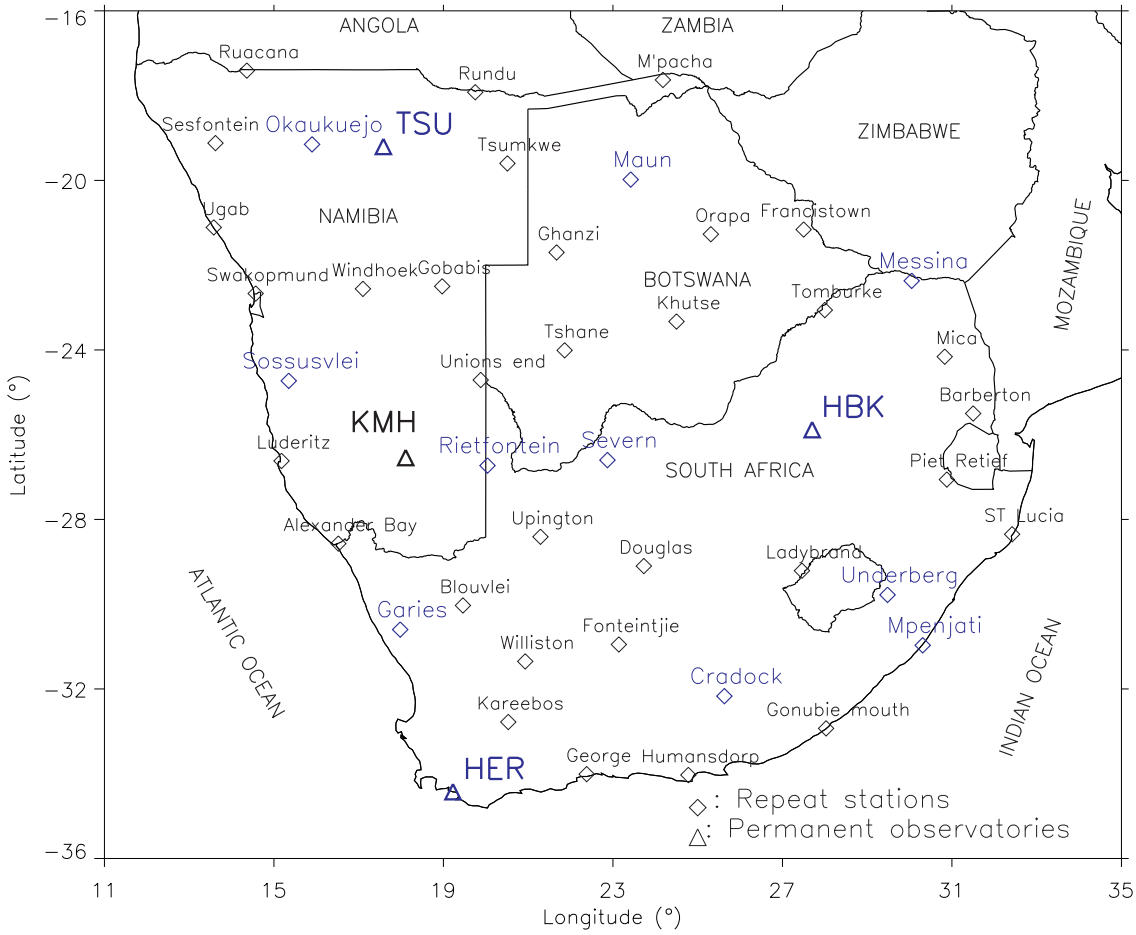

Figure 3.8: The map showing the HMO network of magnetic repeat stations and permanent observatories. The blue points are the only ones used in the validation of the developed geomagnetic SV models.

Table 3.2: Geodetic coordinates of 13 points used in the validation of the developed models.

Station	Latitude (°)	Longitude (°)	Altitude (m)
Cradock (CRA)	-32.2	25.6	847
Garies (GAR)	-30.6	18.0	229
Messina (MES)	-22.4	30.1	484
Okaukuejo (OKA)	-19.2	15.9	1039
Sossusvlei (SOS)	-24.7	15.4	587
Underberg (UND)	-29.8	29.5	1530
Maun (MAU)	-20.0	23.4	907
Rietfontein (RIE)	-26.7	20.0	900
Mpenjati (MPE)	-31.0	30.3	2
Severn (SEV)	-26.6	22.9	890
Hermanus (HER)	-34.4	19.2	26
Hartebeesthoek (HBK)	-25.9	27.7	1555
Tsumeb (TSU)	-19.2	17.6	1273

3.3.2 Geomagnetic instrumentation

The ground data measurements between 2001 and 2005 were executed using various instruments at the permanent observatories and at the repeat stations.

3.3.2.1 Vector Magnetometers

Fluxgate Magnetometer FGE

A Fluxgate Magnetometer (fig. 3.9) manufactured by the Danish Meteorological Institute, Denmark is in operation at all four magnetic observatories (HER, HBK, TSU and KMH).

The sensor unit consists of three orthogonally mounted sensors on a marble cube. To improve long-term stability these sensors have compensation coils wound on quartz tubes in order to obtain sensor drift of only a few nT per year. The marble cube is suspended by two strips of crossed phosphor-bronze working as a Cardan's suspension to compensate for pillar tilting which might cause baseline drift.

The sensors may be set up to record either X, Y and Z or H, D and Z components. The latter orientation has been chosen.

The box containing the electronics is almost magnetic free and is placed about 3 meters

from the sensor. At this distance it has no effect on the recordings. The recording rate is 1 second, but a sample is collected every 5 seconds.

Figure 3.9: A 3 component fluxgate magnetometer with suspended sensor. Figure adopted from the website of Technical University of Denmark (Technical University of Denmark, 2008).

The fluxgate magnetometer is based on a magnetic saturation circuit. Two parallel bars of a ferromagnetic material are placed closely together. The susceptibility of the two bars is large enough so that even the Earth's relatively weak magnetic field can produce near magnetic saturation in both bars (fig. 3.10).

Each bar is wound with a primary coil, but the direction in which the coil is wrapped around the bars is reversed. An alternating current (AC) is passed through the primary coils causing a large, artificial and varying magnetic field in each coil. This produces induced magnetic fields in the two cores that have the same strengths but opposite orientations at any given time during the current cycle.

If the cores are in an external magnetic field, one component of the external field will be parallel to the core axes. As the current in the primary coil increases, the magnetic field in one core will be parallel to the external field and so reinforced by it. The other will be in opposition to the external field and so smaller. The field will reach saturation in one core at a time different from the other core and fall below saturation as the current decreases at a different time. This difference is sufficient to induce a measurable voltage in a secondary coil that is proportional to the strength of the magnetic field in the direction of the cores.

The secondary coil surrounds the two ferromagnetic cores and the primary coil. The magnetic fields induced in the cores by the primary coil produce a voltage potential in

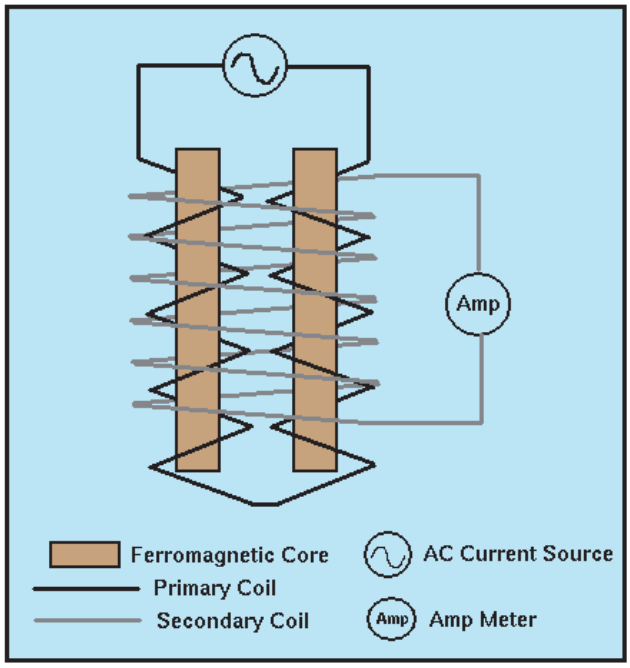

*Figure 3.10: A schematic of the fluxgate magnetometer. Figure adopted from the website of University of Melbourne, Australia (University of Melbourne, n.d.*a*).*

the secondary coil. In the absence of an external field (i.e., if the earth had no magnetic field), the voltage detected in the secondary coil would be zero because the magnetic fields generated in the two cores have the same strength but are in opposite directions (their effects on the secondary coil exactly cancel). In the presence of an external field component, the behaviour in the two cores differs by an amount which depends on the external field.

Thus, the Fluxgate Magnetometer is capable of measuring the strength of any component of the Earth's magnetic field by simply reorienting the instrument so that the cores are parallel to the desired component. The specifications of the Fluxgate Magnetometer used at the permanent stations (HER, HBK, TSU and KMH) are given in Table 3.3.

Table 3.3: Fluxgate Magnetometer technical specifications

Technical specification	Value
Analogue output	$\pm$10 volt
Dynamic range	3000 nT p-p
Resolution	0.2 nT
Scale value	150 nT/volt
Misalignment of sensor axis	$<$ 7 min of arc
Long term drift	3 nT/year
Temperature coefficient, sensor	0.2 nT/°C

Fluxgate Magnetometer LEMI-008

The Fluxgate magnetometer LEMI-008 (Fig. 3.11) was used in 2005 during the survey of the geomagnetic repeat stations. It is designed for the measurement of magnetic field variations in laboratory and field conditions. It is produced on the base of fluxgate sensor and consists of two units: sensor and electronic unit, connected by a cable. The magnetometer sensor has anti-tilt construction, internal FLASH-memory for data accumulation and storage, and GPS-receiver for data sampling synchronisation (Korepanov, 2004). The technical specifications are given in Table 3.4.

Table 3.4: The Fluxgate Magnetometer LEMI-008 technical specifications

Technical specification	Value
Range of magnetic variations (after offset compensation)	±2600 nT
Resolution	0.01 nT
Volume of the internal FLASH-memory	8 MB
Operating temperature range	-5°C to 40°C
Temperature drift	<0.2 nT/°C

Figure 3.11: The LEMI-008 magnetometer sensor on the left side and the electronic box on the right side.

Suspended/Unsuspended dIdD (delta Inclination / delta Declination) Magnetometers

Fluxgate magnetometers are the most frequently used vector magnetometers in current observatory practice. However, alternative solutions, for example dIdD magnetometers are also applied to record the geomagnetic variation. The unsuspended dIdD (fig. 3.12) was a backup instrument for geomagnetic variation between 2001 and 2005 at

HMO. From 2006 onwards, the back up instrument for geomagnetic variation is the Japanese fluxgate magnetometer, and the total field F is obtained from an overhauser sensor which forms part of the suspended dIdD vector magnetometer (Fig. 3.13). The suspended dIdD was designed to replace the unsuspended dIdD with new features like reduction of the spherical coil sensor size and its suspension.

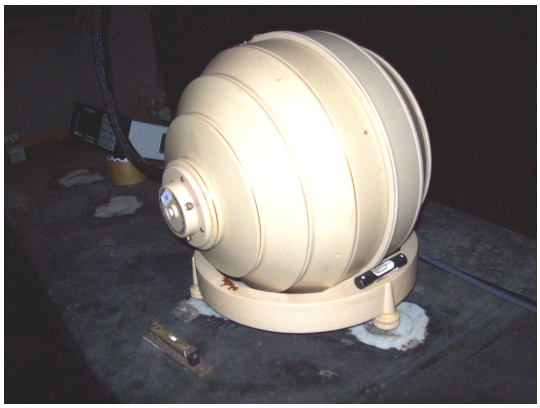

Figure 3.12: The sensor of the unsuspended dIdD vector magnetometer.

The unsuspended dIdD is a vector magnetometer for continuous monitoring of the inclination, declination and total intensity of the Earth's magnetic field. It employs a mutually orthogonal coil system that measures one unbiased and four biased values of total magnetic fields. The axes of the coil are arranged so that the axes of the mutually orthogonal coils are themselves perpendicular to the Earth's magnetic field vector, **F**, in the geomagnetic horizontal and vertical planes.

Equal and opposite currents are sequentially introduced into the *Inclination* (I) coil, which is perpendicular to **F**. These deflection fields lie in the local geomagnetic meridian plane. The resultant deflected values of **F** (I+ and I-) as measured by the Overhauser magnetometer are logged. The undeflected value of **F** is also logged.

Equal and opposite currents are then sequentially introduced into the *Declination* (D) coil which is also perpendicular to **F**. The D deflection fields lie in the horizontal plane. The resultant deflected values of **F** (D+ and D-) as measured by the Overhauser magnetometer are also logged. A simple algorithm is used to determine the instantaneous angular differences between the coil axes and the direction of the earth vector, **F**. These angular differences are dI and dD. Adding dI and dD to baseline values of Inclination and Declination for the coil system gives the instantaneous Inclination and Declination values of **F**. The components H and Z are computed as: $H = F\,cos\,(I)$ and $Z = F\,sin\,(I)$. Table 3.5 shows its technical specifications.

Table 3.5: Unsuspended dIdD Magnetometer technical specifications

Technical specification	Value
Dynamic range	20000 to 120000 nT
Sensitivity	0.01 nT
Resolution	0.01 nT
Absolute accuracy	0.2 nT
Operating temperature	-40°C to 55°C
Temperature coefficient	<0.1 nT/°C
Long term drift	2nT/year

Figure 3.13: The Suspended dIdD magnetometer. Figure adopted from the GEM systems website (GEM systems, 2008).

3.3.2.2 Scalar Magnetometers

Proton Precession Magnetometer (PPM)

The Geometric Proton Precession magnetometer type G-856AX (fig. 3.14) was the source of the total field F at 3 permanent observatories, HBK and TSU (2001 - 2005) and HER (2001 - 2004). It was also used to record the total field during the geomagnetic surveys.

The sensor component of the proton precession magnetometer is a cylindrical container filled with a liquid rich in hydrogen atoms surrounded by a coil (fig. 3.15). Commonly used liquids include water, kerosene and alcohol. The sensor is connected by a cable to a small unit which houses a power supply, an electronic switch, an amplifier and a frequency counter. When the switch is closed, a DC current delivered by a battery is directed through the coil, producing a relatively strong magnetic field in the fluid-filled cylinder. The hydrogen nuclei (protons) which behave like minute spinning

dipole magnets, become aligned along the direction of the applied field (i.e. along the axis of the cylinder). Power is then cut to the coil by opening the switch. Because the Earth's magnetic field generates a torque on the aligned, spinning hydrogen nuclei, they begin to precess around the direction of the Earth's total field. This precession produces a time-varying magnetic field which induces a small alternating current in the coil. The frequency of the AC current is equal to the frequency of precession of the nuclei. Because the frequency of precession is proportional to the strength of the total field and the constant of proportionality is well known (Proton Gyromagnetic Ratio is equal to 0.042576 Hertz/nT), the total field strength can be determined quite accurately(University of Melbourne, n.d.*b*). The PPM technical specifications are shown in Table 3.6.

Figure 3.14: The Proton precession magnetometer console. Figure adopted from the Geometrics website (Geometrics, n.d.).

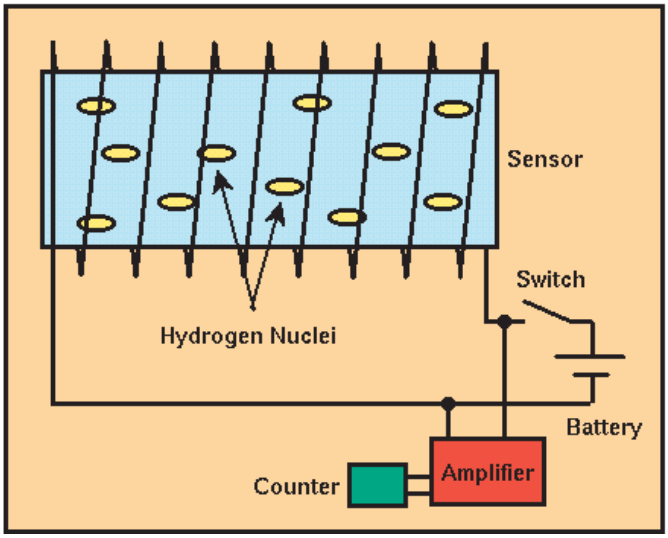

*Figure 3.15: The sketch of the inside of the PPM sensor. Figure adopted from the website of University of Melbourne, Australia (University of Melbourne, n.d.*b*).*

Table 3.6: The Proton Precession Magnetometer technical specifications

Technical specification	Value
Dynamic range	20000 to 90000 nT
Gradient Tolerance	1000 nT/meter
Resolution	0.1 nT
Absolute accuracy	0.5 nT
Operating temperature	-20°C to 50°C

Overhauser Magnetometer

The GSM-19 Overhauser Magnetometer (fig. 3.16) is used at HMO since 2004 as absolute instrument to take the total field site difference between the standard pillar in the absolute hut and the position of the dIdD vector magnetometer in the variometer hut. It is also used at the geomagnetic repeat stations to record the total field F during geomagnetic field surveys.

Overhauser effect magnetometers are essentially proton precession devices except that they produce an order of magnitude with greater sensitivity and deliver high absolute accuracy, rapid cycling (up to 5 readings / second), and exceptionally low power consumption. The Overhauser effect occurs when a special liquid (with unpaired electrons) is combined with hydrogen atoms and then exposed to secondary polarization from a radio frequency (RF) magnetic field. The unpaired electrons transfer their stronger polarization to hydrogen atoms, thereby generating a strong precession signal that is ideal for very high sensitivity total field measurements (http://www.gemsys.ca/prod-overhauser.htm). The technical specifications are shown in Table 3.7.

Figure 3.16: The GSM-19 Overhauser magnetometer console with sensor and cable. Figure adopted from GEM systems website (GEM systems, 2008).

Table 3.7: The Overhauser Magnetometer technical specifications

Technical specification	Value
Dynamic range	10000 to 120000 nT
Sensitivity	0.02nT
Gradient Tolerance	>10000 nT/meter
Resolution	0.01 nT
Absolute accuracy	±0.1 nT
Operating temperature	-40°C to 55°C

3.3.2.3 Declination/Inclination (DI)-Flux Magnetometers

Absolute measurements are essential to obtain base line values of standard variometers. The accuracy of the final magnetic values of an observatory depends on these values. DI-flux magnetometers become the standard instruments for measuring D and I components.

Absolute observations were carried out on a regular basis at each observatory by means of a DI-flux magnetometer (fig. 3.17) for measuring the angles D and I. The DI-flux magnetometer consists of a ZEISS non-magnetic theodolite THEO 010B (HER), a THEO 015B (HBK and TSU) and a single-axis fluxgate sensor mounted on top of the telescope and electronics from Bartington. The single axis fluxgate sensor is connected to Mag-01H single axis magnetometer (fig. 3.17). The Mag-01H is a battery-powered instrument which provides the drive for the sensor and processes its output to show the field strength on an auto-ranging LCD display.

(a) (b)

Figure 3.17: (a) DI-Flux magnetometer. (b) Mag-01H magnetometer.

3.3.3 Observational Procedure at Repeat Stations

Two observational procedures were used during the survey of geomagnetic repeat stations:

Method A: A series of DI-fluxgate readings are taken regularly at intervals of 20-30 min. Simultaneously F readings are recorded exactly when the I readings are done in order to produce H and Z values. The F data are either recorded with a Geometrics magnetometer or an Overhauser magnetometer. The sensor of the Geometrics or the Overhauser magnetometer is mounted on a tripod at a convenient position from the DI-fluxgate (fig.3.18). The time window for this procedure is normally late afternoon to early evening (but before dark) and early morning to reduce the magnetic diurnal effect. This method produces about 14 - 18 observations during the allocated time.

Method B: As method A produces only a small number of observations, the data quality can improve by recording more data for several hours. For this method a tri-axis LEMI-008 fluxgate magnetometer is operated at each field station overnight. The variometer generally has to stabilise for a couple of hours after it has been set up because it is strongly affected by temperature changes of the sensor. Moreover, it probably also needs to recover from mechanical strain induced on some components during transportation over rough roads. To avoid drifting of the base line values, the sensor temperature should be kept stable within a few degrees. To keep the sensor temperature as stable as possible during operation, the variometer is buried in the ground and covered with an insulating lid, which ensures sensor temperature changes of less than 5°C between evening and morning absolute measurements. The variometer, a three-component fluxgate instrument, is oriented to record the field components declination (D), horizontal intensity (H) and vertical intensity (Z) in nT. By means of the evening and morning absolute measurements good baseline control is obtained for the variometer, confirming whether the instrument stabilised by the time the first measurements were taken.

Normally data between 18:00 - 04:00 UT are used although the data are recorded for much longer as the LEMI fluxgate needs time to stabilise. The period 18:00 - 04:00 UT is selected as this is the time when the diurnal variation is at a minimum. Data are either recorded at 1-sec or 5-sec intervals and from these datasets 1-min average data are determined. To calibrate the fluxgate data, DI-fluxgate magnetometer readings and Overhauser magnetometer readings are taken as reported in Method A above. Usually a minimum of 2 sets of observations are obtained during late afternoon and at least another 2 sets during the following morning.

Method A was used between 2001 and 2004 whereas method B was used in 2005 geomagnetic survey. The change of the method A to B was done after obtaining the Fluxgate Magnetometer LEMI-008 to improve the quality of the ground survey data.

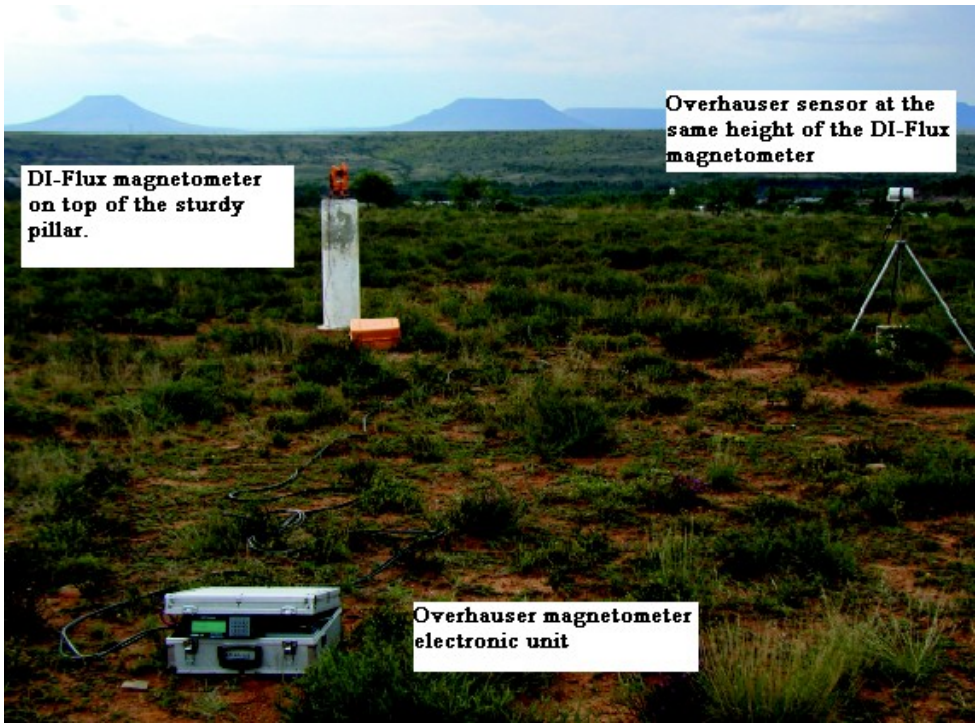

Figure 3.18: Example of a South African repeat station with a DI fluxgate theodolite on the station pillar and a GSM-19 Overhauser magnetometer. The sturdy, non-magnetic beacon ensures exact re-location during subsequent surveys.

3.3.4 Data processing

3.3.4.1 Observatory data (HER, HBK and TSU)

One-minute values

One-minute mean values, centred on the minute, were calculated by applying the Gaussian coefficients (Table 3.8) to a series of 19 samples of 5-second data. For a filter output value to be centred on the minute; the first coefficient was applied 45 seconds before this minute and the last coefficient was applied 45 seconds after the minute.

Daily mean values

Daily mean values, centred on the UT half day, are computed from the one-minute values. A value is not computed if there are more than 144 one-minute values missing.

Table 3.8: The Gaussian coefficients.

coefficient	value	coefficient	value
C0	0.00229315	C10	0.11972085
C1	0.00531440	C11	0.10321785
C2	0.01115655	C12	0.08061140
C3	0.02121585	C13	0.05702885
C4	0.03654680	C14	0.03654680
C5	0.05702885	C15	0.02121585
C6	0.08061140	C16	0.01115655
C7	0.10321785	C17	0.00531440
C8	0.11972085	C18	0.00229315
C9	0.12578865		

Monthly mean values

Monthly mean values are calculated from the daily mean values of H, D and Z. Monthly means are not computed if there is any missing daily value. The mean values of X, Y, F and I are calculated from the corresponding mean values of H, D and Z. Monthly values are also calculated for the five international quiet and disturbed days in each month. The selection of the international quietest days and most disturbed days of each month is deduced from the Kp indices on the basis of three criteria for each day: The sum of the eight Kp values, the sum of squares of the eight Kp values and the maximum of the eight Kp values.

According to each of these criteria, a relative order number is assigned to each day of the month, the three order numbers are averaged and the days with the lowest and the highest mean order numbers are selected as the five quietest and the five most disturbed days: (http://www-app3.gfz-potsdam.de/kp_index/qddescription.html). It should be noted that these selection criteria give only a relative indication of the character of the selected days with respect to the other days of the same month.

3.3.4.2 Repeat station survey data

The data processing consists of two steps. Firstly, one instantaneous absolute value per component is obtained from each set of measurements. This is achieved by the standard procedure used to obtain absolute measurements at geomagnetic observatories and which provides baseline values for the variometer.

With the DI-flux magnetometer, the Declination, D and inclination, I are measured at the repeat station. The total field F is recorded by an absolute instrument like a PPM or an Overhauser magnetometer. The H and Z components are computed using

the following formulae:

$$H = Fcos(I) \tag{3.1}$$

$$Z = Fsin(I) \tag{3.2}$$

The amplitudes of geomagnetic field variations are much smaller than the core field strength, and variometers generally only record the variations while (arbitrary) constant field values of up to several 10000 nT (depending on the component) are compensated for in the instrument. These constant field values are called baseline values, and adding them to the variations in each component provides the complete field vector over the entire time span of recordings. The baseline values are calculated as the difference between the measured absolute values at the repeat station (D, H and Z) and the recorded variations at the same time either from the control observatory variometer or the local variometer in the vicinity of the repeat station.

In the second step the SV at the repeat station of the present survey (epoch T_2) is determined by means of the procedure given by Newitt *et al.* (1996). Consider T_1 as the epoch of the previous survey. For a particular magnetic component E, the differential SV at the field station (FS) relative to that at the control observatory (CO), is given by:

$$\triangle S(E) = \frac{[E_{CO}(T_2) - E_{FS}(T_2)] - [E_{CO}(T_1) - E_{FS}(T_1)]}{T_2 - T_1} \tag{3.3}$$

where $E_{CO}(T_1)$ and $E_{CO}(T_2)$ denote the values of E at the control observatory at epochs T_1 and T_2 respectively, $E_{FS}(T_1)$ and $E_{FS}(T_2)$ denote the values of E at the repeat station at epochs T_1 and T_2 respectively and $\triangle S(E)$ the differential SV for a magnetic component E. These values are computed as the average of recorded component E for the same time interval at the control observatory and at the repeat station.

The SV at the repeat station $S_{FS}(E)$ is given by:

$$S_{FS}(E) = S_{CO} - \triangle S(E) \tag{3.4}$$

where $S_{CO}(E)$ is the annual change at the CO. This annual change at the CO was computed as the difference between the quiet day monthly mean values centered at the middle of the year for two consecutive years. The selection of two years was based on the time when the repeat station survey was conducted. For example if the repeat station survey was conducted in June 2003, then 2002 and 2003 were used to compute the annual change at CO. Furthermore, the CO was one of the three observatories namely HER, HBK and TSU depending on whichever was the closest to the repeat station.

Errors are associated with these measurements taken during a field survey. Possible errors to be considered are instrumental or measurement errors, positioning errors

and errors in reducing data to undisturbed internal field values. For the DI fluxgate theodolite, they might be slightly larger due to the influence of weather conditions or relative stability related to mounting the instrument on a tripod. A good estimate of such errors is obtained from the scatter of individual baseline values at the repeat station. To compute the individual base line values, the CO data was used between 2001 and 2004 survey and the local variometer data was used for 2005 survey. The computation of uncertainty estimates was determined using the following formula:

$$\sigma = \sqrt{\frac{1}{N}\sum_{i=1}^{N}(x_i - \overline{x})^2}, \tag{3.5}$$

where σ is the scatter or standard deviation of N individual base line values x_i and $\overline{x}$ is the arithmetic mean of x_i, defined as:

$$\overline{x} = \frac{1}{N}\sum_{i=1}^{N} x_i \tag{3.6}$$

Table 3.9 shows the uncertainty estimates for each component in each year between 2001 and 2005. The 2005 errors are so much less than previous years due to the method B which was used during the geomagnetic field survey (see subsection 3.3.3). The details of the uncertainty estimates and SV data at the selected 13 points are given in Tables 3.10, 3.11 and 3.12 respectively.

Table 3.9: Summary of uncertainty estimates of recorded data at the selected 10 repeat stations between 2001 and 2005.

Year	component	Uncertainty estimate
	H	±3.7 nT
2001	D	±1.4 min of arc
	Z	±3.7 nT
	H	±1.9 nT
2002	D	±0.9 min of arc
	Z	±2.3 nT
	H	±2.6 nT
2003	D	±0.7 min of arc
	Z	±3.9 nT
	H	±2.7 nT
2004	D	±0.8 min of arc
	Z	±3.9 nT
	H	±0.9 nT
2005	D	±0.4 min of arc
	Z	±1.4 nT

Table 3.10: The uncertainty estimates values (±) of the observed geomagnetic field components H in nT, D in min of arc and Z in nT at the repeat stations. For some repeat stations the survey was not conducted every year between 2001 and 2005. This is indicated by dashed points.

Station	2001			2002			2003			2004			2005		
	H	**D**	**Z**	**H**	**D**	**Z**	**H**	**D**	**Z**	**H**	**D**	**Z**	**H**	**D**	**Z**
CRA	5.4	2.5	5.8	2.1	0.4	3.0	4.2	0.9	8.9	2.3	1.3	2.6	0.5	0.3	1.9
GAR	3.1	0.9	5.4	0.6	0.9	1.0	2.1	0.3	5.2	1.1	0.4	1.7	0.7	0.2	0.9
MES	2.8	1.7	3.8	2.1	0.6	1.0	2.8	0.8	2.7	4.5	0.8	5.5	2.3	0.9	3.4
OKA	0.7	0.6	0.5	0.9	1.2	0.5	2.1	0.9	0.7	0.6	0.7	1.8	0.6	0.8	0.8
SOS	1.0	0.3	0.6	0.6	0.2	0.8	2.9	0.7	2.3	7.8	0.9	8.0	0.9	0.3	1.2
UND	7.0	3.9	6.6	3.8	2.7	3.2	2.8	0.3	5.6	3.5	0.5	4.9	0.3	0.1	0.9
MAU	1.8	0.6	5.3	3.0	0.5	3.1	2.2	0.7	2.2	0.6	0.3	2.1	1.3	0.2	1.5
RIE	10.0	1.5	3.8	2.4	0.7	5.9	-	-	-	-	-	-	-	-	-
MPE	1.4	0.2	1.6	-	-	-	-	-	-	-	-	-	-	-	-
SEV	-	-	-	-	-	-	1.6	1.1	3.5	0.9	1.1	4.8	0.5	0.1	0.3

Table 3.11: The SV data at the selected 13 points for the geomagnetic components H in nT/year, Z in nT/year, D in min of arc/year and the total field F in nT/year. These SV data are for the period between 2001 and 2005 as shown in the table.

Station	2001				2002				2003			
	F	**H**	**Z**	**D**	**F**	**H**	**Z**	**D**	**F**	**H**	**Z**	**D**
CRA	-40.0	6.8	39.6	-9.1	-46.2	8.8	39.3	-10.4	-27.1	1.5	32.3	-9.7
GAR	-60.8	-20.4	51.6	-1.6	-59.0	-17.8	50.3	-1.6	-60.3	-25.5	54.2	-5.1
MES	-29.6	-2.4	32.8	-7.2	-25.2	-0.1	28.1	-7.2	-20.7	1.9	25.4	-3.6
OKA	-50.8	-36.8	37.2	5.8	-46.0	-36.0	32.1	5.0	-48.0	-46.3	29.9	6.1
SOS	-62.3	-36.4	52.0	2.3	-66.0	-35.0	48.4	1.6	-53.9	-49.2	39.6	2.8
UND	-25.4	17.8	32.4	-9.9	-18.1	19.3	25.5	-10.9	-8.4	9.5	15.3	-12.0
MAU	-	-	-	-	-55.1	-15.2	43.6	-0.9	-35.7	-25.1	27.3	0.0
RIE	-65.7	-20.9	60.9	-2.3	-58.6	-16.9	55.9	-2.8	-	-	-	-
MPE	-19.4	23.1	33.4	-10.6	-	-	-	-	-	-	-	-
SEV	-	-	-	-	-	-	-	-	-	-	-	-
HER	-64.5	-7.1	67.5	-7.2	-59.0	-5.0	62.0	-6.7	-50.0	-15.0	48.0	-8.2
HBK	-36.0	8.7	44.7	-7.7	-31.0	11.0	40.0	-7.3	-18.0	2.0	21.0	-8.8
TSU	-52.6	-30.9	42.9	5.1	-48.0	-30.0	38.0	4.3	-45.0	-43.0	28.0	4.8

Table 3.12: The continuation of Table 3.11.

Station	2004				2005			
	F	**H**	**Z**	**D**	**F**	**H**	**Z**	**D**
CRA	-15.8	13.3	27.9	-12.1	-24.7	7.0	29.6	-11.9
GAR	-48.1	-9.6	47.4	-3.3	-54.0	-18.3	48.8	-4.8
MES	-6.1	23.9	17.8	-6.1	-1.7	14.7	8.7	-5.5
OKA	-41.2	-28.0	31.2	7.1	-32.0	-39.4	14.1	5.1
SOS	-61.0	-26.3	59.9	5.4	-35.9	-34.9	13.2	-0.9
UND	-4.0	21.6	17.5	-10.8	-6.8	19.9	16.2	-10.9
MAU	-35.5	0.5	43.6	-0.8	-25.1	-14.1	29.6	2.2
RIE	-	-	-	-	-	-	-	-
MPE	-	-	-	-	-	-	-	-
SEV	-31.4	-0.8	33.8	-	-30.8	-5.1	31.9	-0.8
HER	-49.0	2.0	54.0	-7.8	-48.0	-10.0	49.0	-8.7
HBK	-13.0	20.0	25.0	-5.4	-16.0	8.0	22.0	-8.8
TSU	-43.0	-21.0	37.0	5.4	-32.0	-33	18.0	5.0

Chapter 4

Polynomial modelling

4.1 Introduction

Different methods of regional modelling were reviewed by Haines (1990). The simplest method is the use of polynomial surfaces, a very useful tool in order to represent the geomagnetic field over a small area of the Earth's surface. In this present study, the following surface polynomial was used:

$$B(\varphi, \lambda) = \sum_{n=0}^{N} \sum_{m=0}^{N} k_{mn} \times (\varphi - \varphi_0)^n \times (\lambda - \lambda_0)^m$$

where B is the magnitude of the main field for each element (north component X, east component Y, and vertical component Z) at the point with geographic coordinates φ (latitude) and λ (longitude), k_{mn} is a numerical coefficient and φ_0 and λ_0 are the coordinates of the center of the modelled area: $\varphi_0 = 25°$S and $\lambda_0 = 25°$E. The degree of the polynomial is determined by the value of integer N (N = 1, 2, 3, 4, 5, ...).

By assuming that $B(\varphi, \lambda)$ is the measured magnitude of a main field element or a secular variation value at a given point of latitude φ and longitude λ , and k_{mn} is unknown, a redefined system of conditional equations is obtained and solved by the least squares method. The only terms where the total of the φ and λ powers do not exceed the degree are returned (Queen's University Belfast, 2005).

Without any altitude dependence the polynomial modelling technique requires that data be reduced to the same altitude. As shown in fig. 3.2 in chapter 3, the CHAMP satellite was passing over southern Africa at a varying altitude. And in order to be able to validate the results of the polynomial modelling with the ground survey data, it was necessary to correct satellite data to the ground level (the average elevation of 13 ground points was used: 0.8 km). The correction was calculated using the IGRF 10 model. For a data point value D at a given geodetic coordinate (φ, λ, S), the data

point value at a new altitude N is given as follows:

$$\mathrm{D}_{(\varphi,\lambda,N)} = \mathrm{D}_{(\varphi,\lambda,S)} + (\mathrm{IGRF}\ 10_{(\varphi,\lambda,N)} - \mathrm{IGRF}\ 10_{(\varphi,\lambda,S)}) \tag{4.1}$$

where S is the satellite altitude.

The geomagnetic field components D and H and the total field F were computed from X, Y and Z components using equations 2.2, 2.4 and 2.5 given in chapter 2. The analysis of the effect on the data validity when the correction of satellite data at a certain altitude is done using IGRF 10 model is shown in section 4.3.

4.2 Selection of polynomial degrees for main field and secular variation models

The order of a surface polynomial should be chosen carefully in order to yield a good estimate of the model. Shu *et al.* (1996), referring to Potchtarev (1984), stated that the approximation error of any two dimensional model for a limited area increases towards this area's boundaries. This is due to the lack of observation points outside the area. It follows that the areas where the model estimation can be considered reliable are smaller than those where the data sampling takes place. This is not restricted only to polynomials; all regional modeling techniques inherently have problems of edge effects near the regional boundaries and imperfect spatial data distribution can lead to further artificial structures (Verbanac, 2007).

The choice of an optimum order of the polynomial model depends on several factors including the minimum wavelength of specific features which should be included in the model, the initial data distribution and the root-mean-square (RMS) of initial data (Shu *et al.*, 1996). The RMS of the initial data was computed for main field and SV models on 2001 satellite data as shown in Table 4.1. The RMS values of the deviations of the polynomial models from the IGRF 10 model are also shown in Table 4.2. To compute the difference between two models, data grids of $0.2^\circ \times 0.2^\circ$ were generated over the whole region of study.

Considering the RMS of the main field and SV in Table 4.1, the RMS values decrease with the increase of polynomial degrees and reach a level where the rate of change becomes flat for 2 or 3 consecutive polynomial degrees and then start increasing. In this case, for main field models, all three magnetic field components D, H and Z show the same pattern. For D and H, the RMS values start becoming flat at degree 5 and start increasing at degree 8. For the Z component, the RMS values start becoming flat at degree 5 and start increasing at degree 7. On the other hand, the SV models show that the RMS values start becoming flat at degree 5 but have very similar values for

the first 3 degrees namely 2, 3 and 4 ; and start increasing at degree 8.

Taking into account that the main aim of this project is the core field, characterised by the long minimum wavelength, lower polynomial degrees should be considered. The trade-of was made between the minimum RMS and the lowest polynomial degree that would be suitable to study the core field. The 5^{th} degree was chosen for the main field modelling while the 2^{nd} and 3^{rd} degrees were found to be suitable for the SV field modelling. The comparison between the polynomial models and the IGRF 10 model in Table 4.2 supports this choice. For degrees 4, 5 and 6, polynomials yield the main field models that are close to the IGRF 10 main field model while degrees 2, 3 and 4 indicate SV models are close to the IGRF 10 SV model. The polynomial degrees 2, 3 and 5 are given in equations 4.1, 4.2 and 4.3, respectively.

$$B(\varphi,\lambda) = k_{00} + k_{10}\lambda + k_{20}\lambda^2 + k_{01}\varphi + k_{11}\varphi\lambda + k_{02}\varphi^2 \tag{4.2}$$

$$B(\varphi,\lambda) = k_{00}+k_{10}\lambda+k_{20}\lambda^2+k_{30}\lambda^3+k_{01}\varphi+k_{11}\varphi\lambda+k_{21}\varphi\lambda^2+k_{02}\varphi^2+k_{12}\varphi^2\lambda+k_{03}\varphi^3 \tag{4.3}$$

$$\begin{aligned} B(\varphi,\lambda) = {} & k_{00} + k_{10}\lambda + k_{20}\lambda^2 + k_{30}\lambda^3 + k_{40}\lambda^4 + k_{50}\lambda^5 + k_{01}\varphi + k_{11}\varphi\lambda + k_{21}\varphi\lambda^2 \\ & + k_{31}\varphi\lambda^3 + k_{41}\varphi\lambda^4 + k_{02}\varphi^2 + k_{12}\varphi^2\lambda + k_{22}\varphi^2\lambda^2 + k_{32}\varphi^2\lambda^3 + k_{03}\varphi^3 \\ & + k_{13}\varphi^3\lambda + k_{23}\varphi^3\lambda^2 + k_{04}\varphi^4 + k_{14}\varphi^4\lambda + k_{05}\varphi^5 \end{aligned} \tag{4.4}$$

Table 4.1: The RMS misfit errors between the measured satellite data and data obtained from the main field models (January 2001), and RMS differences between the SV data and data obtained from SV models (January - December, 2001).

Polynomial	Main field			SV		
degree	D (min of arc)	H (nT)	Z (nT)	dD/dt (min of arc/year)	dH/dt (nT/year)	dZ/dt (nT/year)
2	41.42	76.0	382.7	1.21	8.75	3.38
3	13.88	73.2	29.6	0.82	6.74	2.41
4	5.24	14.3	19.5	0.72	4.80	2.03
5	3.52	11.5	3.9	0.24	0.04	0.04
6	2.98	10.5	3.6	0.24	0.04	0.04
7	2.95	11.5	11.1	0.24	0.04	0.04
8	55.5	379.0	806.9	0.79	1.83	0.49
9				12.60	27.32	9.32

Table 4.2: The RMS differences between PolyM and IGRF 10 models (January 2001 for main field and between January and December 2001 for SV).

Polynomial	Main field			SV		
degree	D (min of arc)	H (nT)	Z (nT)	dD/dt (min of arc/year)	dH/dt (nT/year)	dZ/dt (nT/year)
2	44.12	117.0	400.6	1.86	11.44	3.44
3	19.73	115.3	84.1	1.58	11.15	3.72
4	13.72	88.3	80.9	1.61	12.10	3.35
5	13.20	87.9	78.5	1.73	13.05	3.93
6	13.05	87.9	78.2	1.73	13.05	3.93

4.3 The effect on the satellite data validity when the correction to the same altitude (0.8 km) is done using IGRF 10 model.

The investigation was carried out to show how much the satellite data validity is affected when the correction of data is determined at the same altitude. This was achieved by analysing the RMS differences between PolyM and IGRF 10 SV models at different altitudes. The chosen altitudes are 400 km (the mean CHAMP altitude) and 0.8 km (the mean altitude of 13 reference ground points to be used in the PolyM model validation).

The analysis was done using the PolyM SV models for D, H and Z components of the geomagnetic field developed from the satellite data recorded in 2001. The geomagnetic SV models were developed after correcting satellite data to the same altitude of 0.8 km and 400 km. A 5^{th}degree surface polynomial was used to develop the main field models (Table 4.3 and 4.4) and a 3^{rd} degree to develop the SV models (Table 4.5). The models were compared with the IGRF 10 SV model at both altitudes, the differences were plotted and their RMS values were calculated.

Figs. 4.1, 4.2 and 4.3 show the plots of the deviations of satellite data model from the IGRF 10 model. It is clear that in all components D, H and Z the differences of two models at 400 km and 0.8 km are close. This is shown in table 4.6 where the differences between the RMS differences between PolyM and IGRF 10 SV models at 0.8 km and 400 km altitudes are 0.049 min of arc/year, -1.259 nT/year and 0.258 nT/year for D, H and Z components, respectively.

From the results of this analysis, it can be concluded that the validity of satellite data is not much affected when the data is reduced to the same altitude (0.8 km) using the IGRF 10 model, except in the case of the H component.

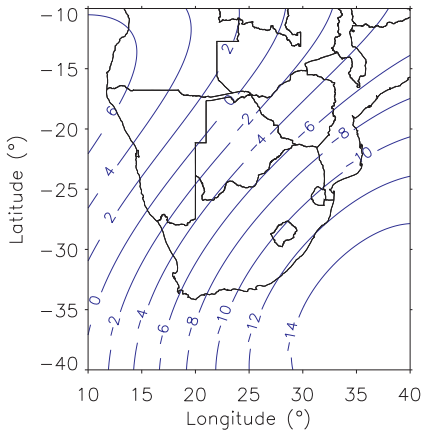

(a) PolyM at 0.8 km: SV in D component (2001)

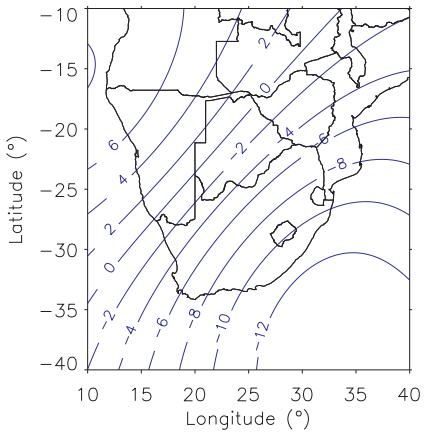

(b) IGRF 10 model at 0.8 km: SV in D component (2001)

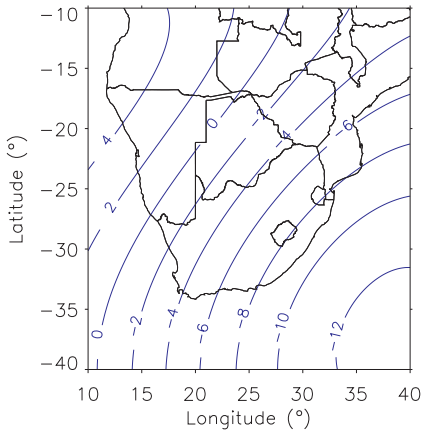

(c) PolyM model at 400 km: SV in D component (2001)

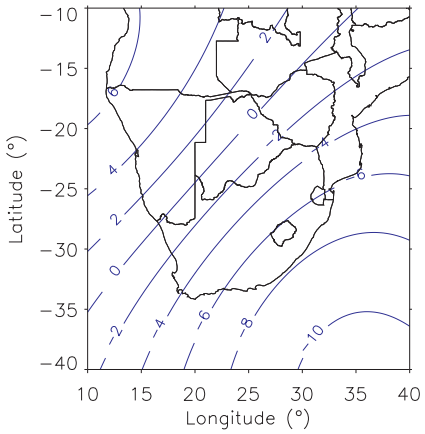

(d) IGRF 10 model at 400 km: SV in D component (2001)

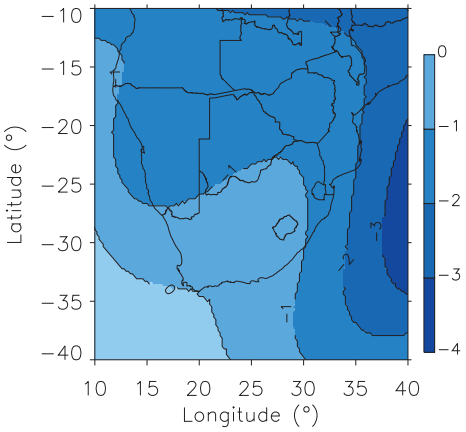

(e) Difference between PolyM and IGRF 10 SV models at 0.8 km: D component (2001)

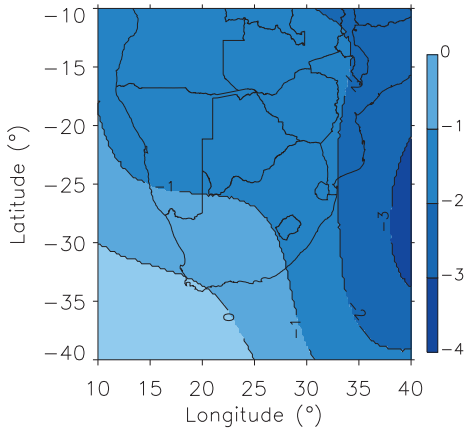

(f) Difference between PolyM and IGRF 10 SV models at 400 km: D component (2001)

Figure 4.1: The contour plots of SV data obtained from PolyM and IGRF 10 SV models in 2001 for D component (min of arc/year) and their differences at 0.8 km and 400 km altitudes.

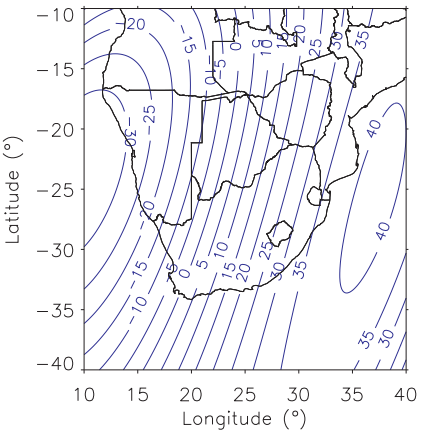

(a) PolyM model at 0.8 km: SV in H component (2001)

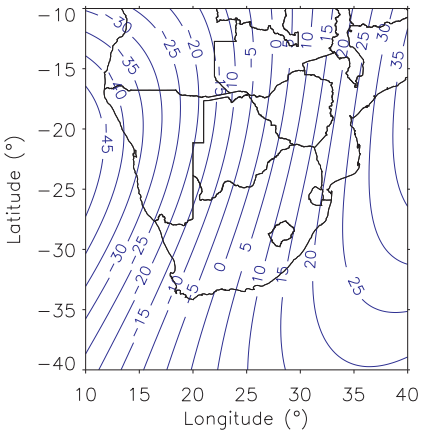

(b) IGRF 10 model at 0.8 km: SV in H component (2001)

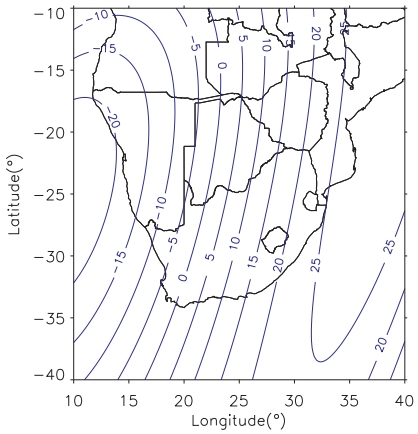

(c) PolyM model at 400 km: SV in H component (2001)

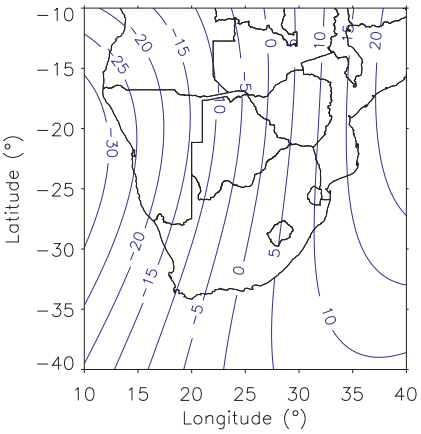

(d) IGRF 10 model at 400 km: SV in H component (2001)

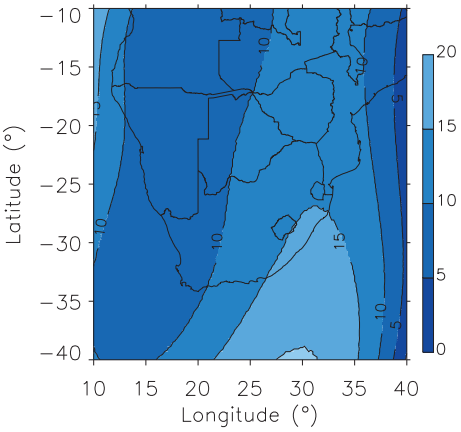

(e) Difference between PolyM and IGRF 10 SV models at 0.8 km: H component (2001)

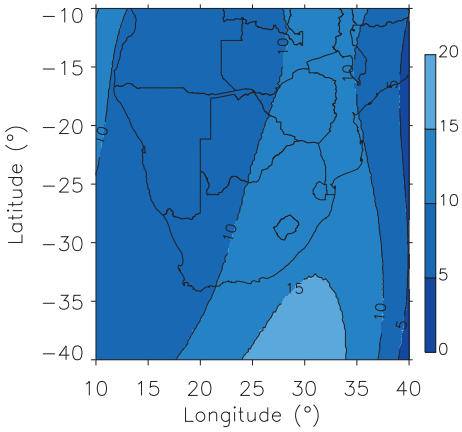

(f) Difference between PolyM and IGRF 10 SV models at 400 km: H component (2001)

Figure 4.2: The contour plots of SV data obtained from PolyM and IGRF 10 SV models in 2001 for H component (nT/year) and their differences at 0.8 km and 400 km altitudes.

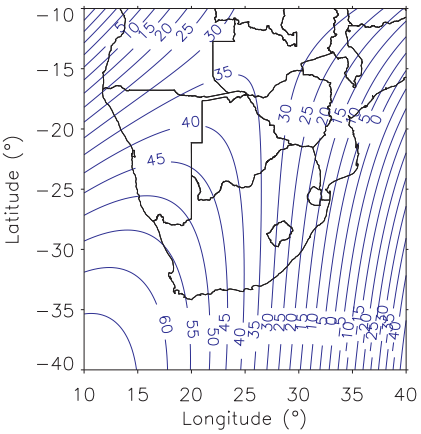

(a) PolyM model at 0.8 km: SV in Z component (2001)

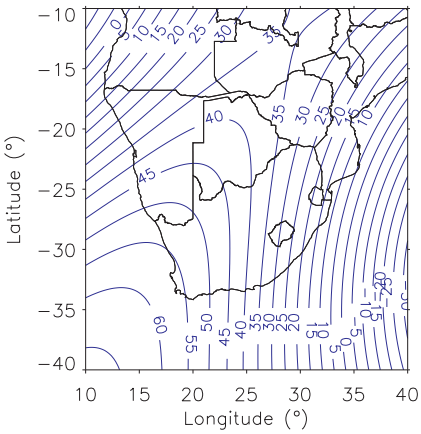

(b) IGRF 10 model at 0.8 km: SV in Z component (2001)

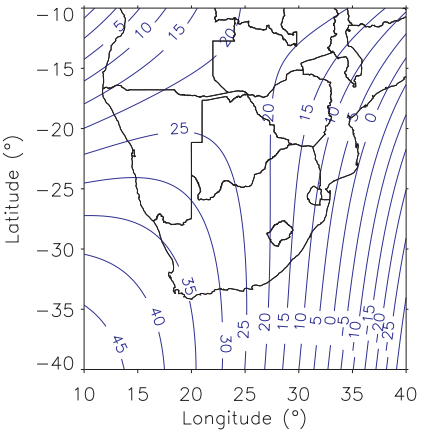

(c) PolyM model at 400 km: SV in Z component (2001)

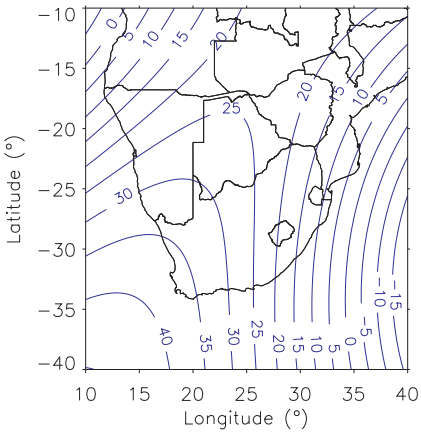

(d) IGRF 10 model at 400 km: SV in Z component (2001)

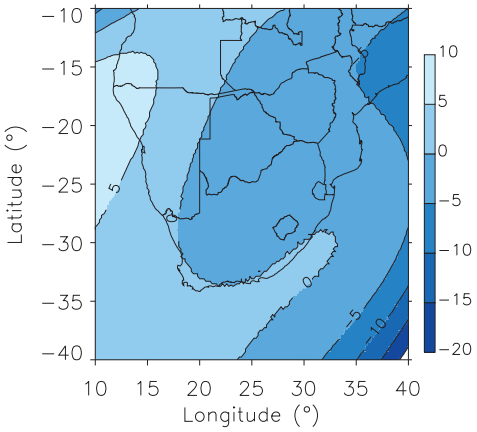

(e) Difference between PolyM and IGRF 10 SV models at 0.8 km: Z component (2001)

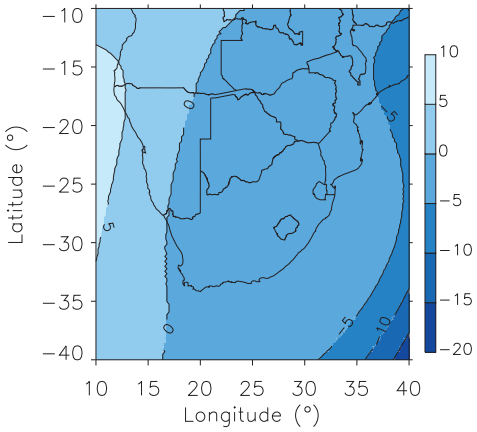

(f) Difference between PolyM and IGRF 10 SV models at 400 km: Z component (2001)

Figure 4.3: The contour plots of SV data obtained from PolyM and IGRF 10 SV models in 2001 for Z component (nT/year) and their differences at 0.8 km and 400 km altitudes.

Table 4.3: The 5^{th} degree polynomial coefficients for January 2001 main field models.

	0.8 km			400 km		
Coef.	D	H	Z	D	H	Z
k_{00}	18.687410	24365.730469	-16685.054687	5.122787	20595.453125	-11993.928711
k_{10}	-1.797953	469.736389	225.175293	-0.639525	366.506256	117.428017
k_{20}	0.074614	-24.176622	-20.555521	0.022840	-20.721151	-12.266032
k_{30}	-0.000750	0.791435	0.964688	0.000357	0.746336	0.629390
k_{40}	-0.000014	-0.014066	-0.016804	-0.000025	-0.013899	-0.011687
k_{50}	0.000000	0.000105	0.000096	0.000000	0.000105	0.000072
k_{01}	4.648957	174.353180	775.096313	2.542450	193.694122	685.342712
k_{11}	-0.233275	25.487614	44.629833	-0.129140	17.787729	25.661131
k_{21}	0.006256	-0.822138	-1.571651	0.003577	-0.578865	-0.867413
k_{31}	-0.000052	0.004378	0.025939	-0.000029	0.004102	0.014807
k_{41}	0.000000	0.000002	-0.000168	0.000000	-0.000010	-0.000099
k_{02}	0.269542	-47.935642	4.170661	0.134579	-28.486757	5.859704
k_{12}	-0.005897	0.029154	1.958275	-0.003202	0.128635	1.131840
k_{22}	0.000128	-0.011118	-0.047417	0.000074	-0.008202	-0.027585
k_{32}	0.000000	0.000031	0.000239	0.000000	0.000024	0.000137
k_{03}	0.010537	-2.089619	-1.303314	0.005340	-1.210469	-0.783467
k_{13}	-0.000008	-0.016561	0.026564	0.000004	-0.007028	0.015570
k_{23}	0.000001	0.000015	-0.000429	0.000001	-0.000005	-0.000254
k_{04}	0.000223	-0.032247	-0.038671	0.000115	-0.017024	-0.023447
k_{14}	0.000001	-0.000181	0.000069	0.000000	-0.000083	0.000044
k_{05}	0.000002	-0.000178	-0.000326	0.000001	-0.000082	-0.000191

Table 4.4: The 5^{th} degree polynomial coefficients for December 2001 main field models.

	0.8 km			400 km		
Coef.	D	H	Z	D	H	Z
k_{00}	20.542955	24997.994141	-11505.925781	7.527905	21717.878906	-11505.925781
k_{10}	-2.427095	299.734100	4.852920	-1.309459	79.478134	4.852920
k_{20}	0.128813	-6.596831	-2.737602	0.080828	7.184217	-2.737602
k_{30}	-0.002831	-0.051673	0.245201	-0.001956	-0.527781	0.245201
k_{40}	0.000025	0.004796	-0.004173	0.000019	0.013555	-0.004173
k_{50}	0.000000	-0.000054	0.000014	-0.000000	-0.000120	0.000014
k_{01}	4.505498	169.088593	694.930908	2.456747	188.609818	694.930908
k_{11}	-0.242153	27.091925	23.903582	-0.135704	19.043966	23.903582
k_{21}	0.007161	-0.891538	-0.783371	0.004194	-0.633361	-0.783371
k_{31}	-0.000073	0.004853	0.013041	-0.000044	0.004412	0.013041
k_{41}	0.000000	0.000009	-0.000086	0.000000	-0.000004	-0.000086
k_{02}	0.257104	-48.150024	5.961800	0.126160	-28.637611	5.961800
k_{12}	-0.005721	0.076424	1.103885	-0.003080	0.160258	1.103885
k_{22}	0.000137	-0.013120	-0.026980	0.000079	-0.009832	-0.026980
k_{32}	0.000000	0.000050	0.000130	0.000000	0.000040	0.000130
k_{03}	0.010190	-2.091960	-0.791512	0.005094	-1.211330	-0.791512
k_{13}	0.000001	-0.016377	0.015367	0.000011	-0.007138	0.015367
k_{23}	0.000001	0.000009	-0.000254	0.000001	-0.000011	-0.000254
k_{04}	0.000220	-0.032257	-0.023689	0.000112	-0.017060	-0.023689
k_{14}	0.000001	-0.000182	0.000043	0.000001	-0.000087	0.000043
k_{05}	0.000002	-0.000178	-0.000193	0.000001	-0.000082	-0.000193

Table 4.5: The 3^{rd} degree polynomial coefficients for 2001 SV models.

	0.8 km			400 km		
Coef.	D	H	Z	D	H	Z
k_{00}	-17.515387	155.973938	-182.359558	-9.399081	102.136734	-85.478371
k_{10}	1.486980	-16.253424	11.778560	1.125593	-10.631302	5.068709
k_{20}	-0.051052	0.593836	-0.134044	-0.044235	0.401803	-0.003302
k_{30}	0.000508	-0.006549	-0.000188	0.000483	-0.004510	-0.001078
k_{01}	-2.835594	12.064991	-10.325313	-1.615996	7.804341	-5.192874
k_{11}	0.083538	-0.509539	0.401645	0.049309	-0.329792	0.229755
k_{21}	-0.000833	0.005390	-0.000516	-0.000504	0.003634	-0.000100
k_{02}	-0.097202	0.257226	-0.096987	-0.057612	0.157680	-0.021079
k_{12}	0.000753	-0.005170	0.004007	0.000380	-0.003241	0.002224
k_{03}	-0.001047	0.001363	0.000256	-0.000652	0.000756	0.000517

Table 4.6: The RMS differences between PolyM and IGRF 10 SV models in 2001 at 0.8 km and 400 km altitudes and their differences.

Component	$\text{RMS}_{400\ km}$	$\text{RMS}_{0.8\ km}$	$\text{RMS}_{400\ km} - \text{RMS}_{0.8\ km}$
D (min of arc/year)	1.624	1.577	0.049
H (nT/year)	9.887	11.145	-1.258
Z (nT/year)	3.466	3.725	0.259

4.4 Results of polynomial modelling

4.4.1 Introduction

The PolyM SV models were developed for each year between 2001 and 2005 at 0.8 km altitude for 3 geomagnetic field components D, H and Z and the total field F. To monitor the geomagnetic time variation within each year, the SV models were developed for a period of six months. This was mainly done for periods January - June and June -December. The 5^{th} degree polynomial was used for main field models and the 3^{rd} degree for SV models. The results of polynomial modelling are shown in figs. 4-23. The polynomial coefficients for main field and SV models for each year are given in the appendices A and B.

4.4.2 PolyM SV models: 2001

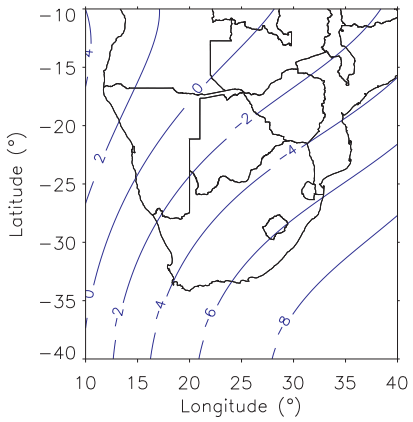

(a) Geomagnetic variation in D component between January and June 2001.

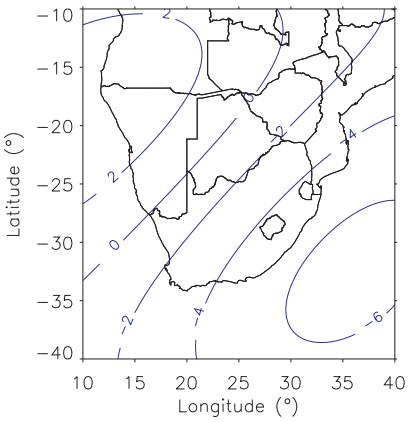

(b) Geomagnetic variation in D component between June and December 2001.

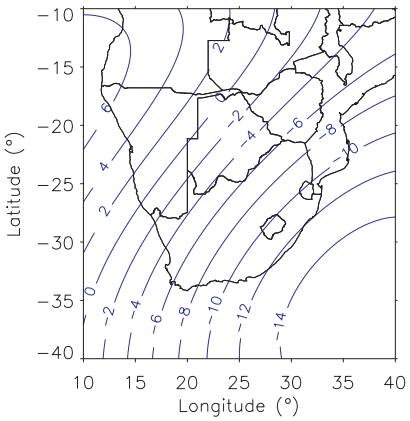

(c) PolyM SV model for D component in 2001 (min of arc/year).

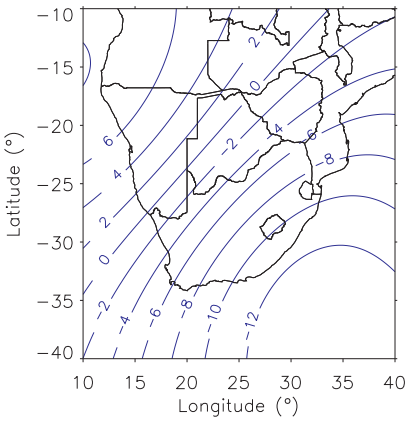

(d) IGRF 10 SV model for D component in 2001 (min of arc/year).

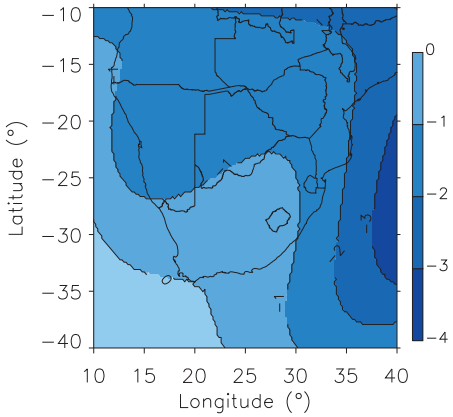

(e) Difference between PolyM and IGRF 10 SV models for D component in 2001 (RMS = 1.58 min of arc/year).

Figure 4.4: The contour plots of SV data obtained from PolyM and IGRF 10 SV models in 2001 for D component and their difference.

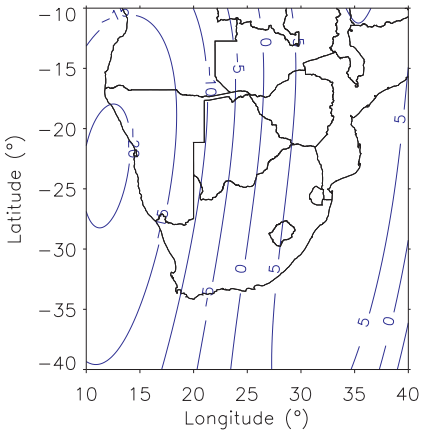

(a) Geomagnetic variation in H component between January and June 2001.

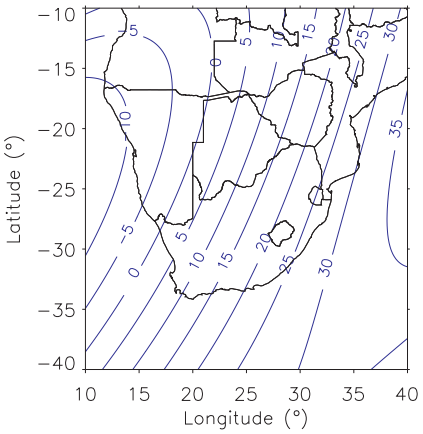

(b) Geomagnetic variation in H component between June and December 2001.

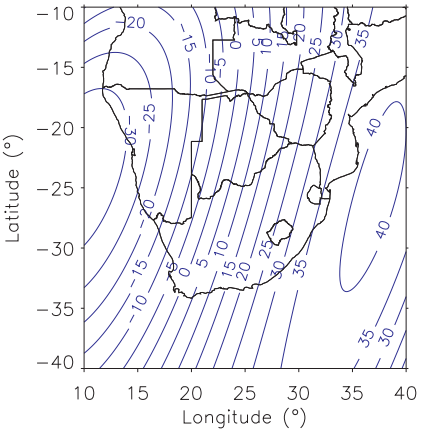

(c) PolyM SV model for H component in 2001 (nT/year).

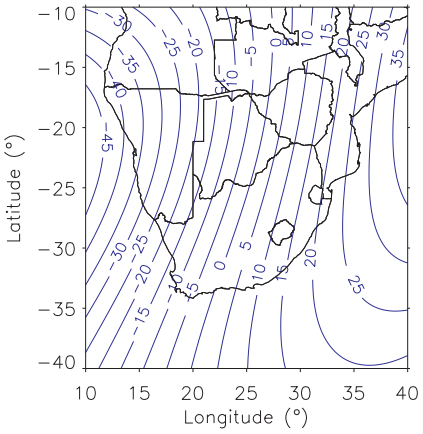

(d) IGRF 10 SV model for H component in 2001 (nT/year).

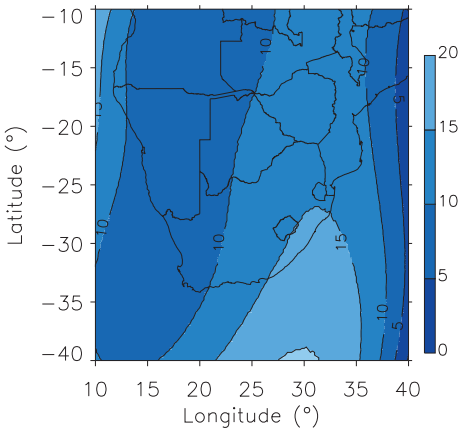

(e) Difference between PolyM and IGRF 10 SV models for H component in 2001 (RMS = 11.15 nT/year).

Figure 4.5: The contour plots of SV data obtained from PolyM and IGRF 10 SV models in 2001 for H component and their difference.

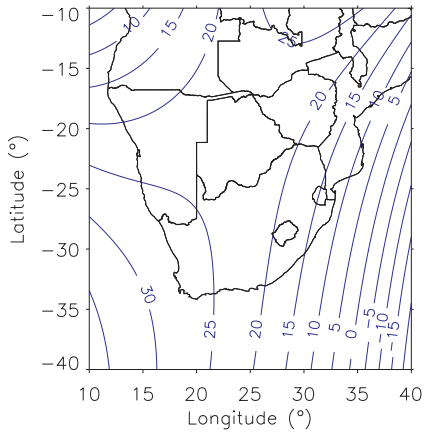

(a) Geomagnetic variation in Z component between January and June 2001.

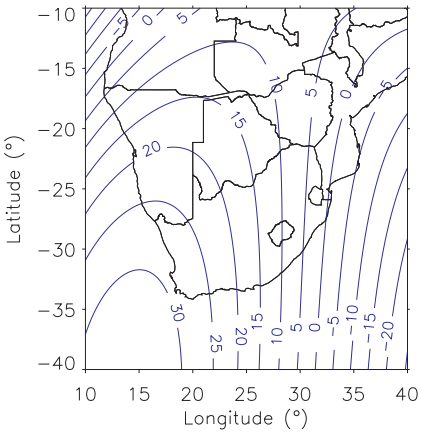

(b) Geomagnetic variation in Z component between June and December 2001.

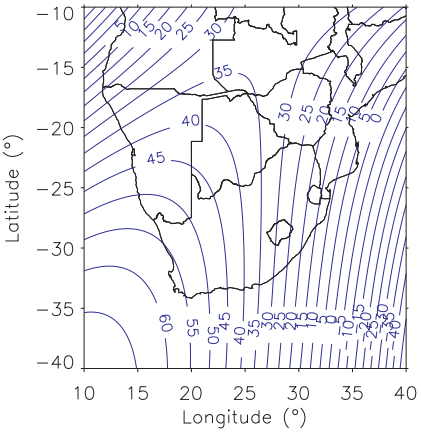

(c) PolyM SV model for Z component in 2001 (nT/year).

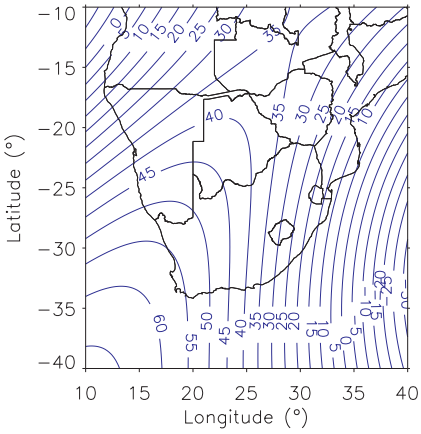

(d) IGRF 10 SV model for Z component in 2001 (nT/year).

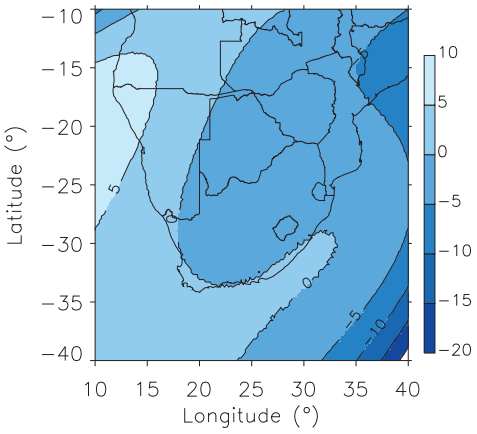

(e) Difference between PolyM and IGRF 10 SV models for Z component in 2001 (RMS = 3.73 nT/year).

Figure 4.6: The contour plots of SV data obtained from PolyM and IGRF 10 SV models in 2001 for Z component and their difference.

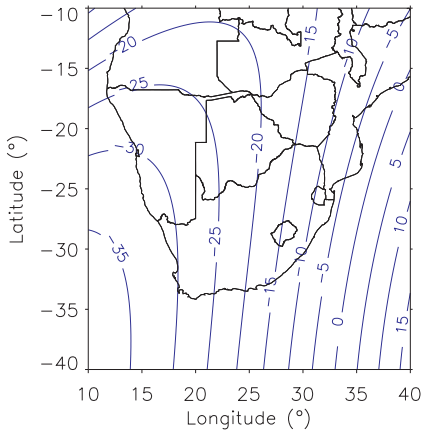

(a) Geomagnetic variation in total field F between January and June 2001.

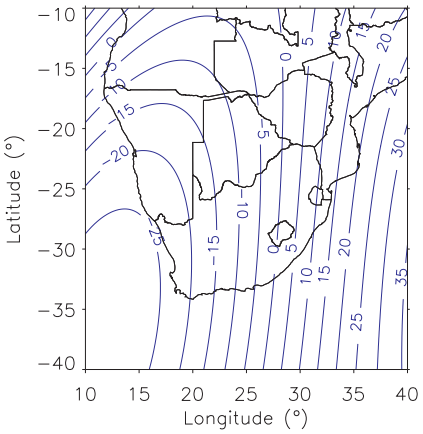

(b) Geomagnetic variation in total field F between June and December 2001.

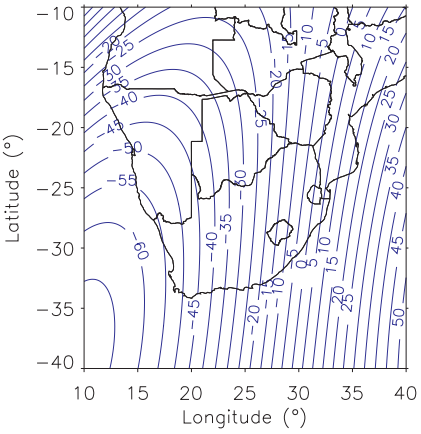

(c) PolyM SV model for total field F in 2001 (nT/year).

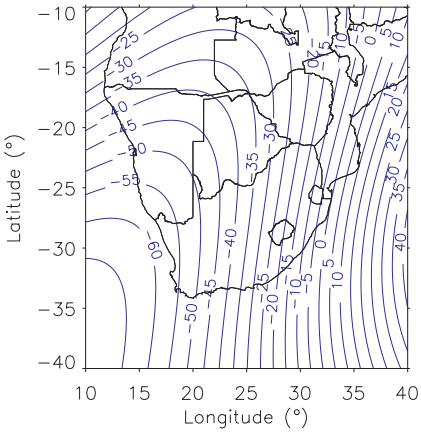

(d) IGRF 10 SV model for total field F in 2001 (nT/year).

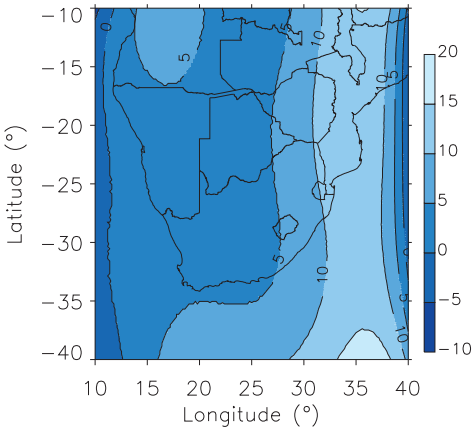

(e) Difference between PolyM and IGRF 10 SV models for total field F in 2001 (RMS = 7.34 nT/year).

Figure 4.7: The contour plots of SV data obtained from PolyM and IGRF 10 SV models in 2001 for total field F and their difference.

4.4.3 PolyM SV models: 2002

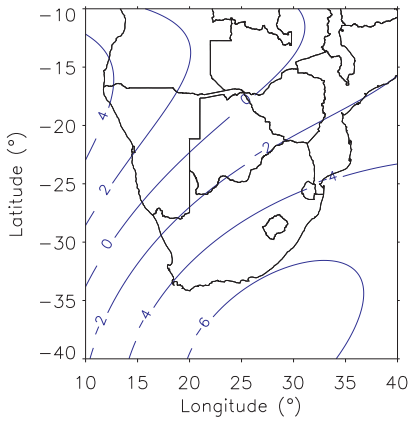

(a) Geomagnetic variation in D component between January and June 2002.

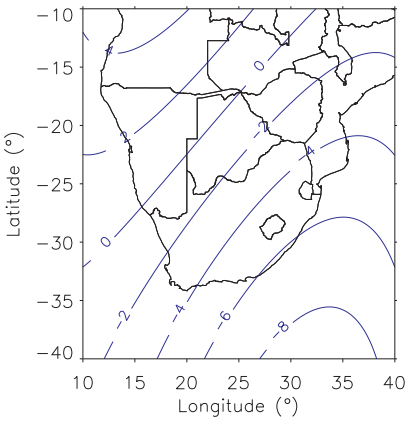

(b) Geomagnetic variation in D component between June and December 2002.

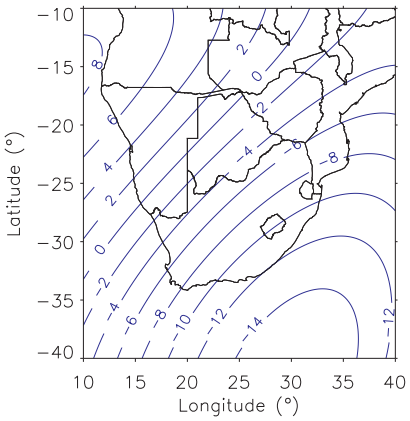

(c) PolyM SV model for D component in 2002 (min of arc/year).

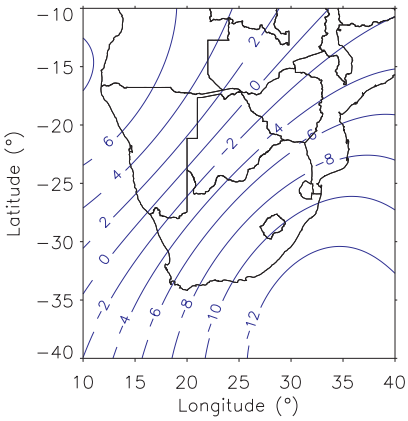

(d) IGRF 10 SV model for D component in 2002 (min of arc/year).

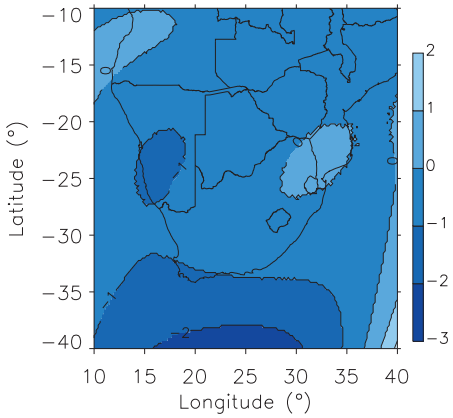

(e) Difference between PolyM and IGRF 10 SV models for D component in 2002 (RMS = 0.81 min of arc/year).

Figure 4.8: The contour plots of SV data obtained from PolyM and IGRF 10 SV models in 2002 for D component and their difference.

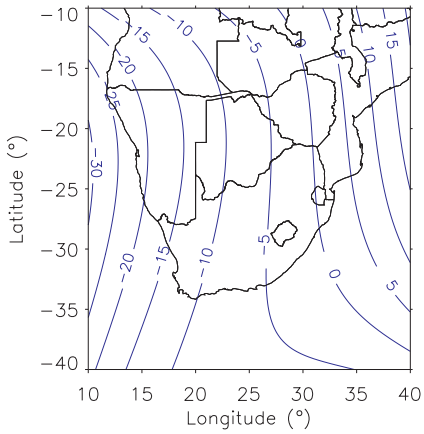

(a) Geomagnetic variation in H component between January and June 2002.

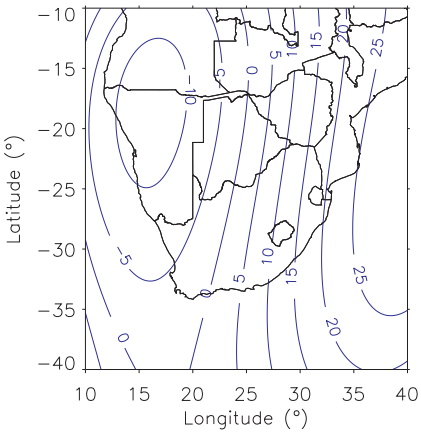

(b) Geomagnetic variation in H component between June and December 2002.

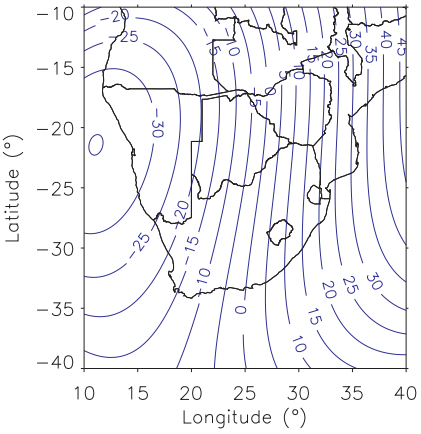

(c) PolyM SV model for H component in 2002 (nT/year).

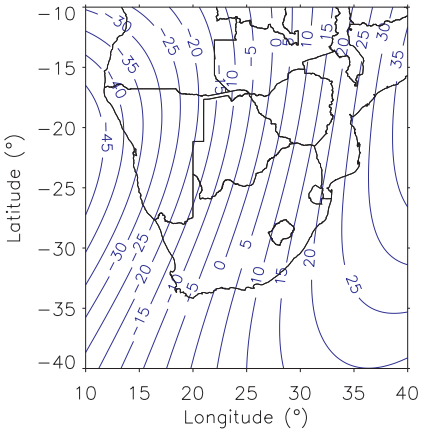

(d) IGRF 10 SV model for H component in 2002 (nT/year).

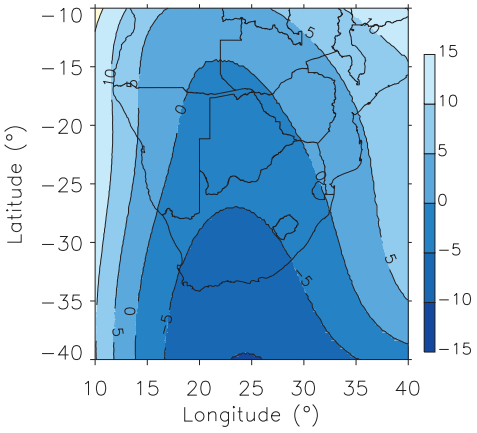

(e) Difference between PolyM and IGRF 10 SV models for H component in 2002 (RMS = 5.60 nT/year).

Figure 4.9: The contour plots of SV data obtained from PolyM and IGRF 10 SV models in 2002 for H component and their difference.

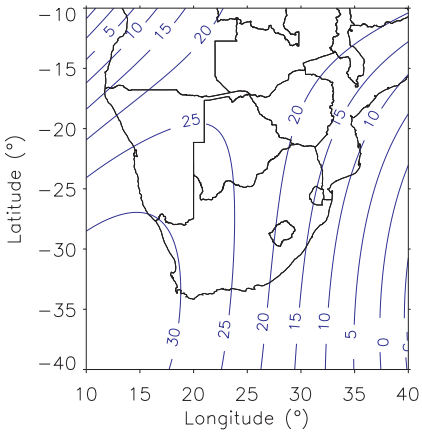

(a) Geomagnetic variation in Z component between January and June 2002.

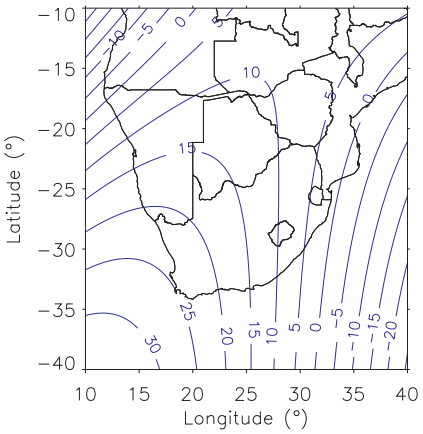

(b) Geomagnetic variation in Z component between June and December 2002.

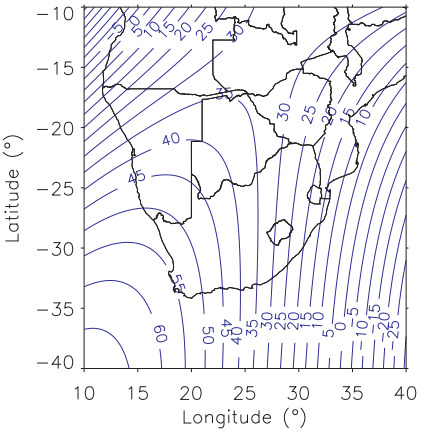

(c) PolyM SV model for Z component in 2002 (nT/year).

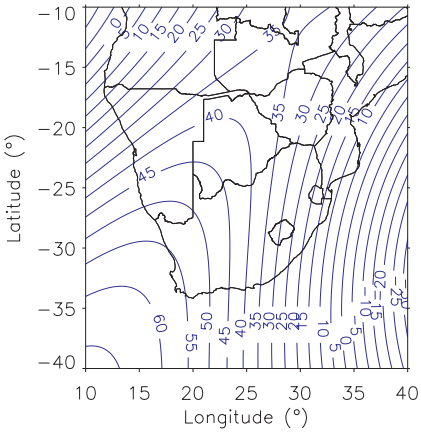

(d) IGRF 10 SV model for Z component in 2002 (nT/year).

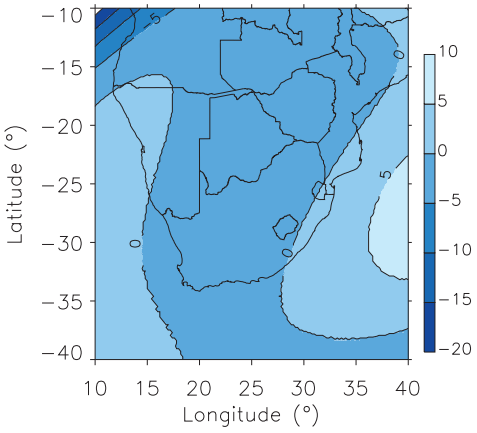

(e) Difference between PolyM and IGRF 10 SV models for Z component in 2002 (RMS = 2.83 nT/year).

Figure 4.10: The contour plots of SV data obtained from PolyM and IGRF 10 SV models in 2002 for Z component and their difference.

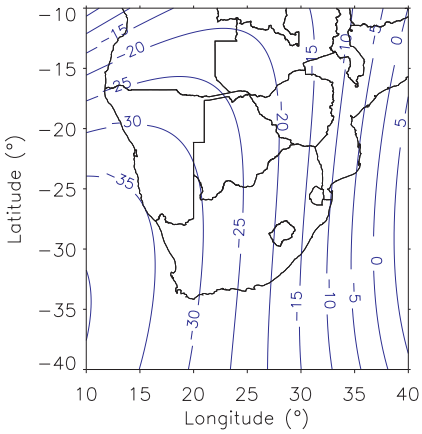

(a) Geomagnetic variation in total field F between January and June 2002.

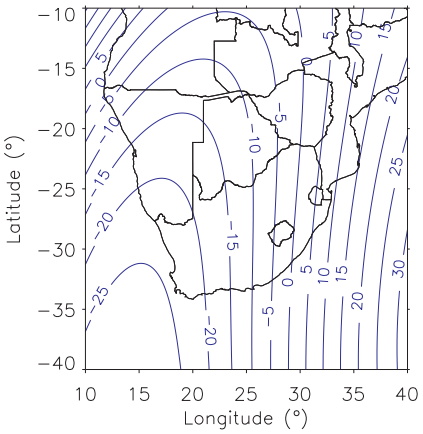

(b) Geomagnetic variation in total field F between June and December 2002.

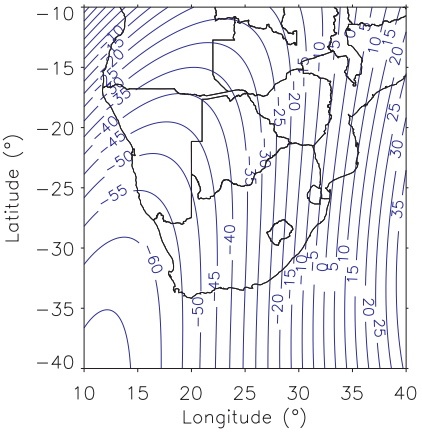

(c) PolyM SV model for total field F in 2002 (nT/year).

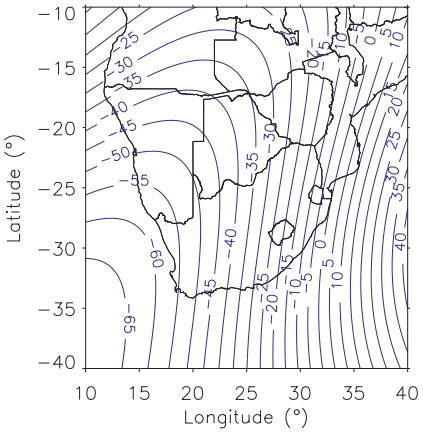

(d) IGRF 10 SV model for total field F in 2002 (nT/year).

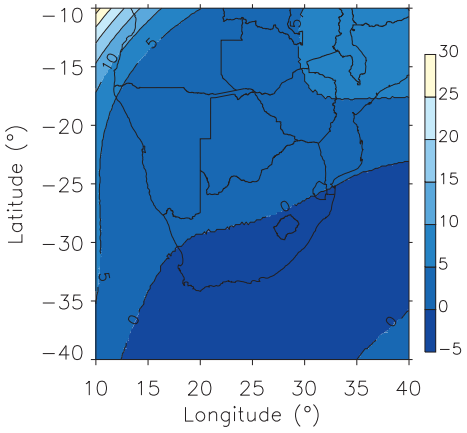

(e) Difference between PolyM and IGRF 10 SV models for total field F in 2002 (RMS = 4.24 nT/year).

Figure 4.11: The contour plots of SV data obtained from PolyM and IGRF 10 SV models in 2002 for total field F and their difference.

4.4.4 PolyM SV models: 2003

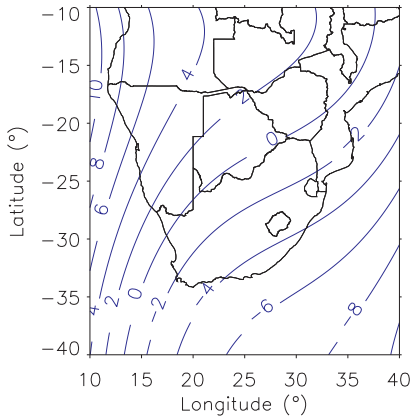

(a) Geomagnetic variation in D component between January and July 2003.

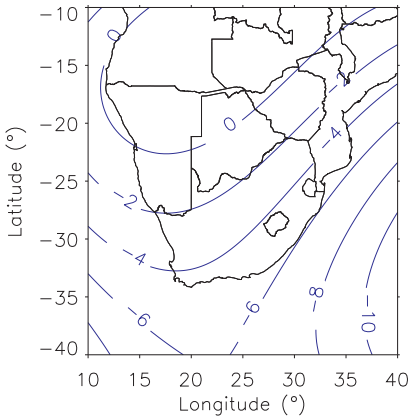

(b) Geomagnetic variation in D component between July and December 2003.

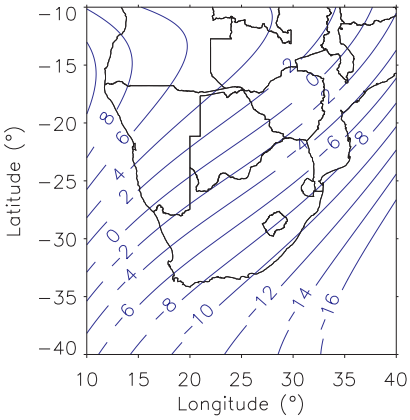

(c) PolyM SV model for D component in 2003 (min of arc/year).

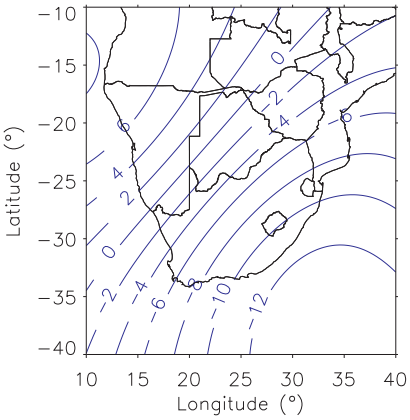

(d) IGRF 10 SV model for D component in 2003 (min of arc/year).

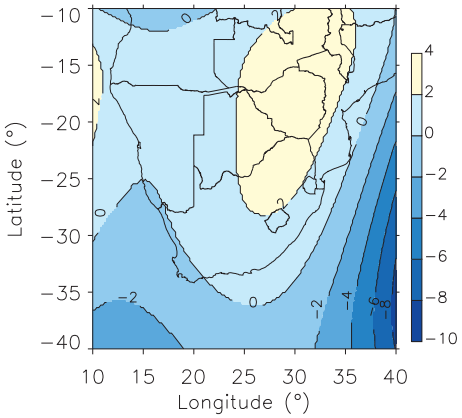

(e) Difference between PolyM and IGRF 10 SV models of D component in 2003 (RMS = 2.10 min of arc/year).

Figure 4.12: The contour plots of SV data obtained from PolyM and IGRF SV models in 2003 for D component and their difference.

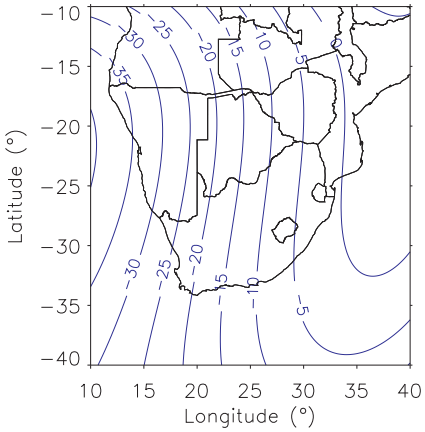

(a) Geomagnetic variation in H component between January and July 2003.

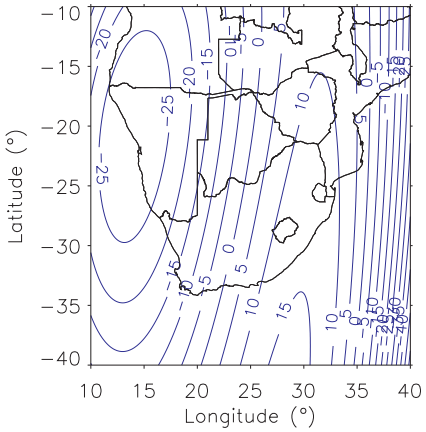

(b) Geomagnetic variation in H component between July and December 2003.

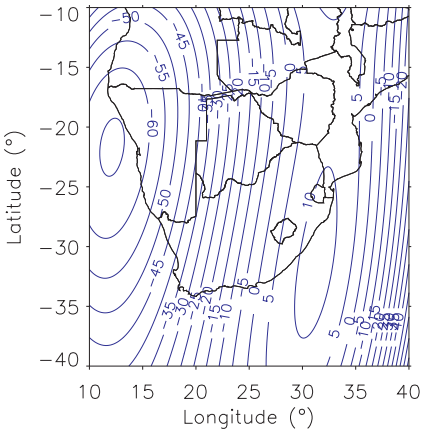

(c) PolyM SV model for H component in 2003 (nT/year).

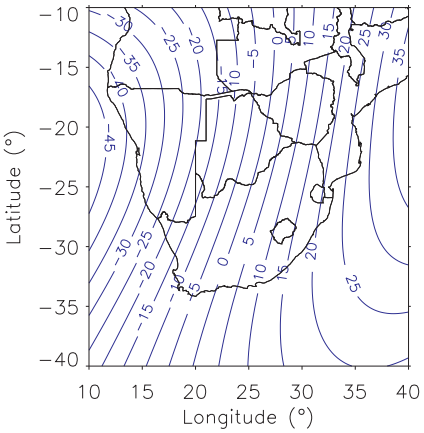

(d) IGRF 10 SV model for H component in 2003 (nT/year).

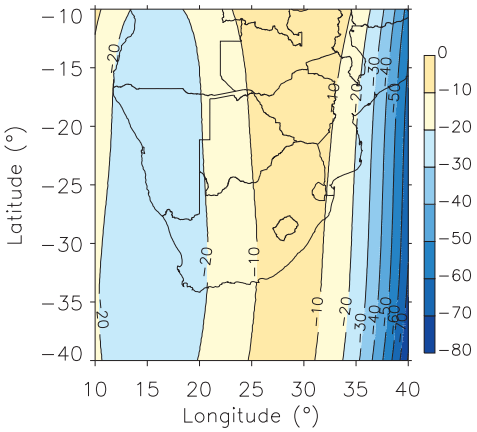

(e) Difference between PolyM and IGRF 10 SV models for H component in 2003 (RMS = 23.98 nT/year).

Figure 4.13: The contour plots of SV data obtained from PolyM and IGRF 10 SV models in 2003 for H component and their difference.

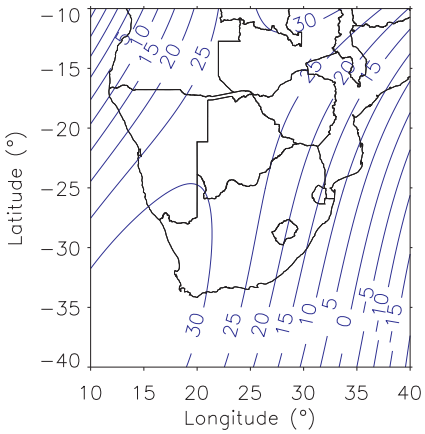

(a) Geomagnetic variation in Z component between January and July 2003.

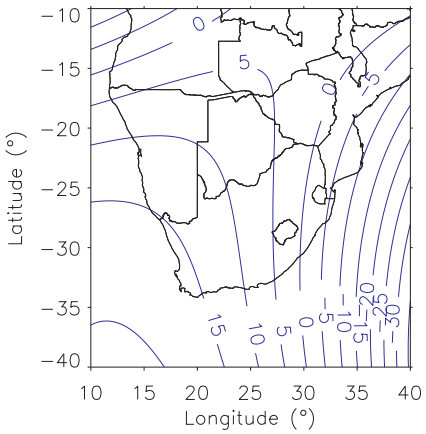

(b) Geomagnetic variation in Z component between July and December 2003.

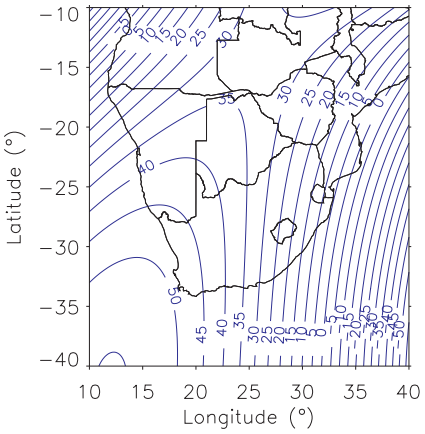

(c) PolyM SV model for Z component in 2003 (nT/year).

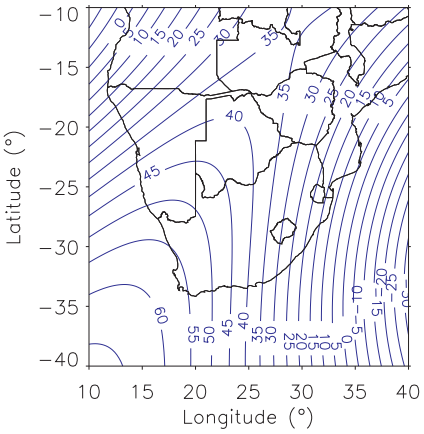

(d) IGRF 10 SV model for Z component in 2003 (nT/year).

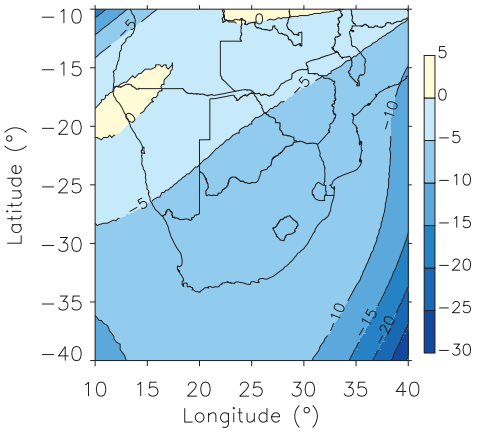

(e) Difference between PolyM and IGRF 10 SV models for Z component in 2003 (RMS= 7.23 nT/year).

Figure 4.14: The contour plots of SV data obtained from PolyM and IGRF 10 SV models in 2003 for Z component and their difference.

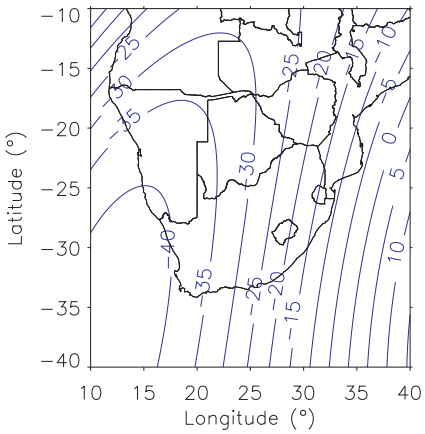

(a) Geomagnetic variation in total field F between January and July 2003.

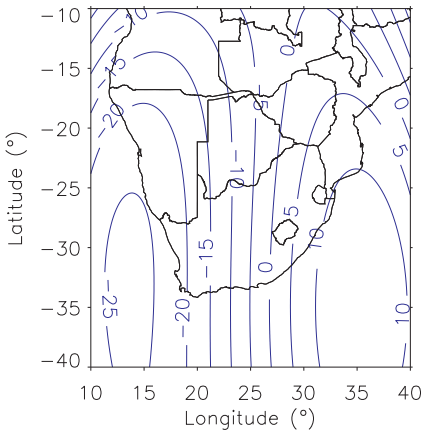

(b) Geomagnetic variation in total field F between July and December 2003.

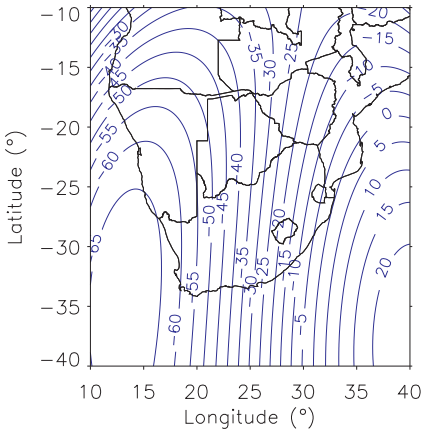

(c) PolyM SV model for total field F in 2003 (nT/year).

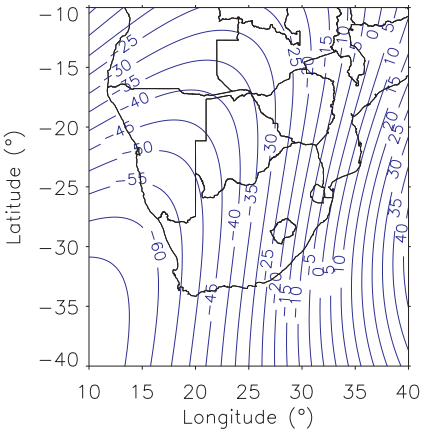

(d) IGRF 10 SV model for total field F in 2003 (nT/year).

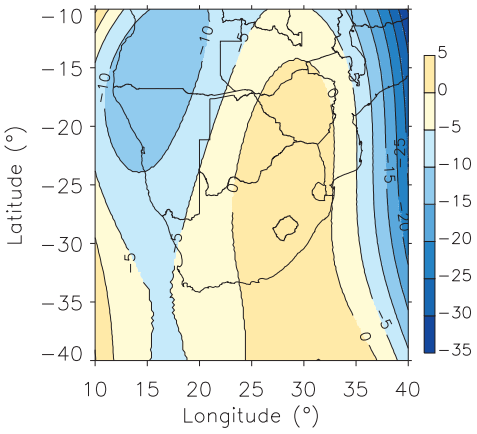

(e) Difference between PolyM and IGRF 10 SV models for total field F in 2003 (RMS = 8.35 nT/year).

Figure 4.15: The contour plots of SV data obtained from PolyM and IGRF 10 SV models in 2003 for total field F and their difference.

4.4.5 PolyM SV models: 2004

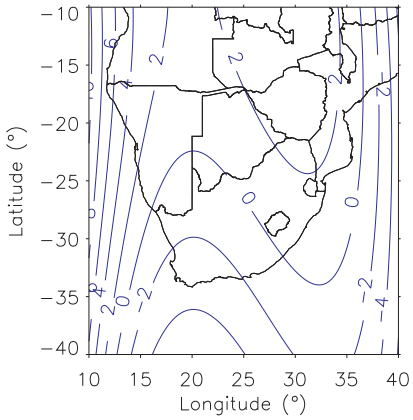

(a) Geomagnetic variation in D component between January and June 2004.

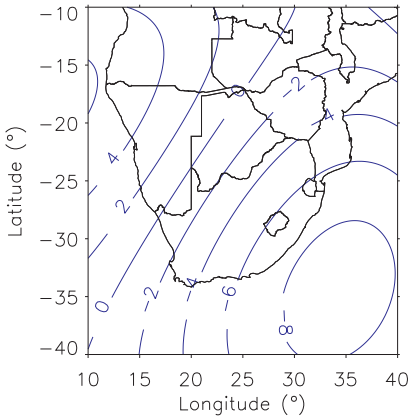

(b) Geomagnetic variation in D component between June and December 2004.

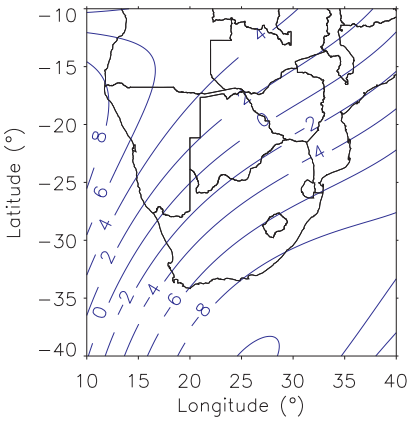

(c) PolyM SV model for D component in 2004 (min of arc/year).

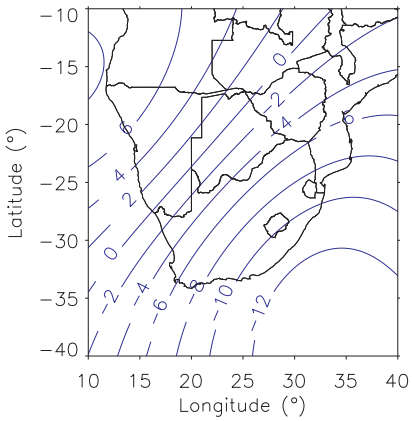

(d) IGRF 10 SV model for D component in 2004 (min of arc/year).

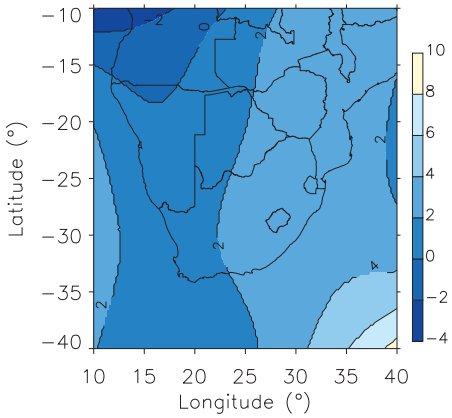

(e) Difference between PolyM and IGRF 10 SV models of D component in 2004 (RMS = 2.52 min of arc/year).

Figure 4.16: The contour plots of SV data obtained from PolyM and IGRF 10 SV models in 2004 for D component and their difference.

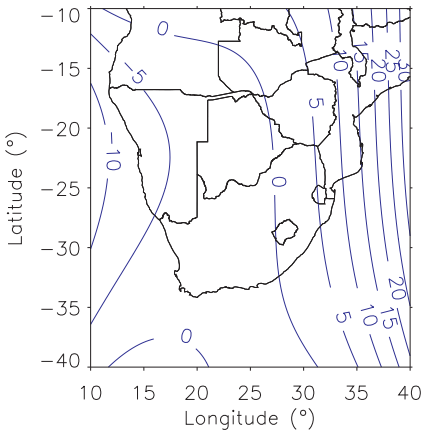

(a) Geomagnetic variation in H component between January and June 2004.

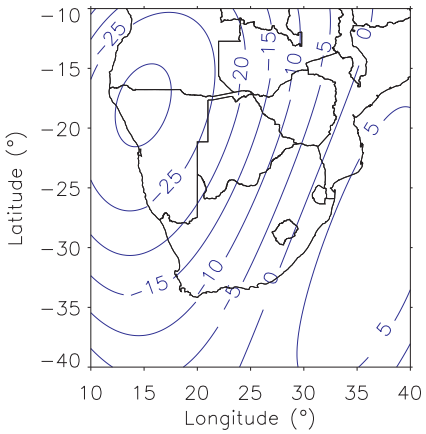

(b) Geomagnetic variation in H component between June and December 2004.

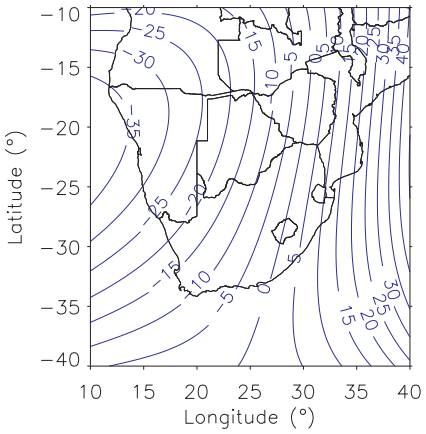

(c) PolyM SV model for H component in 2004 (nT/year).

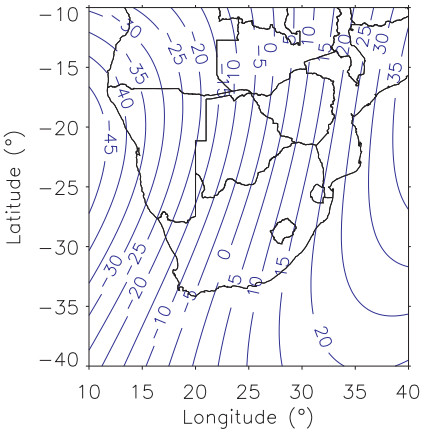

(d) IGRF 10 SV model for H component in 2004 (nT/year).

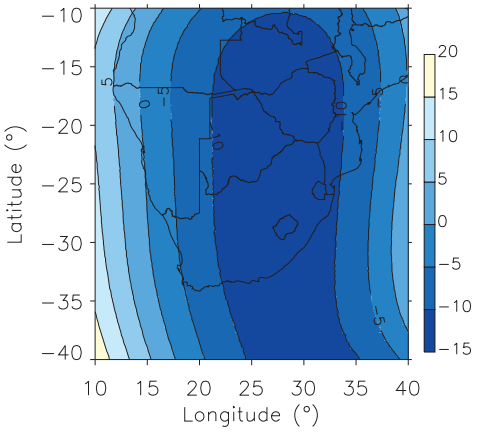

(e) Difference between PolyM and IGRF 10 SV models for H component in 2004 (RMS = 8.89 nT/year).

Figure 4.17: The contour plots of SV data obtained from PolyM and IGRF 10 SV models in 2004 for H component and their difference.

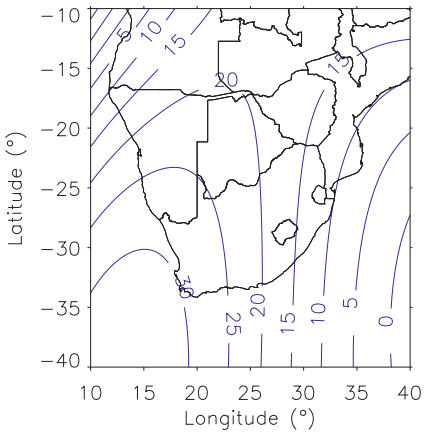

(a) Geomagnetic variation in Z component between January and June 2004.

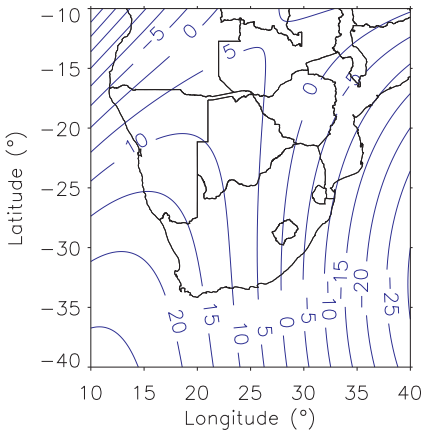

(b) Geomagnetic variation in Z component between June and December 2004.

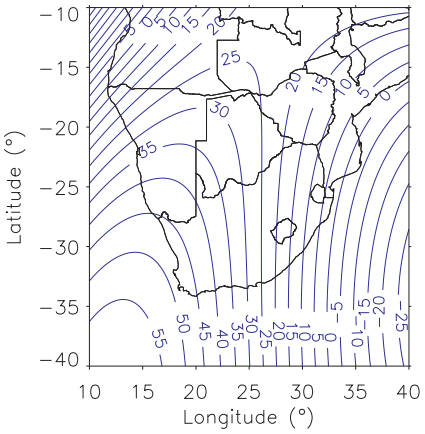

(c) PolyM SV model for Z component in 2004 (nT/year).

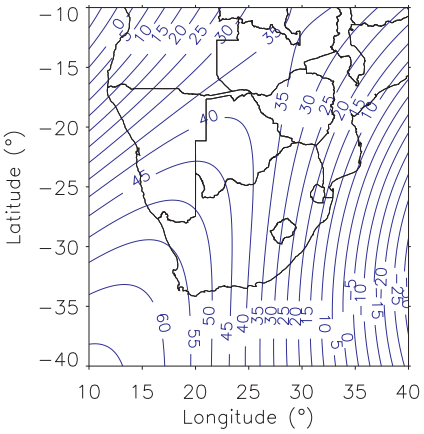

(d) IGRF 10 SV model for Z component in 2004 (nT/year).

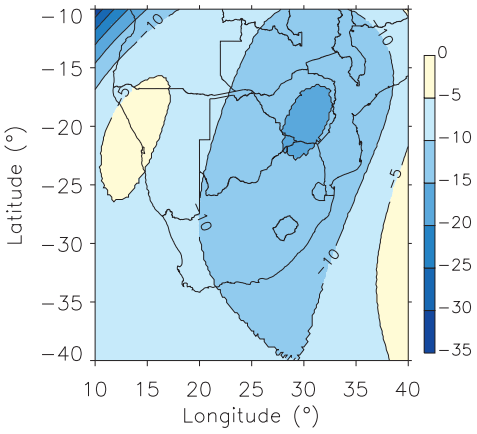

(e) Difference between PolyM and IGRF 10 SV models for Z component in 2004 (RMS = 10.10 nT/year).

Figure 4.18: The contour plots of SV data obtained from PolyM and IGRF 10 SV models in 2004 for Z component and their difference.

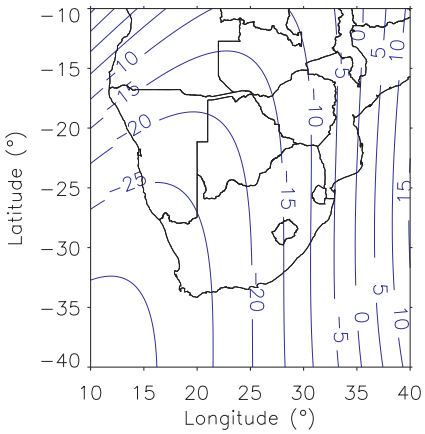

(a) Geomagnetic variation in total field F between January and June 2004.

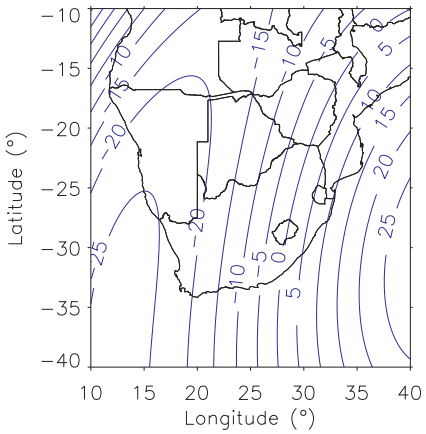

(b) Geomagnetic variation in total field F between June and December 2004.

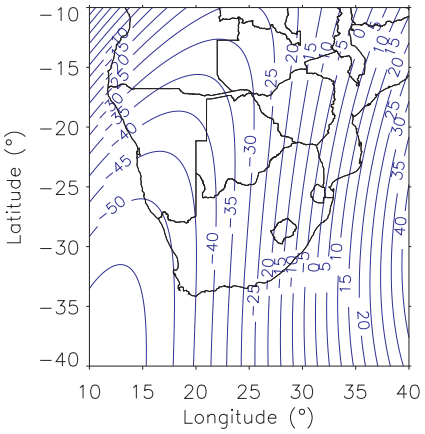

(c) PolyM SV model for total field F in 2004 (nT/year).

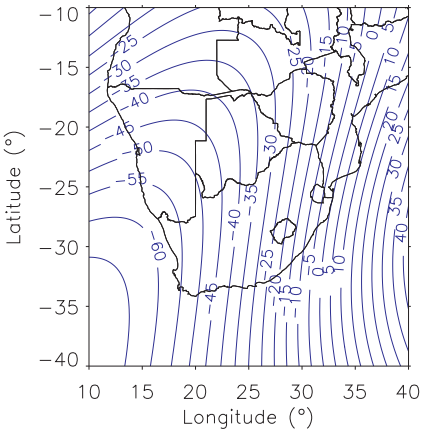

(d) IGRF 10 SV model for total field F in 2004 (nT/year).

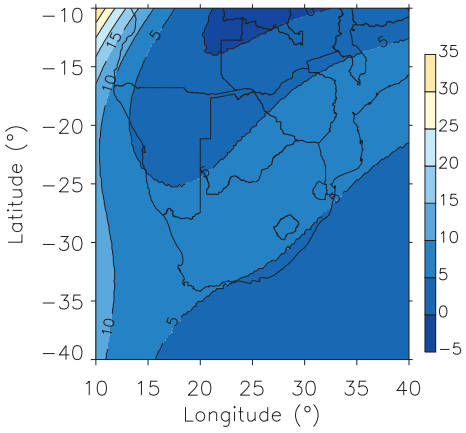

(e) Difference between PolyM and IGRF 10 SV models for total field F in 2004 (RMS = 6.00 nT/year).

Figure 4.19: The contour plots of SV data obtained from PolyM and IGRF 10 SV models in 2004 for total field F and their difference.

4.4.6 PolyM SV models: 2005

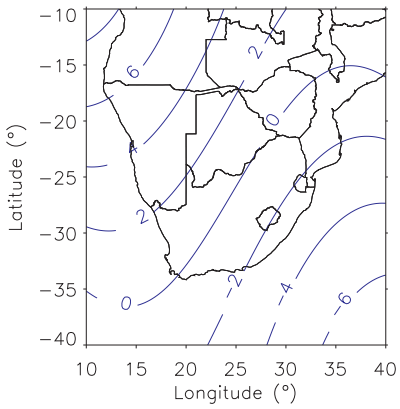

(a) Geomagnetic variation in D component between February and July 2005.

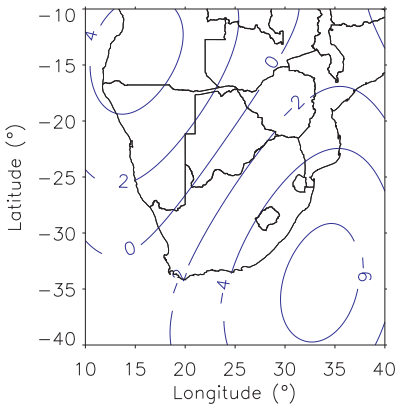

(b) Geomagnetic variation in D component between June and December 2005.

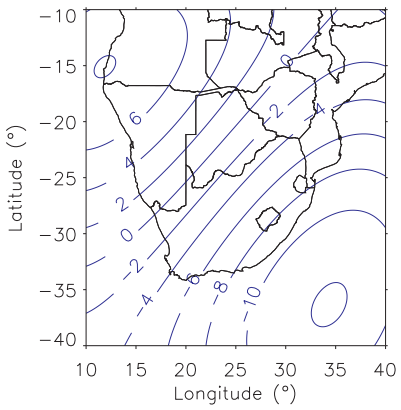

(c) PolyM SV model for D component in 2005 between February and December (min of arc/year).

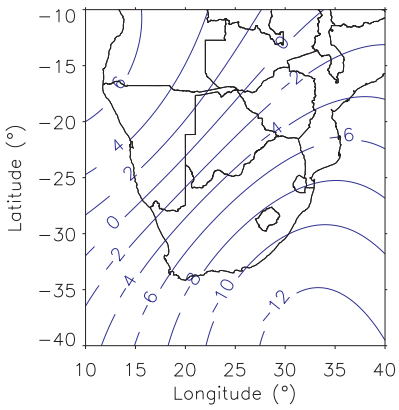

(d) IGRF 10 SV model for D component in 2005 between February and December (min of arc/year).

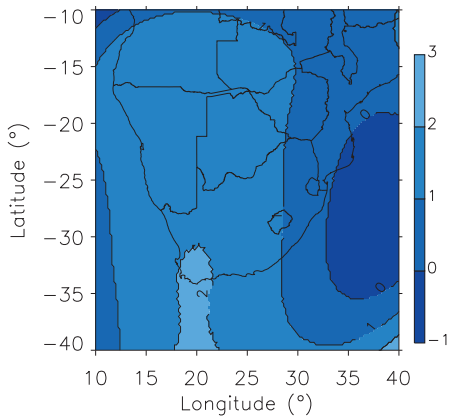

(e) Difference between PolyM and IGRF 10 SV models of D component in 2005 (RMS = 1.23 min of arc/year).

Figure 4.20: The contour plots of SV data obtained from PolyM and IGRF 10 SV models in 2005 for D component and their difference.

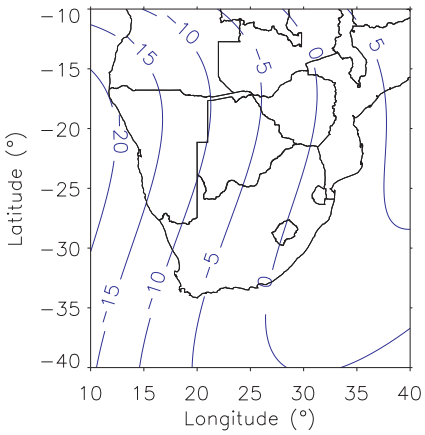

(a) Geomagnetic variation in H component between February and July 2005.

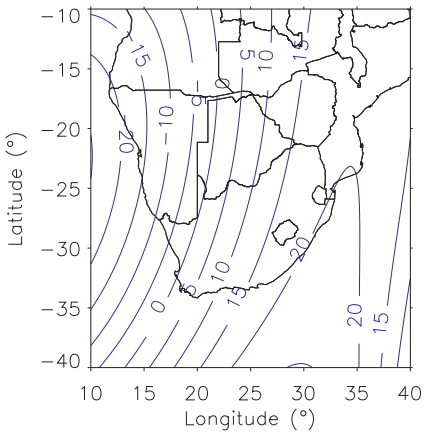

(b) Geomagnetic variation in H component between June and December 2005.

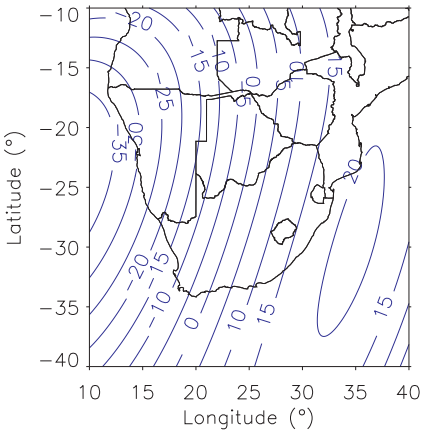

(c) PolyM SV model for H component in 2005 between February and December (nT/year).

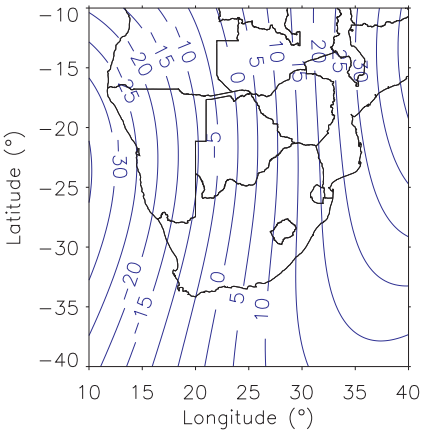

(d) IGRF 10 SV model for H component in 2005 between February and December (nT/year).

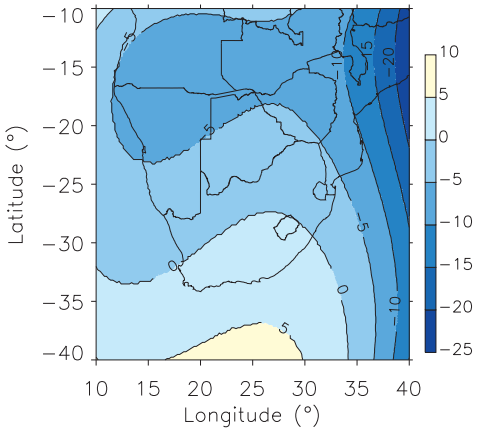

(e) Difference between PolyM and IGRF 10 SV models for H component in 2005 (RMS = 6.93 nT/year).

Figure 4.21: The contour plots of SV data obtained from PolyM and IGRF 10 SV models in 2005 for H component and their difference.

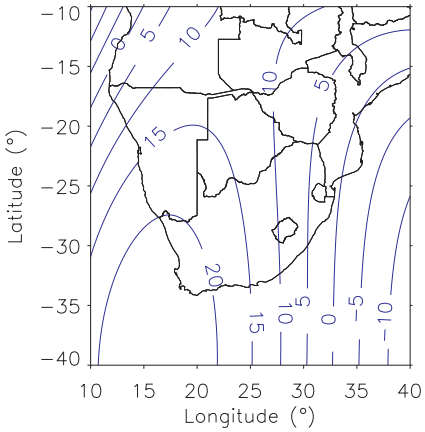

(a) Geomagnetic variation in Z component between February and July 2005.

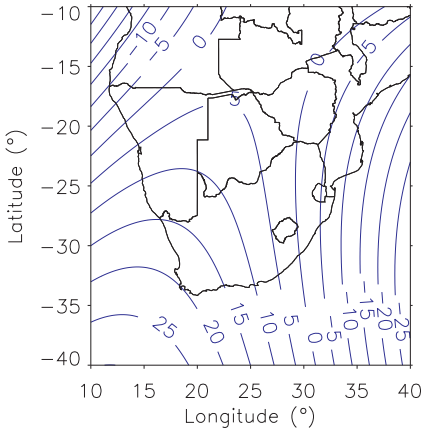

(b) Geomagnetic variation in Z component between June and December 2005.

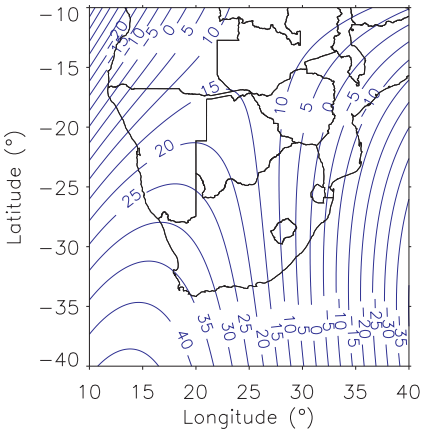

(c) PolyM SV model for Z component in 2005 between February and December (nT/year).

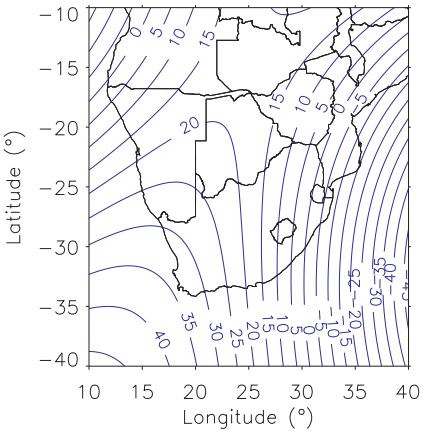

(d) IGRF 10 SV model for Z component in 2005 between February and December (nT/year).

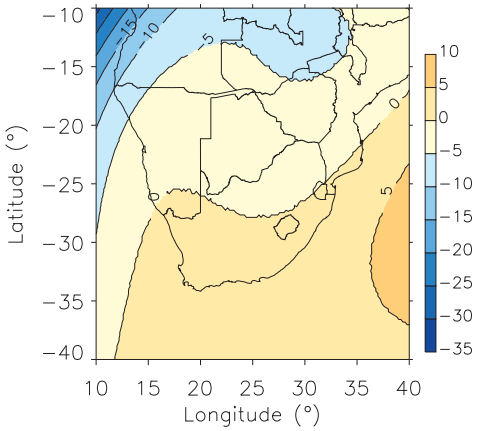

(e) Difference between PolyM and IGRF 10 SV models for Z component in 2005 (RMS = 4.89 nT/year).

Figure 4.22: The contour plots of SV data obtained from PolyM and IGRF 10 SV models in 2005 for Z component and their difference.

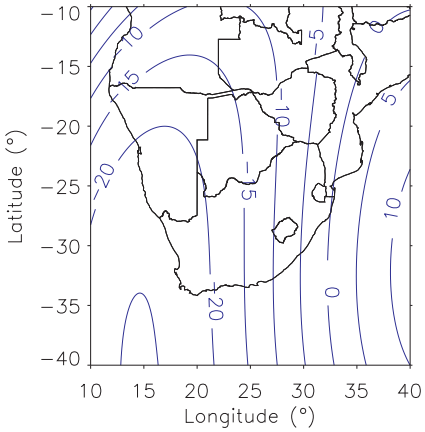

(a) Geomagnetic variation in total field F between February and July 2005.

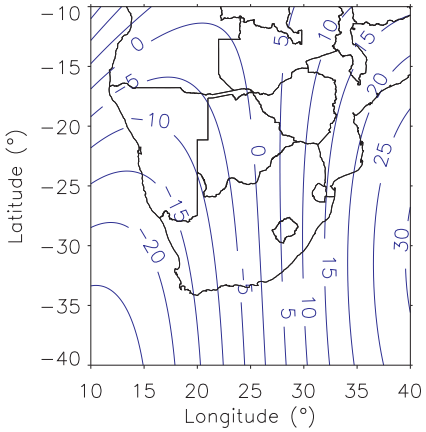

(b) Geomagnetic variation in total field F between June and December 2004.

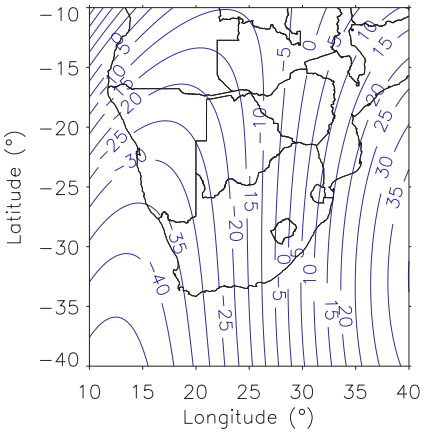

(c) PolyM SV model for F component in 2005 between February and December (nT/year).

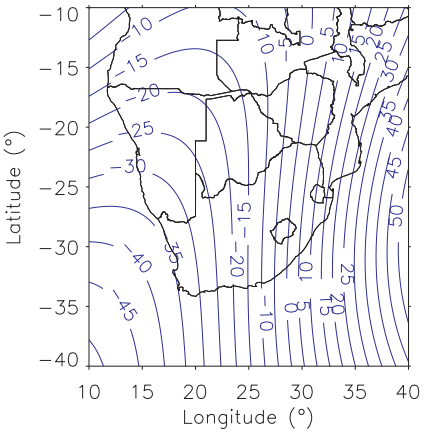

(d) IGRF 10 SV model for F component in 2005 between February and December (nT/year).

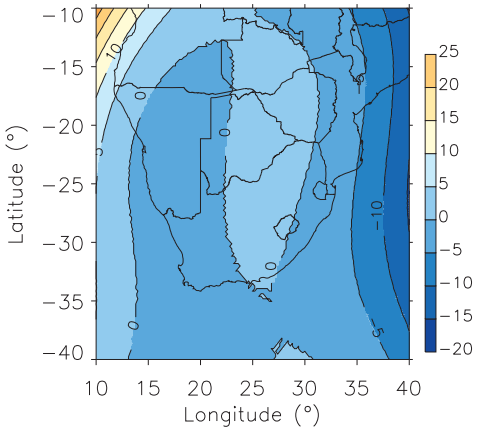

(e) Difference between PolyM and IGRF 10 SV models for total field F in 2005 (RMS = 4.83 nT/year).

Figure 4.23: The contour plots of SV data obtained from PolyM and IGRF 10 SV models in 2005 for total field F and their difference.

4.4.7 Summary of the deviations of PolyM model from IGRF 10 model.

Table 4.7 shows the RMS differences between PolyM and IGRF 10 SV models. The IGRF 10 SV model is the same between 2001 and 2004. The 2002 RMS values are smaller compared to the values for the other 3 years (2001, 2003 and 2004). One of the contributing factors might be that 2002 is in the middle of 5-year IGRF 10 interval (2000.0 - 2005.0) and the good coverage and distribution of 2002 satellite data. The 2005 RMS values were obtained from IGRF 10 SV model for another 5-year interval (2005.0 - 2010.0).

Table 4.7: The RMS differences between PolyM and IGRF 10 SV models.

Component/Total field	2001	2002	2003	2004	2005
D (min of arc/year)	1.7	0.8	2.1	2.5	1.2
H (nT/year)	13.1	5.6	24.0	8.9	6.9
Z (nT/year)	3.9	2.8	7.2	10.1	4.9
F (nT/year)	7.3	4.2	8.4	6.0	4.8

The 2003 RMS value in H component is a large value (24.0 nT/year). The large deviation of satellite data model from IGRF 10 model indicates an unusual SV of H component in 2003. The plot of SV data at one of the selected reference points (Sossusvlei in Namibia) supports the above statement. Fig. 4.24 shows the V shapes in the linear trend of SV between 2001 and 2005.

This observation led to the investigation of SV impulses in X, Y and Z during this 5-year period (2001 - 2005). Using satellite and ground data, two SV impulses were identified during 2003 and 2004. The detail of this investigation is given in section 4.6.

4.5 The validation of PolyM model using ground data and global models (IGRF 10 and CHAOS).

The validation of PolyM was done firstly by plotting the histograms of the SV data from the ground data analysis, PolyM and the two global models IGRF and CHAOS.

The PolyM SV data were calculated between January and December. Due to a very poor quality (in coverage and distribution) of January 2005 CHAMP satellite data, the February and December main field models were used to derive the geomagnetic change during this year.

The comparison was performed on the 3 geomagnetic field components H, D and Z and

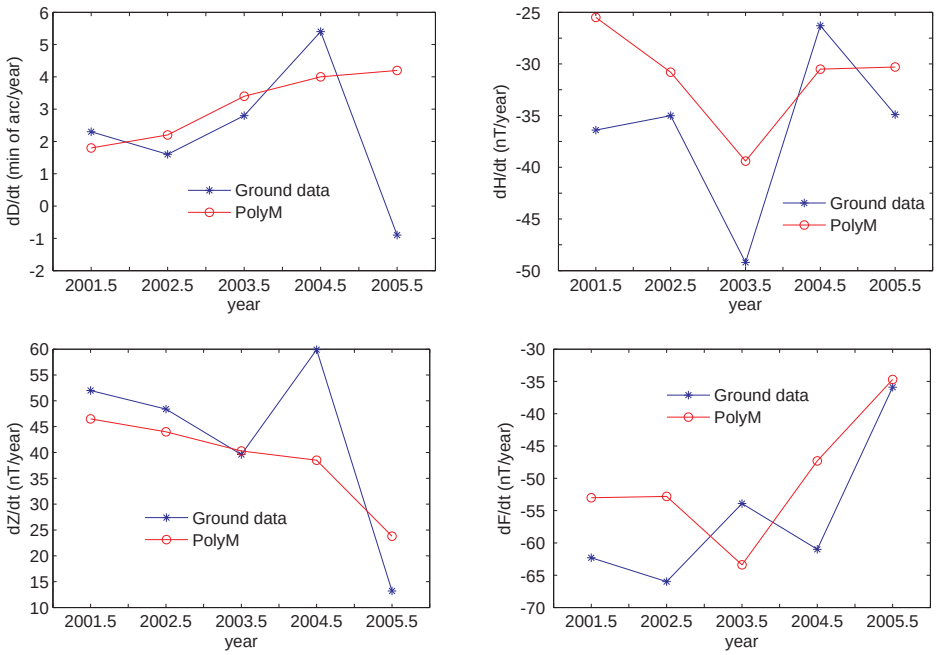

Figure 4.24: The plots of SV between 2001 and 2005 at Sossusvlei (one of the selected reference points) for D, H, Z and F. The SV data were obtained from the measured ground data and PolyM model.

the total field F (figs. 4.25 - 4.29).

Secondly, the bar graphs of the RMS values for each year during the period 2001-2005 calculated using the difference values between the ground survey data and the PolyM model, and the ground survey data and data from two the global models (IGRF 10 and CHAOS) were plotted (fig. 4.30).

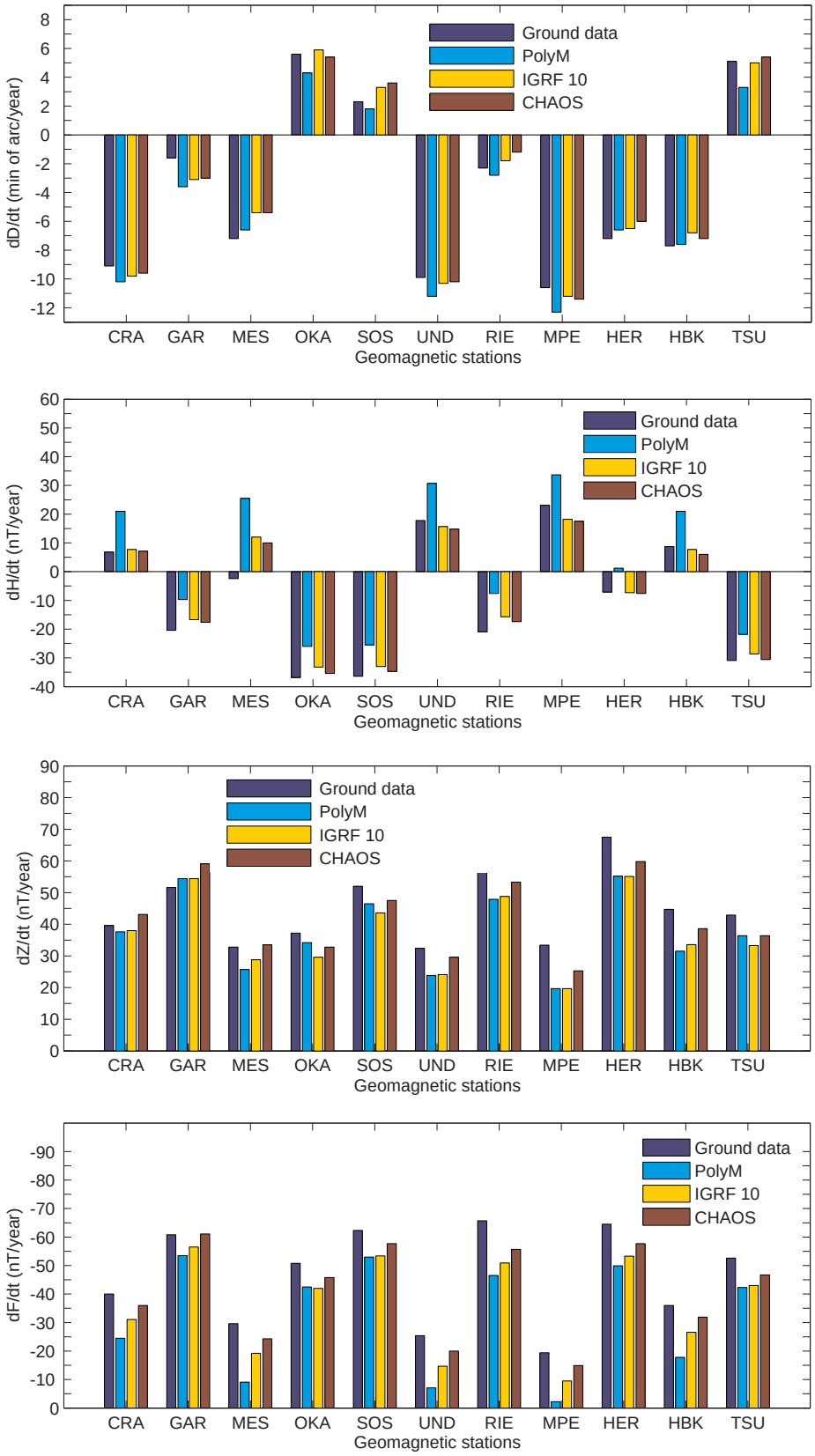

Figure 4.25: The plots of SV in 2001 for D, H, Z and F to compare the PolyM model with ground data and two global models (IGRF 10 and CHAOS) at some selected reference points over southern Africa (fig. 3.8).

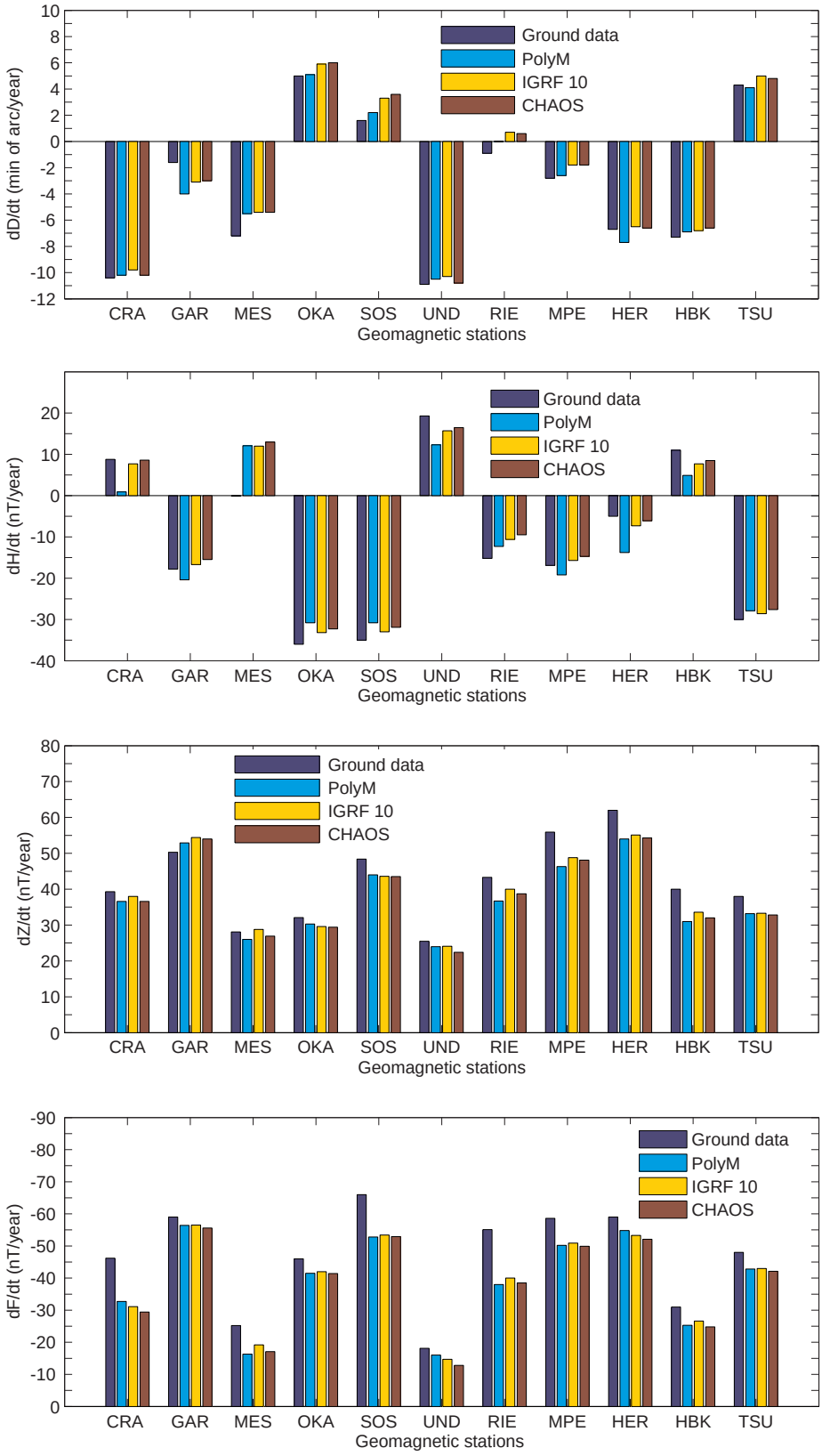

Figure 4.26: The plots of SV in 2002 for D, H, Z and F to compare the PolyM model with ground data and two global models (IGRF 10 and CHAOS) at some selected reference points over southern Africa (fig. 3.8).

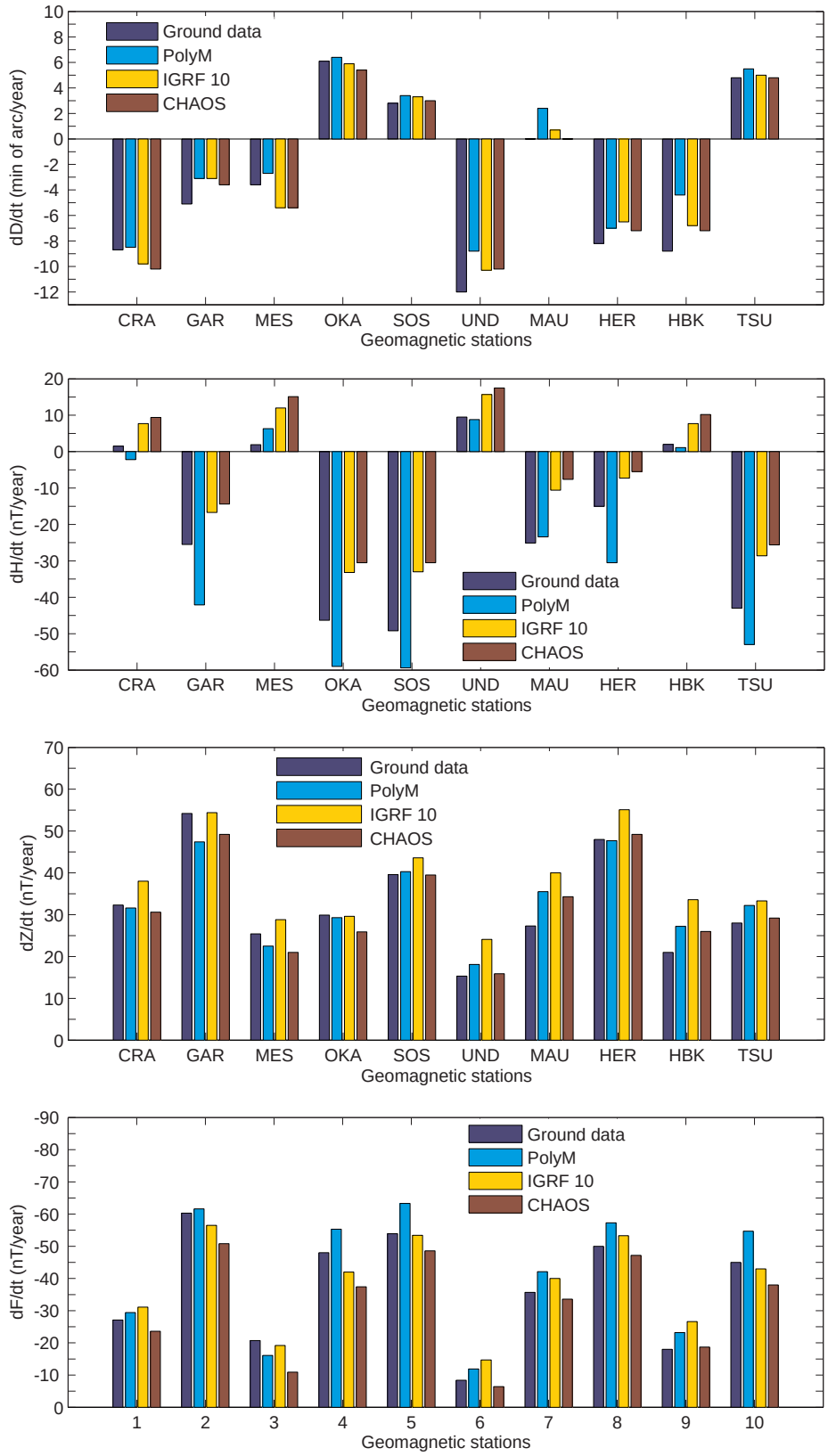

Figure 4.27: The plots of SV in 2003 for D, H, Z and F to compare the PolyM model with ground data and two global models (IGRF 10 and CHAOS) at some selected reference points over southern Africa (fig. 3.8).

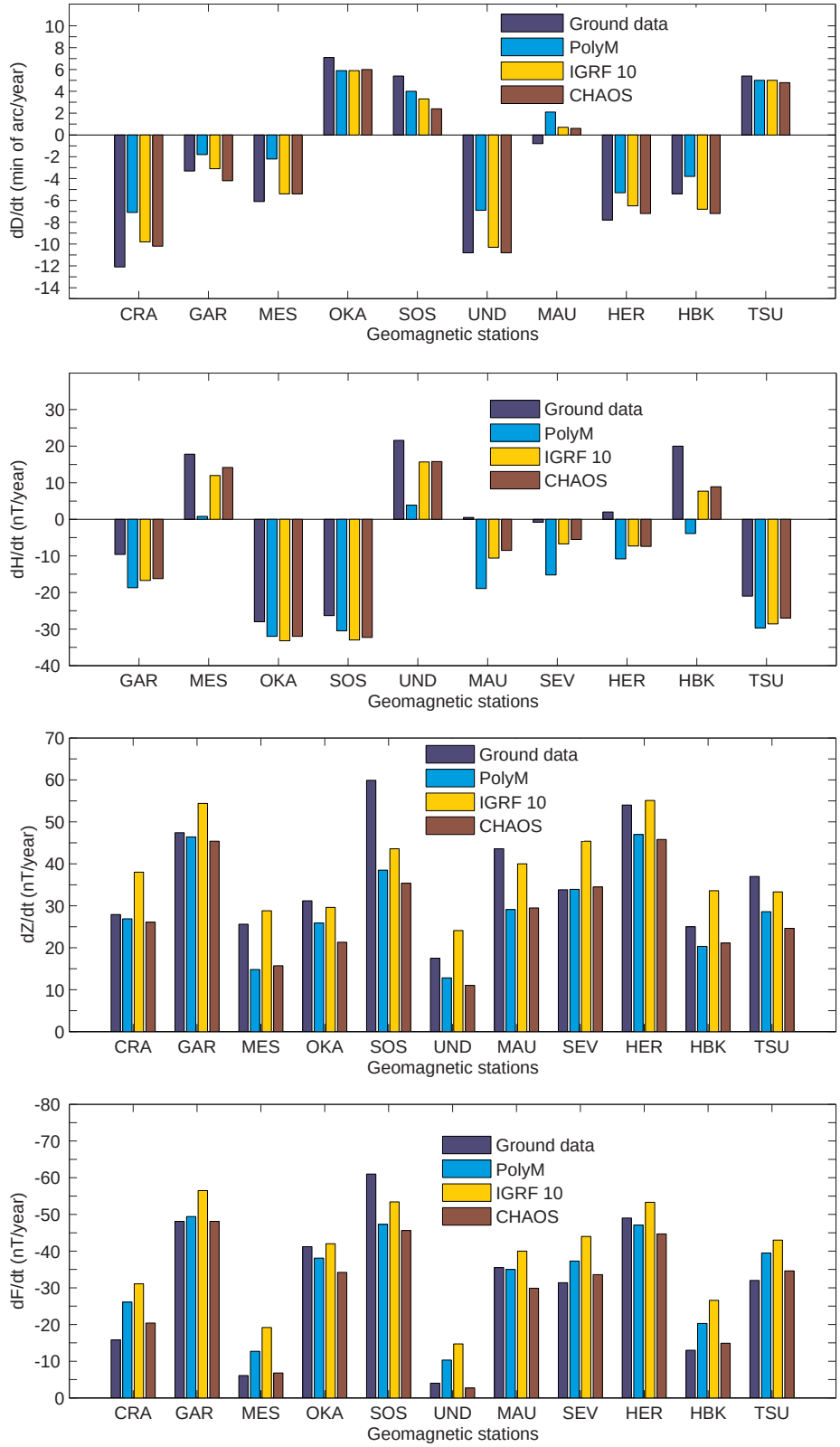

Figure 4.28: The plots of SV in 2004 for D, H, Z and F to compare the PolyM model with ground data and two global models (IGRF 10 and CHAOS) at some selected reference points over southern Africa (fig. 3.8).

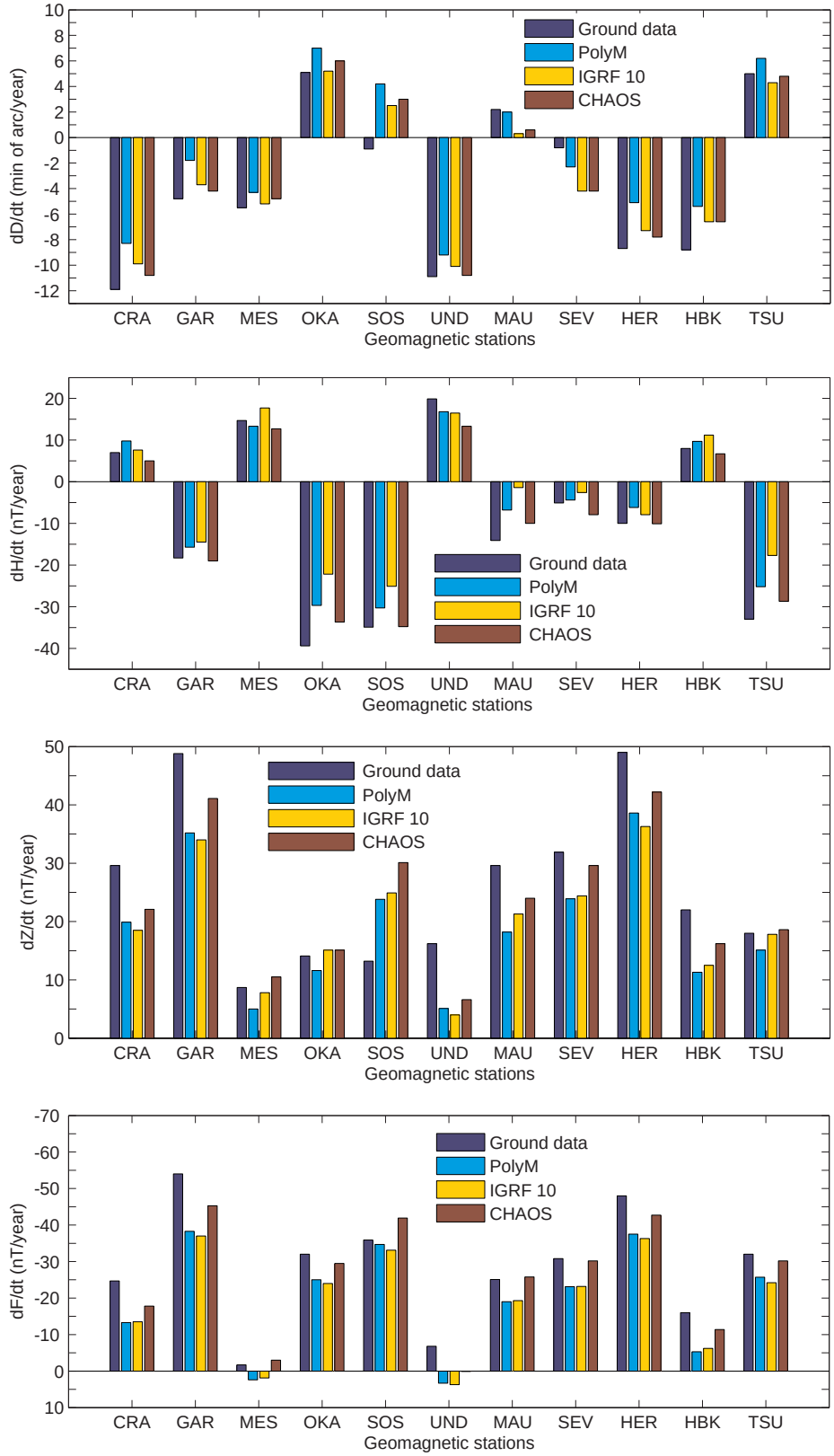

Figure 4.29: The plots of SV in 2005 for D, H, Z and F to compare the PolyM model with ground data and two global models (IGRF and CHAOS) at some selected reference points over southern Africa (fig. 3.8).

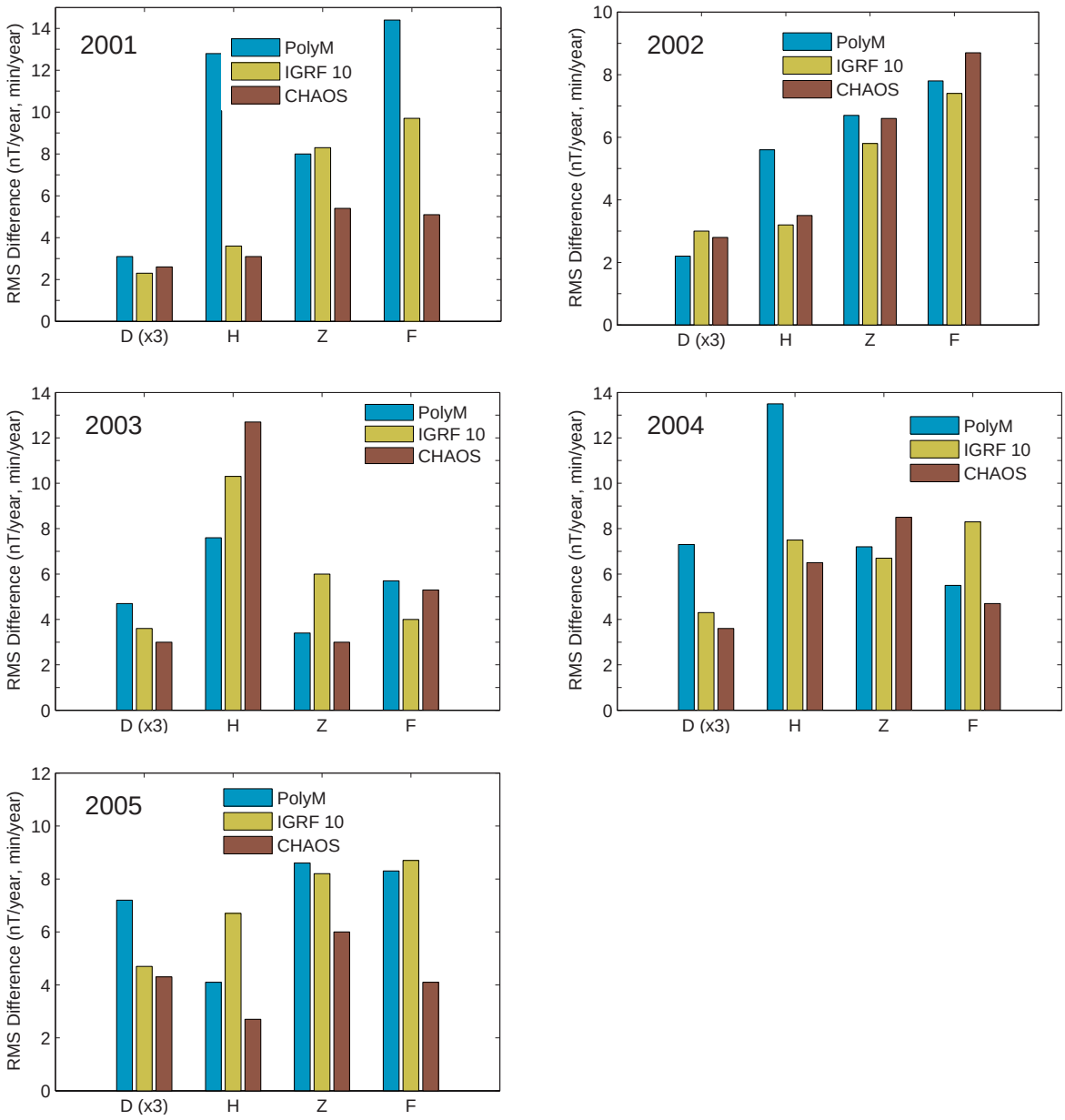

Figure 4.30: Comparison of RMS differences between field survey data and the PolyM model, and field survey data and two global models IGRF 10 and CHAOS. The RMS in D component are multiplied by 3 for the plotting purpose and they are in minutes of arc/year. The RMS were calculated using only the 13 reference points (fig. 3.8).

4.6 Investigation of SV impulses in X, Y and Z components using CHAMP satellite data and ground data between 2001 and 2005 over southern Africa.

This section discusses the modelling of CHAMP vector magnetic field measurements over southern Africa by means of surface polynomial technique (see sections 4.1 and 4.2), using quiet (Dst less than ±20 nT) and night (16:00 - 24:00 and 00:00 - 05:00 UT) data between 2001 and 2005. The satellite data results show the occurrence of SV impulses around 2003.0 and 2004.0 over southern Africa. And the analysis of the monthly time series data for the ground observatories HER and HBK (in South Africa) and TSU (in Namibia) supports these results.

4.6.1 Method and Analytical Techniques

A comparative evaluation of RMS differences between observations and model values showed that a 5^{th} degree polynomial was the best for main field modelling and that 2^{nd} and 3^{rd} degrees were best suited to derive SV field models (see section 4.2). The 2^{nd} degree polynomials were subsequently used in this investigation as they were found to yield the best results for the SV including the reduction of edge effects.

In the present analysis of satellite data, 3 methods were used:

(a) The derivation of an annual SV field model for each component in order to monitor the evolution of SV contour lines.

(b) The second approach was to select 11 reference points at 400 km (the mean CHAMP altitude) as shown in Figure 4.31. In order to limit errors in data, the 11 points are situated few degrees of latitude and longitude away from the boundary of the region of interest.

The generated monthly main field models using only the night and quiet time satellite data (recorded for each particular month) were used to obtain monthly values at corresponding points for years 2001-2005.

(c) The third approach was to create 3 virtual Observatories at 400 km altitude just above 3 permanent observatories (HER, HBK and TSU). The monthly mean values were derived from all CHAMP vector data recorded at all local times and all geomagnetic conditions that are within a radius of 400 km to the target point (Olsen and Mandea, 2007).

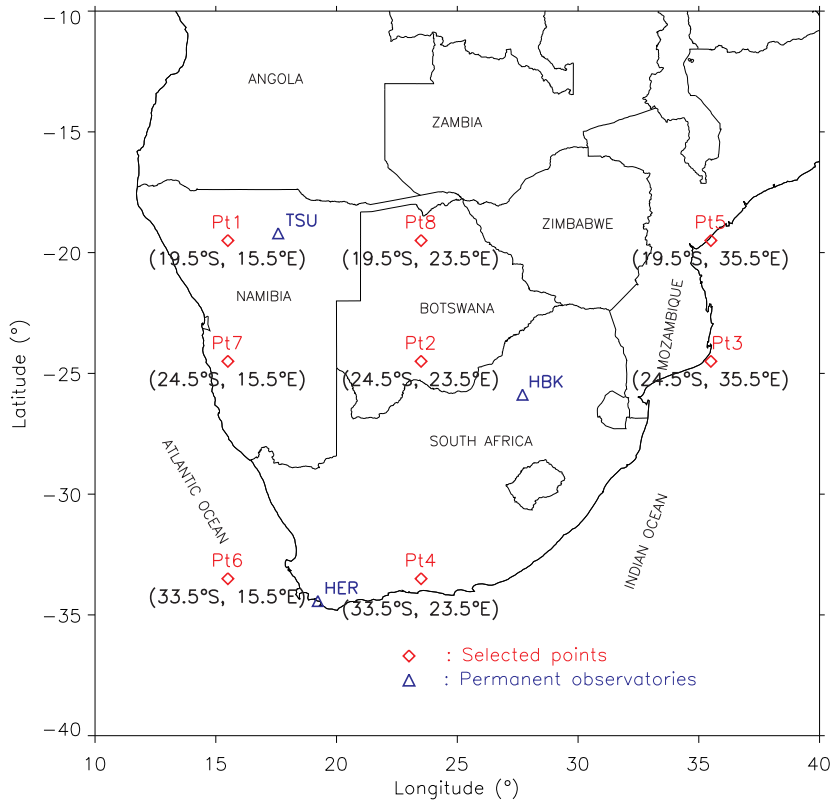

Figure 4.31: The map showing the selected 11 points at 400 km, 8 points (Pt1, Pt2, Pt3, Pt4, Pt5, Pt6, Pt7 and Pt8) and 3 points of permanent observatories (HER, HBK and TSU).

SV values for each of the 3 components (X, Y and Z) in the last 2 approaches mentioned above and in the analysis of ground data at 3 permanent observatories were calculated as follow:

$$dB/dt = \dot{B}(t) = (B(t+6) - B(t-6))/1\text{year} \quad (B = \text{X,Y or Z}), \quad (4.5)$$

where the unit of t is month. In order to remove the annual variation, caused by magnetospheric and ionospheric currents and their earth-induced counterparts, a 12-month running mean was applied to $\dot{B}(t)$ (B = X,Y or Z) (Olsen and Mandea, 2007).

4.6.2 Data selection

The data selection was done on the CHAMP vector magnetic field measurements for years 2001-2005 following the procedure given in chapter 3 (section 3.2) for generating the contour maps for 3 components (X, Y and Z) and for the study of SV at 11 selected points at 400 km altitude. During the data selection process, only the data for 3 months (November 2001, October 2002 and June 2003) out of 60 were not considered due to a lack of sufficient data coverage.

To generate the mean monthly values for the 3 virtual observatories, all CHAMP vector data for all days and geomagnetic conditions were used.

The ground data were collected from the continuous recording of geomagnetic field variations at HER (34° 25.5′S, 19° 13.5′E), HBK (25° 52.9′S, 27° 42.4′E) and TSU (19° 12.1′S, 17° 35.1′E). As mentioned previously, the investigation employed 5-years of 1- monthly averaged data. The TSU and HBK data quality was not acceptable for certain intervals while in some instances a lack of data prevented calculating monthly mean values. The detail of ground data recording and processing is given in chapter 3 under section 3.3.

4.6.3 Polynomial modelling and results

The derivation of annual SV field models for the interval 2001-2005 was done by focusing on January and December months in each year. The annual SV field values were obtained by calculating the change between the main field models of January and December (figs. 4.32, 4.33 and 4.34).

The annual SV at 11 selected points, 3 virtual observatories, and 3 permanent observatories were fitted with a best piece-wise linear fit to identify the epochs of SV impulses of X, Y and Z components (figs. 4.35 - 4.39). The analysis of the strength of SV impulses was done by calculating the gradient of SV before and after the identified epoch of SV impulse (Tables 4.8 - 4.11).

Table 4.8: The identified epochs of SV impulses at 11 selected points (at 400km altitude) using the polynomial monthly main field models.

		Gradient before [nT/yr^2]	Epoch of SV impulse	Gradient after [nT/yr^2]	Gradient before [nT/yr^2]	Epoch of SV impulse	Gradient after [nT/yr^2]
	X	-10.4	2003.2	22.4	22.4	2004.1	-10.0
Pt1	Y	-1.7	2002.5	6.0	6.0	2003.1	-2.7
	Z	-7.7	2003.0	5.8	5.8	2004.0	-9.2
	X	-3.3	2003.0	14.3	14.3	2004.1	-12.1
Pt2	Y	2.9	2003.0	-2.7	-2.7	2004.3	2.4
	Z	-8.9	2003.0	5.1	5.1	2004.0	-9.7
	X	-4.3	2003.1	14.6	14.6	2004.3	-13.0
Pt3	Y	-	-	-	-	-	-
	Z	-8.0	2003.2	3.4	3.4	2004.2	-12.2
	X	-0.3	2003.0	9.4	9.4	2004.0	-9.9
Pt4	Y	4.1	2003.0	-3.6	-3.6	2004.3	1.4
	Z	-10.1	2003.1	6.1	6.1	2004.0	-9.1
	X	-3.9	2003.1	17.2	17.2	2004.3	-13.1
Pt5	Y	-	-	-	-	-	-
	Z	-6.4	2003.2	2.7	2.7	2004.1	-10.7

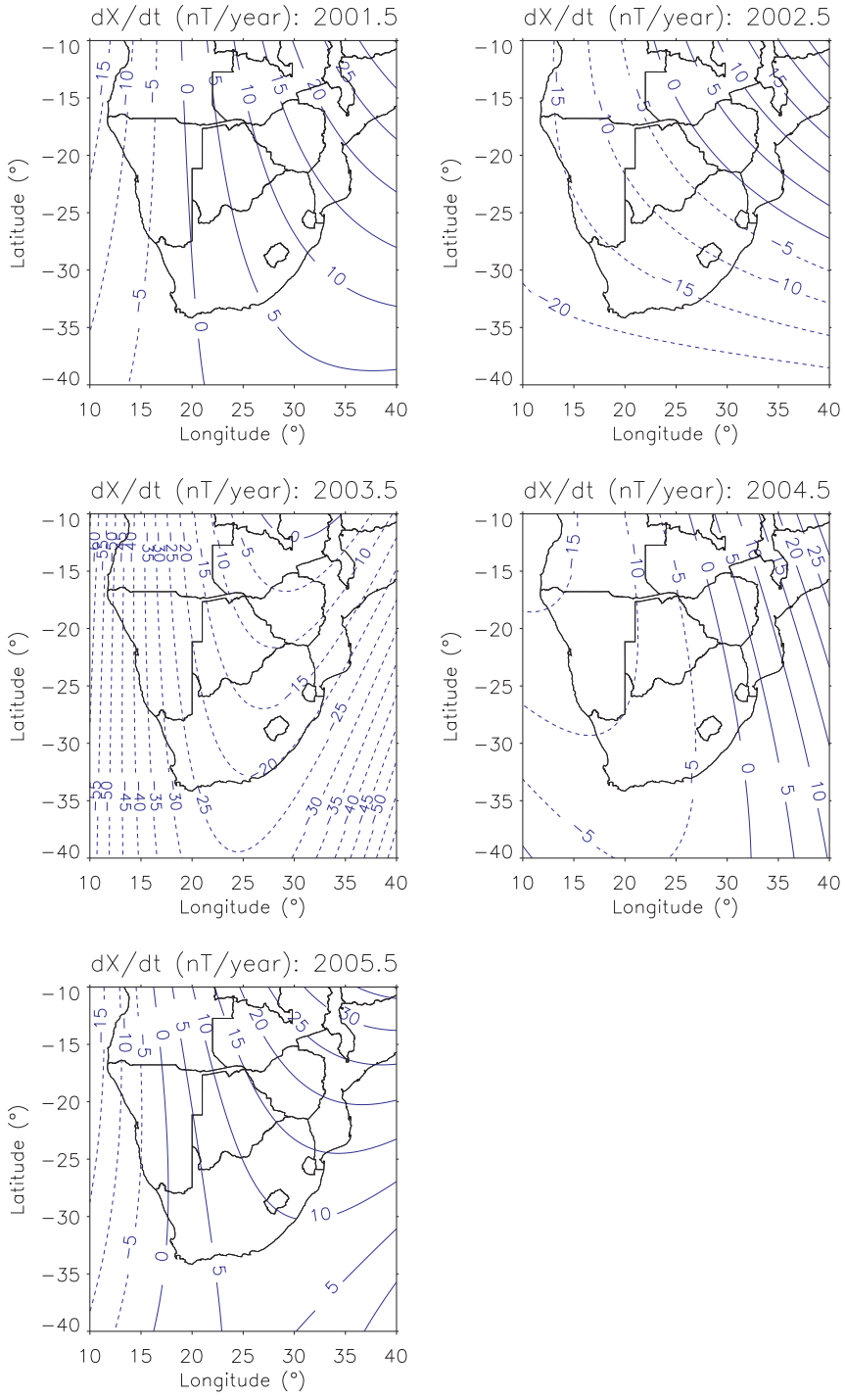

Figure 4.32: The maps showing the first time derivative of north component X at 400 km altitude for years 2001-2005.

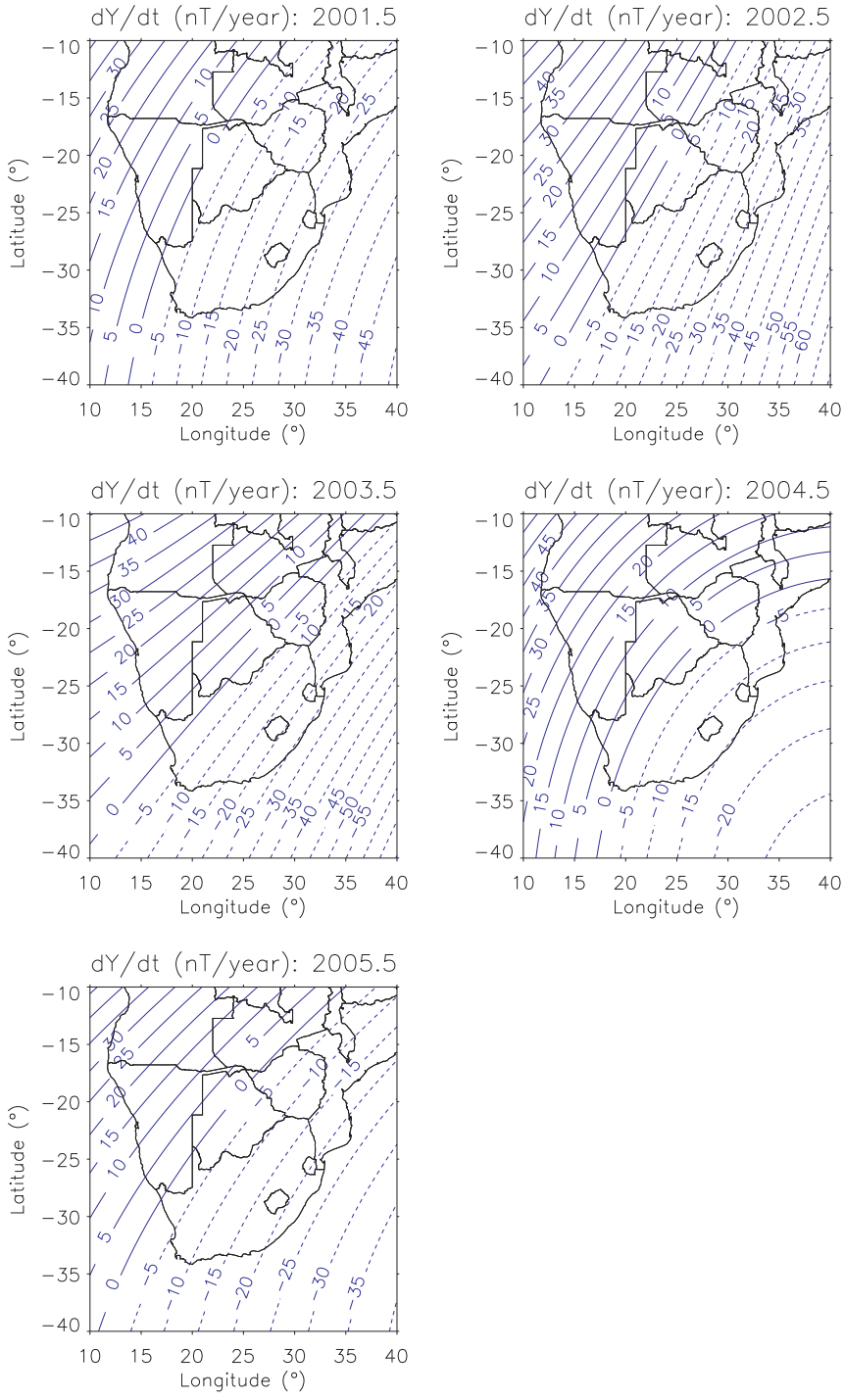

Figure 4.33: The maps showing the first time derivative of east component Y at 400 km altitude for years 2001-2005.

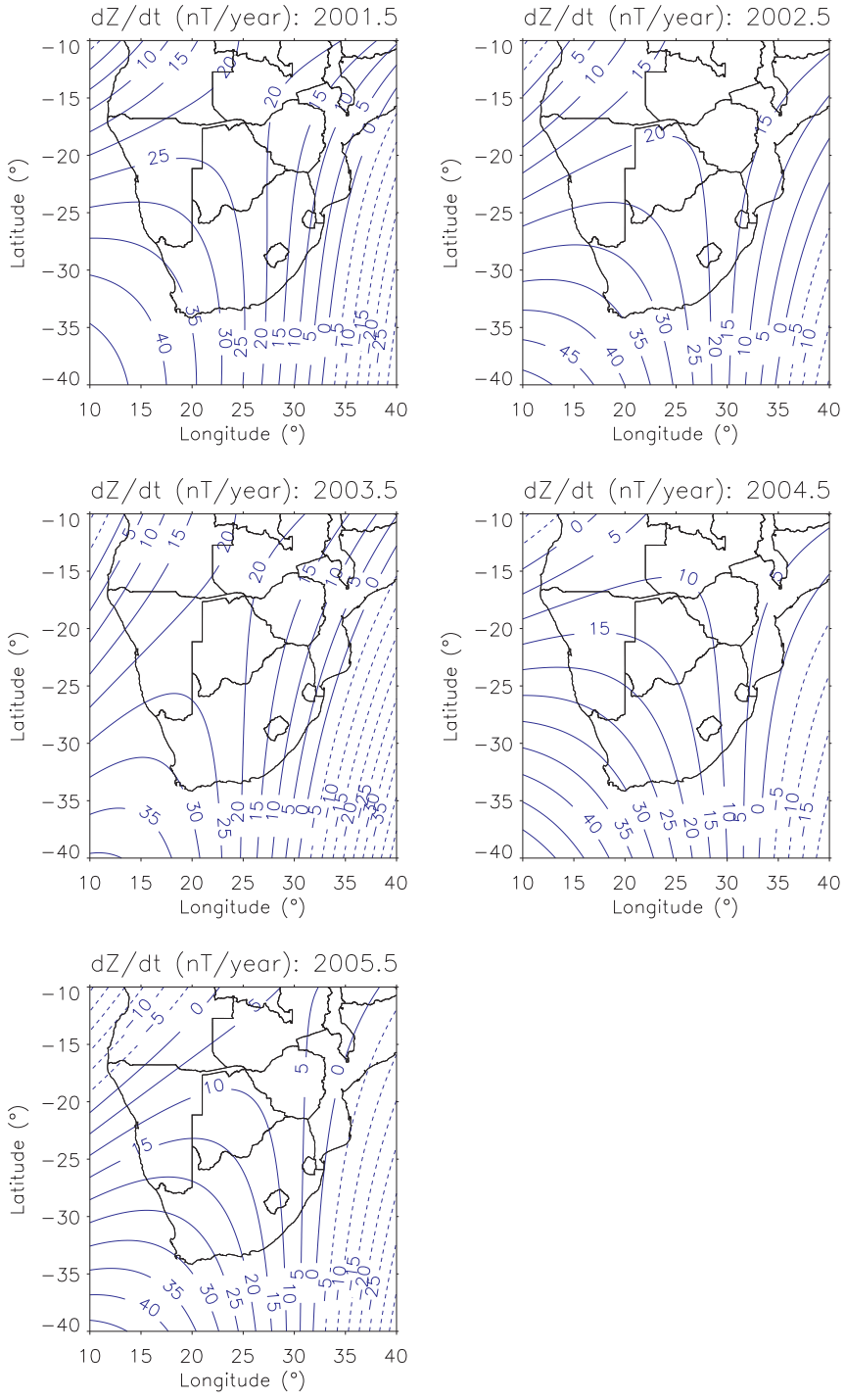

Figure 4.34: The maps showing the first time derivative of vertical component Z at 400 km altitude for years 2001-2005.

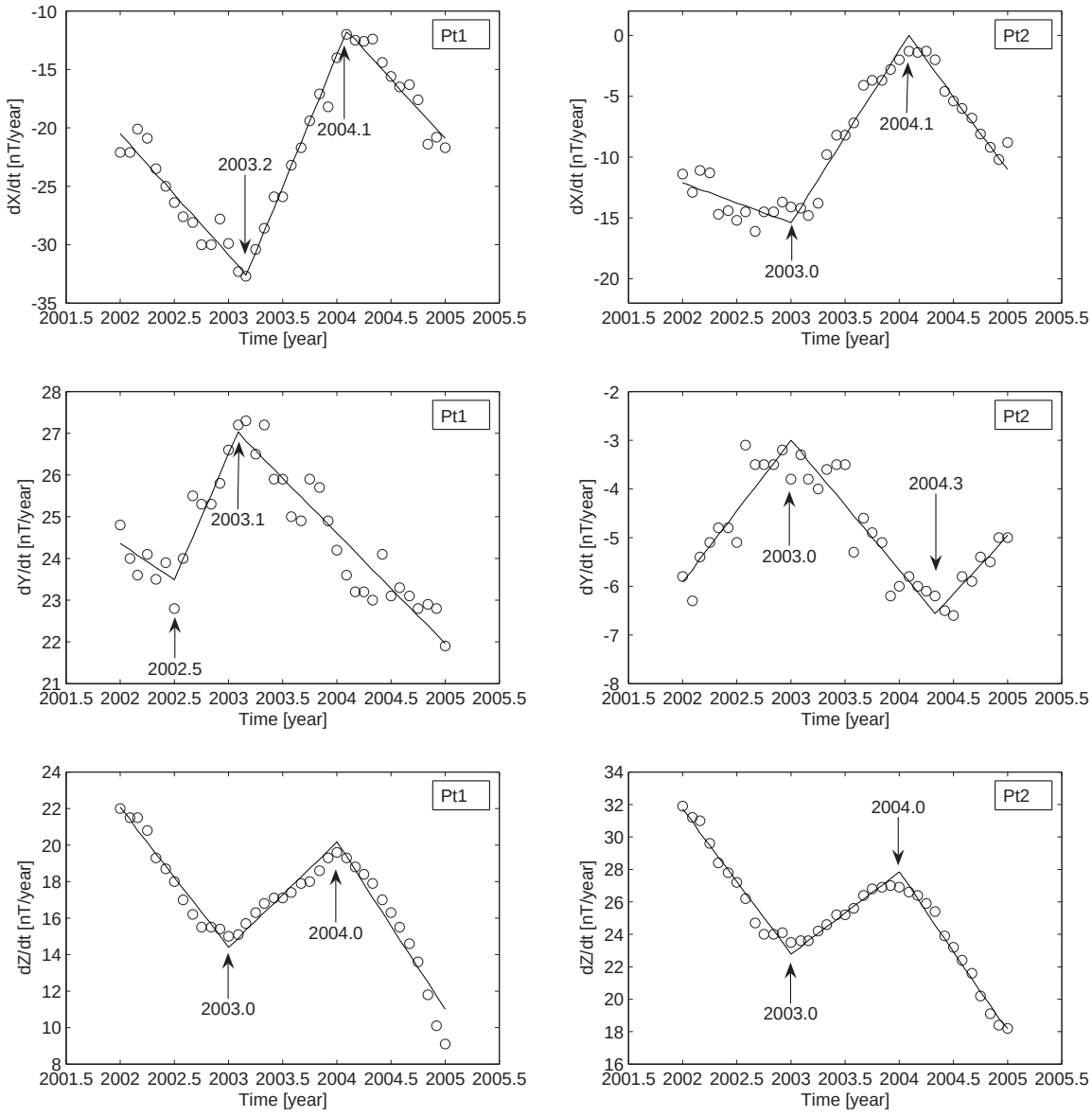

Figure 4.35: The plots of the first time derivative of 3 components (dX/dt, dY/dt and dZ/dt) at the reference points for years 2001-2005. The monthly mean values were generated using the monthly main field models of satellite data at 400 km altitude.

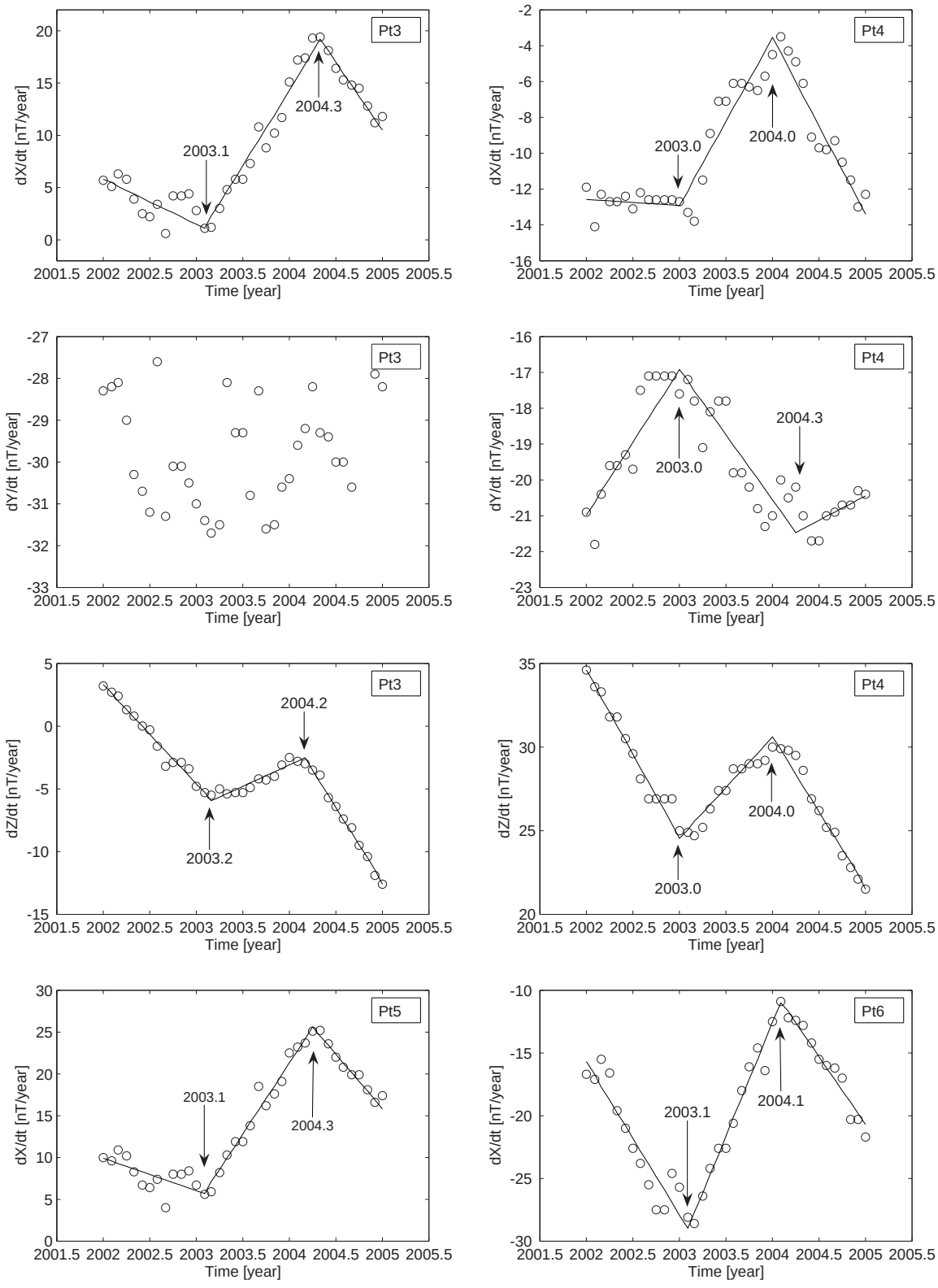

Figure 4.36: The continuation of Fig. 4.35 for reference points Pt3, Pt4, Pt5 and Pt6.

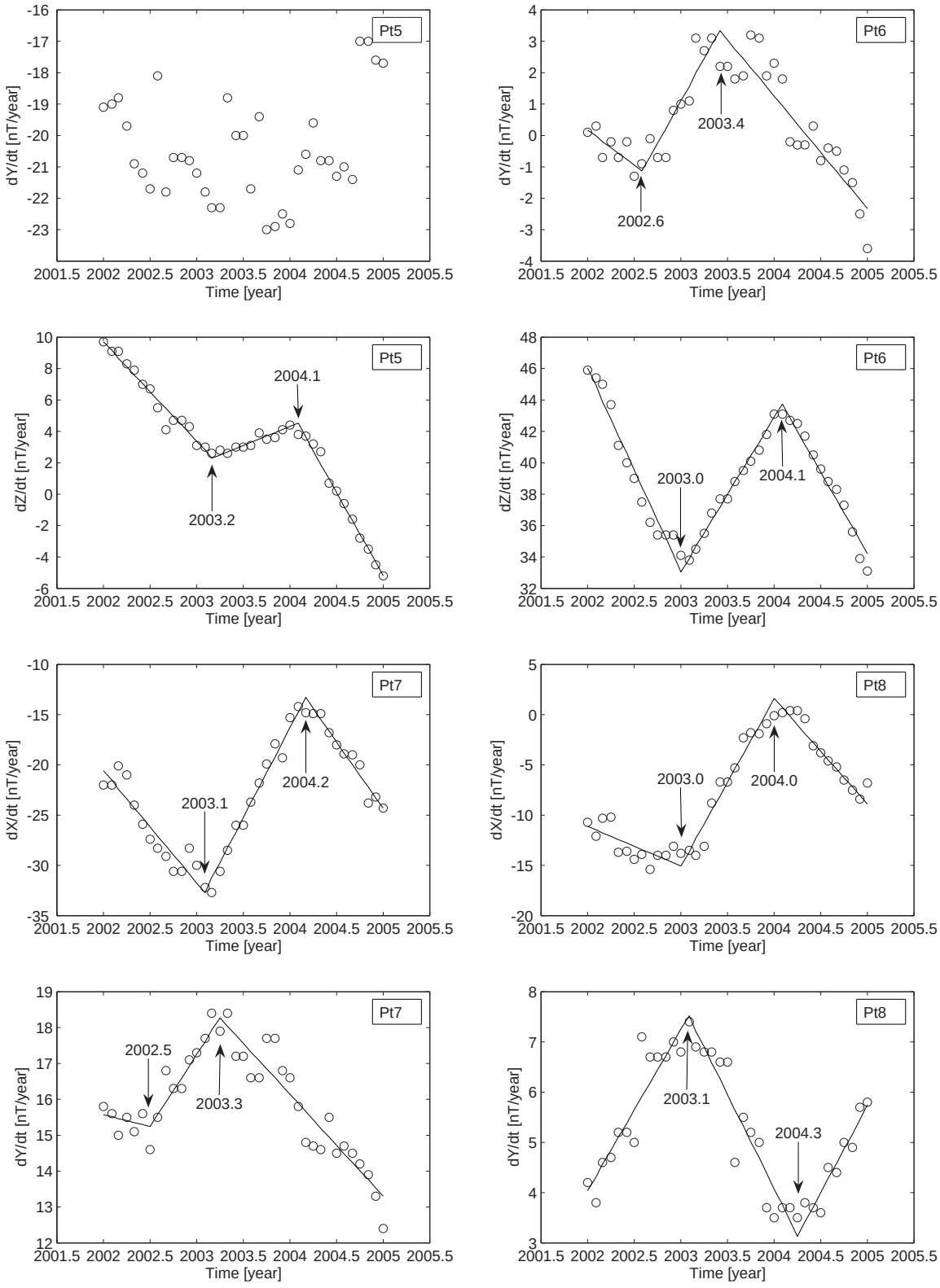

Figure 4.37: The continuation of Fig. 4.35 for reference points Pt5, Pt6, Pt7 and Pt8.

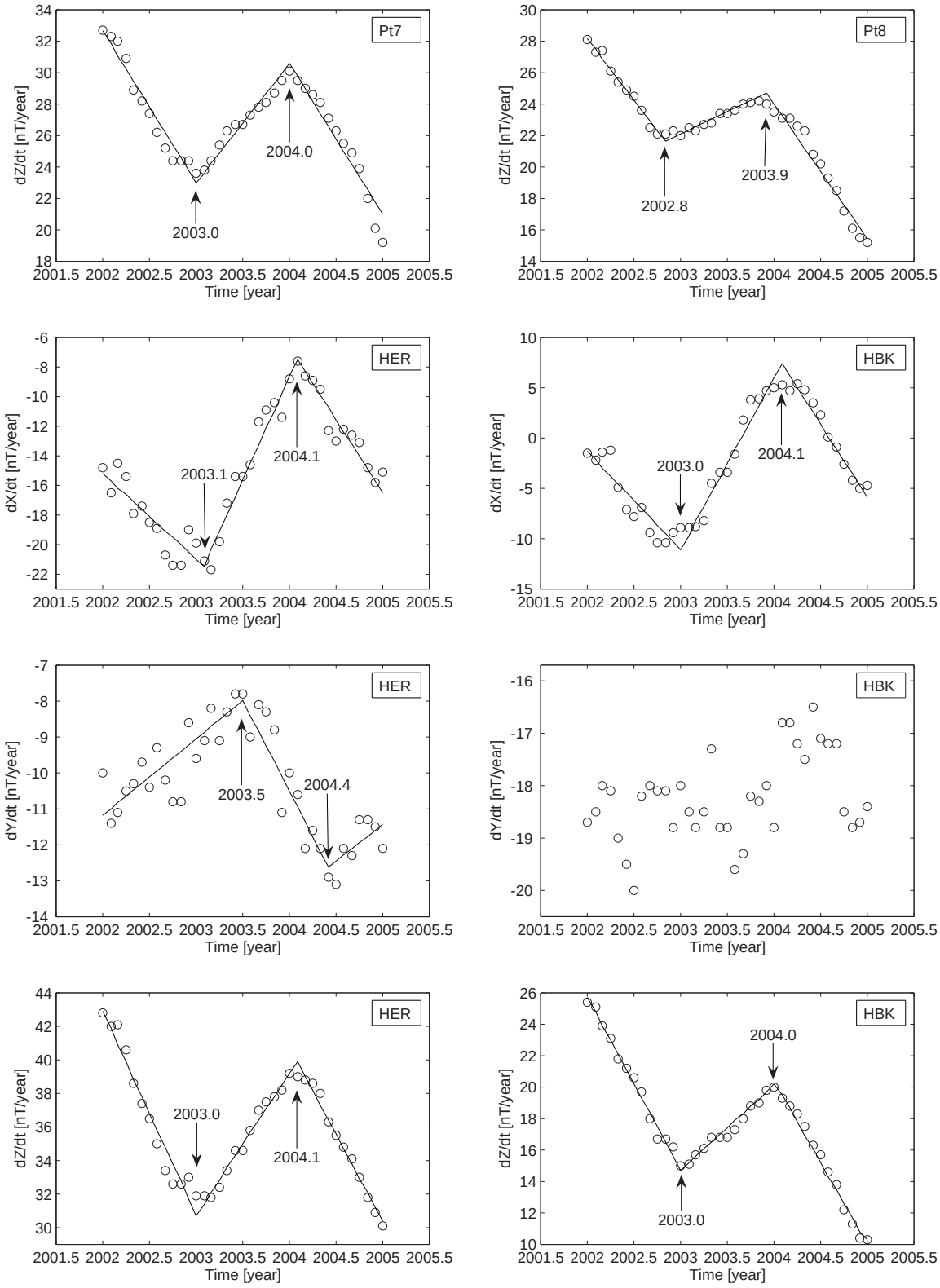

Figure 4.38: The continuation of Fig. 4.35 for reference points Pt7, Pt8, HER and HBK.

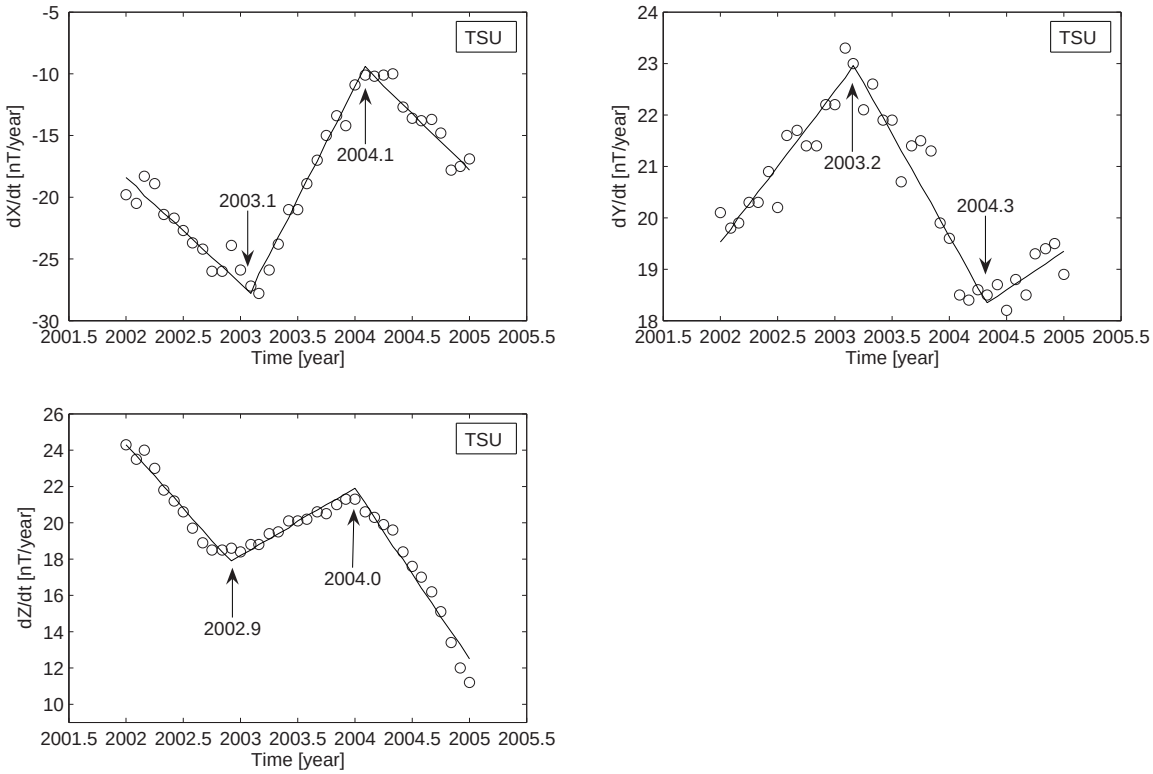

Figure 4.39: The continuation of Fig. 4.35 for reference point TSU.

Table 4.9: The continuation of Table 4.8.

		Gradient before [nT/yr^2]	Epoch of SV impulse	Gradient after [nT/yr^2]	Gradient before [nT/yr^2]	Epoch of SV impulse	Gradient after [nT/yr^2]
	X	-12.2	2003.1	18.0	18.0	2004.1	-10.6
Pt6	Y	-2.2	2002.6	5.3	5.3	2003.4	-3.4
	Z	-13.0	2003.0	9.8	9.8	2004.1	-10.5
	X	-11.1	2003.1	18.3	18.3	2004.2	-13.3
Pt7	Y	-0.7	2002.5	3.4	3.4	2003.3	-2.8
	Z	-9.7	2003.0	7.6	7.6	2004.0	-9.6
	X	-4.0	2003.0	16.7	16.7	2004.0	-10.5
Pt8	Y	3.2	2003.1	-3.8	-3.8	2004.3	3.5
	Z	-7.8	2002.8	2.8	2.8	2003.9	-8.6
	X	-5.8	2003.1	14.0	14.0	2004.1	-9.9
HER	Y	2.0	2003.4	-4.7	-4.7	2004.1	1.2
	Z	-12.2	2003.0	8.4	8.4	2004.1	-10.4
	X	-9.8	2003.0	17.0	17.0	2004.1	-14.6
HBK	Y	-	-	-	-	-	-
	Z	-11.0	2003.0	5.5	5.5	2004.0	-9.9
	X	-8.6	2003.1	18.4	18.4	2004.1	-9.2
TSU	Y	3.0	2003.2	-4.0	-4.0	2004.3	1.9
	Z	-7.0	2002.9	3.7	3.7	2004.0	-9.4

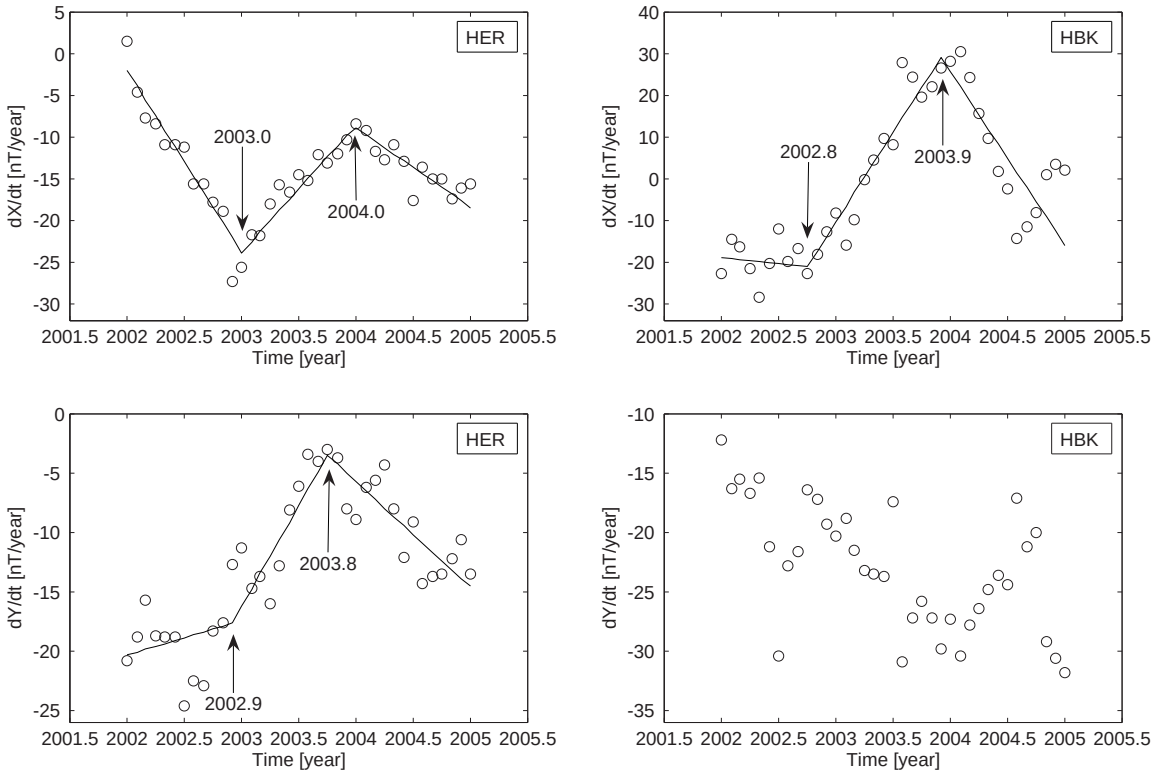

Figure 4.40: The plots of the first time derivative of 3 components (dX/dt, dY/dt and dZ/dt) of 3 virtual observatories of satellite data at 400 km above the 3 permanent observatories (HER, HBK and TSU) for years 2001-2005.

Table 4.10: The identified epochs of SV impulses at the 3 virtual observatories at 400 km altitude just above the 3 permanent observatories (HER, HBK and TSU).

		Gradient before [nT/yr^2]	Epoch of SV impulse	Gradient after [nT/yr^2]	Gradient before [nT/yr^2]	Epoch of SV impulse	Gradient after [nT/yr^2]
	X	-21.9	2003.0	15.0	15.0	2004.0	-9.6
HER	Y	2.9	2002.9	17.2	17.2	2003.8	-8.8
	Z	-1.2	2003.0	15.5	15.5	2004.0	-15.1
	X	-2.8	2002.8	41.8	41.8	2003.9	–41.8
HBK	Y	-	-	-	-	-	-
	Z	-13.9	2003.3	7.4	7.4	2004.4	-28.4
	X	-	-	-	-	-	-
TSU	Y	-	-	-	-	-	-
	Z	-9.5	2003.0	4.3	4.3	2004.0	-6.8

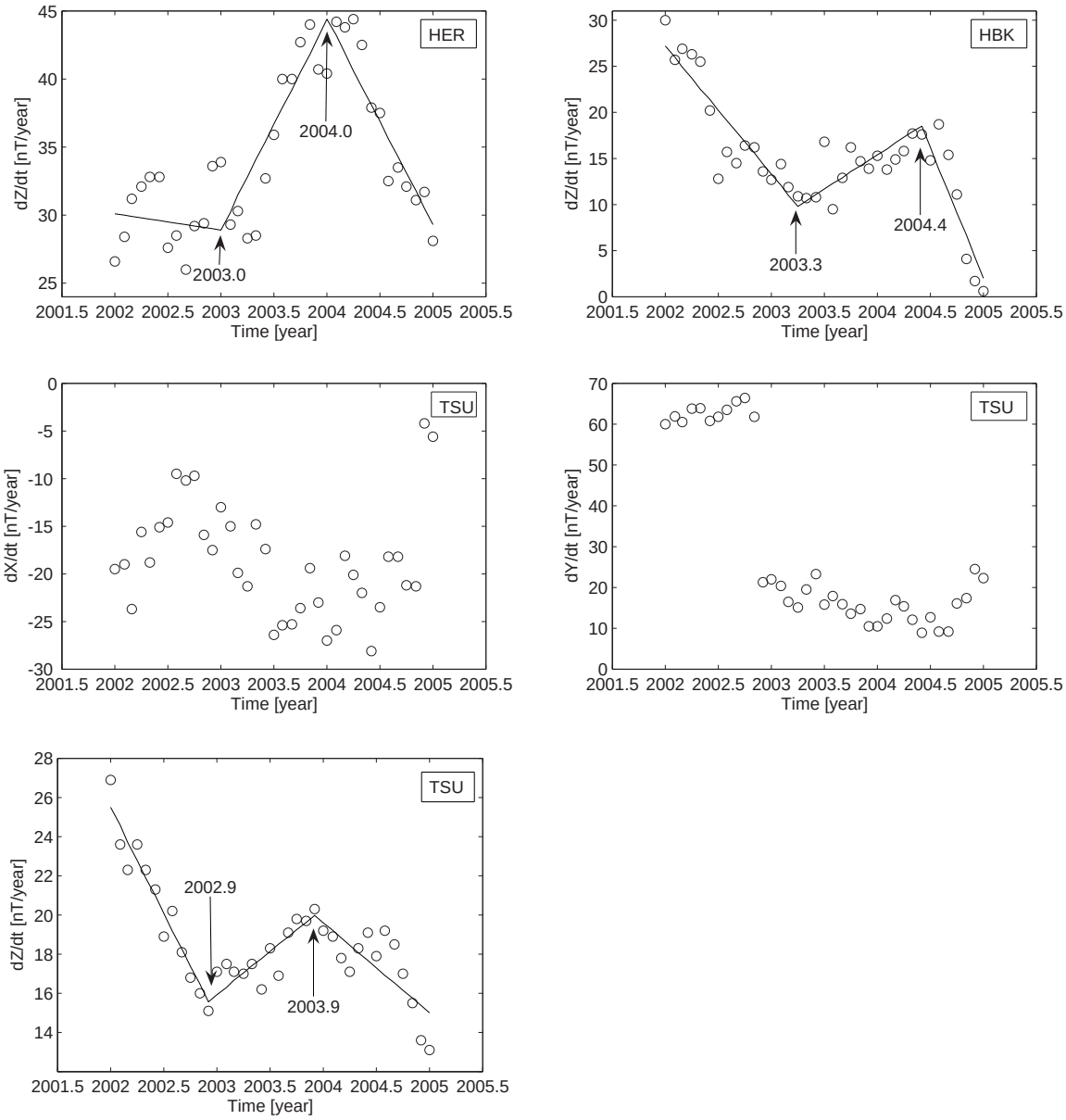

Figure 4.41: The continuation of Fig. 4.40

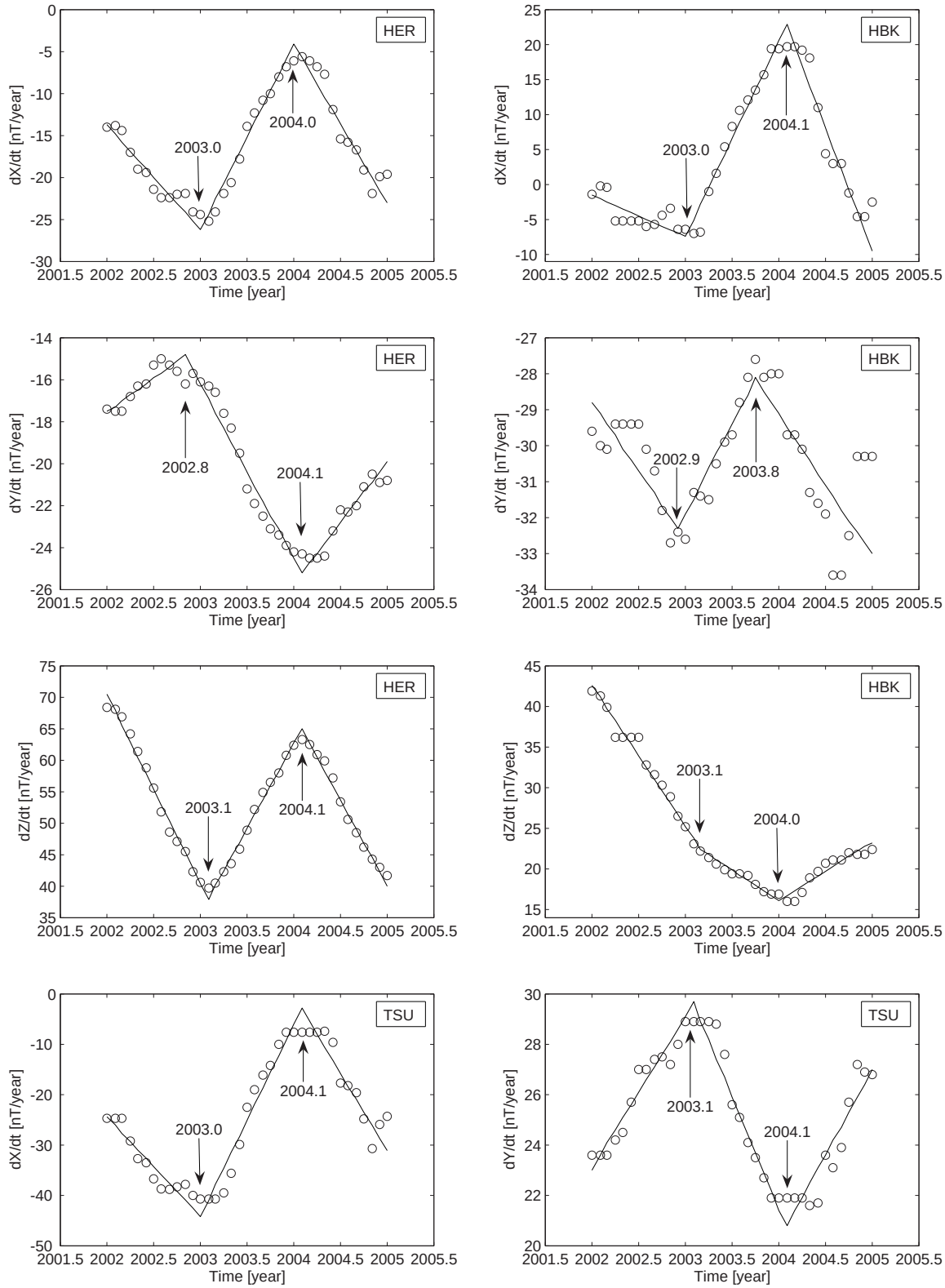

Figure 4.42: The plots of the first time derivative of 3 components (dX/dt, dY/dt and dZ/dt) at 3 permanent ground-based observatories (HER, HBK and TSU) for years 2001-2005.

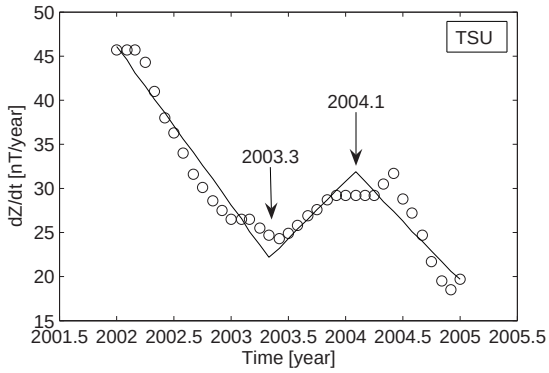

Figure 4.43: The continuation of Fig. 4.42.

Table 4.11: The identified epochs of SV impulses at the 3 permanent observatories using observatory data.

		Gradient before [nT/yr^2]	Epoch of SV impulse	Gradient after [nT/yr^2]	Gradient before [nT/yr^2]	Epoch of SV impulse	Gradient after [nT/yr^2]
	X	-12.5	2003.0	22.1	22.1	2004.0	-18.9
HER	Y	2.7	2002.8	-8.3	-8.3	2004.1	5.8
	Z	-29.9	2003.1	27.1	27.1	2004.1	-27.5
	X	-5.9	2003.0	27.8	27.8	2004.1	-35.6
HBK	Y	-3.8	2002.9	5.1	5.1	2003.8	-3.9
	Z	-12.8	2003.1	-7.2	-7.2	2004.0	10.4
	X	-19.8	2003.0	38.0	38.0	2004.1	-31.1
TSU	Y	6.1	2003.1	-8.9	-8.9	2004.1	6.8
	Z	-18.0	2003.3	12.8	12.8	2004.1	-13.4

4.6.4 Discussion and conclusion

A SV impulse occurs when the SV experiences an abrupt change in its slope. It is generally accepted that it occurs on timescales from months to a few years and is of internal earth origin. During 1983/1984 an abrupt SV change occurred in the southern African subcontinent, which was clearly shown in the D component (Kotzé, 2003). The analysis of CHAMP satellite data for 2001-2005 over the same region, as illustrated in figs. 4.32-4.34 shows the occurrence of a SV impulse during this period as evidenced in all components. It is identified by observing the evolution of the zero SV contour line of a particular component across the region in 5-year period.

It is clearer in X component where the SV pattern changes from 2001.5 with the decrease in SV from west to east and reaches the minimum in 2003.5. After this date the SV starts to gradually increase from east to west and reaches approximately its original pattern in 2005.5. The SV data plots (fig. 4.36) as revealed at the selected points show more detailed structure in the abrupt change of SV than observing the evolution of different contour lines (figs. 4.35 - 4.39). Tables 4.8 and 4.9 show that

all 11 selected reference points support the occurrence of 2 SV impulses in X and Z components around 2003.0 and 2004.0 epochs. The central reference points (Pt2, Pt4 and Pt8 at 23.5°E) indicate the occurrence of SV impulses in Y component around 2003.0 and 2004.0 epochs. The western selected points (Pt1, Pt6 and Pt7 at 15.5°E) show the SV impulses in Y around 2002.5 and 2003.3 epochs. The eastern reference points (Pt3 and Pt5 at 35.5°E and HBK) do not show clear changes in SV patterns of the Y component.

The 3 virtual observatories at 400 km altitude just above 3 permanent observatories, HER, HBK and TSU, show also the occurrence of SV impulses around 2003.0 and 2004.0 (see figs. 4.40 and 4.41 and Table 4.10). The HER virtual observatory data indicate SV impulses around the above mentioned two epochs in all 3 components (X, Y and Z). At HBK virtual observatory, the SV of X and Z components indicates the occurrence of the SV impulses around 2003.0 and 2004.0 epochs. The level of noise in Y SV data does not allow the identification of a clear pattern change. At TSU, only the pattern change in SV in the Z component supports the occurrence of the SV impulses around 2003.0 and 2004.0 epochs. There is too much noise in the data for X and Y components.

The analysis of the monthly time series data for the ground observatories supported these results. At HER and TSU the occurrence of SV impulses in X, Y and Z components is around 2003.0 and 2004.0 epochs (see figs. 4.42 and 4.43, and Table 4.11). At HBK the changes in the X component supports the occurrence of SV impulses around 2003.0 and 2004.0 epochs (see fig. 4.42). However the pattern changes in Y and Z are quite different from the pattern changes as observed at HER and TSU. The pattern change in SV of Z is different from the pattern changes at the virtual observatory and the selected point at 400 km just above HBK (figs. 4.38, 4.40 and 4.42). This difference is highlighted by the gradients before and after the SV impulse epochs (Tables 4.9, 4.10 and 4.11). This is due to the noise in Z component at HBK observatory which is the result of induced electromagnetic noise in the vicinity of the magnetic observatory. No comparison is possible with the pattern change in SV of Y component because there is a high level of noise in Y SV data at the virtual observatory and selected point just above the HBK observatory (figs. 4.38 and 4.40). This can possibly be attributed to external field effects in the satellite data at 400 km altitude.

As shown in figs. 3.32-3.34, the SV of 3 components over the southern African region indicates that dX/dt increases from west to east direction (1 nT/1° long.). For the east component, dY/dt decreases from west to east (1.5 nT/1° long.). And the SV of Z component, dZ/dt decreases from west to east (1 nT/1° long.), but a small west-northern part shows an increase from west to east direction (1.3 nT/1° long.).

These results indicate that southern Africa is a region of complex and rapid SV. The present work also suggests that rapid SV changes can occur on time scales of a few

months (greater than 3 months and less than 1 year), placing an upper limit on the electrical conductivity of the mantle (Mandea Alexandrescu *et al.*, 1999).

4.7 Conclusion

The use of polynomial surface modelling techniques on CHAMP satellite data showed the possibility of developing a geomagnetic SV model using satellite data. The comparison of the PolyM model by means of ground survey data and global models (IGRF 10 and CHAOS) were conducted. The results shown in figs. 4.25 - 4.29 demonstrate that the Z component and the total field F values are in close agreement with 3 models for all 5 years between 2001 and 2005 with the difference between SV values being less than 10 nT/year in most of reference points. The D component has a good correlation among models in 2001 and 2002 (figs. 4.25 and 4.26). The RMS difference in SV values is less than 2 minutes of arc in most of the reference points. The H component correlates well for all the 3 models PolyM, IGRF 10 and CHAOS in 2002 and 2005 where the difference in SV values is less than 10 nT/year in most of the reference points.

Another method used in validating the PolyM is the use of RMS values between the survey ground data at 13 reference points and 3 models PolyM, IGRF 10 and CHAOS. The comparison is made between the RMS obtained using the satellite data model and the ones obtained using the global models. Figure 3.30 shows the bar graphs of the comparison of RMS values between field survey data and the PolyM, and field survey data and two global models IGRF 10 and CHAOS for the period 2001-2005. The RMS values of the PolyM model validation are given in Table 4.12.

Taking ground survey data as reference, the PolyM is better than IGRF 10 for H in 2003 and 2005, Z in 2001 and 2003, and for D in 2002. PolyM is also better than CHAOS for H in 2003, Z in 2004, and for F in 2002. The large RMS values for PolyM are in 2001 for H and F (12.8 nT/year and 14.4 nT/year, respectively) and in 2004 for H with RMS value of 13.5 nT/year. The large values are mainly due to the bad data coverage and distribution in 2001 and 2004 where data selection for December 2001 and January 2004 required data from the closest months (see Table 3.1). Another interesting observation is the large deviation of the global models from the ground survey data in H component in 2003. The RMS of H component for IGRF and CHAOS models are 10.3 nT/year and 12.7 nT/year, respectively.

Despite some shortcomings in satellite data selection, the PolyM was a milestone in investigating the occurrence of SV impulses in 2003 and 2004 over southern Africa as it is illustrated in section 4.6.

Table 4.12: The RMS differences between survey ground data and models at 13 reference points.

Epoch	Component/Total field	PolyM	IGRF	CHAOS
	D (min/year)	1.0	0.8	0.9
2001.5	H (nT/year)	12.8	3.6	3.1
	Z (nT/year)	8.0	8.3	5.4
	F (nT/year)	14.4	9.7	5.1
	D (min/year)	0.7	1.0	0.9
2002.5	H (nT/year)	5.6	3.2	3.5
	Z (nT/year)	6.7	5.8	6.6
	F (nT/year)	7.8	7.4	8.7
	D (min/year)	1.5	1.2	1.0
2003.5	H (nT/year)	7.6	10.3	12.7
	Z (nT/year)	3.4	6.0	3.0
	F (nT/year)	5.7	4.0	5.3
	D (min/year)	2.4	1.4	1.2
2004.5	H (nT/year)	13.5	7.5	6.5
	Z (nT/year)	7.2	6.7	8.5
	F (nT/year)	5.5	8.3	4.7
	D (min/year)	2.4	1.6	1.4
2005.5	H (nT/year)	4.1	6.7	2.7
	Z (nT/year)	8.6	8.2	6.0
	F (nT/year)	8.3	8.7	4.1

Chapter 5

Spherical Cap Harmonic Analysis (SCHA)

5.1 Introduction

Spherical Cap Harmonic Analysis (SCHA) is a mathematical technique developed by Haines (1985) to model a potential field and its spatial derivatives, or a general function and its surface derivatives, on a regional scale in order to overcome the non-orthogonality problem in the case of global spherical harmonic models when applied to restricted areas. The SCHA technique has also been used successfully to derive a regional field model over southern Africa, using the Ørsted vector magnetic field measurements (Kotzé, 2001).

An equation of considerable interest in the geophysical sciences is Laplace's equation in spherical coordinates:

$$\frac{\delta}{\delta r}\left(r^2\frac{\delta V}{\delta r}\right)+\frac{1}{sin\theta}\frac{\delta}{\delta\theta}\left(sin\theta\frac{\delta V}{\delta\theta}\right)+\frac{1}{sin^2\theta}\frac{\delta^2 V}{\delta\lambda^2}=0, \tag{5.1}$$

which r, θ, and λ are geocentric spherical coordinates; radius, colatitude and longitude respectively and V the scalar potential field.

Haines (1988) states that a solution of the above equation is termed a potential field, and the gradient of a scalar potential field is a vector field whose curl and divergence are both identically zero. In the absence of current sources, the geomagnetic and gravity vector fields are important examples of this latter type of field. The solution of Laplace's equation then provides a method of modelling such a vector field not only on a surface but also throughout space.

The solution of Laplace's equation on a whole sphere is used for global modelling (e.g. IGRF)(see section 2.4 of chapter 2). The solution for a spherical cap, which is one

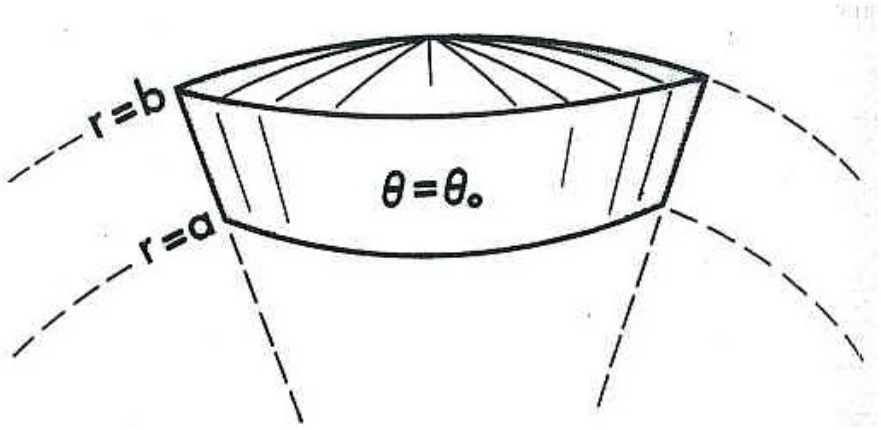

Figure 5.1: Spherical cap of half-angle θ_0. Data may be distributed over surface r=a (surface data) or between surfaces r=a and r=b (satellite data). Figure adopted from Haines (1988).

particular subinterval or subsurface of the sphere is given in section 5.2. Haines (1988) continues stating some differences between the solutions of Laplace's equation for the whole sphere and spherical cap. He states that the basis functions in both situations comprise associated Legendre functions in colatitude, trigonometric functions in longitude, and powers of radial distance. Whereas the associated Legendre functions for the whole sphere have integral degree, those for the spherical cap have real degrees. The practical result of this is that the functions with integral degree can be expressed as polynomials in $cos\theta$ multiplied by a power of $sin\theta$, while those with non-integral degree can only be expressed as infinite series such as the sine and cosine functions themselves. Similarly, the spherical functions include an integral power of radial distance but the spherical cap functions include a non-integral power which is the same as the degree of the Legendre function.

The SCHA method is important theoretically because it constrains a model to be a potential. That is, it constrains the curl and divergence of any field to be zero, such as the geomagnetic field or gravity field, that can be expressed as the gradient of a scalar potential.

However, the method is practically important because it provides a representation of a potential gradient field radially as well as over a surface (Haines, 1988).

In this chapter, the SCHA is applied to the CHAMP vector magnetic measurements between 2001 and 2005 to investigate the development of a geomagnetic SV model using satellite data over southern Africa.

5.2 Mathematical formulation

Haines (1988) gave the solution to Laplace's equation over a spherical cap for internal and external sources and also extended to a time-varying solution, where the coefficients are taken as polynomials of an appropriate degree. The solution is given in the equation below:

$$V(r,\theta,\lambda,t) = a\sum_{k=0}^{KINT}\sum_{m=0}^{k}\left(\frac{a}{r}\right)^{n_k(m)+1} P^m_{n_k(m)}(cos\theta)[g_k^{m,i}(t)cos(m\lambda) + h_k^{m,i}(t)sin(m\lambda)]$$
$$+ a\sum_{k=1}^{KEXT}\sum_{m=0}^{k}\left(\frac{r}{a}\right)^{n_k(m)} P^m_{n_k(m)}(cos\theta)[g_k^{m,e}(t)cos(m\lambda) + h_k^{m,e}(t)sin(m\lambda)] \quad (5.2)$$

where

$$g_k^{m,i}(t) = \sum_{q=0}^{LINT} g_{k,q}^{m,i}(t-t_0)^q \quad (5.3)$$

$$h_k^{m,i}(t) = \sum_{q=0}^{LINT} h_{k,q}^{m,i}(t-t_0)^q \quad (5.4)$$

$$g_k^{m,e}(t) = \sum_{q=0}^{LEXT} g_{k,q}^{m,e}(t-t_0)^q \quad (5.5)$$

$$h_k^{m,e}(t) = \sum_{q=0}^{LEXT} h_{k,q}^{m,e}(t-t_0)^q \quad (5.6)$$

where r, θ, λ are the geocentric spherical coordinates radius, colatitude, and longitude; t is time in any convenient unit, with t_0 a convenient zero time; a is the reference radius; and $P^m_{n_k(m)}(cos\theta)$ is the associated Legendre function of the first kind with integral order m and real degree $n_k(m)$. The parameter k is referred as index, $KINT$ as the maximum index for internal sources, and $KEXT$ as the maximum index for external sources. The parameter q is referred to as the order, and $LINT$, $LEXT$ as the degrees of the polynomials in t for internal and external sources, respectively. The constants $g_{k,q}^{m,i}$, $h_{k,q}^{m,i}$ and $g_{k,q}^{m,e}$, $h_{k,q}^{m,e}$ are termed spherical cap harmonic coefficients. If the half-angle of the spherical cap is denoted by θ_0, then $n_k(m)$ are determined as the roots of the equation, for given m:

$$\frac{dP^m_{n_k(m)}(cos\theta_0)}{d\theta} = 0,\ k-m = \text{even} \quad (5.7)$$

and additionally, if differentiability with respect to θ is required:

$$P^m_{n_k(m)}(cos\theta_0) = 0,\ k-m = \text{odd}. \quad (5.8)$$

The index k orders the roots of both equations, starting at m. For large k and small m, the degree is given approximately by:

$$n_k(m) \approx \frac{90}{\theta_0}\left(k + \frac{1}{2}\right) - \frac{1}{2}$$

where θ_0 is in degrees.

As reported by Haines (1988), Bullard (1967) states that the wavelength corresponding to a spherical harmonic of degree n is :

$$\omega = 360^\circ/n$$

or, at the Earth's surface, (40000 km)/n. Thus, if the minimum wavelength to be represented in the model is ω_{min}, the maximum index would be approximately

$$K_{max} \approx \frac{\theta_0}{90^\circ}\left(\frac{360^\circ}{\omega_{min}} + \frac{1}{2}\right) - \frac{1}{2}.$$

The associated Legendre function, for integral m and real n, can be expressed as a truncated power series in $sin^2(\theta/2)$, and computed recursively:

$$P_n^m(cos\theta) = \sum_{j=0}^{J} A_j(m,n) sin^{2j}(\theta/2) \tag{5.9}$$

where

$$A_0(m,n) = K_n^m sin^m\theta \tag{5.10}$$

and for $j > 0$:

$$A_j(m,n) = \frac{(j+m-1)(j+m) - n(n+1)}{j(j+m)} \times A_{j-1}(m,n) \tag{5.11}$$

and K_n^m is a normalizing constant. For Schmidt normalization, the constant K_n^m for $n > m > 0$ may be taken (Haines, 1985) as:

$$K_n^m = \frac{2^{-m}}{(m\pi)^{1/2}}\left(\frac{n+m}{n-m}\right)^{n/2+1/4} p^{m/2} exp(e_1 + e_2) \tag{5.12}$$

where

$$P = (n/m)^2 - 1$$

$$e_1 = -(1 + 1/p)/(12m)$$

$$e_2 = (1 + 3/p^2 + 4/p^3)/(360\, m^3).$$

For $n \geqslant m = 0$, $K_n^m = 1$. Although $P_n^m(cos\theta)$, for nonintegral n, is not a polynomial

(finite-series) but rather an infinite power series, it nevertheless can be truncated at order J depending on the accuracy desired, limited of course by the numerical precision of the computer.

The derivative of the associated Legendre function is given simply by:

$$\frac{dP_n^m(cos\theta)}{d\theta} = \frac{sin\theta}{2}\sum_{j=1}^{J} jA_j(m,n)sin^{2(j-1)}(\theta/2) \tag{5.13}$$

when $m = 0$, and by

$$\frac{dP_n^m(cos\theta)}{d\theta} = \frac{sin\theta}{2}\sum_{j=1}^{J} jA_j(m,n)sin^{2(j-1)}(\theta/2) + cos\theta\left[\frac{m}{sin\theta}P_n^m(cos\theta)\right] \tag{5.14}$$

when $m > 0$.

The truncation level J is not fixed and each recursive term is checked for the desired accuracy during computation.

A field B which can be expressed as the negative gradient of the scalar potential V has north, east, and vertical components:

$$\begin{aligned} B_N = &\sum_{k=1}^{KINT}\sum_{m=0}^{k}\left(\frac{a}{r}\right)^{n_k(m)+2}\frac{dP^m_{n_k(m)}(cos\theta)}{d\theta}[g_k^{m,i}(t)cos(m\lambda) + h_k^{m,i}(t)sin(m\lambda)] \\ &+ \sum_{k=1}^{KEXT}\sum_{m=0}^{k}\left(\frac{r}{a}\right)^{n_k(m)-1}\frac{dP^m_{n_k(m)}(cos\theta)}{d\theta}[g_k^{m,e}(t)cos(m\lambda) + h_k^{m,e}(t)sin(m\lambda)] \end{aligned} \tag{5.15}$$

$$\begin{aligned} B_E = &\sum_{k=1}^{KINT}\sum_{m=1}^{k}\left(\frac{a}{r}\right)^{n_k(m)+2}\frac{mP^m_{n_k(m)}(cos\theta)}{sin\theta}[g_k^{m,i}(t)sin(m\lambda) - h_k^{m,i}(t)cos(m\lambda)] \\ &+ \sum_{k=1}^{KEXT}\sum_{m=1}^{k}\left(\frac{r}{a}\right)^{n_k(m)-1}\frac{mP^m_{n_k(m)}(cos\theta)}{sin\theta}[g_k^{m,e}(t)sin(m\lambda) - h_k^{m,e}(t)cos(m\lambda)] \end{aligned} \tag{5.16}$$

$$\begin{aligned} B_V = &\sum_{k=0}^{KINT}\sum_{m=0}^{k}[n_k(m)+1]\left(\frac{a}{r}\right)^{n_k(m)+2}P^m_{n_k(m)}(cos\theta)[g_k^{m,i}(t)cos(m\lambda)+h_k^{m,i}(t)sin(m\lambda)] \\ + &\sum_{k=1}^{KEXT}\sum_{m=0}^{k}n_k(m)\left(\frac{r}{a}\right)^{n_k(m)-1}P^m_{n_k(m)}(cos\theta)[g_k^{m,e}(t)cos(m\lambda) + h_k^{m,e}(t)sin(m\lambda)] \end{aligned} \tag{5.17}$$

where $g_k^{m,i}(t)$, $h_k^{m,i}(t)$ and $g_k^{m,e}(t)$, $h_k^{m,e}(t)$ are given by Equations (5.3)-(5.6).

5.3 Spherical cap modelling

5.3.1 Modelling a synthesized data set

In order to understand how well the SCHA technique can be applied to CHAMP satellite data, an IGRF data set was generated for four months (Jan 2001, Dec 2001, Jan 2002 and Dec 2002). The data set was generated at 400 km altitude with a grid of $0.3^\circ \times 0.3^\circ$. A total of 10,201 data points were created for each month over the area between 10°S and 40°S in latitude and between 10°E and 40°E in longitude. When applying SCHA it is recommended to remove a global spherical harmonic potential from the total potential in order to improve convergence as well as extrapolation beyond the spherical boundary (Haines, 1985). A known spherical harmonic potential V_{SH} was subtracted from the total potential V_{TOT} and spherical cap harmonic coefficients were computed from a residual $\triangle V$:

$$\triangle V = V_{TOT} - V_{SH}$$

The IGRF 10 model was used as V_{SH} and the reference field was calculated at an altitude and epoch of 400 km and 2000.0, respectively. The resulting residual data were converted from a geocentric coordinate system to a new pole at 25°S, 25°E. A half-cap angle of 18° was selected. In this study, only the part of the Laplace's equation solution for internal sources without the time-varying part was used.

$$V(r,\theta,\lambda) = a \sum_{k=0}^{KINT} \sum_{m=0}^{k} \left(\frac{a}{r}\right)^{n_k(m)+1} P^m_{n_k(m)}(cos\theta)[g_k^{m,i} cos(m\lambda) + h_k^{m,i} sin(m\lambda)]. \quad (5.18)$$

The selection of the optimum KINT was determined by looking at the RMS misfit errors at different KINT values between 1 and 7 (see Table 5.1).

The misfit errors as displayed in Table 5.1 indicate that the increase in KINT results in decrease in misfit errors. From KINT = 5 there is a very small decrease in RMS misfit errors as one moves to higher KINT. This is shown by the closeness of the RMS misfit errors for KINT = 5 and KINT = 7. Since the main aim is to study the core field characterised by the long minimum wavelength, the trade-off was made between the minimum RMS misfit error and the lowest KINT that would be suitable to study the core field. At KINT=5, the minimum wavelength resolution is approximately 1300 km. Therefore the data was fitted with the SCHA with KINT = 5 and the RMS misfit error and RMS difference between IGRF 10 and SCHA were computed for 4 months at 3 different altitudes (400 km, 200 km and 0.8 km) to investigate the prediction error in downward continuation. The SV between January and December 2001 was computed

and compared with the SV obtained from IGRF 10 model.

The results of the SCHA modelling of a synthesized data set are shown in Table 5.2 and figs. 5.2-5.3. Looking at the RMS misfit errors and RMS differences between the SCHA model and IGRF at different altitudes, it is clear that the RMS values increase as the residual values (ΔV) increase. This led to a conclusion of taking the global reference field epoch to be 2003.5, that is, the middle of the interval time of study (2001-2005). It was decided to take a single global reference field epoch in order to avoid errors due to the SV in the global reference field. Another observation is that the RMS values increase as one moves away (downward) from the data fitting altitude (400 km) as illustrated in Table 5.2. The fact that the CHAMP satellite data was recorded in a small range of altitude between 350 km and 450 km implies that the SCHA model derived from these data cannot be used to predict data at the ground level. In case of comparing the SCHA model with ground survey data, the best option is to fit data after reducing it to ground level.

Table 5.1: The RMS misfit errors of different KINT values when fitting the synthesized data set generated from IGRF 10 model at 400 km altitude.

KINT	D (min)	H (nT)	Z (nT)	F (nT)
1	4.9	16.9	12.0	13.4
3	1.0	4.0	6.3	6.0
4	0.6	2.4	4.7	3.6
5	0.5	2.3	2.8	2.1
7	0.3	1.6	2.0	2.3

Figs 5.2-5.3 show the plots of SV data computed from the SCHA model (derived from the synthesized data set) and IGRF model at 400 km altitude in 2001 for D, H and Z components and the total field F, as well as the difference between these two models. The RMS differences of SV values between the SCHA model and IGRF 10 model for D, H, Z and F are 0.44 min/year, 1.99 nT/year, 2.49 nT/year and 1.88 nT/year respectively, showing very good agreement.

Table 5.2: The RMS misfit errors and RMS difference between IGRF 10 and SCHA at 3 different altitudes, 400 km, 200 km and 0.8 km.

RMS description	Component/ Total field	2001 Jan	2001 Dec	2002 Jan	2002 Dec
RMS misfit errors at 400 km	D (min)	0.50	0.94	0.98	1.42
	H (nT)	2.3	4.3	4.4	6.4
	Z (nT)	2.8	5.3	5.6	8.1
	F (nT)	2.1	4.0	4.2	6.1
RMS difference between IGRF 10 and SCHA at 200 km	D (min)	0.99	1.80	1.94	2.83
	H (nT)	4.7	8.9	9.2	13.4
	Z (nT)	4.4	8.3	8.7	12.6
	F (nT)	5.0	9.4	9.8	14.2
RMS difference between IGRF 10 and SCHA at 0.8 km	D (min)	2.30	4.20	4.43	6.43
	H (nT)	11.2	21.1	22.0	31.9
	Z (nT)	14.8	27.9	29.1	42.1
	F (nT)	14.7	27.6	28.8	41.7

5.3.2 Spherical cap modelling of CHAMP satellite data

5.3.2.1 Spherical cap modelling of CHAMP satellite data in X, Y and Z components at 400 km altitude

The SCHA is applied on the CHAMP satellite data measured between 350 km and 450 km altitude. The SV model was developed at 400 km altitude and the SCHA model was compared with the global models IGRF 10 and CHAOS as well as with the polynomial modelling results given in chapter 4 under section 4.3.

The investigation of the optimum KINT was carried out using the CHAMP satellite data measured in 2001. Table 5.3 shows the RMS misfit errors between the SCHA model and the measured values for different KINT values, and the RMS differences between main field values generated from SCHA and IGRF models. The KINT = 4 and 5 yield the best SV models that are very close (Table 5.4). Even if the SV model of KINT = 5 is slightly better than the one with KINT = 4 as in this case for 2001, KINT = 4 was chosen as it reduces the edge effects at the boundary of region and some distorted patterns in SV when the data coverage is not satisfactory. This allowed a good observation of the evolution of SV contour lines over 5-year period to identify the occurrence of SV impulses observed in the polynomial modelling results in chapter 4.

Modelling of CHAMP satellite data was done using a half-cap angle of 18° with KINT = 4, resulting in a minimum wavelength resolution of approximately 1600 km and these results are shown in figs. 5.4-5.6.

The spherical cap model coefficients are given in the appendix C. Table 5.5 displays the RMS misfit errors between the two models (SCHA and IGRF models) and the measured values. For main field models, the developed SCHA (regional model) provides a better alternative than IGRF 10 and CHAOS (the global models) as shown in Table 5.5. The IGRF 10 and CHAOS RMS differences are more than 3 times larger than the RMS misfit errors obtained with SCHA in X and Z components for the 5 years (2001-2005). This demonstrates clearly that the regional model is a substantial improvement to the global models for southern Africa. The statistical comparison between SCHA and PolyM SV models are shown in Table 5.6. The RMS difference values were calculated using a grid of $0.2^\circ \times 0.2^\circ$ over the whole region of investigation. The two regional models (SCHA and PolyM) were compared with the two global models (IGRF 10 and CHAOS). The RMS differences between SCHA and PolyM showed how these two regional models are in close agreement with each other. RMS differences in Table 4.6 show that the two regional models compare favorably with each other, in sharp contrast to the global field models. For example in 2003 the RMS difference in X component between SCHA and PolyM is 10.9 nT/year whereas the RMS differences between regional models, SCHA and PolyM, and CHAOS are 19.8 nT/year and 24.1 nT/year respectively.

Table 5.3: The RMS misfit errors between SCHA model and measured values in 2001 and RMS difference between IGRF and SCHA models at 400 km altitude.

KINT		2		3		4		5		7	
Month		Jan	Dec	Jan	Dec	Jan	Dec	Jan	Dec	Jan	Dec
misfit errors	X (nT)	30.4	27.0	23.9	22.3	21.3	20.4	19.1	18.4	13.5	13.7
SCHA-CHAMP	Y (nT)	16.2	13.2	11.3	11.2	11.4	11.5	11.0	11.1	07.6	08.1
	Z (nT)	29.9	27.8	22.8	20.7	15.6	14.1	11.5	11.4	13.9	15.8
IGRF-SCHA	X (nT)	81.3	73.0	90.1	82.1	94.5	86.9	96.5	88.9	97.3	90.0
at 400 km	Y (nT)	23.2	23.0	19.4	23.5	19.4	25.1	18.7	25.4	17.2	24.7
	Z (nT)	93.1	95.2	88.5	90.4	84.4	86.0	81.8	83.1	79.8	80.9

5.3.2.2 Spherical cap modelling of CHAMP satellite data in X, Y and Z components at ground level.

The spherical cap modelling of a synthesised data set (subsection 4.3.1) has revealed that the downward error of the model from the CHAMP satellite altitude to the ground level (mean altitude of the ground reference points to be used in model validation, 0.8 km) is very significant (Table 5.2). Before applying the SCHA on CHAMP satellite data it was first reduced to the ground level using the IGRF 10 model and equation

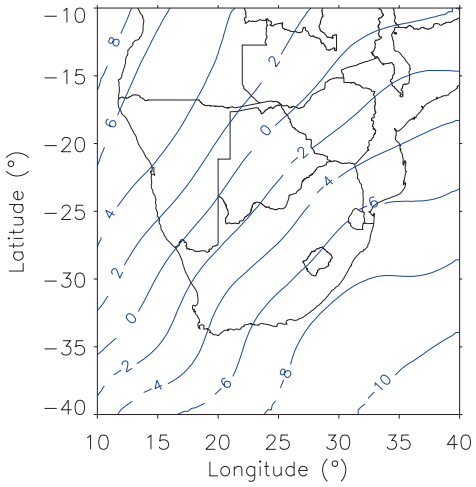

(a) SCHA model: D (min of arc/year).

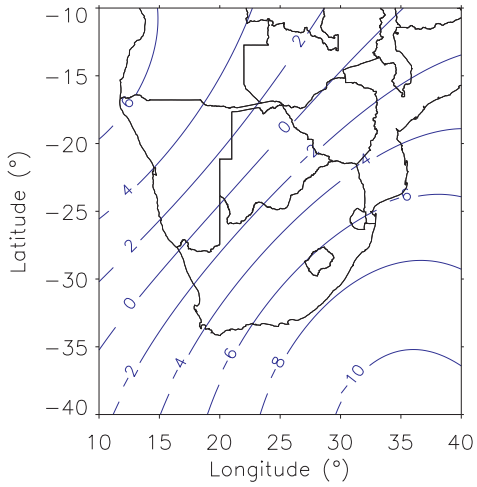

(b) IGRF model: D (min of arc/year).

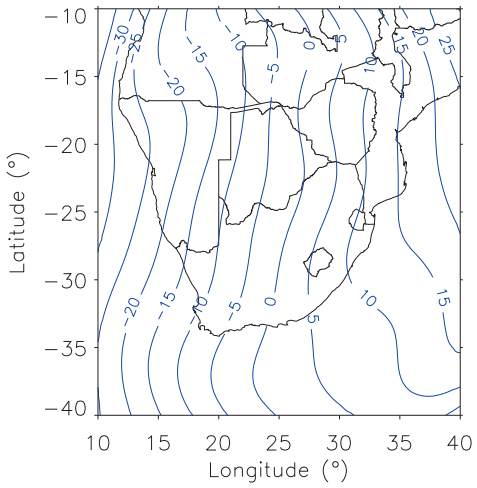

(c) SCHA model: H (nT/year).

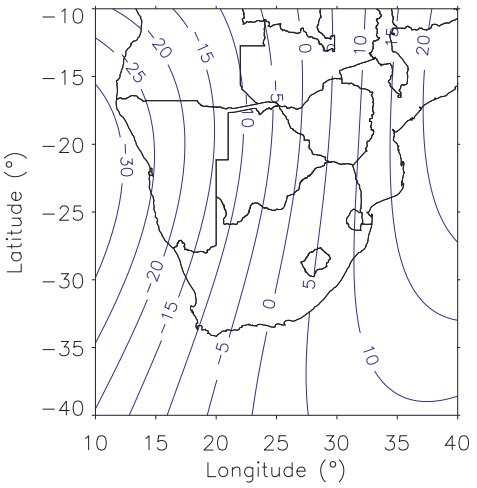

(d) IGRF model: H (nT/year).

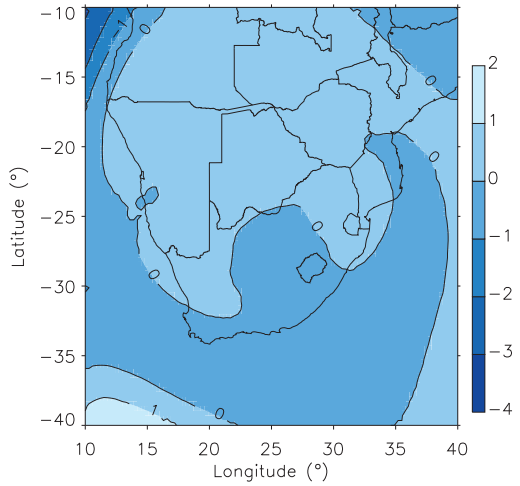

(e) Difference between SCHA and IGRF models: D (RMS = 0.44 min of arc/year).

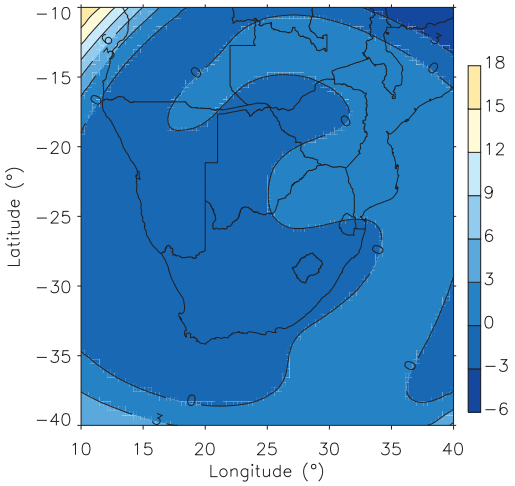

(f) Difference between SCHA and IGRF models: H (RMS = 1.99 nT/year).

Figure 5.2: The plots of SV data computed from the SCHA model (derived from the synthesized data set) and IGRF model at 400 km altitude in 2001 for D, and H components and the difference between two models.

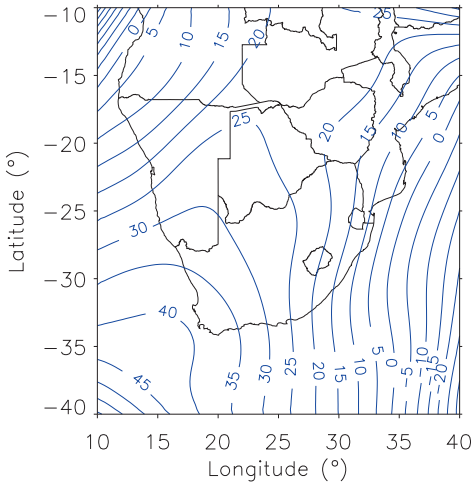

(a) SCHA model: Z (nT/year).

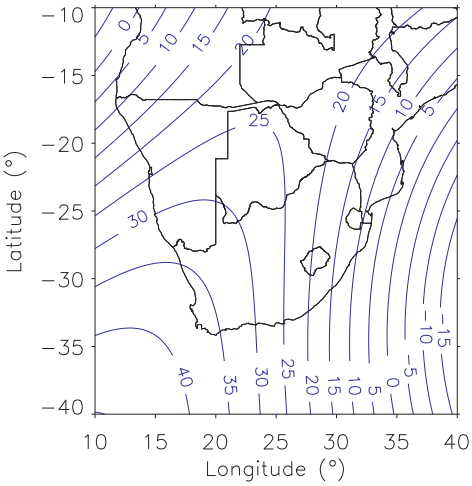

(b) IGRF model: Z (nT/year).

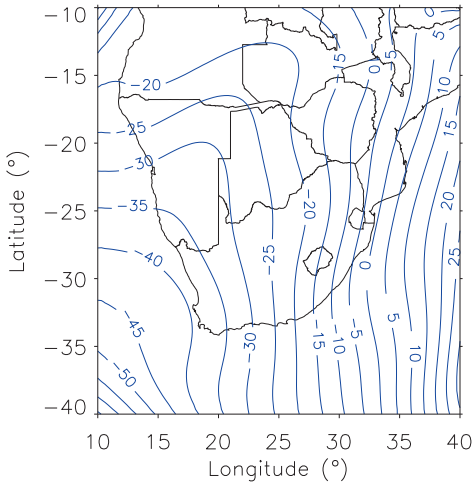

(c) SCHA model: F (nT/year).

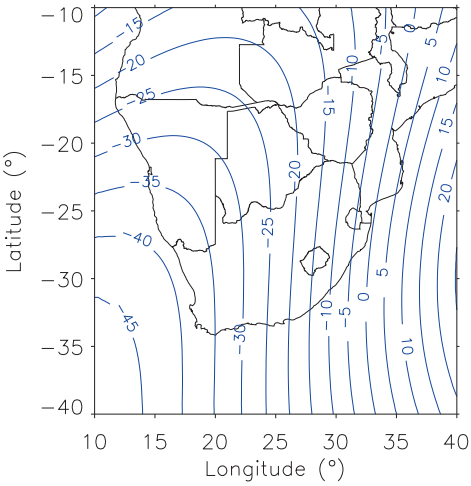

(d) IGRF model: F (nT/year).

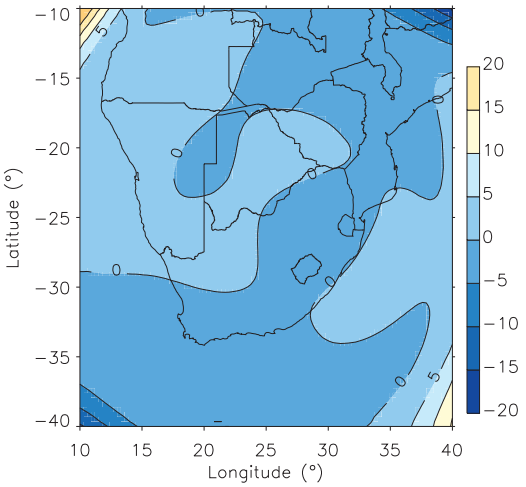

(e) Difference between SCHA and IGRF models: Z (RMS = 2.49 nT/year).

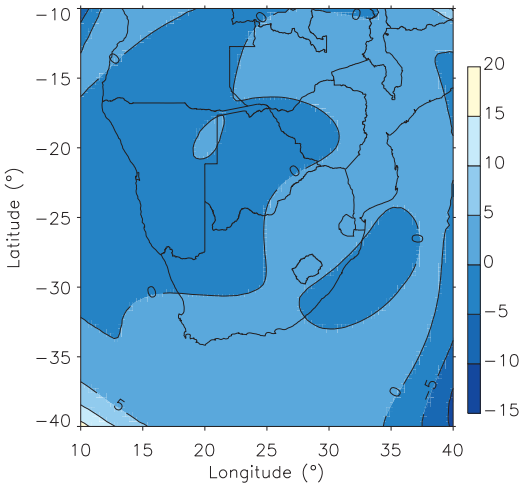

(f) Difference between SCHA and IGRF models: F (RMS = 1.88 nT/year).

Figure 5.3: The continuation of Fig. 5.2 for Z component and total field F.

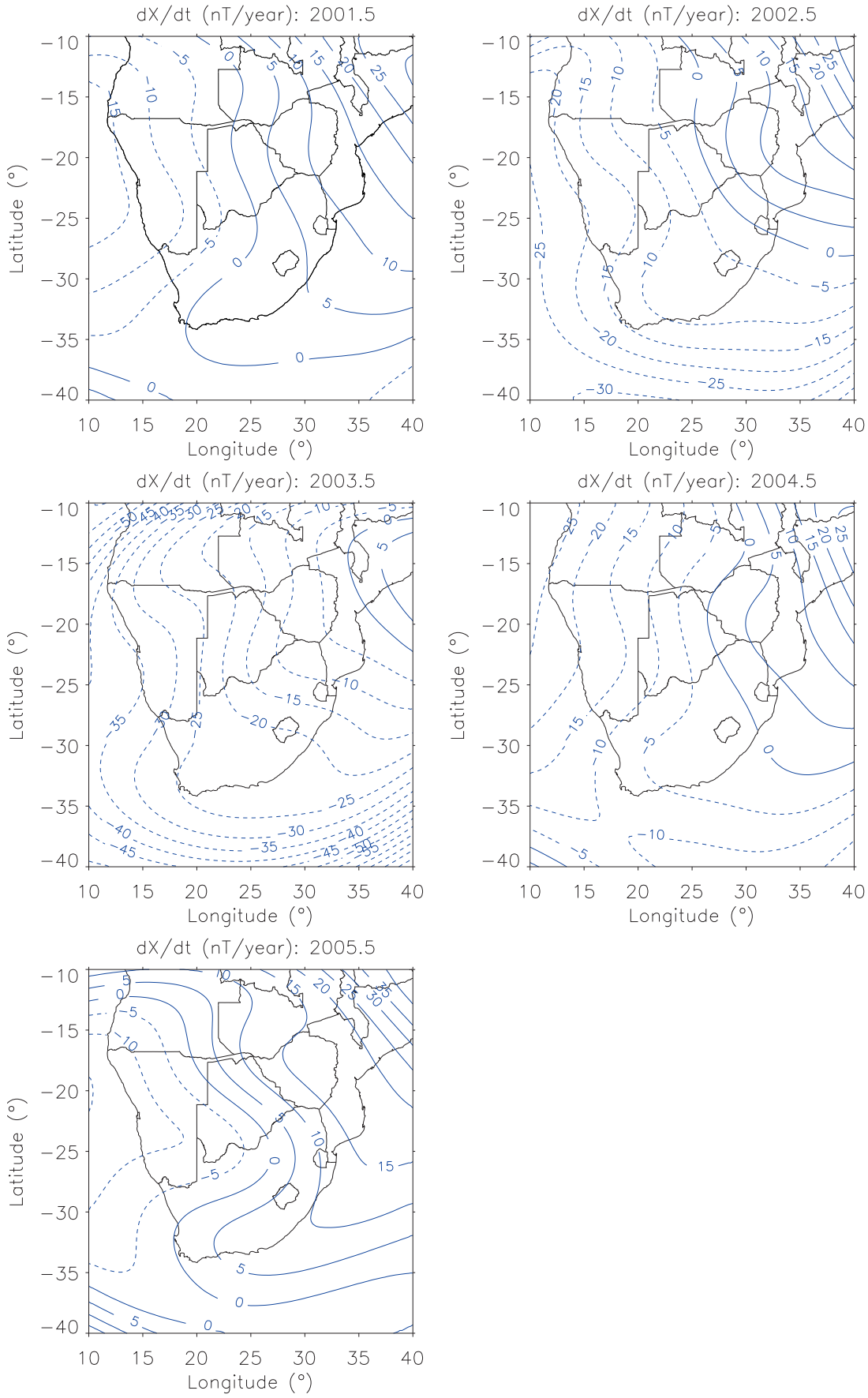

Figure 5.4: The plots of SV in the X component at 400 km altitude between 2001 and 2005 for SCHA model.

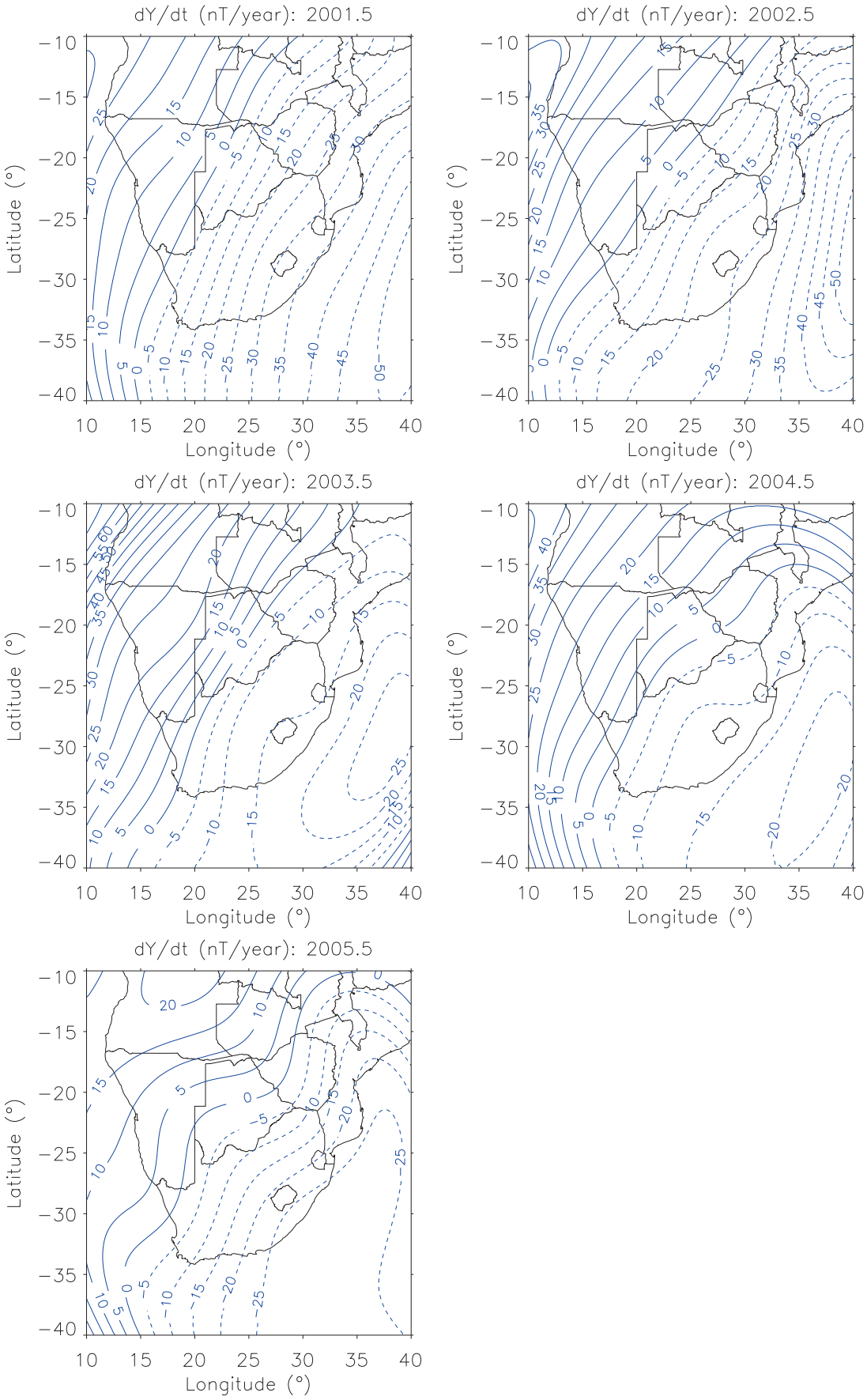

Figure 5.5: The plots of SV in the Y component at 400 km altitude between 2001 and 2005 for SCHA model.

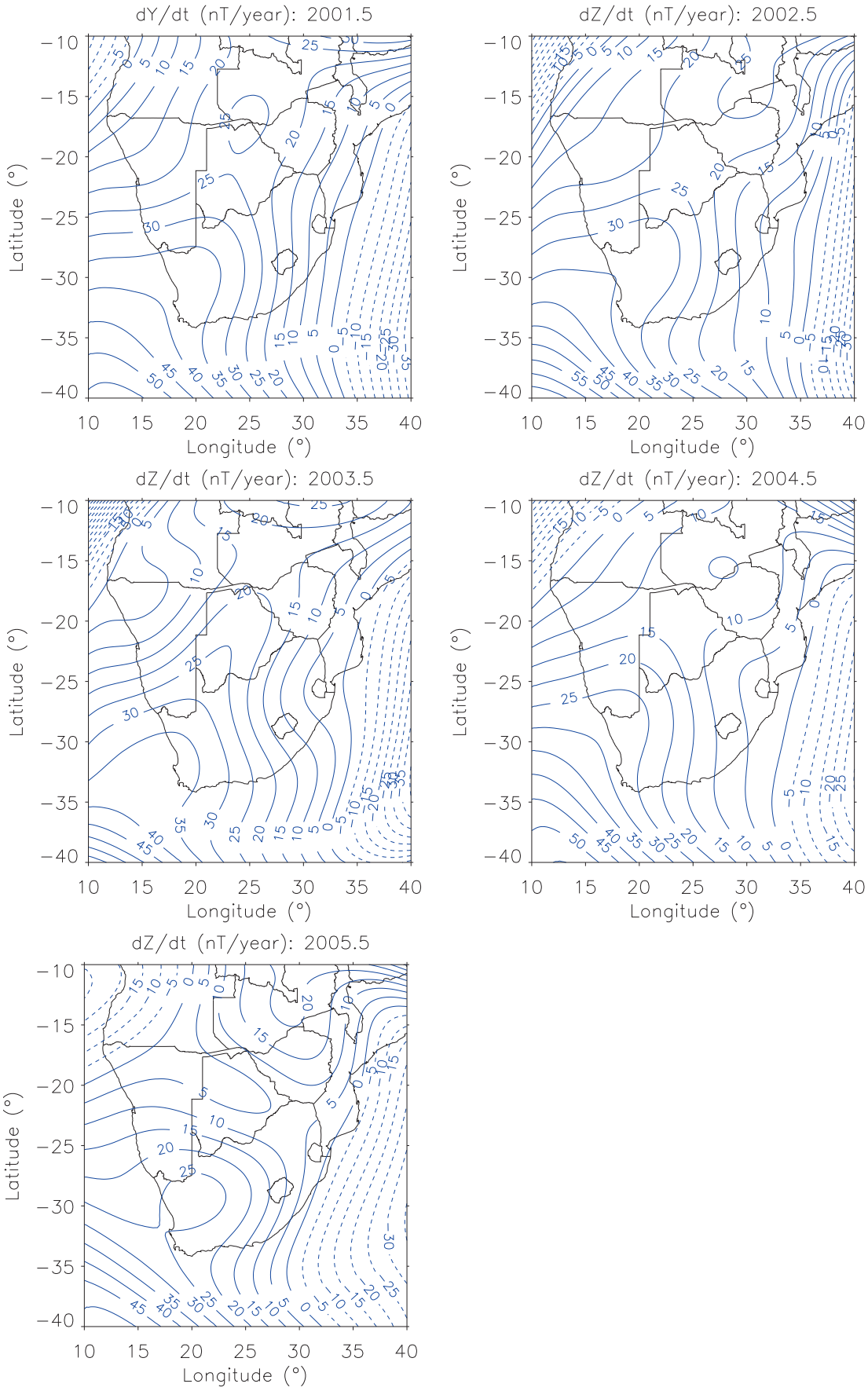

Figure 5.6: The plots of SV in the Z component at 400 km altitude between 2001 and 2005 for SCHA model.

Table 5.4: The RMS difference between SV data generated from IGRF 10 and SCHA models at 400 km altitude (January 2001-December 2001).

KINT		2	3	4	5	7
RMS difference	X (nT/year)	10.1	9.0	8.2	8.0	8.4
between SCHA and	Y (nT/year)	9.7	8.6	8.5	8.7	9.0
IGRF 10 (SV) at 400 km	Z (nT/year)	7.3	5.9	4.8	4.4	5.1
RMS difference	X (nT/year)	10.4	9.5	8.9	8.7	9.2
between SCHA	Y (nT/year)	9.9	8.8	8.6	8.8	9.1
and CHAOS (SV) at 400 km	Z (nT/year)	9.5	8.1	7.0	6.5	6.8

Table 5.5: The comparison between the regional (SCHA) and global (IGRF 10 and CHAOS) main field models using the CHAMP satellite data measured between 2001 and 2005. The unit of the X, Y and Z components is nT.

Year		2001		2002		2003		2004		2005	
Month		Jan	Dec	Jan	Dec	Jan	Dec	Jan	Dec	Jan	Dec
RMS misfit errors	X	21.3	20.4	18.7	20.1	19.5	30.4	26.1	24.5	26.1	20.9
SCHA - CHAMP	Y	11.4	11.5	11.2	13.5	10.7	17.2	16.1	13.8	19.8	14.3
	Z	15.6	14.1	13.6	13.3	13.2	19.7	16.4	19.6	20.8	19.3
RMS difference:	X	98.0	91.5	93.2	95.4	94.6	115.1	103.1	101.9	104.5	98.3
IGRF 10	Y	16.9	23.4	19.4	32.1	20.2	15.3	26.0	16.5	22.9	19.8
- CHAMP	Z	78.6	78.9	78.4	78.3	81.7	87.7	86.9	93.3	91.1	93.0
RMS difference:	X	93.3	86.1	87.7	90.8	90.1	112.3	100.5	93.7	104.2	91.4
CHAOS	Y	17.5	24.4	19.9	23.7	21.0	15.4	26.5	16.8	24.8	22.1
- CHAMP	Z	89.2	92.1	91.9	91.2	94.6	96.6	95.3	99.8	92.4	93.8

4.1 given in chapter 4. The geomagnetic field components D and H and the total field F were computed from X, Y and Z components using equations 2.2, 2.4 and 2.5 given in chapter 2.

The spherical cap modelling of CHAMP satellite data at ground level enables us to validate the performance of the regional model using the ground survey data recorded between 2001 and 2005 over southern Africa.

Champ satellite data, reduced to ground level, were modelled by SCHA with a half-cap angle of 18° and KINT = 5 for every January and December of each year. However, due to poor data coverage in 2005, February data were used instead of January. Table

Table 5.6: The RMS difference between SV data generated from global models (IGRF 10 and CHAOS) and regional models (SCHA and PolyM) at 400 km altitude (Jan - Dec) for years between 2001 and 2005. The RMS difference values were calculated using a grid of $0.2^\circ \times 0.2^\circ$ over the whole region of investigation.

Epoch	Component [nT/year]	SCHA - IGRF 10	PolyM - IGRF 10	SCHA - CHAOS	PolyM - CHAOS	SCHA - PolyM
	X	8.2	11.6	8.9	12.4	5.1
2001.5	Y	8.5	6.2	8.6	6.3	4.2
	Z	4.8	3.5	7.0	5.9	4.3
	X	5.4	6.1	5.7	6.4	4.1
2002.5	Y	6.0	8.6	5.9	8.6	6.5
	Z	5.5	3.8	5.5	3.9	5.9
	X	18.2	22.6	19.8	24.1	10.9
2003.5	Y	9.4	6.9	9.6	7.2	12.7
	Z	8.2	7.2	6.1	3.7	7.2
	X	4.3	6.9	5.4	7.6	5.9
2004.5	Y	9.8	10.2	9.1	9.7	4.0
	Z	9.5	7.9	5.3	5.2	5.4
	X	6.9	10.8	10.5	14.9	6.2
2005.5	Y	3.9	2.5	4.6	3.3	5.8
	Z	7.0	6.5	5.6	4.5	6.5

5.7 shows the RMS misfit errors between SCHA and CHAMP satellite data reduced to 0.8 km altitude using the IGRF 10 model. The modelling results are shown in figs. 5.7-5.10 and Tables 5.7 and 5.8. The spherical cap model coefficients are given in the appendix D.

Taking reference of the two global models, SCHA is better than PolyM for H component in all 5 years, total field F in 2001 and 2003, and D in 2003, 2004 and 2005 whereas the PolyM is better than SCHA for Z component in all 5 years, total field F in 2002, 2004 and 2005, and D in 2001 and 2002. The general view of the RMS difference values in Table 5.8 is that the two regional models are in close agreement each other in comparison with the global field models as shown when modelling CHAMP data at 400 km altitude in the X, Y and Z components (Table 5.6). For example in 2003 the RMS difference in H component between SCHA and PolyM is 15.2 nT/year whereas the RMS differences between regional models, SCHA and PolyM, and CHAOS are 24.0

nT/year and 25.9 nT/year, respectively.

Table 5.7: The RMS misfit errors between SCHA model and CHAMP satellite data values reduced to 0.8 km altitude using IGRF 10 model between 2001 and 2005.

Year		2001		2002		2003		2004		2005	
Month		Jan	Dec	Jan	Dec	Jan	Dec	Jan	Dec	Feb	Dec
misfit:	X (nT)	20.0	18.4	16.7	17.6	16.8	29.6	23.1	23.4	19.2	19.1
SCHA	Y (nT)	15.2	13.6	13.3	13.1	12.7	20.6	17.7	16.2	15.4	16.0
- CHAMP	Z (nT)	12.6	12.0	11.8	12.0	12.1	15.8	14.7	16.4	15.3	16.2

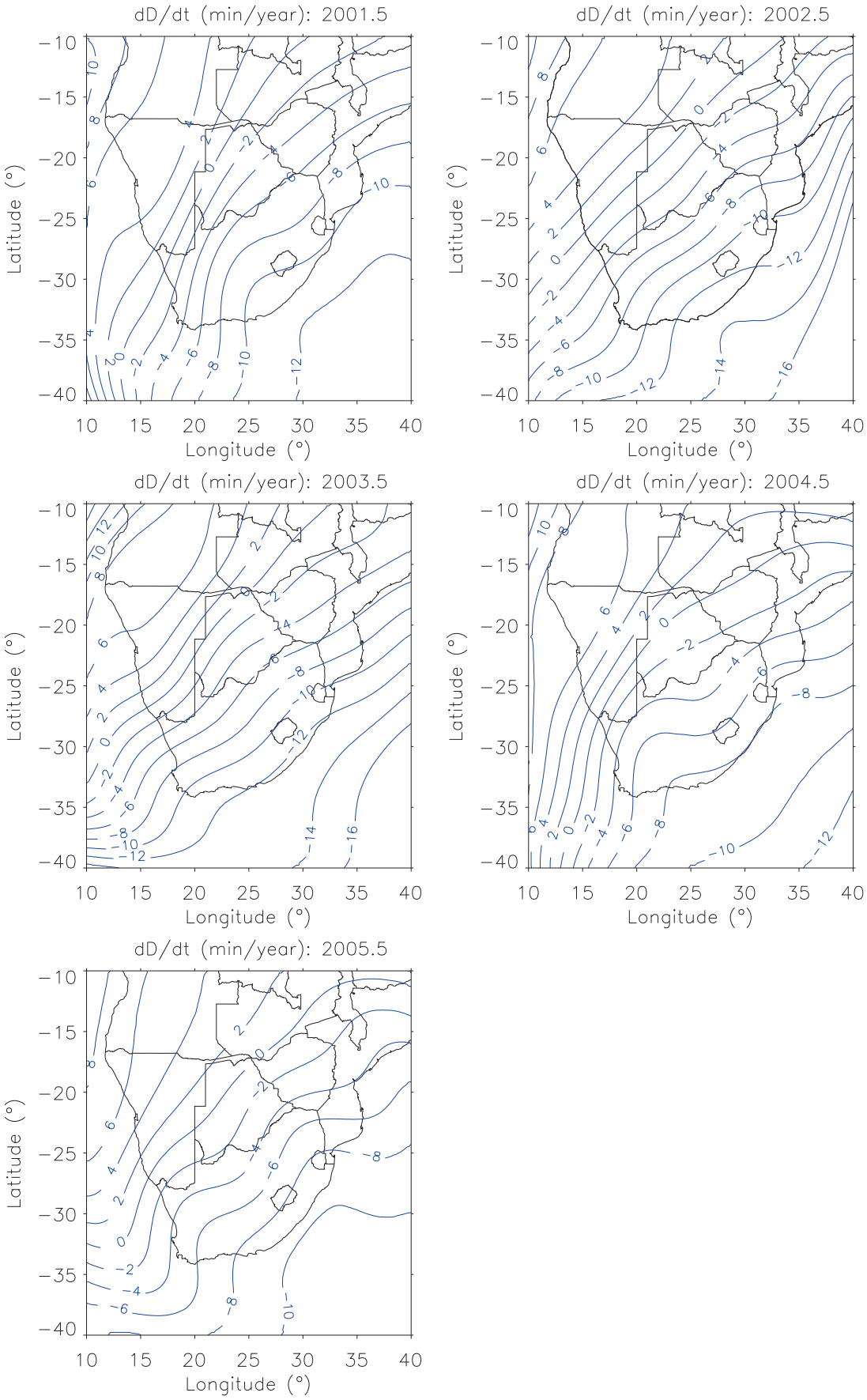

Figure 5.7: The plots of SV in the D component at 0.8 km altitude between 2001 and 2005 for SCHA model.

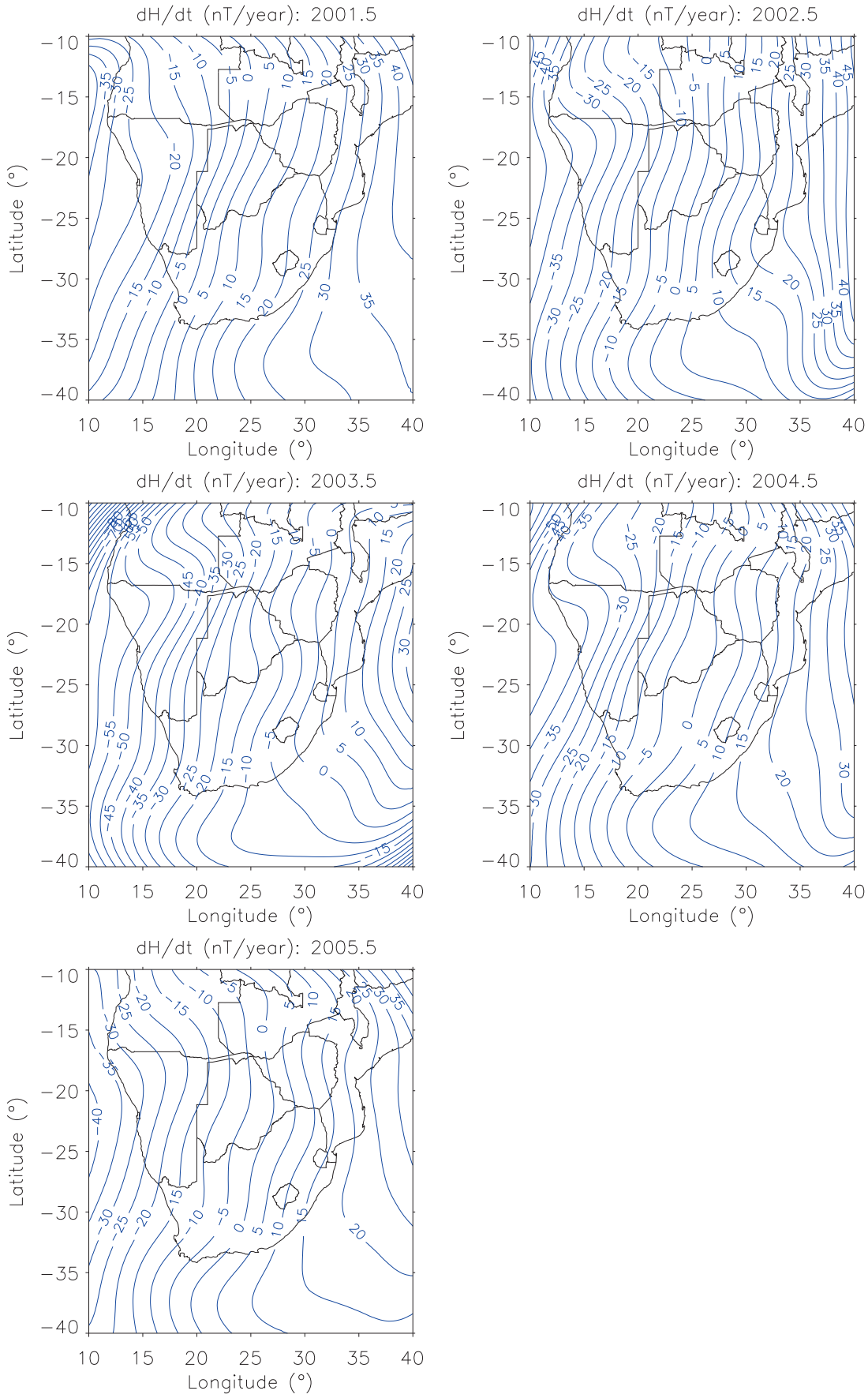

Figure 5.8: The plots of SV in the H component at 0.8 km altitude between 2001 and 2005 for SCHA model.

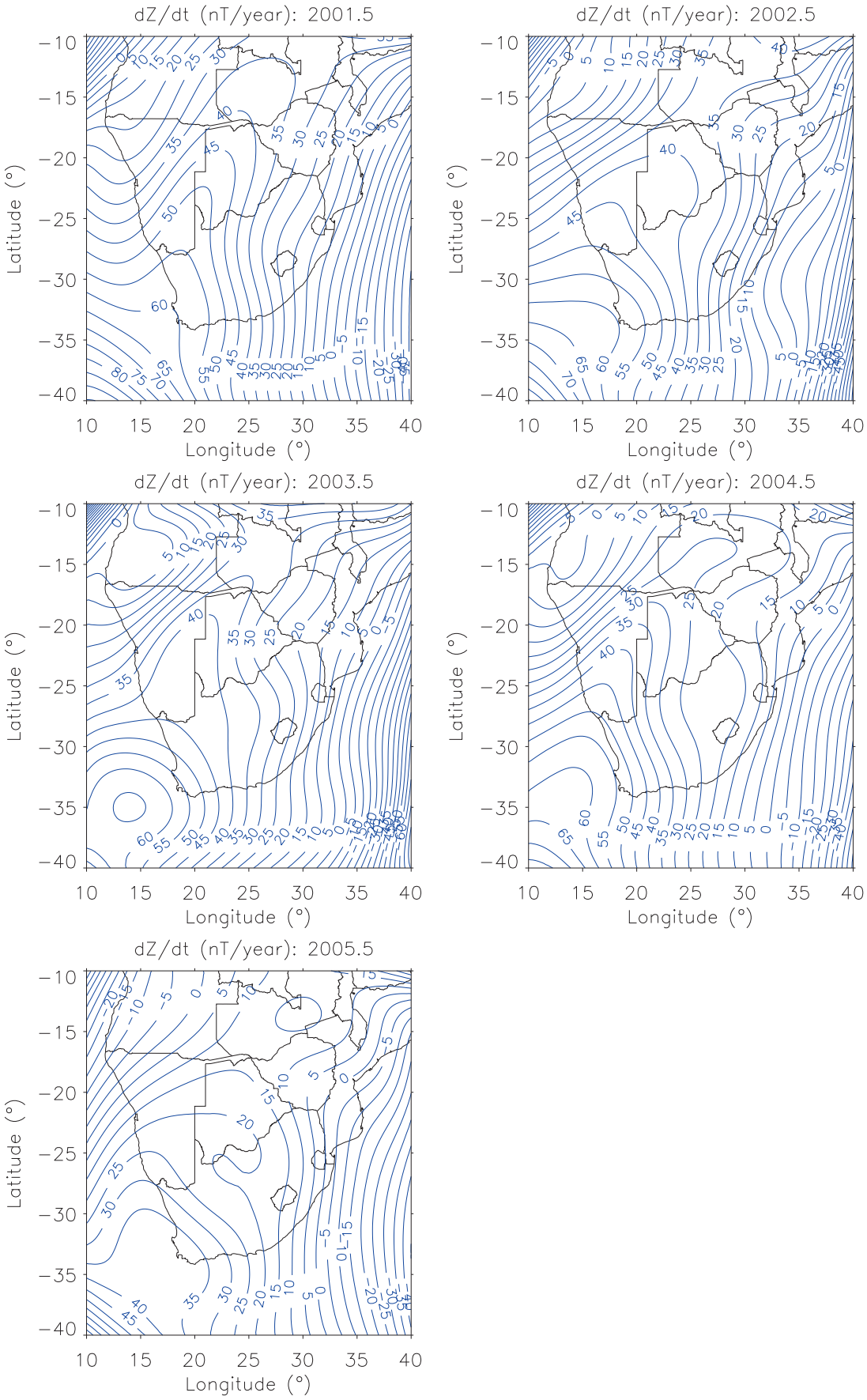

Figure 5.9: The plots of SV in the Z component at 0.8 km altitude between 2001 and 2005 for SCHA model.

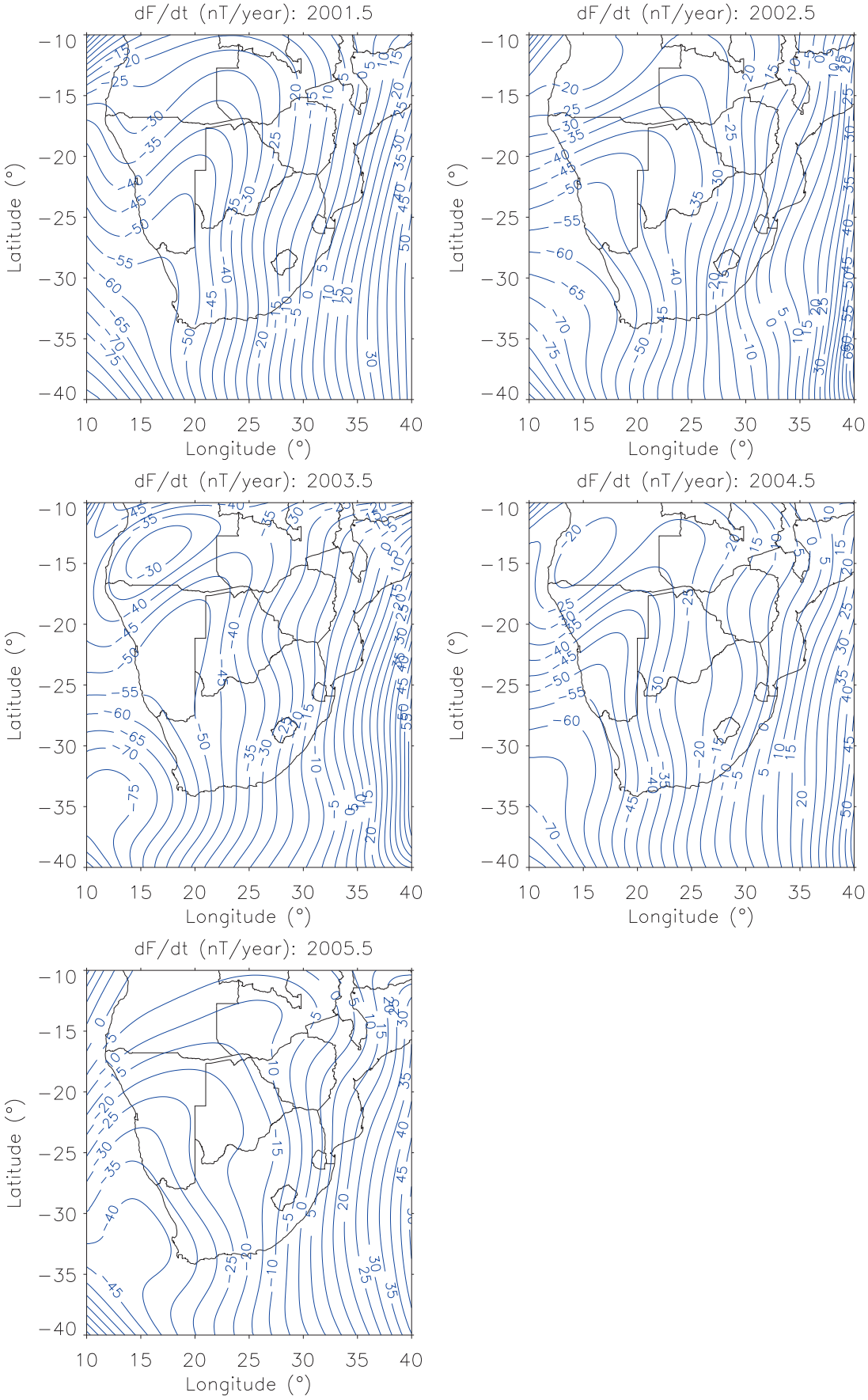

Figure 5.10: The plots of SV in the total field F at 0.8 km altitude between 2001 and 2005 for SCHA model.

5.3.3 The validation of SCHA model using ground data and global models IGRF 10 and CHAOS.

The validation of SCHA model was done by plotting bar graphs (fig. 5.11) of the RMS differences for each year during the period 2001-2005 between the ground survey data and both the regional models (SCHA and PolyM), and two global models (IGRF 10 and CHAOS). The ground survey data are the SV data obtained from the geomagnetic field surveys between 2001 and 2005 at 13 reference ground points (Table 3.11).

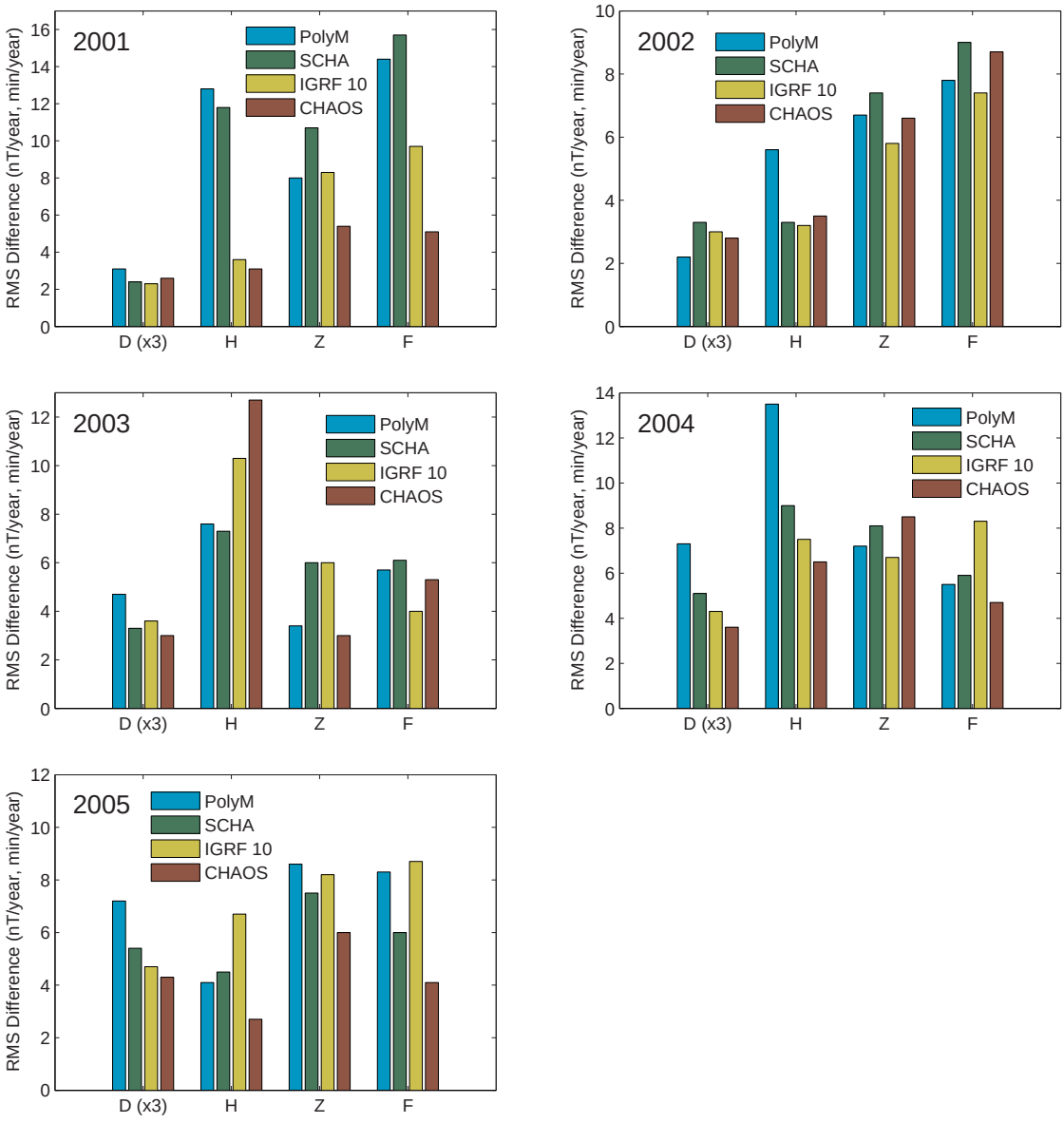

Figure 5.11: Comparison of RMS differences between field survey data and the regional models (PolyM and SCHA), and field survey data and two global models IGRF 10 and CHAOS. The RMS in D component are multiplied by 3 for the plotting purpose and they are in minutes of arc/year. The RMS were calculated using only the 13 ground reference points (fig. 3.8).

5.4 Conclusion

Geomagnetic SV models were developed using the SCHA technique and CHAMP satellite data. A half-cap angle 18° and the maximum spatial indices, KINT = 4 at 400 km altitude and KINT= 5 at ground level, were found suitable for spherical cap modelling of CHAMP satellite data over southern Africa.

Firstly, a SCHA model was developed for X, Y and Z components at 400 km altitude using data as recorded between 350 km and 450 km above sea level by the CHAMP satellite. The results are shown in figs. 5.4-5.6. This model was then validated against the global field models IGRF 10 and CHAOS as well as the polynomial model that was developed in chapter 4 (Table 5.6). The observation of the evolution of zero contour line in X component between 2001 and 2005 shows clearly the occurrence of a SV impulse in 2003 as identified in chapter 4 after applying the polynomial modelling technique to CHAMP satellite data. Table 5.6 shows a substantial deviation of SCHA model from global field models during 2003 particulary for the X component. The RMS differences between the SCHA model and the global field models IGRF 10 and CHAOS are 18.2 nT/year and 19.8 nT/year, respectively. This might be attributed to the SV impulses that occurred in 2003 and 2004 over southern Africa (see chapter 4, section 4.6). Apart from this, the RMS differences in all 5 years between 2001 and 2005 for all components X, Y and Z are less than 10 nT/year except for the X component in 2005 when SCHA and CHAOS differed by 10.5 nT/year. In general, the SCHA model is in a better agreement with the polynomial model in comparison to the global field models.

Secondly, a SCHA model was developed for X, Y and Z components at the ground level. The D and H components and the total field F were computed from X,Y and Z components using equations 2.2, 2.4 and 2.5 in order to validate SCHA model against global field models (IGRF 10 and CHAOS) using the ground survey data. CHAMP data were first reduced to the ground level (0.8 km altitude, the mean altitude of 13 ground reference points) using the IGRF 10 model and equation 4.1 given in chapter 4 and results are shown in figs. 5.7-5.10. The SCHA model was subsequently compared with IGRF 10 and CHAOS, as well as the polynomial model derived in chapter 4 (Table 5.8). Table 5.8 shows a considerable deviation of SCHA model from global field models in 2003 particulary for the H component. The RMS differences between SCHA and global field models IGRF 10 and CHAOS are 19.3 nT/year and 21.3 nT/year, respectively. Apart from this substantial deviation, the RMS differences in all 5 years between 2001 and 2005 for H, Z and F are less than 11 nT/year except the Z component in 2003 where the RMS difference between SCHA and IGRF 10 is 11.3 nT/year. The RMS differences in the D component are less or equal to 2.6 minutes of arc/year.

On the other hand, the SCHA model was also validated against the global field models (IGRF 10 and CHAOS) as well as the polynomial model (PolyM) using the ground

survey data as illustrated in fig. 5.11. A summary of the RMS differences between the models and ground survey data is given in Table 5.9. Using ground survey data as reference and evaluating every component, it can be concluded that SCHA can be applied with varying levels of success to derive a regional field model, based entirely on satellite data.

In addition, the SCHA technique can also be used to develop a geomagnetic SV model over southern Africa. The challenges were encountered in data selection where the data coverage and distribution were not satisfactory in some months like December 2001 and it was therefore necessary to obtain data from previous or next months. This is reflected in the performance of the SCHA model in 2001. Table 5.9 shows that the RMS differences between the SCHA model and ground survey data are 11.8 nT/year, 10.7 nT/year and 15.7 nT/year for H, Z and total field F, respectively.

Table 5.8: The RMS difference between SV data generated from global models (IGRF 10 and CHAOS) and regional models (SCHA and PolyM) at 0.8 km altitude (Jan - Dec for years between 2001 and 2004 and Feb - Dec for 2005). The RMS difference values were calculated using a grid of $0.2^\circ \times 0.2^\circ$ over the whole region of investigation.

Epoch	Component/Total field	SCHA - IGRF 10	PolyM - IGRF 10	SCHA - CHAOS	PolyM - CHAOS	SCHA - PolyM
	D (min/year)	1.6	1.6	1.5	1.6	1.7
2001.5	H (nT/year)	9.6	11.1	10.7	12.2	4.7
	Z (nT/year)	5.0	3.7	7.5	6.7	4.8
	F (nT/year)	6.6	7.1	10.5	11.2	4.7
	D (min/year)	2.3	0.8	2.4	0.8	2.0
2002.5	H (nT/year)	4.7	5.6	4.7	5.5	5.6
	Z (nT/year)	5.4	2.8	5.3	2.8	5.1
	F (nT/year)	4.9	4.2	4.8	4.1	5.6
	D (min/year)	2.2	2.1	2.2	2.2	2.1
2003.5	H (nT/year)	19.3	24.0	21.3	25.9	15.2
	Z (nT/year)	8.3	7.2	5.9	3.2	5.7
	F (nT/year)	7.2	8.4	11.8	13.3	9.7
	D (min/year)	2.2	2.5	2.4	2.6	1.7
2004.5	H (nT/year)	5.0	7.6	6.2	8.6	8.0
	Z (nT/year)	9.9	9.1	6.1	4.7	5.3
	F (nT/year)	7.5	6.2	6.3	6.1	6.3
	D (min/year)	1.0	1.2	1.1	1.2	1.2
2005.5	H (nT/year)	5.2	6.9	3.2	5.4	4.7
	Z (nT/year)	6.3	4.9	5.5	4.8	3.7
	F (nT/year)	5.1	4.8	5.7	5.7	4.3

Table 5.9: The RMS differences between survey ground data and models at 13 reference points.

Epoch	Component/Total field	PolyM	SCHA	IGRF 10	CHAOS
	D (min/year)	1.0	0.8	0.8	0.9
2001.5	H (nT/year)	12.8	11.8	3.6	3.1
	Z (nT/year)	8.0	10.7	8.3	5.4
	F (nT/year)	14.4	15.7	9.7	5.1
	D (min/year)	0.7	1.1	1.0	0.9
2002.5	H (nT/year)	5.6	4.1	3.2	3.5
	Z (nT/year)	6.7	6.8	5.8	6.6
	F (nT/year)	7.8	7.6	7.4	8.7
	D (min/year)	1.5	1.1	1.2	1.0
2003.5	H (nT/year)	7.6	7.3	10.3	12.7
	Z (nT/year)	3.4	6.0	6.0	3.0
	F (nT/year)	5.7	6.1	4.0	5.3
	D (min/year)	2.4	1.7	1.4	1.2
2004.5	H (nT/year)	13.5	9.0	7.5	6.5
	Z (nT/year)	7.2	8.1	6.7	8.5
	F (nT/year)	5.5	5.9	8.3	4.7
	D (min/year)	2.4	1.8	1.6	1.4
2005.5	H (nT/year)	4.1	4.5	6.7	2.7
	Z (nT/year)	8.6	7.5	8.2	6.0
	F (nT/year)	8.3	6.0	8.7	4.1

Chapter 6

Conclusions and discussions

Satellite data has been used to develop a geomagnetic SV field model based on CHAMP satellite data for the period 2001-2005 over southern Africa covering the area between 10°S and 40°S in latitude and 10°E and 40°E in longitude. In particular, only quiet time data corresponding to a Dst index between -20 nT and +20 nT measured during the universal time intervals 16:00 - 24:00 and 00:00 - 05:00 were considered. SV models were developed by calculating the time variation of various geomagnetic components between January and December of the same year. During the data selection process lack of suitable data coverage and distribution were taken care of by adding the last few days of the previous month or the first few days of the next month, as shown in Table 3.1.

Two regional modelling techniques (surface polynomials and SCHA) were subsequently applied to derive SV models at both 400 km (mean altitude of CHAMP satellite) and 0.8 km (mean altitude of 13 ground reference points used in model validation) altitudes. For the surface polynomial technique a 5^{th} degree was chosen for main field models while 2^{nd} and 3^{rd} degrees were suitable for the SV field models. A half-cap angle of 18° was chosen for SCHA modelling, and the IGRF 10 model was used as a known spherical harmonic potential for the reference field which was calculated at epoch of 2003.5. The resulting residual data were converted from a geocentric coordinate system to a new pole at 25°S, 25°E. In addition, low maximum indices of expansion of internal sources (KINT = 4 and KINT = 5 yielding a minimum wavelength of approximately 1300 km and 1600 km, respectively) produced the best SV models.

The two regional SV field models (PolyM and SCHA) were also compared with global field models (IGRF 10 and CHAOS). The results obtained show that it is possible to derive SV models over southern Africa based entirely on satellite data as illustrated in figs. 4.24-4.29, 4.30 and 5.11 and Table 5.9.

Surface polynomial modelling of CHAMP satellite data also led to the identification of two SV impulses in the X, Y and Z field components around 2003.0 and 2004.0 epochs

over southern Africa (figs 4.32-4.38). The analysis of monthly time series data for the magnetic observatories HER and HBK (in South Africa) and TSU (in Namibia) also support these results as illustrated in figs. 4.42-4.43. Clear supporting evidence of SV impulses between 2001 and 2005 were also found in the SCHA modelling results, as shown in figs. 5.4-5.6. The evolution of the zero SV contour line of the X component across the region of investigation between 2001 and 2005 is a clear illustration of the occurrence of SV impulses.

Particularly for main field models, the developed SCHA regional models provide a better alternative to IGRF 10 and CHAOS (global models) as illustrated in Table 5.5. The IGRF 10 and CHAOS RMS differences are sometimes more than 3 times larger than the RMS misfit errors obtained with SCHA in both X and Z components for the 5 year period (2001-2005).

The final comparative evaluation of the regional SV models (PolyM and SCHA) and global SV field models (IGRF 10 and CHAOS) was done using ground survey data during the same period, obtained from 13 reference points scattered over southern Africa (fig. 3.8 and Tables 3.11 and 3.12). RMS results are summarised in Table 5.9.

Table 6.1 compares the performance of the regional SV models (PolyM and SCHA) to the global SV field models (IGRF 10 and CHAOS). The unexpected poor performance in 2001 particularly in H, Z and F can mainly be attributed to a data coverage particulary in December 2001. For the remaining 4 years (2002-2005) there is a good agreement with global field models. However, the regional SV models can be substantially improved using both high quality satellite and ground survey data. The R-SCHA technique can be used to develop a regional model by integrating both satellite and ground survey data as it correctly takes into account the radial dependence, unlike SCHA (Thébault *et al.*, 2004).

Future modelling should take into account longer time series of satellite data and then use spline modelling techniques to obtain a smooth time-varying model of the geomagnetic field over southern Africa. This together with R-SCHA will greatly enhance the accuracy of SV models. The accurate regional SV models can play an important role in studying core-mantle interactions to understand better the geomagnetic polarity reversals (Gubbins, 1994).

Table 6.1: A comparative evaluation between the RMS differences for D, H and Z components and total field F obtained from Table 5.9. Positive values indicate that a global field model is to be preferred to a regional field model.

Epoch	Component/ Total field	RMS_{PolyM} -RMS_{IGRF10}	RMS_{PolyM} -RMS_{CHAOS}	RMS_{SCHA} -RMS_{IGRF10}	RMS_{SCHA} -RMS_{CHAOS}
	D (min/year)	0.2	0.1	0.0	-0.1
2001.5	H (nT/year)	9.2	9.7	8.2	8.7
	Z (nT/year)	-0.3	2.6	2.4	5.3
	F (nT/year)	4.7	9.3	6.0	10.6
	D (min/year)	-0.3	-0.2	0.1	0.2
2002.5	H (nT/year)	2.4	2.1	0.9	0.6
	Z (nT/year)	0.9	0.1	1.0	0.2
	F (nT/year)	0.4	-0.9	0.2	-1.1
	D (min/year)	0.3	0.5	-0.1	0.1
2003.5	H (nT/year)	-2.7	-5.1	-3.0	-5.4
	Z (nT/year)	-2.6	0.4	0.0	3.0
	F (nT/year)	1.7	0.4	2.1	0.8
	D (min/year)	1.0	1.2	0.3	0.5
2004.5	H (nT/year)	6.0	7.0	1.5	2.5
	Z (nT/year)	0.5	-1.3	1.4	-0.4
	F (nT/year)	-2.8	0.8	-2.4	-1.2
	D (min/year)	0.8	1.0	0.2	0.4
2005.5	H (nT/year)	-2.6	1.4	-2.2	1.8
	Z (nT/year)	0.4	2.6	-0.7	-1.5
	F (nT/year)	-0.4	1.9	-2.7	2.1

References

Alexandrescu, M., D. Gilbert, G. Hulot, J.-L. Le Mouël and G. Saracco (1996). Worldwide wavelet analysis of geomagnetic jerks. *Journal of Geophysical Research* **101**, 21975–21994.

Bartels, J., N. H. Heck and H. F. Johnston (1939). The three-hour-range index measuring geomagnetic activity. *Journal of Geophysical Research* **44**, 411–418.

Bellanger, E., J.-L. Le Mouël, M. Mandea and S. Labrosse (2001). Chandler Wobble and geomagnetic jerks. *Physics of the Earth and Planetary Interiors* **124**, 95–103.

Bloxham, J., S. Zatman and M. Dumberry (2002). The origin of geomagnetic jerks. *Nature* **420**, 65–68.

Campbell, W. H. (1997). *Introduction to Geomagnetic Fields*. Cambridge University Press.

Chambodut, A., C. Eymin and M. Mandea (2007). Geomagnetic jerks from the earth's surface to the top of the core. *Earth Planets and Space* **59**(7), 675–684.

Chapman, S. (1964). *Solar Plasma Geomagnetism and Aurora*. Blackie and Son Limited.

Courtillot, V., J.-L. Le Mouël and J. Ducruix (1984). On backus'mantle filter theory and the 1969 geomagnetic impulse. *Geophysical Journal of Royal Astronomical Society* **78**, 619–624.

Davis, T. N. and M. Sugiura (1966). Auroral electrojet activity index AE and its universal time variations. *Journal of Geophysical Research* **71**, 785–791.

De Santis, A., M. Chiappini, G. Dominici and A. Meloni (1997). Regional geomagnetic field modelling: the contribution of the istituto nazionale di geofisica. *Annali di Geofisica*.

Encyclopeadia Britannica, Inc. (1994). Earth: dipolar magnetic field. Available at: http://www.britannica.com/EBchecked/topic-art/175962/1163/ (Accessed: May 25, 2008).

Fox, N. and P. Murdin (2001). Solar-terrestrial connection: Space weather predictions. In: *Encyclopedia of Astronomy and Astrophysics*. Bristol: Institute of Physics Publishing.

GEM systems, Inc. (2008). Magnetometer, Gradiometer and Magnetic Sensor Solutions for Magnetic Observatories. Available at: http://www.gemsys.ca/apps_observatory.htm (Accessed: March 23, 2009).

Geometrics, Inc. (n.d.). Geometrics' Magnetometers - Land, Sea, and Air. Available at: http://www.geometrics.com/geometrics-products/geometrics-magnetometers/ (Accessed: Jan 23, 2009).

Gubbins, D. (1994). Geomagnetic polarity reversals: A connection with secular variation and core-mantle interaction?. *Rev. Geophys.* **32**(1), 61–83.

Haines, G. V. (1985). Spherical cap harmonic analysis. *Journal of Geophysical Research* **90**, 2593–2598.

Haines, G. V. (1988). Computer programs for spherical cap harmonic analysis of potential and general fields. *Computers and Geosciences* **14**, 413–447.

Haines, G. V. (1990). Regional magnetic field modelling: a review. *Journal of Geomagnetism and Geoelectricity* **42**, 1001–1018.

INTERMAGNET, Org. (2007). Magnetic Observatories (Map). Available at: http://ottawa.intermagnet.org/Imomap_e.php (Accessed: February 26, 2009).

Kivelson, M. and C. Russell (1995). *Introduction to Space Physics*. Cambridge Univ. Press, UK.

Korepanov, V. (2004). Fluxgate Magnetometer LEMI-008 Technical Description and Operation Manual. Technical report. Lviv Centre of Institute of Space Research, Ukraine.

Korte, M., M. Mandea, P. B. Kotzé, E. Nahayo and B. Pretorius (2007). Improved observations at the southern African geomagnetic repeat station network. *South African Journal of Geology* **110**, 175–186.

Kotzé, P. B. (2001). Spherical cap modelling of Ørsted magnetic field vectors over southern africa. *Earth Planets Space* **53**, 357–361.

Kotzé, P. B. (2003). The time-varying geomagnetic field of southern Africa. *Earth Planets Space* **55**, 111–116.

Kyoto University, Uni. (1991). On Dst Index. Available at: http://wdc.kugi.kyoto-u.ac.jp/dstdir/dst2/onDstindex.html (Accessed: Jan 18, 2009).

Langlais, B. and M. Mandea (2000). A IGRF candidate main geomagnetic field model for epoch 2000 and secular varation model for 2000-2005. *Earth Planets Space* **52**, 1137–1148.

Lühr, H. (2001). Announcement of Opportunity for CHAMP. Technical report. GeoForschungsZentrum, Potsdam, Germany.

Mandea Alexandrescu, M., D. Gilbert, J.-L. Le Mouël, G. Hulot and G. Saracco (1999). An estimate of average lower mantle conductivity by wavelet analysis of geomagnetic jerks. *Journal of Geophysical Research* **104**, 17735–17745.

Mandea, M., Bellanger E. and J.-L. Le Mouël (2000). A geomagnetic jerk for the end of the 20th century?. *Earth and Planetary Science Letters* **183**, 369–373.

Mandea, M., M. Korte, D. Mozzoni and P. B. Kotzé (2007). The magnetic field changing over the southern African continent: a unique behaviour. *South African Journal of Geology* **110**, 193–202.

Maus, S., S. McLean, D. Dater, H. Lühr, M. Rother, W. Mai and S. Choi (2005). Ngdc/gfz candidate models for the 10th generation international geomagnetic reference field. *Earth Planets Space* **57**, 1151–1156.

Nahayo, E. (2006). Geomagnetic secular variation observations in southern Africa, 2005. Technical report. Hermanus Magnetic Observatory, South Africa.

NASA (n.d.). What is a solar flare?. Available at: http://hesperia.gsfc.nasa.gov/ sftheory/flare.htm (Accessed: April 4, 2009).

Nemiroff, R. (2007). A Coronal Mass Ejection. Available at: http://apod.nasa.gov/apod/ap070206.html (Accessed: August 15, 2008).

Newitt, L.R., C.E. Barton and J. Bitterly (1996). *Guide for Magnetic Repeat Station Surveys*. International Association of Geomagnetism and Aeronomy.

NRCan, Inst. (2008). Generation of the Earth's magnetic field. Available at: http://gsc.nrcan.gc.ca/geomag/field/field_e.php (Accessed: March 15, 2008).

Olsen, N. and M. Mandea (2007). Investigation of a secular variation impulse using satellite data: The 2003 geomagnetic jerk. *Earth and Planetary Science Letters* **255**, 94–105.

Olsen, N., H. Lühr, T. J. Sabaka, M. Mandea, M. Rother, L. T∅ffner-Clousen and S. Choi (2006). CHAOS - A Model of Earth's Magnetic Field derived from CHAMP, ∅rsted, and SAC-C magnetic satellite data. *Geophysical Journal International* **166**, 67–75.

Pulkkinen, A., O. Amm, A. Viljanen and BEAR working group (2003). Separation of the geomagnetic variation field on the ground into external and internal parts using the spherical elementary current system method. *Earth Planets Space* **55**, 117–129.

Queen's University Belfast, Uni. (2005). Sfit. Available at: http://star.pst.qub.ac.uk/idl/SFIT.html (Accessed: March 28, 2008).

Reigber, C., H. Lühr and P. Schwintzer (2002). CHAMP mission status. *Advances in Space Research* **30**(2), 129–134.

Shu, Y., C. An, P. Golovkov, N. M. Rotanova and T. N. Bondar (1996). Analysis of geomagnetic secular variations in eastern Asia during the last 30 years. *International Journal of Geomagnetism and Aeronomy* **35**, 871–875.

Stone, H. (2008). Earth's Magnetosphere. Available at: http://www.eoearth.org/ article/Earth's_Magnetosphere (Accessed: June 21, 2008).

Sugiura, M. (1964). Hourly values of equatorial dst for IGY. *Annals of the International Geophysical Year* **35**(9), 945–948.

Technical University of Denmark, Inst. (2008). 3-axis Fluxgate Magnetomer Model FGM-FGE. Available at: http://www.space.dtu.dk/English/Research/ Instruments_Systems_Methods/3-axis_Fluxgate_Magnetometer_Model_FGM-FGE.aspx (Accessed: Jan 21, 2009).

Thébault, E. (2003). Modélisation régionale du champ magnétique terrestre. PhD thesis. Université Louis Pasteur, Strasbourg I, France.

Thébault, E. (2006b). Global lithospheric magnetic field modelling by successive regional analysis. *Earth Planets Space* **58**, 485–495.

Thébault, E., J. J. Schott and M. Mandea (2006a). Revised spherical cap harmonic analysis(r-scha): Validation and properties. *Journal of Geophysical Research* **111**, B01102.

Thébault, E., J. J. Schott, M. Mandea and J. P. Hoffbeck (2004). A new proposal for spherical cap harmonic modelling. *Geophysical Journal International* **159**, 83–103.

University of Melbourne, Uni. (n.d.*a*). Fluxgate Magnetometer. Available at: http://www.earthsci.unimelb.edu.au/ES304/MODULES/MAG/NOTES/fluxgate.html (Accessed: Jan 19, 2009).

University of Melbourne, Uni. (n.d.*b*). Proton Precession Magnetometer. Available at: http://www.earthsci.unimelb.edu.au/ES304/MODULES/MAG/NOTES/proton.html (Accessed: Jan 19, 2009).

Verbanac, G. (2007). On regional modelling of the main geomagnetic field. *Geofizika* **24**(1), 1–27.

Wardinski, I. and R. Holme (2006). A time-dependent model of the earth's magnetic field and its secular variation for the period 1980 to 2000. *Journal of Geophysical Research* **111**, B12101.

Zirin, H. (1988). *Astrophysics of the sun*. Cambridge University Press.

Appendix A: The PolyM main field model coefficients for D, H and Z components at 0.8 km altitude

Table A.1: PolyM main field model coefficients for January and December 2001.

	January			December		
Coef.	D	H	Z	D	H	Z
k_{00}	18.687410	24365.730469	-16685.054687	20.542955	24997.994141	-16102.478516
k_{10}	-1.797953	469.736389	225.175293	-2.427094	299.734100	96.000130
k_{20}	0.074614	-24.176622	-20.555521	0.128813	-6.596831	-9.728696
k_{30}	-0.000750	0.791435	0.964688	-0.002831	-0.051673	0.532297
k_{40}	-0.000014	-0.014066	-0.016804	0.000024	0.004796	-0.008393
k_{50}	0.000000	0.000105	0.000096	0.000000	-0.000054	0.000032
k_{01}	4.648957	174.353180	775.096313	4.505498	169.088592	799.433716
k_{11}	-0.233275	25.487614	44.629833	-0.242153	27.091925	41.828442
k_{21}	0.006256	-0.822138	-1.571651	0.007161	-0.891538	-1.451955
k_{31}	-0.000052	0.004378	0.025939	-0.000073	0.004853	0.023691
k_{41}	0.000000	0.000002	-0.000168	0.000000	0.000009	-0.000152
k_{02}	0.269542	-47.935642	4.170661	0.257104	-48.150024	5.269371
k_{12}	-0.005897	0.029154	1.958275	-0.005721	0.076423	1.896506
k_{22}	0.000128	-0.011118	-0.047417	0.000317	-0.013120	-0.046153
k_{32}	0.000000	0.000031	0.000239	0.000000	0.000050	0.000226
k_{03}	0.010537	-2.089619	-1.303314	0.010189	-2.091960	-1.279308
k_{13}	-0.000008	-0.016561	0.026564	0.000001	-0.016377	0.025909
k_{23}	0.000001	0.000015	-0.000429	0.000001	0.000009	-0.004278
k_{04}	0.000223	-0.032247	-0.038671	0.000220	-0.032257	-0.038375
k_{14}	0.000001	-0.000181	0.000069	0.000001	-0.000182	0.000064
k_{05}	0.000002	-0.000178	-0.000326	0.000002	-0.000178	-0.000324

Table A.2: PolyM main field model coefficients for January and December 2002.

	January			December		
Coef.	D	H	Z	D	H	Z
k_{00}	21.049513	24860.576172	-16048.883789	27.290510	25253.880859	-16410.320312
k_{10}	-2.368232	329.652466	99.249580	-3.307931	203.915146	166.436279
k_{20}	0.123027	-10.459841	-10.435756	0.188557	2.138227	-15.683715
k_{30}	-0.002695	0.175900	0.564342	-0.005132	-0.415231	0.771525
k_{40}	0.000024	-0.001101	-0.008962	0.000070	0.012242	-0.012780
k_{50}	0.000000	0.000001	0.000035	0.000000	-0.000114	0.000060
k_{01}	4.718123	153.866302	818.959229	5.097194	124.732956	812.456848
k_{11}	-0.249969	27.295431	40.784904	-0.276391	29.251049	41.792465
k_{21}	0.007196	-0.877259	-1.450185	0.007851	-0.960159	-1.512921
k_{31}	-0.000071	0.004771	0.024267	-0.000079	0.006769	0.026379
k_{41}	0.000000	0.000004	-0.000161	0.000000	-0.000012	-0.000187
k_{02}	0.272982	-49.686466	6.515875	0.290866	-51.642216	6.388535
k_{12}	-0.006231	0.117729	1.830670	-0.007170	0.173029	1.856509
k_{22}	0.000139	-0.012941	-0.045299	0.000153	-0.013470	-0.045791
k_{32}	0.000000	0.000043	0.000223	0.000000	0.000050	0.000222
k_{03}	0.010718	-2.151241	-1.248892	0.011097	-2.217594	-1.257913
k_{13}	-0.000012	-0.014978	0.0246774	-0.000027	-0.013741	0.025465
k_{23}	0.000001	0.000002	0.000419	0.000001	0.000004	-0.000431
k_{04}	0.000227	-0.033241	-0.038067	0.000230	-0.03405	-0.038252
k_{14}	0.000001	-0.000171	0.000057	0.000001	-0.000158	0.000061
k_{05}	0.000002	-0.000184	-0.000323	0.000002	-0.000189	-0.000324

Table A.3: PolyM main field model coefficients for January and December 2003.

	January			December		
Coef.	D	H	Z	D	H	Z
k_{00}	25.014049	24422.687500	-16008.557617	20.798462	25398.058594	-15782.083008
k_{10}	-2.823938	417.027649	84.822639	-2.326875	236.069702	46.316582
k_{20}	0.149486	-17.622253	-9.315380	0.120527	-3.997045	-6.838222
k_{30}	-0.003524	0.455783	0.533727	-0.002557	-0.041227	0.462465
k_{40}	0.000037	-0.006362	-0.008637	0.000021	0.002502	-0.007653
k_{50}	0.000000	0.000040	0.000034	0.000000	-0.000022	0.000028
k_{01}	5.133140	146.109467	827.745056	4.741321	179.072571	859.839111
k_{11}	-0.277363	27.709030	39.745056	-0.25638	26.151333	36.866131
k_{21}	0.008130	-0.892904	-1.409329	0.007712	-0.840181	-1.312744
k_{31}	-0.000087	0.004602	0.023550	-0.000081	0.003454	0.022197
k_{41}	0.000000	0.000009	-0.000154	0.000000	0.000023	-0.000150
k_{02}	0.296424	-50.599869	6.819195	0.279085	-49.262367	8.623961
k_{12}	-0.007087	0.140365	1.816170	-0.006463	0.122884	1.723397
k_{22}	0.000156	-0.013898	-0.045267	0.000154	-0.013600	-0.043607
k_{32}	0.000000	0.000047	0.000225	0.000001	0.000051	0.000207
k_{03}	0.011428	-2.187744	-1.254703	0.011064	-2.151057	-1.210391
k_{13}	-0.000023	-0.014926	0.023550	-0.000011	-0.014788	0.023501
k_{23}	0.000001	0.000005	-0.000422	0.000001	0.000000	-0.000419
k_{04}	0.000239	-0.033925	-0.038381	0.000236	-0.033220	-0.037839
k_{14}	0.000001	-0.000174	0.000060	0.000001	-0.000168	0.000050
k_{05}	0.000002	-0.000189	-0.000326	0.000002	-0.000183	-0.000323

Table A.4: PolyM main field model coefficients for January and December 2004.

	January			December		
Coef.	D	H	Z	D	H	Z
k_{00}	31.481194	24240.369141	-15724.206055	21.992994	24292.335938	-16107.728516
k_{10}	-3.979970	419.547943	52.843754	-2.348363	497.820404	132.088837
k_{20}	0.240190	-17.117367	-7.386899	0.122006	-27.602161	-14.019315
k_{30}	-0.007259	0.456534	0.473727	-0.002709	0.968776	0.747656
k_{40}	0.000114	-0.006878	-0.007572	0.000025	-0.018046	-0.013017
k_{50}	-0.000001	0.000047	0.000026	0.000000	0.000138	0.000067
k_{01}	5.532511	92.348823	877.473083	5.015568	167.021042	887.615234
k_{11}	-0.311969	32.403175	37.373146	-0.263715	27.670496	36.811298
k_{21}	0.009057	-1.027606	-1.373146	0.007694	-0.930599	-1.384267
k_{31}	-0.000096	0.007472	0.024063	-0.000080	0.006558	0.024888
k_{41}	0.000000	-0.000014	-0.000166	0.000000	-0.000015	-0.000180
k_{02}	0.318063	-53.839035	10.449401	0.301298	-50.100609	11.290086
k_{12}	-0.008442	0.339614	1.704059	-0.007074	0.160924	1.653361
k_{22}	0.000179	-0.015321	-0.043554	0.000154	-0.013088	-0.043172
k_{32}	-0.000001	0.000057	0.000213	0.000001	0.000039	0.000207
k_{03}	0.012021	-2.273592	-1.136768	0.0118154	-2.175045	-1.127500
k_{13}	-0.000047	-0.010023	0.023059	-0.000029	-0.013218	0.022118
k_{23}	0.000001	-0.000014	-0.000414	0.000001	-0.000004	-0.000415
k_{04}	0.000246	-0.034586	-0.036378	0.000246	-0.033182	-0.036601
k_{14}	0.000000	-0.000128	0.000048	0.000001	-0.000154	0.000042
k_{05}	0.000002	-0.000186	-0.000312	0.000002	-0.000179	-0.000316

Table A.5: PolyM main field model coefficients for February and December 2005.

	February			December		
Coef.	D	H	Z	D	H	Z
k_{00}	24.530907	25089.111328	-15546.500976	24.576349	25189.017578	-16020.481445
k_{10}	-2.909584	264.621063	-2.643878	-2.701355	227.427093	89.711990
k_{20}	0.170228	-4.917253	-3.091601	0.146006	-0.970553	-10.779878
k_{30}	-0.004743	-0.055486	0.322699	-0.003521	-0.246137	0.638563
k_{40}	0.000068	0.003660	-0.005099	0.000039	0.008101	-0.011265
k_{50}	-0.000000	-0.000037	0.000010	0.000000	-0.000076	0.000056
k_{01}	5.047962	146.869614	883.399475	5.271298	139.344772	882.485718
k_{11}	-0.268478	27.750978	34.942989	-0.281240	27.715444	34.996696
k_{21}	0.007851	-0.926479	-1.286241	0.008437	-0.894004	-1.313682
k_{31}	-0.000078	0.005625	0.022213	-0.000092	0.004674	0.023609
k_{41}	0.000000	-0.000003	-0.000150	0.000000	-0.000008	-0.000168
k_{02}	0.300958	-51.807133	9.965588	0.317386	-53.008022	9.983193
k_{12}	-0.007131	0.170137	1.631593	-0.007490	0.224088	1.613099
k_{22}	0.000163	-0.014493	-0.043108	0.000167	-0.014754	-0.042642
k_{32}	-0.000001	0.000047	0.000213	0.000001	0.000048	0.000208
k_{03}	0.011787	-2.242635	-1.195049	0.012427	-2.281282	-1.208771
k_{13}	-0.000024	-0.013893	0.021728	-0.000033	-0.012280	0.021740
k_{23}	0.000001	-0.000016	-0.000411	0.000001	-0.000019	-0.000413
k_{04}	0.000247	-0.034668	-0.038118	0.000258	-0.035011	-0.038531
k_{14}	0.000001	-0.000166	0.000039	0.000001	-0.000152	0.000041
k_{05}	0.000002	-0.000192	-0.000328	0.000002	-0.000191	-0.000332

Appendix B: The PolyM SV model coefficients for D, H, Z and F at 0.8 km altitude

Table B.1: PolyM SV model coefficients for D, H, Z and F in 2001.

Coef.	D	H	Z	F
k_{00}	-17.515387	155.973938	-182.359558	212.526916
k_{10}	1.486980	-16.253424	11.778560	-17.668518
k_{20}	-0.051052	0.593836	-0.134044	0.448978
k_{30}	0.000508	-0.006549	-0.000188	-0.003606
k_{01}	-2.835594	12.064991	-10.325313	12.440616
k_{11}	0.083538	-0.509539	0.401645	-0.478600
k_{21}	-0.000833	0.005390	-0.000516	0.002757
k_{02}	-0.097202	0.257226	-0.096987	0.162936
k_{12}	0.000753	-0.005170	0.004007	-0.004261
k_{03}	-0.001047	0.001363	0.000256	0.000306

Table B.2: PolyM SV model coefficients for D, H, Z and F in 2002.

Coef.	D	H	Z	F
k_{00}	-17.010551	124.990471	-250.104858	263.647034
k_{10}	1.958858	-10.879457	16.757252	-19.883448
k_{20}	-0.070497	0.366370	-0.277384	0.467367
k_{30}	0.000726	-0.003423	0.001419	-0.003260
k_{01}	-2.604044	11.885235	-13.241467	15.385441
k_{11}	0.094455	-0.351736	0.530421	-0.536431
k_{21}	-0.001180	0.002510	-0.002127	0.003454
k_{02}	-0.084938	0.320015	-0.143544	0.248260
k_{12}	0.000745	-0.005209	0.004877	-0.004850
k_{03}	-0.000836	0.002280	-0.000037	0.001247

Table B.3: PolyM SV model coefficients for D, H, Z and F in 2003.

Coef.	D	H	Z	F
k_{00}	-7.943142	207.502579	-223.546554	238.122131
k_{10}	-0.687071	-28.973209	13.649333	-23.870306
k_{20}	0.050796	1.292884	-0.147054	0.785785
k_{30}	-0.000775	-0.017568	-0.000270	-0.009293
k_{01}	-3.596575	13.343215	-12.831584	13.141871
k_{11}	0.071546	-0.486333	0.473571	-0.4405655
k_{21}	-0.000105	0.005150	-0.000484	0.001201
k_{02}	-0.129464	0.316787	-0.172394	0.234014
k_{12}	0.001176	-0.005413	0.005320	-0.005105
k_{03}	-0.001219	0.002037	0.000337	0.001123

Table B.4: PolyM SV model coefficients for D, H, Z and F in 2004.

Coef.	D	H	Z	F
k_{00}	-31.365240	83.279724	-298.204590	269.485046
k_{10}	1.496794	-3.948256	22.350540	-20.856300
k_{20}	-0.007385	0.016147	-0.512495	0.475174
k_{30}	-0.000234	0.001439	0.004478	-0.003165
k_{01}	-4.548652	12.464340	-14.499251	15.500732
k_{11}	0.164621	-0.372165	0.589118	-0.597764
k_{21}	-0.001499	0.002192	-0.002854	0.004106
k_{02}	-0.123486	0.334911	-0.184343	0.251270
k_{12}	0.001746	-0.005874	0.005560	-0.005486
k_{03}	-0.001017	0.002127	-0.000474	0.001257

Table B.5: PolyM SV model coefficients for D, H, Z and F in 2005.

Coef.	D	H	Z	F
k_{00}	-26.198227	95.043800	-249.555222	234.636642
k_{10}	2.576878	-8.935762	18.498241	-19.640516
k_{20}	-0.095512	0.356295	-0.397646	0.548443
k_{30}	0.001150	-0.004391	0.003022	-0.005270
k_{01}	-3.095240	10.468071	-10.065312	11.300705
k_{11}	0.081204	-0.350474	0.445757	-0.440725
k_{21}	-0.000610	0.003108	-0.001811	0.002606
k_{02}	-0.108652	0.250260	-0.096824	0.166888
k_{12}	0.001001	-0.004271	0.004058	-0.003967
k_{03}	-0.001093	0.001486	-0.000057	0.000816

Appendix C: The coefficients of SCHA main field models at CHAMP satellite altitude

Table C.1: The SCHA coefficients for 2001 main field models at CHAMP satellite altitude.

				January		December	
k	m	$n_k(m)$	K_{mn}	$g_{n_k}^{m,i}$	$h_{n_k}^{m,i}$	$g_{n_k}^{m,i}$	$h_{n_k}^{m,i}$
0	0	0.0000	0.100000E+01	96.846		101.211	
1	0	7.1493	0.100000E+01	15.431		6.075	
1	1	5.4224	0.417495E+01	-65.400	10.077	-62.326	15.261
2	1	11.7070	0.862878E+01	61.285	-25.047	56.524	-22.547
2	2	9.3168	0.168142E+02	18.749	-26.856	6.562	-16.403
3	1	16.4882	0.120133E+02	-55.322	21.980	-51.305	18.380
3	2	15.8857	0.472426E+02	-8.961	17.886	-0.795	12.655
3	3	13.0083	0.708784E+02	3.784	-2.006	2.521	-3.306
4	1	21.8369	0.157986E+02	22.783	-9.206	21.053	-7.299
4	2	20.8844	0.806191E+02	4.330	-9.461	0.156	-6.974
4	3	19.8810	0.246803E+03	-0.761	2.200	0.346	3.124
4	4	16.6055	0.304013E+03	-0.530	0.938	-0.572	0.748

Table C.2: The SCHA coefficients for 2002 main field models at CHAMP satellite altitude.

k	m	$n_k(m)$	K_{mn}	January $g_{n_k}^{m,i}$	January $h_{n_k}^{m,i}$	December $g_{n_k}^{m,i}$	December $h_{n_k}^{m,i}$
0	0	0.0000	0.100000E+01	96.351		80.935	
1	0	7.1493	0.100000E+01	6.443		9.553	
1	1	5.4224	0.417495E+01	-65.961	11.376	-70.143	13.900
2	1	11.7070	0.862878E+01	61.398	-19.151	64.175	-14.492
2	2	9.3168	0.168142E+02	6.397	-15.481	-9.005	-3.886
3	1	16.4882	0.120133E+02	-56.127	17.116	-56.801	10.797
3	2	15.8857	0.472426E+02	-1.130	11.623	10.285	4.733
3	3	13.0083	0.708784E+02	2.906	-2.012	1.388	-3.569
4	1	21.8369	0.157986E+02	23.370	-6.934	22.560	-3.466
4	2	20.8844	0.806191E+02	0.335	-6.404	-4.728	-2.866
4	3	19.8810	0.246803E+03	-0.350	2.622	0.761	2.982
4	4	16.6055	0.304013E+03	-0.780	0.183	0.602	-0.126

Table C.3: The SCHA coefficients for 2003 main field models at CHAMP satellite altitude.

k	m	$n_k(m)$	K_{mn}	January $g_{n_k}^{m,i}$	January $h_{n_k}^{m,i}$	December $g_{n_k}^{m,i}$	December $h_{n_k}^{m,i}$
0	0	0.0000	0.100000E+01	88.730		84.379	
1	0	7.1493	0.100000E+01	5.494		3.336	
1	1	5.4224	0.417495E+01	-69.600	12.858	-89.193	4.863
2	1	11.7070	0.862878E+01	63.664	-13.059	86.654	4.423
2	2	9.3168	0.168142E+02	-5.936	-4.257	-18.624	5.793
3	1	16.4882	0.120133E+02	-56.927	11.269	-76.662	-4.488
3	2	15.8857	0.472426E+02	7.690	5.377	15.572	0.122
3	3	13.0083	0.708784E+02	1.795	-2.687	0.431	-3.471
4	1	21.8369	0.157986E+02	23.500	-4.298	31.157	2.363
4	2	20.8844	0.806191E+02	-3.772	-3.088	-7.419	-0.336
4	3	19.8810	0.246803E+03	0.278	2.784	1.695	3.082
4	4	16.6055	0.304013E+03	0.381	0.109	0.805	-0.363

Table C.4: The SCHA coefficients for 2004 main field models at CHAMP satellite altitude.

k	m	$n_k(m)$	K_{mn}	January $g_{n_k}^{m,i}$	January $h_{n_k}^{m,i}$	December $g_{n_k}^{m,i}$	December $h_{n_k}^{m,i}$
0	0	0.0000	0.100000E+01	82.807		86.178	
1	0	7.1493	0.100000E+01	1.331		-4.660	
1	1	5.4224	0.417495E+01	-78.638	15.151	-80.861	7.620
2	1	11.7070	0.862878E+01	73.119	-8.814	72.753	7.000
2	2	9.3168	0.168142E+02	-20.890	10.086	-27.662	19.898
3	1	16.4882	0.120133E+02	-64.589	7.887	-62.700	-5.972
3	2	15.8857	0.472426E+02	17.543	-4.643	21.256	-9.679
3	3	13.0083	0.708784E+02	0.549	-2.528	-0.826	-2.666
4	1	21.8369	0.157986E+02	26.291	-2.758	24.945	2.815
4	2	20.8844	0.806191E+02	-9.169	2.565	-10.200	4.970
4	3	19.8810	0.246803E+03	1.009	2.590	2.294	2.508
4	4	16.6055	0.304013E+03	-0.059	-0.182	0.519	-0.476

Table C.5: The SCHA coefficients for 2005 main field models at CHAMP satellite altitude.

k	m	$n_k(m)$	K_{mn}	January $g_{n_k}^{m,i}$	January $h_{n_k}^{m,i}$	December $g_{n_k}^{m,i}$	December $h_{n_k}^{m,i}$
0	0	0.0000	0.100000E+01	76.022		77.244	
1	0	7.1493	0.100000E+01	0.382		-2.131	
1	1	5.4224	0.417495E+01	-81.929	10.912	-77.081	12.395
2	1	11.7070	0.862878E+01	74.674	4.895	66.098	47.223
2	2	9.3168	0.168142E+02	-31.171	22.089	-39.181	32.575
3	1	16.4882	0.120133E+02	-64.444	-4.482	-55.725	-5.781
3	2	15.8857	0.472426E+02	23.656	-11.076	27.601	-16.560
3	3	13.0083	0.708784E+02	-0.850	-2.793	0.121	-2.346
4	1	21.8369	0.157986E+02	26.104	2.412	21.054	2.167
4	2	20.8844	0.806191E+02	-11.622	5.217	-12.718	8.441
4	3	19.8810	0.246803E+03	2.185	2.083	1.251	1.582
4	4	16.6055	0.304013E+03	1.072	-0.805	1.173	-0.456

Appendix D: The coefficients of SCHA main field models at 0.8 km altitude

Table D.1: The SCHA coefficients for 2001 main field models at 0.8 km altitude.

k	m	$n_k(m)$	K_{mn}	January $g_{n_k}^{m,i}$	January $h_{n_k}^{m,i}$	December $g_{n_k}^{m,i}$	December $h_{n_k}^{m,i}$
0	0	0.0000	0.100000E+01	88.180		88.143	
1	0	7.1493	0.100000E+01	14.539		8.434	
1	1	5.4224	0.417495E+01	-48.263	20.462	-45.033	22.929
2	1	11.7070	0.862878E+01	40.985	-30.384	36.775	-26.672
2	2	9.3168	0.168142E+02	18.059	-19.492	7.762	-11.202
3	1	16.4882	0.120133E+02	-35.490	23.479	-31.565	20.442
3	2	15.8857	0.472426E+02	-9.318	9.099	-2.731	5.439
3	3	13.0083	0.708784E+02	1.482	-2.774	1.078	-2.863
4	1	21.8369	0.157986E+02	17.716	-10.317	15.651	-9.199
4	2	20.8844	0.806191E+02	5.238	-4.761	1.345	-2.896
4	3	19.8810	0.246803E+03	0.249	2.744	0.385	2.540
4	4	16.6055	0.304013E+03	-0.872	-0.357	-0.639	-0.264
5	1	26.6828	0.192276E+02	-5.295	2.498	-4.580	2.521
5	2	26.3164	0.126905E+03	-1.329	1.156	-0.289	0.750
5	3	25.0785	0.489762E+03	-0.440	-1.337	-0.415	-1.063
5	4	23.7640	0.125379E+04	0.361	0.293	0.269	0.261
5	5	20.1463	0.131525E+04	0.158	0.049	0.252	0.244

Table D.2: The SCHA coefficients for 2002 main field models at 0.8 km altitude.

k	m	$n_k(m)$	K_{mn}	January $g_{n_k}^{m,i}$	January $h_{n_k}^{m,i}$	December $g_{n_k}^{m,i}$	December $h_{n_k}^{m,i}$
0	0	0.0000	0.100000E+01	87.861		71.265	
1	0	7.1493	0.100000E+01	6.516		9.382	
1	1	5.4224	0.417495E+01	-48.727	20.978	-53.666	23.835
2	1	11.7070	0.862878E+01	40.753	-25.178	45.352	-20.133
2	2	9.3168	0.168142E+02	7.221	-9.971	-5.319	0.869
3	1	16.4882	0.120133E+02	-35.235	19.613	-38.944	12.939
3	2	15.8857	0.472426E+02	-2.668	4.398	5.249	-1.124
3	3	13.0083	0.708784E+02	1.011	-2.484	-0.882	–4.231
4	1	21.8369	0.157986E+02	17.588	-8.755	19.407	–4.124
4	2	20.8844	0.806191E+02	1.384	–2.131	-2.479	0.785
4	3	19.8810	0.246803E+03	0.442	2.334	1.804	3.160
4	4	16.6055	0.304013E+03	-0.698	-0.634	0.401	-1.309
5	1	26.6828	0.192276E+02	-5.271	2.253	-5.683	0.646
5	2	26.3164	0.126905E+03	-0.378	0.441	0.344	-0.252
5	3	25.0785	0.489762E+03	-0.514	-1.025	-1.045	-1.163
5	4	23.7640	0.125379E+04	0.217	0.339	-0.258	0.648
5	5	20.1463	0.131525E+04	0.194	0.129	0.450	0.217

Table D.3: The SCHA coefficients for 2003 main field models at 0.8 km altitude.

k	m	$n_k(m)$	K_{mn}	January $g_{n_k}^{m,i}$	January $h_{n_k}^{m,i}$	December $g_{n_k}^{m,i}$	December $h_{n_k}^{m,i}$
0	0	0.0000	0.100000E+01	80.016		71.255	
1	0	7.1493	0.100000E+01	4.724		5.715	
1	1	5.4224	0.417495E+01	-53.171	24.106	-70.744	21.910
2	1	11.7070	0.862878E+01	44.511	-22.180	62.934	-13.070
2	2	9.3168	0.168142E+02	-2.959	-0.026	-14.425	10.682
3	1	16.4882	0.120133E+02	-38.361	16.766	-53.991	8.402
3	2	15.8857	0.472426E+02	3.179	-0.289	9.869	-6.159
3	3	13.0083	0.708784E+02	-0.406	-3.145	-1.614	-4.092
4	1	21.8369	0.157986E+02	19.229	-7.114	26.985	–2.890
4	2	20.8844	0.806191E+02	-1.416	0.336	-4.757	3.686
4	3	19.8810	0.246803E+03	1.353	2.647	2.258	2.886
4	4	16.6055	0.304013E+03	0.096	-1.001	0.791	-1.533
5	1	26.6828	0.192276E+02	-5.790	1.761	-7.959	0.712
5	2	26.3164	0.126905E+03	0.149	-0.137	0.868	-1.220
5	3	25.0785	0.489762E+03	-0.869	-1.086	-1.205	-1.046
5	4	23.7640	0.125379E+04	-0.083	0.512	-0.318	0.654
5	5	20.1463	0.131525E+04	0.275	0.199	1.027	0.218

Table D.4: The SCHA coefficients for 2004 main field models at 0.8 km altitude.

k	m	$n_k(m)$	K_{mn}	January $g_{n_k}^{m,i}$	January $h_{n_k}^{m,i}$	December $g_{n_k}^{m,i}$	December $h_{n_k}^{m,i}$
0	0	0.0000	0.100000E+01	73.062		74.176	
1	0	7.1493	0.100000E+01	0.478		9-2.513	
1	1	5.4224	0.417495E+01	-62.947	27.480	-65.565	23.186
2	1	11.7070	0.862878E+01	54.228	-19.294	55.404	-9.059
2	2	9.3168	0.168142E+02	-14.893	12.712	-23.877	22.616
3	1	16.4882	0.120133E+02	-46.524	14.126	-47.106	5.191
3	2	15.8857	0.472426E+02	10.159	-8.030	16.409	-13.476
3	3	13.0083	0.708784E+02	-1.073	-3.500	-2.988	-3.941
4	1	21.8369	0.157986E+02	23.289	-5.639	23.439	-0.965
4	2	20.8844	0.806191E+02	-5221	5.057	-8.822	8.348
4	3	19.8810	0.246803E+03	1.866	2.734	3.317	2.961
4	4	16.6055	0.304013E+03	0.155	-1.401	0.650	-1.585
5	1	26.6828	0.192276E+02	-6.965	1.303	-6.918	-0.090
5	2	26.3164	0.126905E+03	0.940	-1.501	2.006	-2.598
5	3	25.0785	0.489762E+03	-1.191	-1.089	-1.629	-1.132
5	4	23.7640	0.125379E+04	-0.230	0.692	-0.314	0.671
5	5	20.1463	0.131525E+04	0.538	0.077	0.736	0.193

Table D.5: The SCHA coefficients for 2005 main field models at 0.8 km altitude.

k	m	$n_k(m)$	K_{mn}	February $g_{n_k}^{m,i}$	February $h_{n_k}^{m,i}$	December $g_{n_k}^{m,i}$	December $h_{n_k}^{m,i}$
0	0	0.0000	0.100000E+01	57.936		65.299	
1	0	7.1493	0.100000E+01	2.380		-1.646	
1	1	5.4224	0.417495E+01	-61.641	25.733	-63.496	26.446
2	1	11.7070	0.862878E+01	51.881	-10.127	52.223	-6.330
2	2	9.3168	0.168142E+02	-25.982	25.075	-34.037	33.920
3	1	16.4882	0.120133E+02	-344.153	6.380	-44.124	2.714
3	2	15.8857	0.472426E+02	17.773	-14.326	22.026	-19.433
3	3	13.0083	0.708784E+02	-2.133	-3.719	-2.293	-4.068
4	1	21.8369	0.157986E+02	22.000	-1.965	21.748	0.262
4	2	20.8844	0.806191E+02	-9.877	8.533	-11.897	11.627
4	3	19.8810	0.246803E+03	2.794	2.447	2.713	2.589
4	4	16.6055	0.304013E+03	0.393	-1.358	0.929	-1.649
5	1	26.6828	0.192276E+02	-56.532	0.359	-6.361	-0.497
5	2	26.3164	0.126905E+03	2.299	-2.422	2.700	-3.402
5	3	25.0785	0.489762E+03	-1.575	-0.836	-1.522	-0.935
5	4	23.7640	0.125379E+04	-0.230	0.700	-0.398	0.818
5	5	20.1463	0.131525E+04	0.401	0.142	0.421	0.083